2024

FACETING OF TUNGSTEN VIA ENVIRONMENTAL CONTROL OF TEMPERATURE, PRESSURE AND CHEMISTRY, AND EVOLUTION OF THERMIONIC CATHODE MATERIALS

Huanhuan Bai
University of Kentucky, huanhuan.bai@uky.edu
Author ORCID Identifier:
https://orcid.org/0000-0003-0097-3286
Digital Object Identifier: https://doi.org/10.13023/etd.2024.316

Right click to open a feedback form in a new tab to let us know how this document benefits you.

FACETING OF TUNGSTEN VIA ENVIRONMENTAL CONTROL OF
TEMPERATURE, PRESSURE AND CHEMISTRY, AND EVOLUTION OF
THERMIONIC CATHODE MATERIALS

_____

DISSERTATION
_____

A dissertation submitted in partial fulfillment of the
requirements for the degree of Doctor of Philosophy in the
College of Engineering
at the University of Kentucky

By
Huanhuan Bai
Lexington, Kentucky
Director: Dr. T. John Balk, Professor of Chemical and Materials Engineering
Lexington, Kentucky
2024

ABSTRACT OF DISSERTATION

FACETING OF TUNGSTEN VIA ENVIRONMENTAL CONTROL OF
TEMPERATURE, PRESSURE AND CHEMISTRY, AND EVOLUTION OF
THERMIONIC CATHODE MATERIALS

Scandate cathode presents a great potential of being used as electron emitters in vacuum electron device due to its excellent emission performance. However, it is burdened by several issues, including poor emission uniformity, inadequate reproducibility, and limited lifetime, which have impeded its further industrial application. Therefore, extensive efforts and studies need to be conducted to obtain a more comprehensive understanding of scandate cathode.

W particles, as the base material, play a fundamental role in scandate cathode. Most recent experimental research has reported that the highly faceted crystallography of W grains contributes to the properties of scandate cathode. In order to fully understand the mechanism of W particles surface faceting, both nanoscale and bulk W were investigated in the current study.

Nano scale W particles were fabricated utilizing PVD technique. A pre-heating step was applied to these nanoscale particles in a vacuum chamber. It is found that the deposited nanoscale W network transformed into individual, highly faceted nanoparticles when first pre-heated at an intermediate temperature, followed by annealing at 1100 °C, under a pressure of 10^{-7} Torr. Wulff analysis indicated that these well-developed W particles are dominated by {110} faces.

Meanwhile, surface faceting of bulk W pellets was investigated by *in situ* heating in environmental scanning electron microscope (ESEM), which allows direct, high-fidelity observation of the morphology changes during high temperature annealing in low vacuum. Here *in situ* Environmental SEM heating was performed on W pellets with a surrounding pressure of 0.8 Torr. For comparison, another group of samples was annealed in an Ultra High Vacuum chamber (UHV). Surface faceting was observed during ESEM annealing, while UHV heating will not cause any faceting of W surface. With the combination application of EBSD, stereo imaging, as well as the Slice and View technique, it proves that the faceting of bulk W surface is {110} faces dominated, which aligns with nano W particle faceting.

Additionally, more characterization of scandate cathode was performed in this project. A series of *in situ* heating experiments were conducted on as-received un-activated impregnated scandate fragments by using a MEMS based heater chip in a modern SEM under a pressure of 10^{-6} -10^{-7} mbar. The results demonstrated the faceting, growth and migration of impregnates in cathodes at elevated temperatures, which are favorable for better understanding the behavior of scandate cathode. It was the first time to report the real time observations of scandate cathode with a high-resolution technique in a high vacuum chamber close to its actual operate condition, which will provide an insight on the morphology evolvement of impregnated materials.

Furthermore, to gain more deep understanding of cathodes, a cross-section analysis through entire cathode thickness was performed for the first-ever time by Broad ion beam milling technique, which provides a view of the full-length cathode cross section, including emitting surface and bottom of a scandate cathode. With the full-length cathode cross section available, distribution of impregnated materials and tungsten particle faceting along the cross section were observed and analyzed by SEM and EDS. The results also extensively reveal the influence of impregnated materials on W faceting, and provide a new method to evaluate the property of cathodes.

KEYWORDS: Scandate dispenser cathode, Physical Vapor Deposition, Tungsten, Faceting, *in situ* heating, Characterization.

Huanhuan Bai
(Name of Student)

07/31/2024
Date

FACETING OF TUNGSTEN VIA ENVIRONMENTAL CONTROL OF
TEMPERATURE, PRESSURE AND CHEMISTRY, AND EVOLUTION OF
THERMIONIC CATHODE MATERIALS

By
Huanhuan Bai

Dr. Thomas John Balk
Director of Dissertation

Dr. Fuqian Yang
Director of Graduate Studies

07/31/2024
Date

ACKNOWLEDGMENTS

The following dissertation, although an individual endeavor, has been enriched by the invaluable support, insights, and guidance of several individuals.

First and foremost, I would like to express my sincere gratitude to my Ph.D. advisor, Prof. Dr. T. John Balk, for providing me with the invaluable opportunity to embark on my doctoral journey in 2018. This opportunity came at a critical time in my life, as I was facing significant challenges in securing admission for my doctoral studies. What made this even more remarkable was that Dr. T. John Balk embodies the epitome of scholarly excellence that I aspire to achieve.

Throughout my entire Ph.D. study, Dr. T. John Balk has consistently been an amazing academic mentor. His unwavering enthusiasm and abundant professional guidance have played an instrumental role in molding me into a proficient scientist. Furthermore, his exceptional patience and willingness to afford me ample freedom and time to explore novel ideas and refine my skills have facilitated a profound understanding of the fundamental principles of engineering. Moreover, I express deep appreciation for the considerable amount of time that Dr. Balk dedicated to meticulously reviewing and revising my paper.

Additionally, I would like to express gratitude to Prof. Dr. Matthew J. Beck and Dr. Mujan N. Seif for their insightful discussions and invaluable feedback during our weekly cathode group meetings. Each of them offered perspectives that guided and challenged my thinking, resulting in substantial improvements to the final outcome. Furthermore, I am indebted to Prof. Dr. Martin E. Kordesch from Ohio University for his

TABLE OF CONTENTS

LIST OF TABLES

LIST OF FIGURES

xii

LIST OF EQUATIONS

$$f\varepsilon = 1e\varepsilon - \mu KT + 1$$

$$j = AT2\exp(-e\emptyset KT)$$

PV = NRT

P $\propto$ N

W (s) + O_2 (g) $\leftrightarrow$ WO_2 (s)

WO_2 (s) + ½ O_2 (g) $\leftrightarrow$ WO_3 (s)

$3WO_3$ (s) $\leftrightarrow$ $(WO_3)_3$ (g)

2 W_3O (s) = 5 W (s) + WO_2 (s)

WO_2 (g) $\rightarrow$ W (s) + O_2 (g)

WO_3 (g) $\rightarrow$ W (s) + 3/2 O_2 (g)

W (s) + O_2 (g) $\leftrightarrow$ WO_2 (s)

WO_2 (s) + ½ O_2 (g) $\leftrightarrow$ WO_3 (s)

$3WO_3$ (s) $\leftrightarrow$ $(WO_3)_3$ (g)

LIST OF ACRNOYMS

ALD – Atomic Layer Deposition

BIB – Broad ion beam

BSE – Backscattered Electron

CBS – Concentric Backscatter

CCC – Cathode Characterization Chamber

CVD – Chemical Vapor Deposition

DC – Direct Current

EBSD – Electron Backscatter Diffraction

EDS – X-Ray Energy Dispersive Spectroscopy

FIB – Focused Ion Beam

ICD – In Column Detector

LAD – Laser Ablation Deposition

MD – Mirror Detector

PVD – Physical Vapor Deposition

SEM – Scanning Electron Microscopy / Microscope

SE – Secondary Electron

TLD – Through Lens Detector

TEM – Transmission Electron Microscope

UHV – Ultra-High Vacuum

XPS – X-ray photoelectron spectroscopy

CHAPTER 1. INTRODUCTION

1.1   Introduction to Dissertation

This dissertation generally covers two aspects of tungsten-based dispenser cathodes related work: fundamental studies of tungsten surface faceting and advanced/updated materials characterizations of scandate tungsten-based dispenser cathodes.

The fundamental studies of tungsten surface faceting include studies of faceting of both nano scale tungsten particles (generated by Physical Vapor Deposition method) and bulk tungsten pellet (made of micron scale tungsten grains), which will be discussed in detail in chapter 5 and 6, respectively. The reason why tungsten came to this subject was because nowadays dispenser cathode commonly applies tungsten as matrix – typically, the tungsten particle in dispenser cathode is micron scale, but based on recent report [1, 2], it can be nanoscale as well, which was the reason why both nano scale and bulk tungsten were studied in this work. Meanwhile, recent research [3, 4] has shown that scandate dispenser cathodes have highly faceted tungsten grains when they exhibit good emission performance. The research in this dissertation explored the process and mechanism of tungsten faceting- in both micron scale and nano scale, aimed to provide insight into the possibility of optimizing and/or controlling tungsten surface faceting, which shall probably eventually contribute to improving the emission performance of scandate dispenser cathode.

The advanced materials characterizations of scandate dispenser cathode include *in situ* observation of scandate dispenser cathode at high temperature in a pressure close to the real operating pressure of a cathode. Because when dispenser cathode being used a thermionic emitter, it is operated at high temperature under a high vacuum environment,

1

besides dispenser cathode traditionally is made of nanoscale and/or micron scale materials, thus it is extremely challenging to observe the behavior of materials in dispenser cathode in real time with a high resolution. The work in this dissertation presents the first-ever time observations on scandate cathode in a real time, revealed the behavior of impregnated materials during the heating process.

Another updated method of materials characterization of scandate dispenser cathodes in this dissertation is full length cross sectioning of dispenser cathode with Broad ion beam (BIB) milling technique. Using this technique, the entire cross section of the cathode becomes available for observation. With the combination of scanning electron microscopy (SEM) and Energy Dispersive X-Ray Spectroscopy (EDS), the distribution of the impregnates and the faceting of tungsten faceting were revealed and discussed in this dissertation.

1.2   Outline of Dissertation

This dissertation starts with an opening chapter (chapter 2) introducing the perspective and scientific background of thermionic cathodes, which provides an overview of dispenser cathodes and the historical progress on this topic. Meanwhile, thin film deposition techniques (such as vacuum technology and physical vapor deposition) will be introduced briefly in this beginning chapter, as well. Moreover, motivation and goal of this dissertation will be talked about in this chapter, too.

Following that, the dissertation moves to the materials and methods chapter (chapter 3), where samples and equipment involved in the work will be described. It will cover a brief introduction of nanoparticle generator and methods for materials characterization.

Details of nanoparticle generator will be depicted in Chapter 4, since this is custom-made equipment, parameters' exploration process will be included in detail. The effect of each parameter on the deposited samples will be extensively discussed in this chapter. Furthermore, characterization of nanoparticles on copper will be presented, and deposition on different substrates will be discussed summarily as well.

Then the dissertation moves to the following chapter with focuses on the thermally induced faceting of nano scale tungsten particles (chapter 5). To study the influence of temperature and pressure on the stability and morphology of tungsten nanoparticles, a multitude of varying pre-heating steps were applied to these nanoscale tungsten particles in a vacuum chamber. The morphology and structure of the annealed tungsten particles were investigated by a series of materials characterization techniques including SEM, EDS and XPS.

As a comparison, bulk tungsten surface faceting will be reported in Chapter 6, where crystallographic faceting of bulk tungsten surfaces observed during *in situ* heating in an environmental SEM will be explored thoroughly. Additionally, a second set of tungsten samples annealed in an ultra-high vacuum chamber (10^{-8} Torr) is included in this chapter as well. More importantly, this chapter discusses relevant techniques for identifying the crystallographic indices of surface facets, will could be critical to the research of surface faceting indexing.

Then the following two chapters (chapter 7 and chapter 8) present the results of new characterization techniques applied to scandate dispenser cathodes. Chapter 7 talks about the results of *in situ* heating of scandate cathode particles in a high vacuum chamber

on a MEMS heater, and chapter 8 illustrates the full-length cross-sectioning characterization of various stages of scandate dispenser cathodes.

Last but not least, chapter 9 concludes the dissertation with the highlight and key findings of this dissertation and will look forward to the work that could be done in the future with the results presented in the chapters above.

2.1   *Thermionic Emission*

At the beginning of this present work, it is worth pointing out that nowadays 'cathode' is conventionally used to describe the materials in batteries, for instance, in Lithium battery, the 'cathode' is the sink for the lithium ions [5]. However, in this dissertation, the 'cathode' is a material, which is mainly a tungsten (W) based material now, used at specific occasions as thermionic emitters, details discussed below.

2.1.1   Thermionic Emission- Definition

To better define 'cathode', it is essential to know the phenomenon *Thermionic emission* which is first established by Thomas A. Edison when he discovered that electron escapes from hot filaments in 1883, thus this phenomenon was also named 'Edison Effect' and at that time 'electron' was called 'carrier' [6]. Despite that, as early as in 1873, this phenomenon had drawn the attention of Frederick Guthrie when he researched the relation between heat and electricity [7], but at that time his attention was primarily focused on heat and current when he performed his experiment. Until in 1897, Joseph John Thomson (or J. J. Thomson) proposed his assumption and demonstrated that those 'carriers' in 'Edison Effect' were negatively electrified 'particles' when he further researched *cathode* rays [8, 9] , Figure 2.1 is the schematic of equipment of his experiment, in which *C* represented the cathode. While those 'particles' were called 'electrons' several years later [6] by Larmor [10]. Because of this breaking through achievement on electrons, J. J. Thomson was awarded Nobel Prize in 1906 [11]. Hence it could be seen that as early as in 1897 of J. J. Thomson's research, the 'hot filament' or the equivalent role was called '*cathode*'.
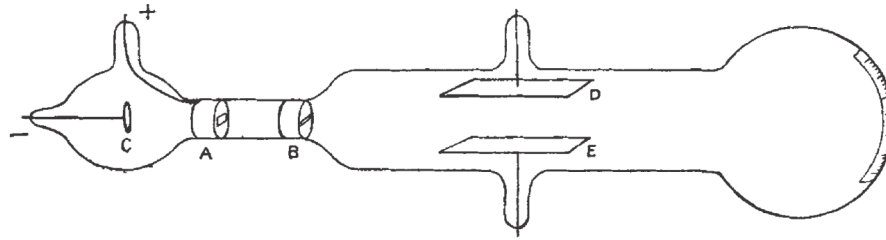
Figure 2.1 Schematic of equipment in J. J. Thomson paper [7]

From then on, thermionic emission drew lots of attention from researchers and it is gradually better understood and developed both theoretically and experimentally. In 1909, O. W. Richardson [12] first suggested the word 'thermionic' because it can literally describe thermal, electron and even ion of this phenomenon. In 1934, Arnold L. Reimann [13] defined 'thermionic emission' as a phenomenon happens when a conductive body is heated to a sufficiently high temperature, electrically charged particles which may be electrons or ions, are emitted from it and might be drawn off by a suitable electric field. Reimann also pointed out that 'thermionic emission' is basically 'thermal electron emission' in his book [13]. Later in 1956, this phenomenon is identified as 'the emission of electrons across the boundary surface that separates a heated electronic conductor from an otherwise nonconducting space' in W.B. Nottingham's research [14]. Based on description from both W. B. Nottingham and Arnold L. Reimann, there are two principal components, electron emission and heated conductors, in the term 'thermionic emission'. Hence the conductors which could emit electrons during heating are 'cathode' in current work.

2.1.2   Mechanism of Thermionic Emission

It is well demonstrated by both classic physics and modern physics that free electrons mobile with different velocities within conductors. The distribution of their

velocities is called Fermi-Dirac distribution, which can be described with equation (1) as following [15]:

$$f(\varepsilon) = \frac{1}{e^{\frac{\varepsilon - \mu}{KT}} + 1} \tag{1}$$

where $f(\varepsilon)$ is the probability that an orbital at energy ϵ will be occupied by ideal electrons, μ is referred to as the Fermi level, while K is Boltzmann's constant, and finally T is absolute temperature (K).

According to equation (1), distribution of electron velocities depends upon temperature, that is, more electrons intend to have higher velocities as the temperature rises. Electrons are eventually able to surmount the potential energy barrier of surface when they have sufficient high velocities at high temperature [6, 10, 16], as depicted in Figure 2.2. The barrier of surface which keeps electrons from getting out of conductors is nowadays called 'work function' [17], the strict definition of which is the energy required for an electron to move from Fermi level to vacuum level [18]. Above is a brief interpretation of the mechanism of thermionic emission.
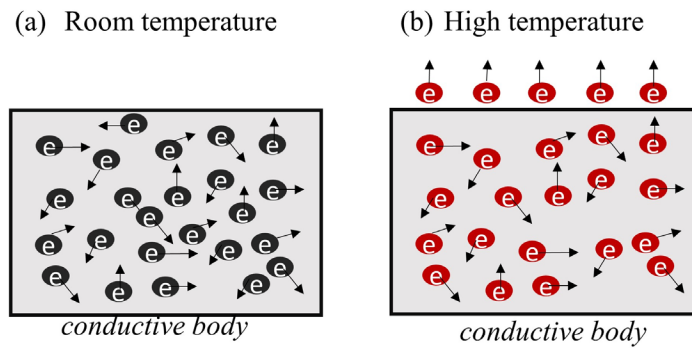
Figure 2.2 Mechanism of thermionic emission: electrons stay in the conductive body at room temperature and will be able to emit from the surface when temperature is high enough.

The early development of quantitative theory of thermionic emission relied significantly on the success of electrons theory, O. W. Richardson [6, 12, 19] was one of pioneers who dedicated decade of years on it, he derived the thermionic emission density equation (2) as:

$$j = AT^2 \exp\left(-\frac{e\emptyset}{KT}\right) \qquad\qquad (2)$$

Where j is current density during thermionic emission (A/cm^2), $A = \frac{4\pi k^2}{h^3}$, $\emptyset$ is work function (eV), K and T are Boltzmann's constant and absolute temperature, separately, just as same as they are in equation (1). But later researchers, for instance, Child and Langmuir [6], gradually realized that thermionic emission is more dependent on properties of materials, even different shape of cathodes have different thermionic emission intensity. Therefore, increasing interest has been raised on what kind of materials could be more suitable as thermionic emitters and how to optimize those materials.

Nowadays, thermionic emission materials are extensively applied in such fields requiring high current and high reliability as cathode ray tubes, transmission and receiving tubes, x-ray sources and various electron beam machines [19], here the thermionic emission materials are also named as 'cathodes' in this dissertation.

2.2   Cathodes

2.2.1   Application of Cathodes

As the earliest commercialized material of cathode, one of W materials well-known application is as a light source in electric bulbs invented by General Electric Company at 1900s [19]. Another well-known but unfortunately no longer prevail application of cathode is to produce the electron beam for television which had a fluorescent screen [18, 20], the

reason why it is not prevail any longer is that new technology, like LCD or OLED screen, has been applied for television.

Meanwhile, since the beginning of vacuum tube industry in the 20th century, cathode has been extensively used for civilian communication, space as well as military, as an electron source in varies of vacuum devices, including electron microscope, travelling wave tube, high-power microwave devices [3, 4, 18, 21, 22]. Figure 2.3 [18] shows a schematic of a traveling wave-tube amplifier which uses cathode to generate electron beam. Besides, cathodes can also be applied to industrial heating, medical treatment, and scientific research [23].
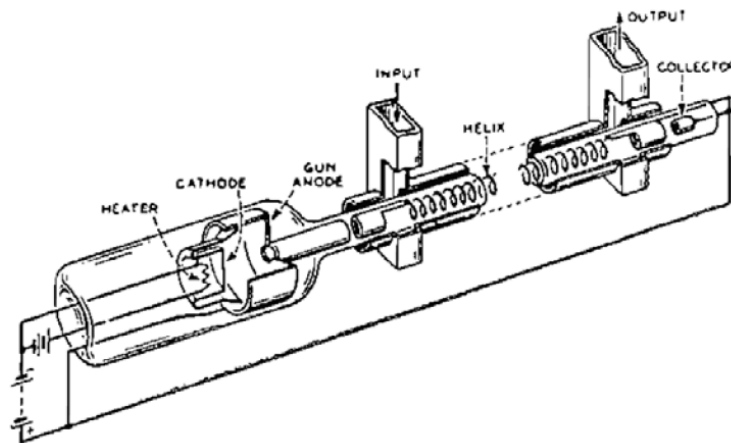
Figure 2.3 A schematic of a traveling wave-tube amplifier, cathode is located between heater and gun anode [18].

Above is an outline of cathode's application. Perhaps partially because of its use in military, in spite of the considerable demand of high-performance cathode, only few of academic researchers have explored the details of cathode's application, like whether all the devices need same high-level performance cathode, what kind of cathode is currently used in equipment. Yan-Wen Liu et.al. [24] particularly pointed it out that cathodes, as electron sources, are critical for high-power microwave source which are used in areas like

radar, space technology, electron accelerator and free-electron lasers because their performances highly depend on the properties of microwave source. Diana Gamzina [25] specifically stated that micro vacuum electronic devices have a wide application such as remote and early detection of chemical and biological warfare agents, high resolution imaging of biological system, high data rate communication, airborne synthetic aperture radar for detecting condition of bad weather and medical imaging for detecting early cancer and tooth decay.

2.2.2   Historical Review of Cathodes

As described above, thermionic emission theoretically happens on conductors. Metals, as the most universal natural conductors, were consequently considered as potential materials of cathode for thermionic emission. At the same time, since cathode needs to be heated at high temperature to have thermionic emission, so refractory metal, such as W (melting point 3422 °C), was the firstly considered material for cathode. Meanwhile, as mentioned above, current density during thermionic emission highly depends on work function (as described in equation (2)), while work function is a property depends on materials, environment and its surface property. Yamamoto [19] summarized that work function of single elements depends linearly on electronegativity; for binary compounds, the work function is primarily determined by one of the component elements [19], additionally, work function changes when the surface absorbs atom and molecules, therefore work function of surface in vacuum environment will be significantly different from it when exposed in air. Mantica [26] also observed that when metals with different work function contact each other thermally and electrically, the final work function will go

somewhere between the individual metals. With those findings, lots of effort has been made to modify the surface of cathodes to lower the work function [19], such as using the cathode in a high vacuum chamber, coating the surface of a cathode with a layer of thin metal film, or fill the cathode with alkali-earth oxides [19]. Figure 2.4 shows the development history of cathodes and their electron emission capacities at 1030 °C during the past 100 years. Herein most of the cathodes will be briefly introduced.
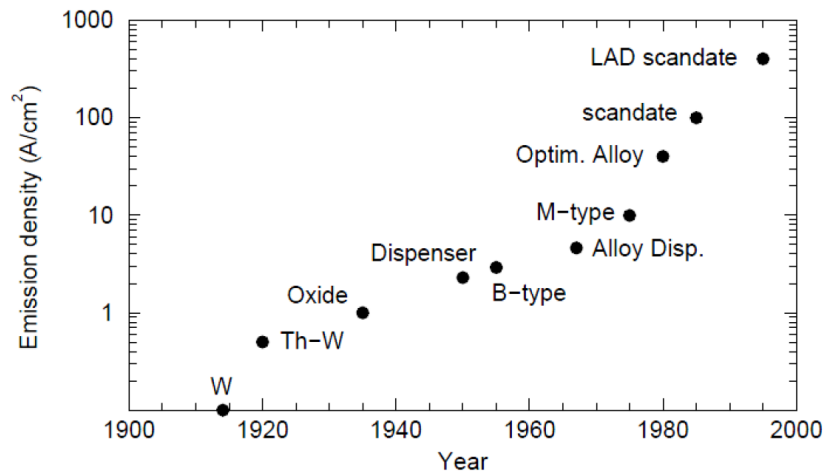
Figure 2.4 Development of emission capacities of different cathodes in past 100 years [25].

2.2.3 W and Th-W Cathodes

W cathode is developed by Langmuir et al [6, 19]and is the first commercialized cathode because it exhibits a relative high current density close to 1 A/cm^2, the disadvantage of W cathode is it has high work function, which means it is quite energy consuming. Later it was found that electron emission density of W cathode could be enormously improved when adding ThO$_2$ on the top of W cathode, which was called Th-W cathode subsequently which turned out to be the earliest mode of modern cathodes due to its structure. The problem of Th-W cathode is the additive ThO$_2$, is a radioactive material which could probably be unharmonious for humans.

11

2.2.4 Oxide Cathodes

Oxide cathode has been widely used in numerous areas since it was developed by Wehnelt in 1904 [19]. As aforementioned, cathodes were applied as electron source in television in early years, at that time the cathode was the oxide cathode. Due to its excellent reliability and stability, low work function plus low production cost, it was even claimed that '*no other cathode can and will be able to catch up with oxide cathode*' in 2006 [19]. Whereas, its emission capacity, which is limited by its Ni substrate materials, is only slightly higher than 1 A/cm^2. Figure 2.5 is the schematic of typical oxide cathode which has BaO materials on the top of substrate to reduce work function of cathode.
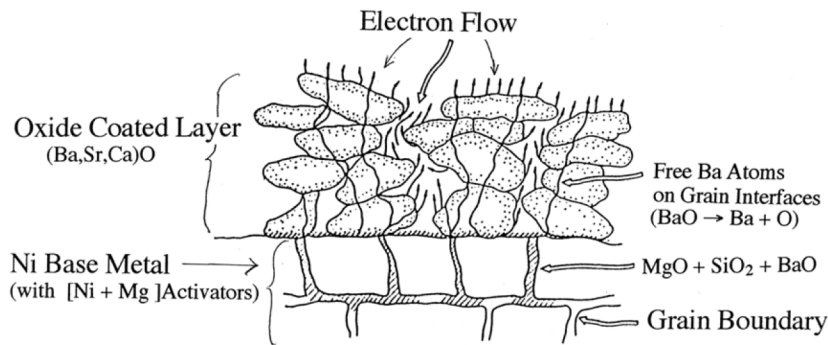
Figure 2.5 Schematic of typical oxide cathode with Ni based metal as substrate [19]

2.2.5 Impregnated Cathodes

To improve electron emission capacity of cathode, Philips Research Laboratories developed a series of cathodes since 1950, which includes dispenser cathode, B type cathode, M type cathode, Scandate cathode and LAD cathode. These cathodes apply porous tungsten as the matrix and BaO materials as impregnant – a monolayer of BaO will form on the top of cathode during thermionic emission, which will lower the work function

significantly to about 2.1 eV [19] and eventually enhance the emission performance of cathodes.

The name of 'Dispenser cathode' was used to describe a stream of electron emission from the cathode during thermionic emission [18]. Figure 2.6 show a schematic of typical dispenser cathode design [27], due to which structure they also are named impregnated cathode. Because of their high electron emission capacity (more than 5 A/cm^2), those cathodes are also called high current density cathodes. The drawback of those cathodes, for instance, scandate cathode, is lack of repeatability and stability, which limits their commercial use [1, 28, 29].
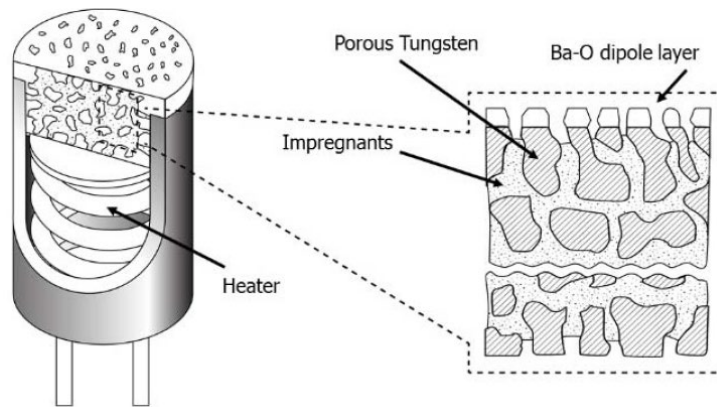
Figure 2.6 Schematic of typical dispenser cathode [27]

Here several impregnated cathodes that nowadays attract most attention from industry and academy will be introduced [4, 19]:

2.2.5.1 B type Cathodes

Standard cathodes use porous tungsten as matrix and apply a mixture of BaO-CaO-Al$_2$O$_3$ as impregnated materials. Depending on the ratio of the mixture, there are serval different types of standard cathodes: A type cathode, B type cathode, and S type cathode where A type cathode only has BaO and Al$_2$O$_3$ as impregnated materials, while the mole

ration of the mixture of BaO-CaO-Al$_2$O$_3$ in B type cathode and S type cathode are 5:3:2 and 4:1:1, respectively. Figure 2.7 illustrates the morphology of an un-activated B type cathode, indicates that the cathode has porous structure and it has impregnated materials.
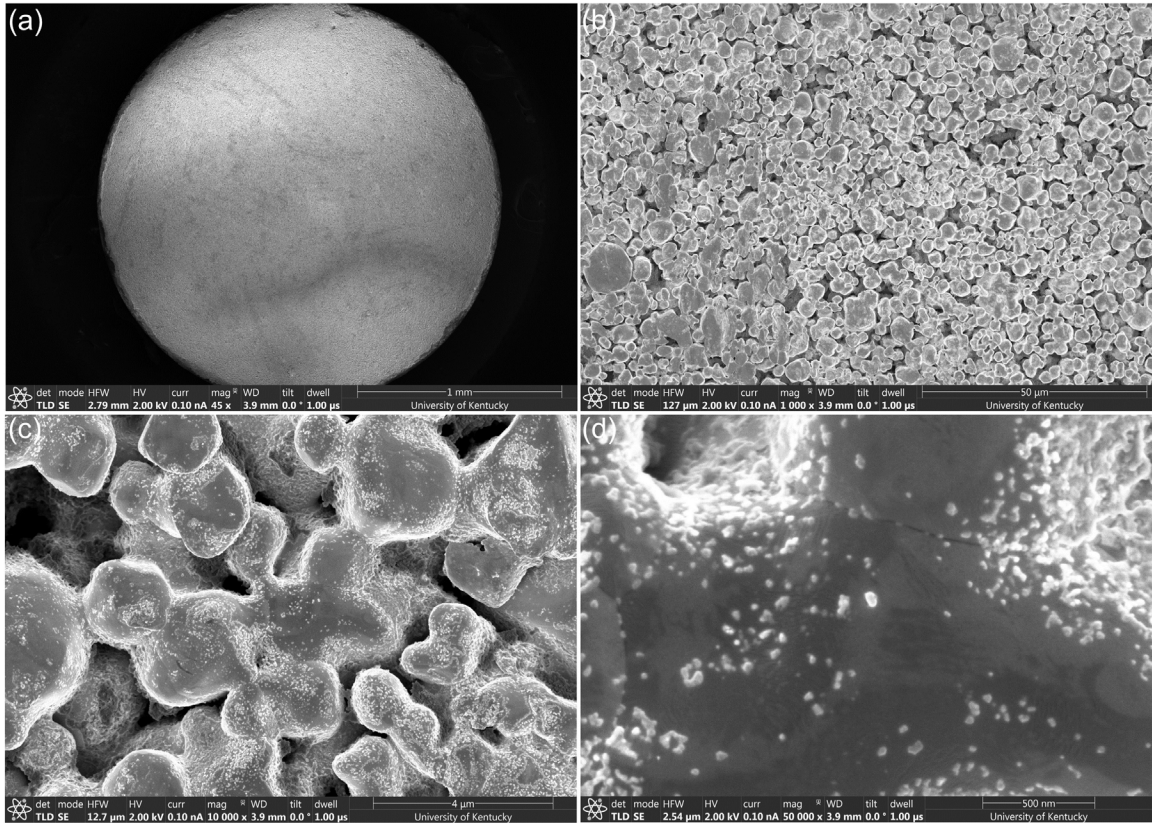
Figure 2.7 Micrography of an un-activated B-type cathode: (a) overview of the cathode pellet; (b) high resolution SE image shows the tungsten grains in the cathode; (c) zoomed in images shows the porous structure of the cathode; (d) higher resolution image of (c) showing the nanoscale impregnates on the tungsten grain.

2.2.5.2 M type Cathodes

M type cathode applies a layer of coating (Osmium, Iridium or Rhenium) on standard cathode, the coating of which could be 0.1-1.0 μm thick. Because the current density of this cathode is so high that its operation temperature can be lower as much as 100 °C, it was named as 'Magic cathode' or 'M cathode'. Figure 2.8 presents the SEM

results of an un-activated M type cathode with 4BaO-1CaO-1Al$_2$O$_3$ impregnates from 3M (Saint Paul, MN, USA), where the topography images show that the tungsten grains are coated.
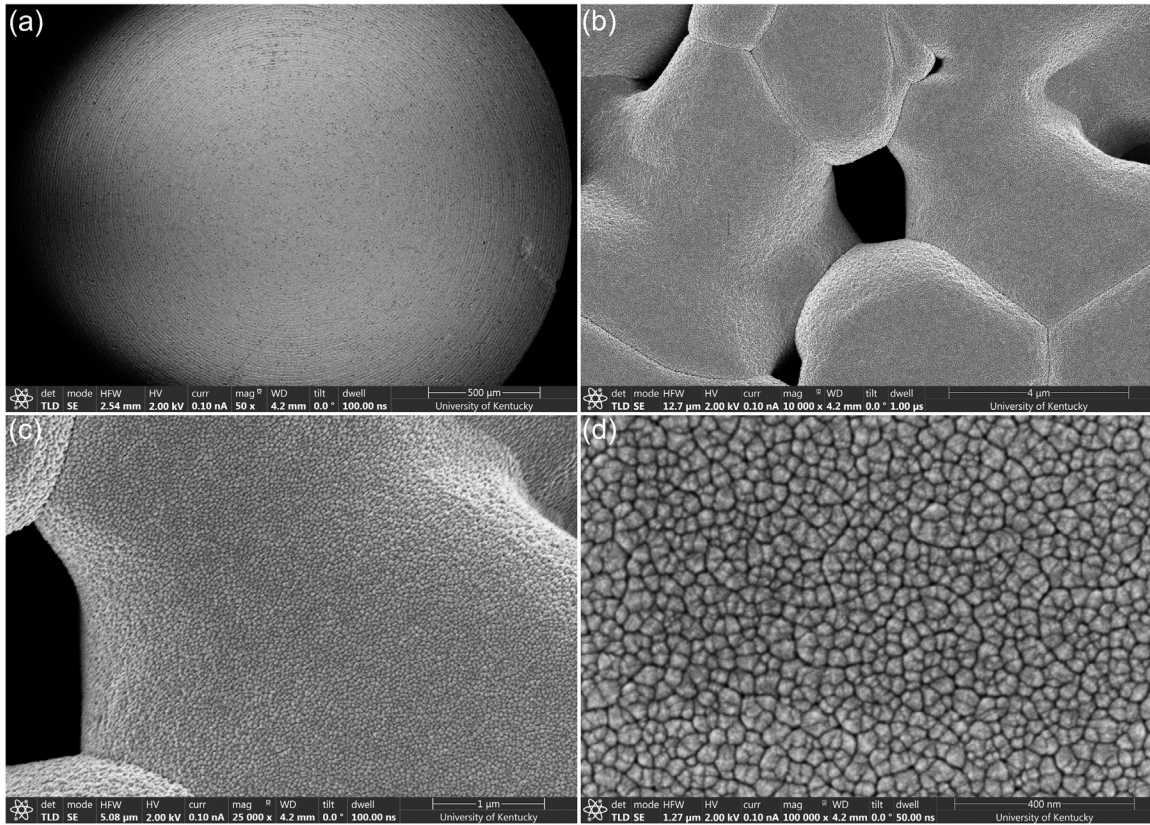
Figure 2.8 SEM results of a un-activated M-type cathode: (a) overview of the cathode; (b) Topography of this cathode; (c) high resolution of image (b); (d) zoomed in image of (c).

2.2.5.3 Scandate Cathodes

It has been reported that when adds Sc$_2$O$_3$ to standard cathode; the emission property of cathode gets significantly improved [19]. This Sc$_2$O$_3$ added impregnated dispenser cathode is scandate cathode. interestingly, the emission property of scandate cathode varies when the fabrication process changes [4]. When a layer of scandium is deposited on the top of B type cathode by Laser Ablation Deposition (LAD) technique, it is named LAD scandate cathode. From Figure 2.4, it can be seen that scandate cathode is

the latest cathode so far and its emission capacity is impressive compared with all other types of cathodes. And most of the cathodes in this dissertation will be scandate cathodes. Figure 2.9 provides SEM results of an un-activated scandate cathode with impregnates $6BaO-1CaO-2Al_2O_3$ from 3M (Saint Paul, MN, USA). It is made by 4.5 microns tungsten grains with 70% density.
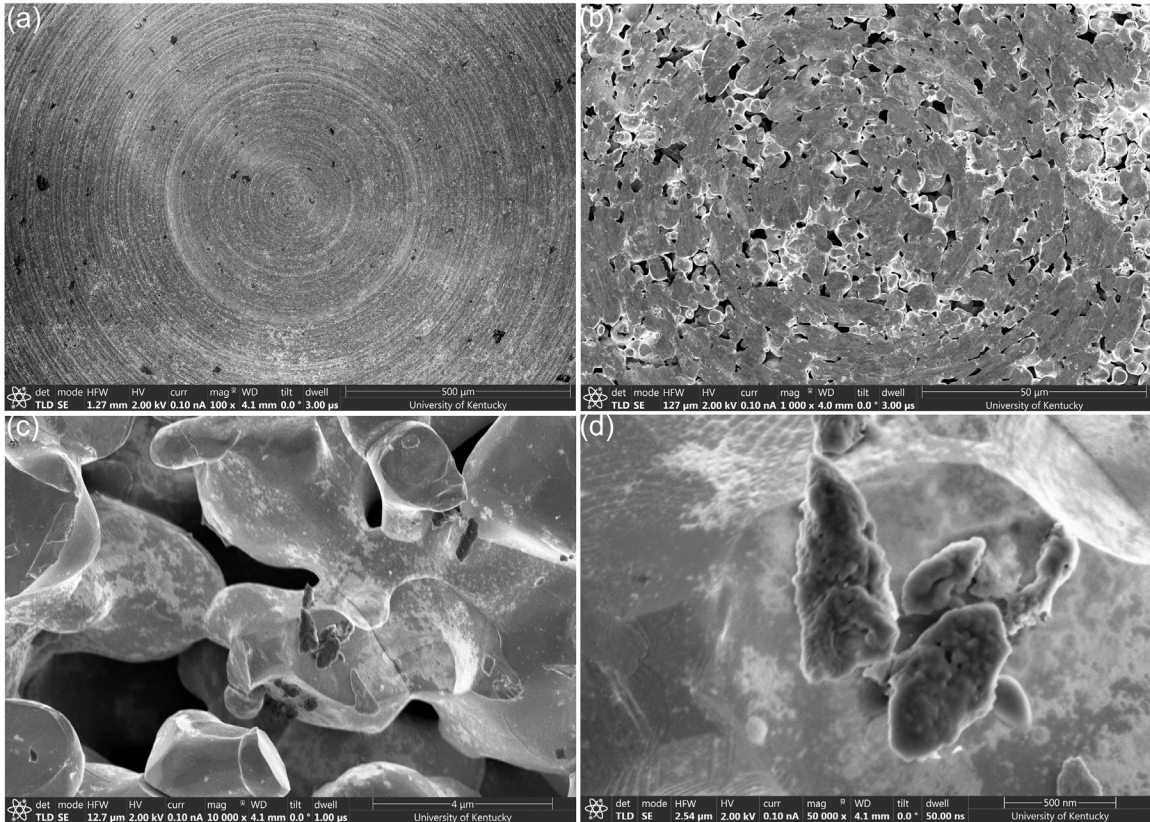
Figure 2.9 Morphology of an un-activated scandate cathode: (a) overview of the cathode; (b) a closer look of this cathode; (c) high resolution image of this cathode, showing the porous structure and tungsten grain; (d) zoomed in image of (b) showing the impregnates on tungsten grain.

2.2.5.4 3D printed Cathodes.

Recently, 3D printing technology was attempted on manufacturing standard cathode, M cathode and Scandate cathode. While by the time of this dissertation, no

reports/publications of the emission performance of 3D printed cathodes are available yet, and whether 3D printed cathodes have been officially commercialized is still unknown. Figure 2.10 shows the morphology of an un-activated 3D printed scandate cathode 4BaO-1CaO-1Al$_2$O$_3$ impregnates from 3M (Saint Paul, MN, USA). It was made by 4.5 microns tungsten grains with 70% density.
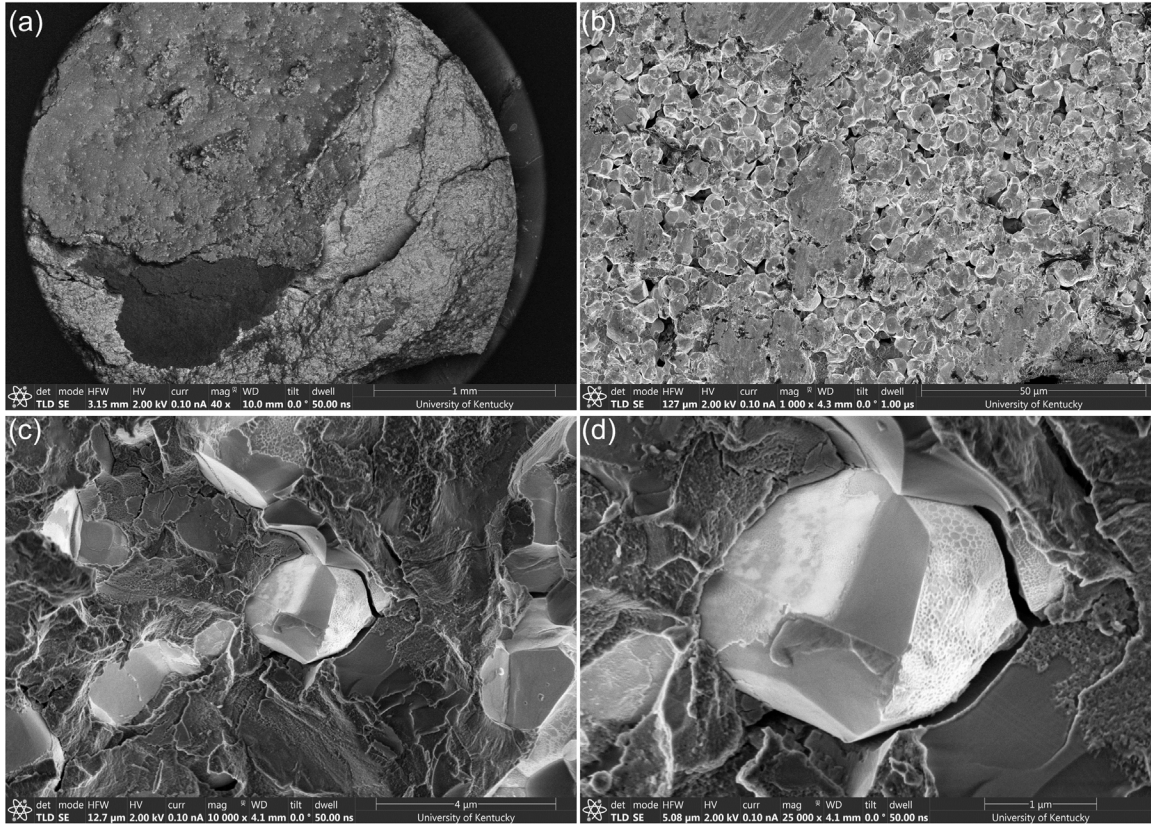
Figure 2.10 Morphology of an un-activated 3D printed scandate cathode: (a) overview of the cathode; (b) a closer look of this cathode; (c) high resolution image of this cathode, showing the impregnates and tungsten grain; (d) zoomed in image of (b).

2.2.6   Life of Impregnated Cathodes

The general fabrication process of impregnated cathode includes tungsten powder selection, powder mixing and pressing, infiltration and sintering, impregnation and washing, following by activation, and testing.

Mechanism of impregnated cathode has been well explained, it has a monolayer of barium oxide at the top at the early life of cathode, as the cathode continues working, this monolayer gets evaporated but impregnated BaO which fills inside the porous tungsten will migrate out and form the monolayer on the top of cathode, as displayed in Figure 2.11 (a) which is the early life of cathode [4, 30]. When the cathode continues working, the impregnant near surface gradually becomes less, the distance for impregnant to reach surface becomes longer, as a result, it needs more time to form the monolayer, then the amount of BaO at the surface becomes less than it in the early life of cathode, as described in Figure 2.11 (b). Eventually it is unbale to maintain the monolayer at the surface, as shown in Figure 2.11 (c) which is the end of cathode's life.
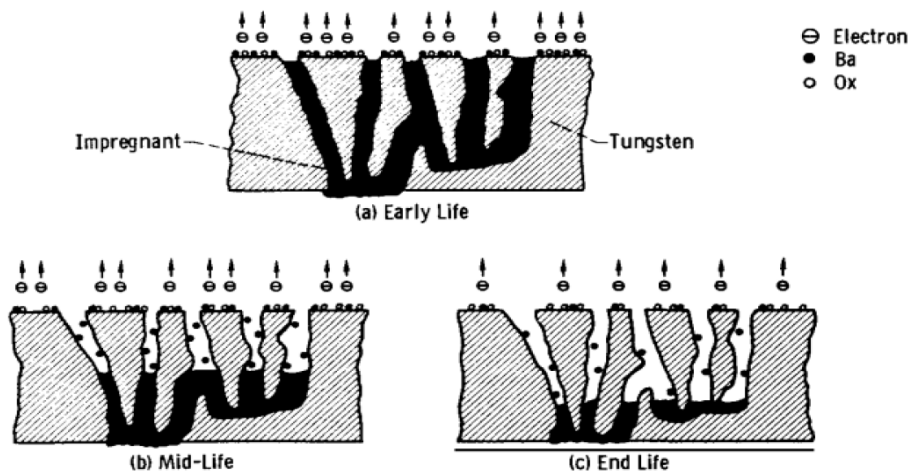
Figure 2.11 Schematic of changing during cathode's life [4]

This procedure also explains why impregnated cathode has better emission capacity than oxide cathode. For oxide cathode, all the barium oxides are at the top of the substrate but not uniformly cover the surface of base metal, as shown in Figure 2.5, which makes all the electrons are emitted at the same site [19]. On the other hand, impregnated cathode,

which has a porous structure, the surface is uniformly covered by monolayer barium oxides, as shown in Figure 2.6 and Figure 2.7.

2.3 *Thin Film Deposition*

2.3.1 Vacuum Technology

In this section, we shall embark upon an elucidation of some fundamental concepts pertaining to the realm of vacuum technology. As is common knowledge, the terrestrial atmosphere comprises a diverse array of gaseous constituents, including, with a high degree of probability, water vapor [31]. When molecules of gases impinge upon the internal surface of a vacuum chamber, they give rise to a discernible pressure phenomenon. Consider, for instance, a system endowed with a volumetric parameter denoted as V, concomitant with a pressure component designated as P. In accordance with the precepts of the ideal gas law, expressed as:

$$PV = NRT \qquad\qquad (3)$$

Herein, P represents the prevailing pressure, V signifies the volumetric capacity, N signifies the quantity of substance, R is the constant universal gas constant, and T corresponds to the temperature prevailing within the system. For a particular system configuration, it is pertinent to note that both V and R assume the status of constants, whereas T is held constant at the ambient temperature, typically set at 25 °C. Consequently, we may deduce that:

$$P \propto N \qquad\qquad (4)$$

In the event of the presence of a gas-extraction mechanism within the system, signifying a diminution in the quantity of substance (N), one may anticipate a concomitant

reduction in the influx of gaseous or substantive species onto the internal surfaces of the vacuum chamber, leading to a commensurate diminishment in the prevailing pressure (P).

Above is a brief description of a vacuum theory. However, in reality, leak of the system must be considered. Figure 2.12 is a schematic diagram of a pumping system where the leak is considered.
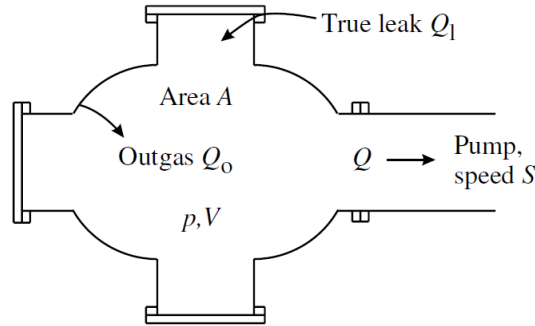
Figure 2.12 Schematic diagram of a pumping system, comprising the volume V, internal area A, pumping speed S and leak rate Q, comprising outgas Q_o and true leaks Q_l. [32]

In vacuum technology, as the pressure gets lower and lower, vacuum range is divided into low vaccum, high vaccum, and ultra-high vaccum (UHV), as shown in Figrue 2.13.
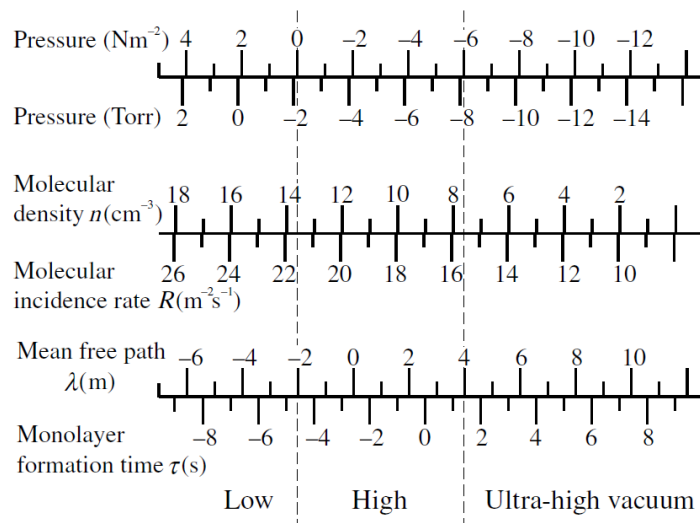
Figure 2.13 Plot of n (cm^3), R (atoms $\cdot$ m^{-2} $\cdot$ s^{-1}), λ (m) and τ(s) for CO at temperature

$T = 300$K, as a function of pressure p, on a logarithmic scale in units of 1 mbar=100 Pascal or Nm^2, and the older unit 1 Torr=1.333 mbar. The division into low, high and ultra-high vacuum regimes are approximate terms based on usage. [32]

In this dissertation, it involves experiments in an atmosphere of low vacuum, high vacuum and ultra-high vacuum. For example, the *in situ* heating experiments on bulk tungsten pellets were done in an environmental SEM with pressure around 0.8 torr, and the nanoparticle generator has a vacuum pressure around 1 x 10^{-7} torr; a custom-made Cathode Characterization Chamber (CCC) in our lab, which was introduced in details by Mantica [26], can reach a pressure as low as 10^{-10} torr.

To analyze the residual gas in a vacuum chamber, Residual Gas Analyzer (RGA) is typically employed, nowadays there are two types of RGA commercially available, open ion source and closed ion source systems, with the operation range 10^{-4}-10^{-14} and 10^{-2}-10^{-11} torr, respectively [33]. Please note that it also means the residual gas in a system with pressure higher than 10^{-2} torr is not commonly tested. Figure 2.14 presents the screenshot of the results from RGA, showing that when total pressure is 10^{-7} torr, the gas in the chamber contains water, some oxygen and so on.
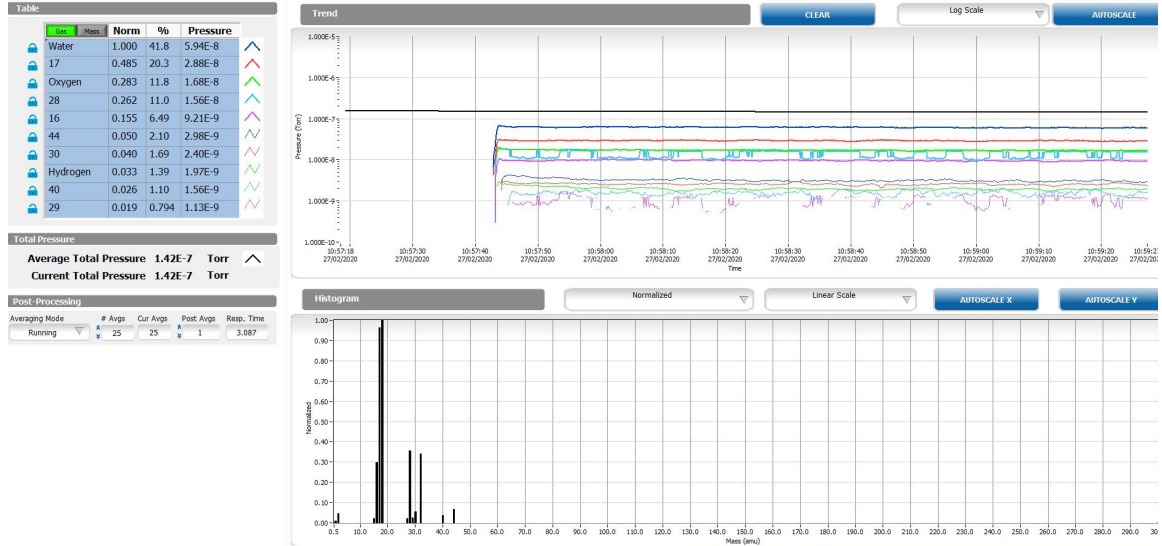
Figure 2.14 Screenshot of the monitoring results from RGA on Cathode Characterization Chamber at University of Kentucky.

2.3.2 Physical Vapor Deposition

Thin film deposition is a process that transfer atoms controllably from a source to a substrate (usually silicon wafer or sapphire), during which process film forms and grows atomically [34]. Nowadays there are several methods to deposit thin films on a substrate, such as chemical vapor deposition (CVD), physical vapor deposition (PVD), and atomic layer deposition (ALD). During CVD process, a volatile compound reacts with other gases, and produces a nonvolatile solid that deposited on a suitable substrate, ALD is a process similar to CVD but has sequential and self-limiting chemical reactions [35], while PVD is a process of materials evaporating or sputtering from a condensed phase [34].

In this dissertation, thin films and nano porous materials were fabricated by PVD method, and atoms were sputtered by direct current (DC) power from surface of a solid target with high purity in a high vacuum chamber.

22

The sputtering typically occurs in a high vacuum environment, because when atoms come out from the source, they need a clear pathway to reach the substrate. Additionally, a high vacuum environment will significantly reduce the contamination of reactive gases (O_2, H_2O, and so on) to the source materials. On the other hand, the sputtering rate and deposition rate are influenced by pressure as well. To maintain and/or adjust the pressure of a vacuum chamber, argon is commonly used during sputtering and deposition process because argon will not react with source materials. Figure 2.15 presents a diagram showing the relationship between working pressure, current and deposition rate for non-magnetron sputtering.

In this work, a custom-made physical vapor deposition system named 'nanoparticle generator' was used, parameters exploration of this equipment will be discussed in chapter 4.
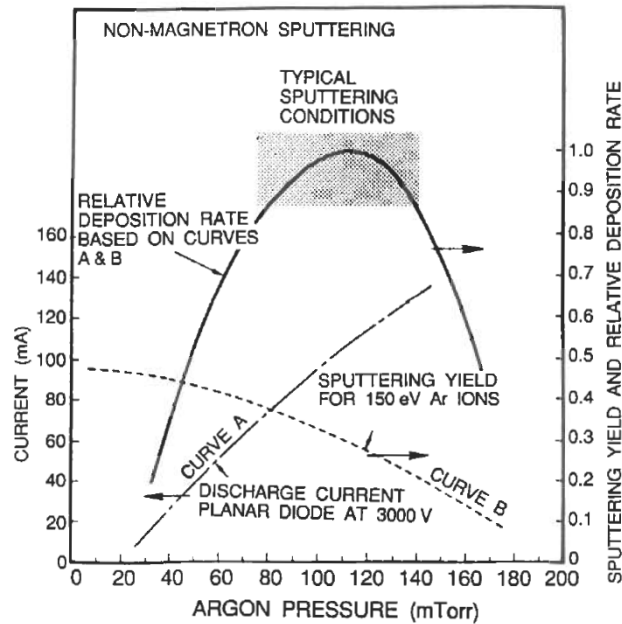
Figure 2.15 Influence of working pressure and current on deposition rate for non-magnetron sputtering [34].

2.4   Surface Faceting

2.4.1   Nanoparticle Deposition

Nanoscale metal particles have wide applications such as catalysis, biomedical research, and semiconductor [36, 37]. And the techniques to synthesis nano scale metal particles are similar to thin film deposition, including electron gun evaporation, physical vapor deposition (PVD), plasma enriched chemical vapor deposition (PECVD), electrochemical deposition, chemical vapor deposition, electrophoretic deposition, laser metal deposition, and atomic layer deposition (ALD), thermophoretic deposition, supercritical deposition, spin coating, and dip coating [37]. In this dissertation, a nanoparticle generator which applies physical vapor deposition (PVD) technique was used to deposit nanoscale metal particles.

When there are sufficient nanoparticles deposited on substrates, they usually form a continuous porous structure which can also be called 'Thin Film' [2]. However, this 'Thin Film' may aggregate and form individual particles after annealing [36], during which procedure faceting could also be reached.

2.4.2   Faceting of Tungsten

Faceting of nanoparticles is believed to a thermodynamic process when it occurs in a nanoscale [38] on metallic materials, while large scale (100s nm to um) faceting could be different in terms of drive force. In this dissertation, the driving force of nanoscale faceting and bulk scale faceting of tungsten was discussed, in chapter 5 and 6, separately.

2.5   Motivation of This Research Project

From the brief introduction of different cathodes, it can be seen tungsten as a substrate or matrix, plays a fundamental role in all the cathodes except oxide cathode. And one interesting thing is that it has been experimentally investigated by Gotoh et al. [39] that W crystal facets (011), (111), (112) and (121) have different work function, which are 5.4 eV, 4.41 eV, 4.85 eV, 4.85 eV, separately. Additionally, some research has been done on controlling the crystalline of W and WO_3. Zhou et al. [40] proved that crystal grow orientation of nano size WO_{3-x} could be controlled when it experiences thermal process. Xie et al. [41] showed in their work how to get WO_3 with chemical methods. Yamazaki et al. [42] published their paper about how Oxygen will decorate W after W (001) surface annealed at 1200 K. Woodward et al. [43] studied structure refinement of triclinic tungsten trioxide, as shown in Figure 2.16.
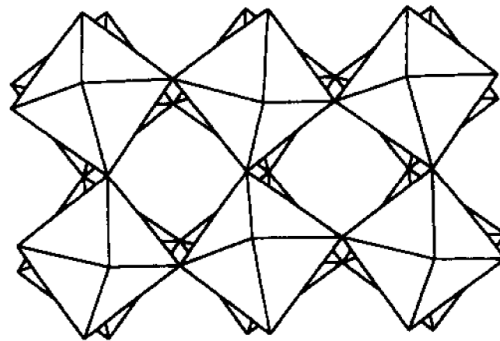
Figure 2.16 Tilt pattern of WO_3: Triclinic (001) projection, x-axis vertical [43]

All the work mentioned above presented a promising possibility of designing tungsten crystal shape and orientation based on requirement. On the other hand, aforementioned, scandate cathode exhibits a great potential of being used as a new thermionic electron source in vacuum electron devices due to its excellent emission

performance at relatively low temperature. Despite the remarkable current emission performance of the scandate-add dispenser cathode, it is burdened by several issues, including poor emission uniformity, inadequate reproducibility, and limited lifetimes, which have impeded its widespread industrial application. Therefore, Extensive efforts and studies need to be conducted to obtain a more comprehensive understanding of the scandate cathode.

Thus, the great potential of scandate disperser cathodes and the promising of tungsten surface optimization become the most important motivation of this project.

2.6   Goal of Research

In order to improve the performance of cathodes, effort needs to be made to further understand the role of tungsten in cathode, as well as explore the possibility to optimize tungsten materials for cathode. This dissertation explored the factors that could affect the crystallography of tungsten, including temperature, pressure and chemistry. It is noted that '*chemistry*' in this study refers to the oxygen concentration in the environment during tungsten faceting procedure. With the investigation on the tungsten surface faceting, the project also aims to provide insight of crystal materials surface tailoring engineering.

Furthermore, this research aims to enhance the overall understanding of scandate dispenser cathodes with the knowledge of materials – structure – property – process, with focuses on the fundamental relationships between material properties and cathode performance. With this goal, more advanced materials characterization on various stages of dispenser cathodes were conducted, which can provide a better understanding of scandate cathode structures, process and its property.

CHAPTER 3. MATERIALS AND METHODS

3.1   Materials

3.1.1   Deposited Tungsten Nanoparticles

In the present work we apply 99.95% purity tungsten targets purchased from AJA international, Inc. (N. Scituate, MA, USA), with 38.10 mm (1.5 inch) in diameter, 3.175 mm (0.125 inch) in thickness, for nano particle generation.

3.1.2   Dispenser Cathodes

Dispenser cathodes with various status are studied in this dissertation, including W-Sc pellet, impregnated but inactivated scandate dispenser cathodes, impregnated and activated scandate cathode. These cathodes are provided by E. Beam Inc. (Beaverton, OR, USA) and 3M (Saint Paul, MN, USA). The cathodes from E. Beam Inc. are typically made by Liquid-Liquid doping technology, some of them are activated, some are not. While the cathodes from 3M are un-activated cathodes. Details will be described in the chapters 7 and 8.

3.1.3   Pure Tungsten Pellets

These tungsten pellets are from 3M Technical Ceramics with a size of 3.09 mm in diameter, 1.30 mm of thickness, and 30% porosity [44].

3.2   Methods

3.2.1   Nanoparticle Generator

The Nanoparticle generator in this work was modified and re-designed based on work of Sneha G. Pandya [45] in Ohio University. It applies physical vapor deposition (PVD) technique to fabricate nano scale particles, a photo of the equipment is shown in

Figure 3.1. The base pressure of the nanoparticle generator can reach 10^{-7} torr. During deposition, the pressures in the condensation chamber and deposition chamber were maintained around 0.9 Torr and 10^{-3} Torr, respectively, with using argon as the process gas. The main parameters that influence nanoparticle size are aggregation length (distance between sputter target and nozzle plate) and the ratio of pressures between the two chambers. In the nanoparticle generator, tungsten atoms come out from the target and collide with Argon molecules during nano particle generation.

Details of the deposition process will be explored in Chapter 4.
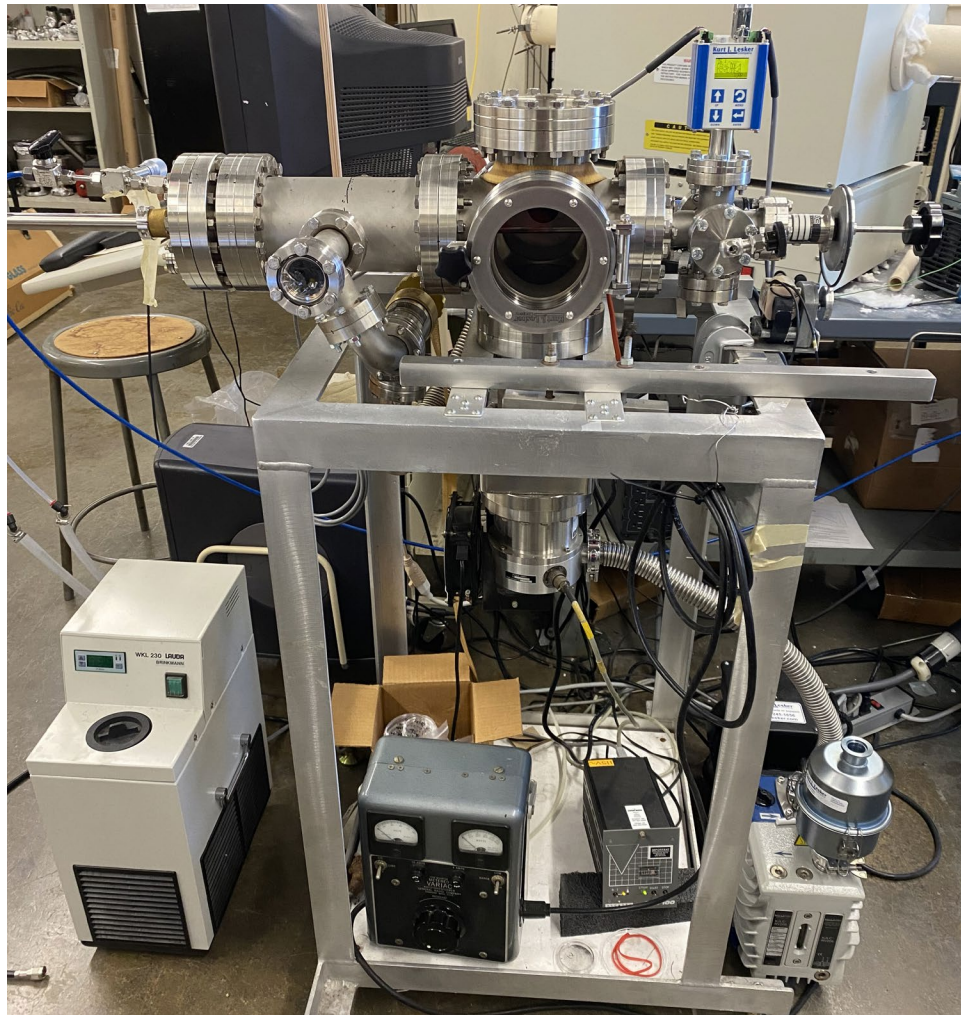
Figure 3.1 A photo of nanoparticle generator showing different components and features.

3.2.2 Environmental SEM

In Situ heating stage of Quanta Scanning Electron Microscopy (FEI Quanta FEG 250) allows users to observe the sample, take secondary electron images as well as heat sample (from ambient temperature to 1400 °C) at the same time. The pressure during heating could vary from 0.1 Torr to 1 Torr, heating speed is adjustable from 0 to 50 °C/min. Figure 3.2 shows a picture of *In Situ* Heating stage of Quanta SEM at use. All the heating experiment done so far in current work is performed with this equipment.
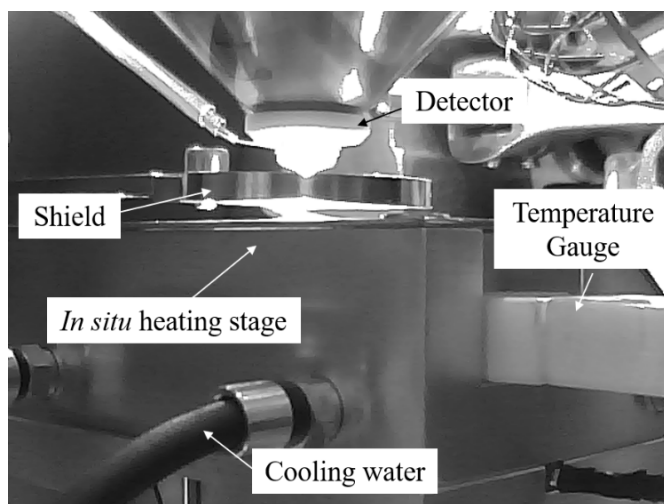
Figure 3.2 Photo of *In Situ* Heating stage of Quanta SEM at use.

3.2.3 Helios SEM

FEI/Thermo Helios G3 dual-beam FIB-SEM (Helios SEM) is the most used equipment for characterization in this project. Compared with Quanta SEM, Helios SEM has a higher imaging resolution of about 10 nm. Meanwhile, this facility has Concentric Backscatter (CBS) detector, In Column Detector (ICD) and Mirror Detector (MD) which are dedicated to detecting backscattered electrons (BSE), as shown in Figure 3.3, thus most

of imaging work (such as secondary electron imaging, BSE imaging and cross-section imaging) is done with Helios Nanolab 660. Besides, all the TEM lamellar and cross section imaging work are done by this Helios SEM since it is equipped with Focused Ion Beam (FIB) which can mill sample precisely in a nano scale range.

SE: Secondary Electron, less than 50 eV of energy
BSE: Backscatter electron, same energy as beam (1 - 30 keV)
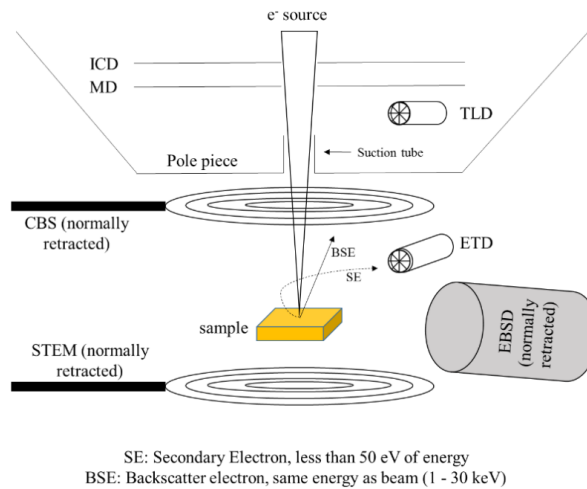
Figure 3.3 Helios SEM 660 detectors (from the manual pdf)

3.2.3.1 SE and BSE images

When an electron beam interacts with a sample's surface in a scanning electron microscope, it can produce both secondary electron (SE) and backscattered electron (BSE) images. Typically, SE images provide information about the surface's topography, while BSE images reveal the composition distribution of the surface. Leng [46] explained the mechanism of images contrast during the formation of SE and BSE images in his book <Materials Characterization> [46]. Based on his explanation, upon the impingement of high-energy electrons upon a specimen, these electrons undergo scattering interactions with the constituent atoms of the specimen, thereby engendering a perturbation in the direction of electron propagation beneath the specimen's surface, as illustrated in Figure

3.4 (a). This electron-atom interaction transpires within a delimited spatial domain beneath the specimen's surface.

Furthermore, Leng [46] introduced the difference between SE and BSE in details. That is, SEs are a result of inelastic scattering, having an energy level of several keV. As shown in Figure 3.4 (b), within the interaction zone, SEs escape from a shallow volume near the specimen surface, approximately 5 ~ 50 nm deep, even though they are generated throughout a broader pear-shaped zone. Conversely, BSEs are products of elastic scattering with energy levels similar to incident electrons, allowing them to escape from deeper within the interaction zone, typically around 50–300 nm in depth. The lateral spatial resolution of an SEM image depends on the volume from which these signal electrons emerge, as depicted in Figure 3.4 (b).
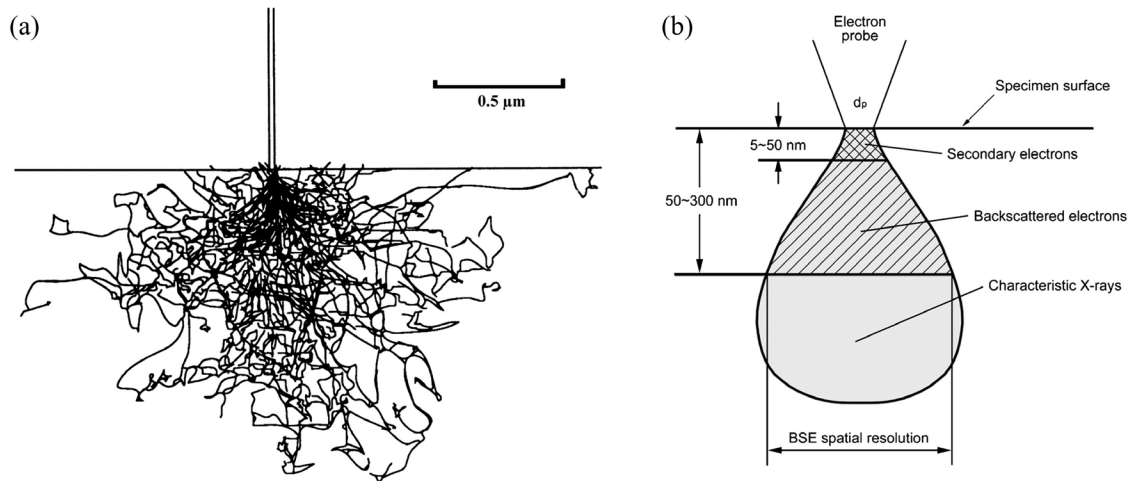
Figure 3.4 (a) Monte Carlo electron trajectory simulation of an electron beam interaction with iron E_0 = 20 keV; (b) The interaction zone of electrons and specimen atoms below a specimen surface.[46]

More important, Leng [46] discussed the mechanism of image contrast for SE and BSE images. He stated that the contrast effect of a SEM image emanates from two primary phenomena: the trajectory effect and the electron number effect. The trajectory effect

results from differences in how the specimen surface aligns with the detector. Electrons emitted from specimen surfaces oriented towards the detector are collected efficiently, rendering the corresponding areas in the image appear bright. Conversely, electrons emanating from surfaces not directly facing the detector face challenges in reaching it, causing the corresponding image regions to appear dark.

The electron number effect, which is also named 'edge effect', can result in areas of brightness that don't align with the actual surface contours of the specimen. When the electron probe impacts a surface at an angle, it allows more electrons to escape from the specimen compared to when the probe strikes a flat surface head-on. Consequently, specific regions of the specimen, like the edges of spherical particles, raised sections, and cavities, will appear brighter in the SEM image, as demonstrated in Figure 3.5 [46].

Besides the topographic contrast, there is another critical contrast: compositional contrast, which is very common for BSE images. For a BSE image, bright area is corresponding to higher atomic number elements and dark area is due to the lower atomic number.

In addition to the well-recognized topographic and compositional contrast mechanisms, Leng also mentioned another two noteworthy modes of contrast merit consideration: crystallographic contrast, alternatively denoted as electron channeling contrast, and magnetic contrast.

Crystallographic contrast in SEM derives its manifestation from the intrinsic interplay between the backscattered electron coefficient and the orientation of crystallographic planes in relation to the incident electron beam's path. This orientation critically impacts the depth of electron beam penetration into the crystalline structure due

to the variable atomic packing densities inherent to distinct crystallographic planes. Consequently, greater penetration depth corresponds to a reduced backscattering coefficient. In this context, a substantial single crystal surface can yield an electron channeling pattern, which serves as a means to elucidate the crystallographic orientation of a surface layer at a resolution of approximately 50 nanometers. Furthermore, SEM exhibits the capacity to unveil distinctive contrast patterns pertaining to the magnetic domains within ferromagnetic materials.

In this work, topographic contrast, compositional contrast as well as crystallographic contrast were common during the SEM characterization of dispenser cathodes, nanoscale particles. Details will be discussed in the following chapters.
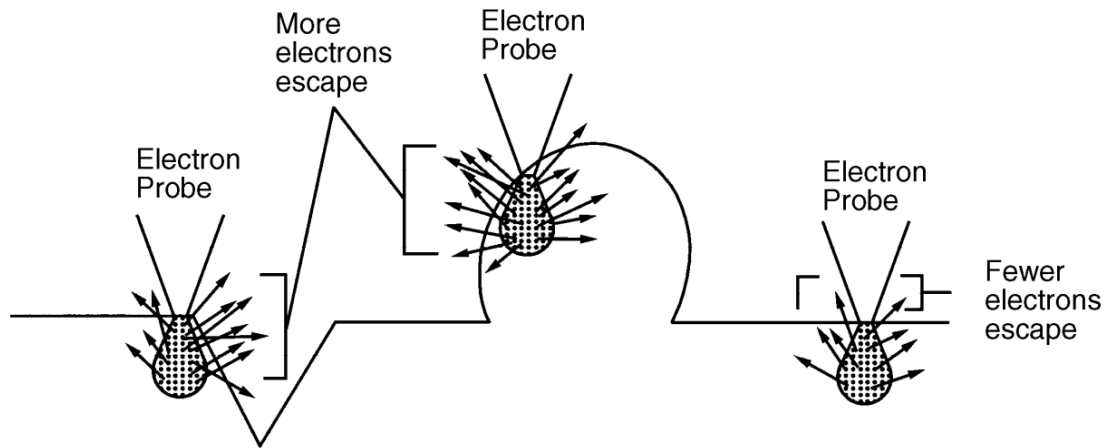
Figure 3.5 Electron number effects due to surface topography. More secondary electrons can escape from the edges of topographical features than from a flat surface.[46]

3.2.3.2 EDS

X-ray energy-dispersive spectroscopy (EDS) is one of the most critical methods for elemental composition measurement of a sample on the microstructural scale since 1951 [47]. The Oxford X-Max 80 mm^2 EDS detector, which is also equipped with Helios SEM, is used for elemental analysis of the samples in this work. X-rays are emitted when inner-

shell electrons are excited by incident electrons, causing an inner shell electron to move to a higher energy level and emit a characteristic X-ray with energy between the two levels [48]. Depending on the applied voltage, sample surface density, working distance and beam diameter, spatial resolution of EDS analysis typically varies from 100s nm to μm depth. Recently, it is reported that higher spatial resolution of EDS (10s nm) can be carried out with thin film processing and low accelerating voltage [49].

3.2.3.3 EBSD

In addition to SEM imaging and EDS analysis, electron backscatter diffraction (EBSD) was also performed in this work to identify the crystal orientation of tungsten grains. In this dissertation, EBSD results help to explain the relationship between grain orientation and faceting structure.

3.2.3.4 3D reconstruction (Slice & View tomography)

3D reconstruction involves data acquisition through milling sample slices with a focused ion beam (FIB) and imaging/mapping each slice to reveal material and channeling contrast, using multiple SEM and FIB detectors. Those acquired images can be interpreted by software and reconstructed the milled section of the sample. In this work, 3D reconstruction was conducted on an annealed tungsten pellet, to reveal the surface faceting structure of a certain tungsten grain.

3.2.3.5 MEMS chip/heater

Microelectromechanical systems (MEMS) chip is nowadays a strong support for nanoscale or micro scale materials research because it allows researchers to run *in situ*

heating experiment in SEM and/or TEM with a high resolution [50, 51]. In this project, a series of *in situ* heating of scandate cathode particles was performed with a micro-electromechanical system (MEMS) chip equipped heating stage with a pressure of 10^{-7} Torr. And the MEMS chips in this work are Fusion Select Heating E-chips (Protochips. Inc Morrisville, NC 27560 USA) which are comprised of a central ceramic heating membrane supported by a silicon substrate. Nine 8-micron holes are located in the center of the membrane to provide an electron transparent area for TEM imaging. These holes are arranged in a 3x3 array with 12 microns between holes [52], as shown in Figure 3.6. Details of these *in situ* heating experiments will be discussed in Chapter 8.
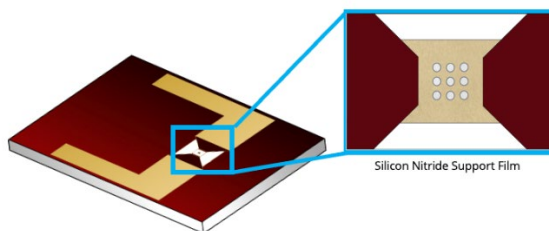
Figure 3.6 Heating E-chips - Fusion Select [52].

3.2.4   CCC

As mentioned earlier, a custom-built cathode characterization chamber (CCC) which was thoroughly introduced by Mantica [26], was used in this work for annealing. Tungsten nanoparticles and bulk tungsten pellets were heated by this chamber because of its ultra-high vacuum. Details of those experiments will be included in chapter 5 and 6.

3.2.5 TEM

The transmission electron microscope (TEM) involved in this work was FEI Talos F200X, which has a resolution of as high as atomic level. SEM and TEM differ primarily in their imaging formation methods. SEM forms images by capturing reflected or ejected electrons from sample, whereas TEM relies on transmitted electrons that traverse the sample to produce images. Consequently, TEM yields insights into the internal characteristics of the specimen, including crystal structure, shape, and stress-related details, while SEM furnishes data about the surface properties and elemental composition of the sample [53].

3.2.6 XPS

X-ray photoelectron spectroscopy (XPS) is a useful technique for chemical elements of a sample surface. In this work, the XPS equipment is Thermo K-Alpha XPS, which has an Al Kα X-ray monochromator for high chemical state resolution [54]. Compared with EDS, XPS is sensitive to sample surface, and is idea for surface analysis in depth of top 10 nm [4, 54]. Furthermore, XPS has an extensive module for ambient work function measurement, which is helpful for dispenser cathode characterization.

3.2.7 BIB

In this project, Cooling Cross-Section Polisher (JEOL IB-19520 CCP cryo cross-section ion polisher) was applied for full length cross section of dispenser cathodes. This cross-section ion polisher uses a board ion beam which allows to cut through the sample within a range of millimeters.

CHAPTER 4. NANOPARTICLES GENERATOR

4.1   Development of Nanoparticles Generator

As mentioned in Chapter 3.2.1, this nanoparticle generator was lent from Ohio University, and significant development work was done on this equipment to improve and optimize its function. For example, it came with rubber O-rings sealing each chamber gate, then those were replaced by copper gaskets. And substrate rotation function was added to the system which allows depositing nanoparticles with two options: substrate stationary mode and substrate rotation mode. Additionally, the pressure gauge to each chamber was updated to the latest version, a new mechanic pump was attached to the system, and gas flow tube and valves were redesigned and replaced. More importantly, a new tungsten target/source was used for the equipment.

With those updates, a series of deposition experiments were performed to test and verify the function of the system, detailed results were discussed below.

4.2   Parameter Exploration of Nano particle Deposition

4.2.1   Process of Nanoparticle Deposition

A schematic diagram of the nanoparticle generator was presented in Figure 4.1 (a). And Figure 4.1 (b) shows the mechanism of deposition. As it can be seen, the nanoparticle generator primarily contains two chambers: condensation chamber and deposition, with a copper plate with 25 holes inserted between two chambers. These 25 small holes which are 0.35 mm in diameter, are distributed uniformly in the center of copper plate, the distance between holes is 4 mm.
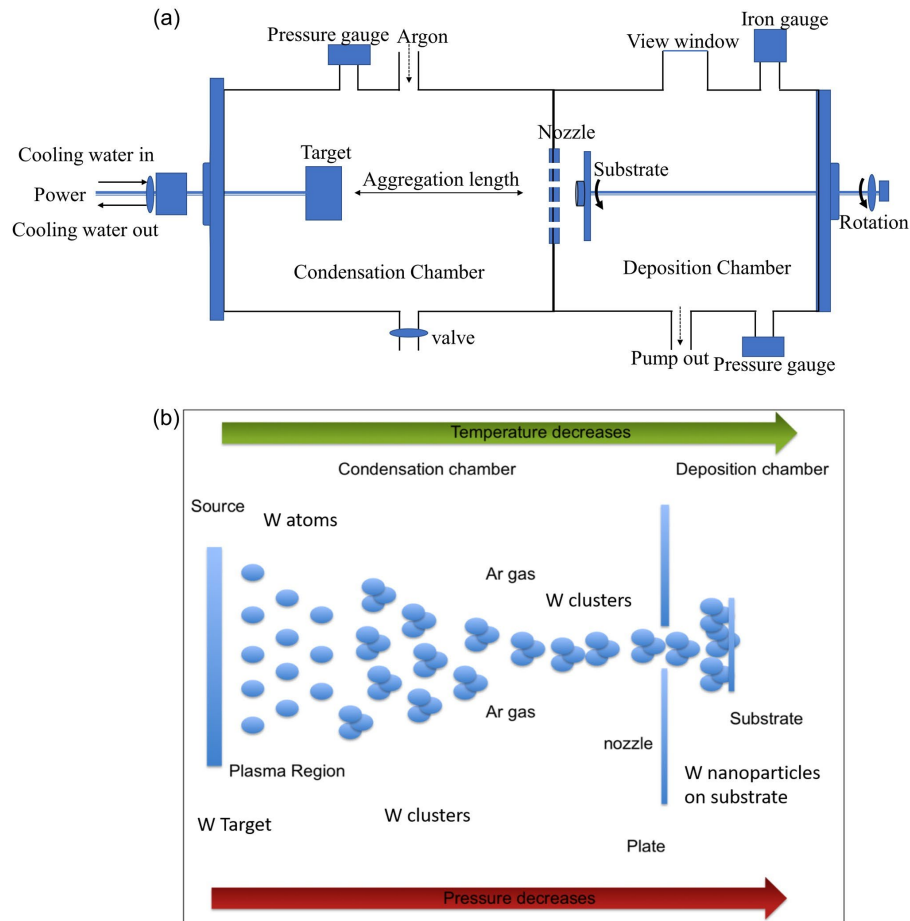
Figure 4.1 Schematic diagram of the nanoparticle generator (a) and the mechanism of deposition (b).

Deposition was performed at ambient temperature with a base pressure before deposition of 10^{-7} Torr. To reach that pressure, the nanoparticle generator needs to be pumped with a mechanical pump and a turbo pump to get base pressure lower than 5×10^{-7} Torr in both chambers. To reduce water vapor in the chamber, the equipment usually is baked overnight. Next step is to run water chiller and let Argon gas flow in condensation chamber to maintain the pressure in condensation chamber at about 1 Torr. Adjust the valves so that the pressure in deposition chamber will increase to 10^{-3} Torr.

When turn on power of plasma, tungsten atoms evaporated from the target will be present in condensation chamber, collide with Argon molecules and grow into bigger size clusters. Due to pressure difference between two chambers, those tungsten clusters will eventually flow through 25 holes into lower pressure chamber (deposition chamber) and finally deposit on substrate, as shown in Figure 4.1 (b).

When applied with higher power, there will be more tungsten atoms evaporated from target. At the same time, the difference of pressure provides driving force for tungsten atoms moving into lower pressure chamber, which means the bigger difference between the condensation chamber, there will be more nano particles deposited at the substrate. As for aggregation length, if it is longer, then tungsten atoms will have longer time to grow into bigger size clusters, as exhibited in Table 4.1 [45]. Therefore, theoretically we can obtain maximum amount of nano particle deposition with increasing sputtering power, insert gas pressure and aggregation length.

However, increasing power will also increase the temperature of the source materials/target, which decreases the average particle size. Moreover, increasing gas pressure will influence the magnet of sputtering gun. As a result, the parameter in Table 4.1 does not match with experimental results.

Table 4.1 Parameters affecting the average particle size [45]

Parameter (increasing)	Average particle size
Sputtering power	increases
Insert gas pressure	Increases
Insert gas temperature	Decreases
Insert gas flow rate	Decreases
Aggregation length	Increases

4.2.2 The Color of Plasma

On the other hand, the color of plasma changing during the procedure of sputtering is well-known and observed by researchers conducting experiments with PVD [55-57] or plasma [58, 59]. Hence, plasma color can characteristically show the species in plasma, for example, Argon is reported to be violet in plasma by Mattox [57], Tungsten is reported to be blue by Hattori [40], and WO_3 is reported to be blue white in plasma by Tracy [59].

During various experiments in present work, it was found that color of plasma changes based on pressure when applied with same power. When sputtering is 125 W, if pressure in condensation chamber was lower than 0.8 Torr, the color of plasma would be blue-white, while it was between 0.8 and 0.91 Torr, color of plasma turned out as blue. It will be purple when the pressure is higher than 0.93 Torr but lower than 1 Torr, as shown in Figure 4.2. In the first case, no deposition could be observed on substrate; and in the second case, it is highly possible to get nano particle deposition; while in the third case, when plasma was purple, no deposition could be found on substrate, either. When pressure is somewhere higher than 0.91 Torr but lower than 0.93 Torr, the color of plasma is in transition between purple and blue. When the pressure of the condensation chamber is higher than 1 Torr, the target did not work (no plasma was observed).
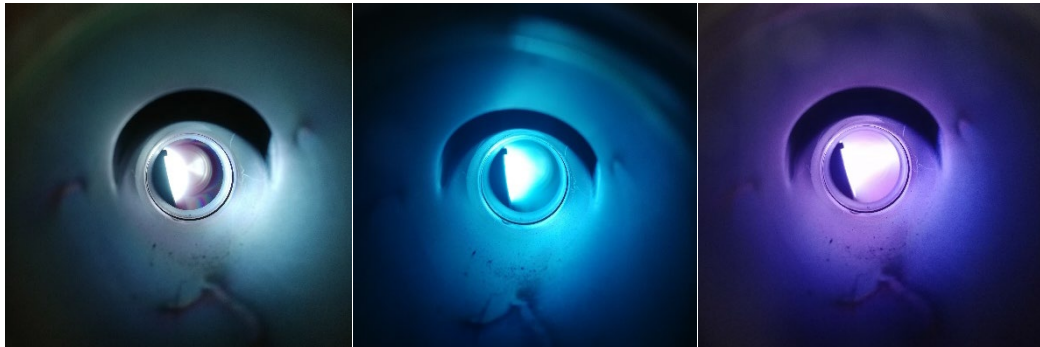
Figure 4.2 The color of plasma at power 125 W: blue-white when pressure is lower than 0.8 Torr (left), blue when pressure is between 0.8 Torr and 0.91 Torr (middle), purple when pressure is higher 0.93 Torr (right).

4.2.3 Deposition on Cu Substrate
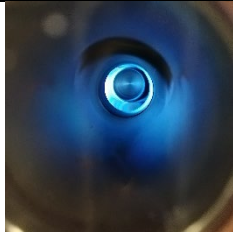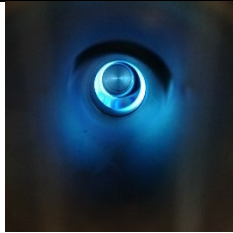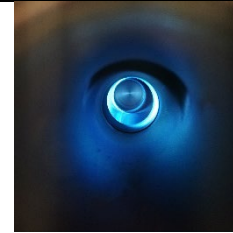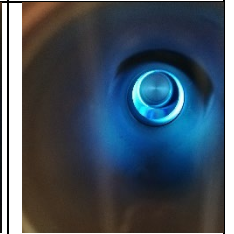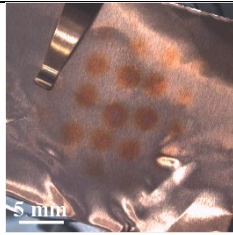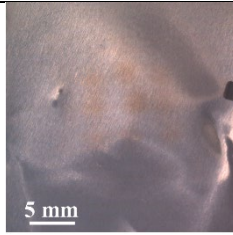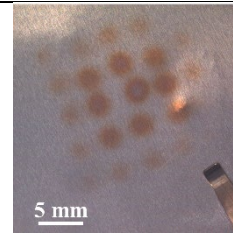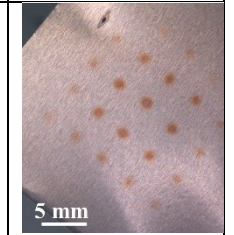
In this work, a series of experiments have been performed, and parameters of this nanoparticle generator have been explored, as listed in Table 4.2, and representative results with a stationary substrate are displayed in Table 4.3.

Table 4.2 Range of parameters of nano particle generation

Parameter	Range
Base pressure	$< 5 \times 10^{-7}$ Torr
Pressure in condensation chamber	$0.8 - 1$ Torr
Pressure in deposition chamber	$< 5 \times 10^{-3}$ Torr
Aggregation length	5 cm – 15 cm
Substrate	Silicon wafer, Copper, Tungsten pellet, Cathode, Sapphire
Distance from substrate to 25 holes	3 mm–15 mm
Substrate Temperature	Ambient temperature
Substrate Rotary	Rotatory/Stationary
Sputtering Power	30 – 130 W
Sputtering duration	15 min – 60 min

Table 4.3 Nanoparticle deposition with a stationary substrate (no rotation of the substrate)

Parameter	Value			
Experiment	#1	#2	#3	#4
Date	06-18-2019	07-04-2019	07-05-2019	07-07-2019
Base pressure	4.04×10^{-7} Torr	1.95×10^{-7} Torr	2.56×10^{-7} Torr	1.15×10^{-7} Torr
Pressure A*	9.09×10^{-1} Torr	8.91×10^{-1} Torr	9.09×10^{-1} Torr	9.02×10^{-1} Torr
Pressure B*	2.70×10^{-3} Torr	2.60×10^{-3} Torr	2.60×10^{-3} Torr	2.60×10^{-3} Torr
Aggregation length	15 cm	15 cm	15 cm	15 cm
Power	125 W	125 W	125 W	125 W
Substrate	Copper foil	Copper foil	Copper foil	Copper foil

Distance (substrate to 25 holes)	8.5 mm	8.5 mm	8.5 mm	3 mm
Duration	40 min	40 min	50 min	20 min
Color of plasma				
Deposition results	5 mm	5 mm	5 mm	5 mm

*Pressure A is pressure in condensation chamber; Pressure B is pressure in deposition chamber.

According to parameters in Table 4.2 and results in Table 4.3, it can be seen that deposition amount/area could be different even apply the similar parameters. Results in experiment #1 differ from that of experiment #2, which could be attributed to the consuming of target material during experiment, as the target will become thinner as depositing goes, consequently deposition results could be different. While result of experiment #3 shows that increasing time might be helpful to get expected results as experiment #1. Meanwhile, deposition results in experiment #4 indicate that distance from substrate to 25 holes has an influence on the size of 25 dots deposited on substrate.

Interestingly, the results in Table 4.3 also demonstrated that copper could be used as a substrate since it can be an easy and straight method to verify whether there is deposition because of color change caused by 25 deposited dots, which can be seen by naked eyes. For experiment with silicon wafer as substrate, which has been done but was not included in Table 4.3, changes cannot be seen by naked eyes.

4.3 Characterization of Nanoparticles Deposited on Copper

As displayed in Table 4.2, there are 25 deposited dots on copper substrate in experiment #1 when the substate was stock-still without rotatory. The morphology and composition of this sample were characterized by scanning electron microscopy (SEM) and x-ray energy dispersive spectroscopy (EDS). An electron-transparent lamella was extracted for imaging and EDS in the transmission electron microscope (TEM).

4.3.1 SEM Observations

As shown by the discolored spots in Figure 4.3 (a), deposition on the substrate occurred in an array pattern corresponding to the nozzle plate. Positions *b* and *c* are at the substrate edge and within the central spot, respectively, and their microstructures are shown in Figure 4.3 (b) and (c). Figure 4.3 (c) indicates that a nanoporous network of nanoparticles was deposited at position *c*, while at position *b*, the substrate remained bare. Figure 4.3 (d) shows a cross-section at position *c*, revealing the thickness of the deposited layer to be 43 nm. Most tungsten nanoparticles were ~10 nm in diameter.
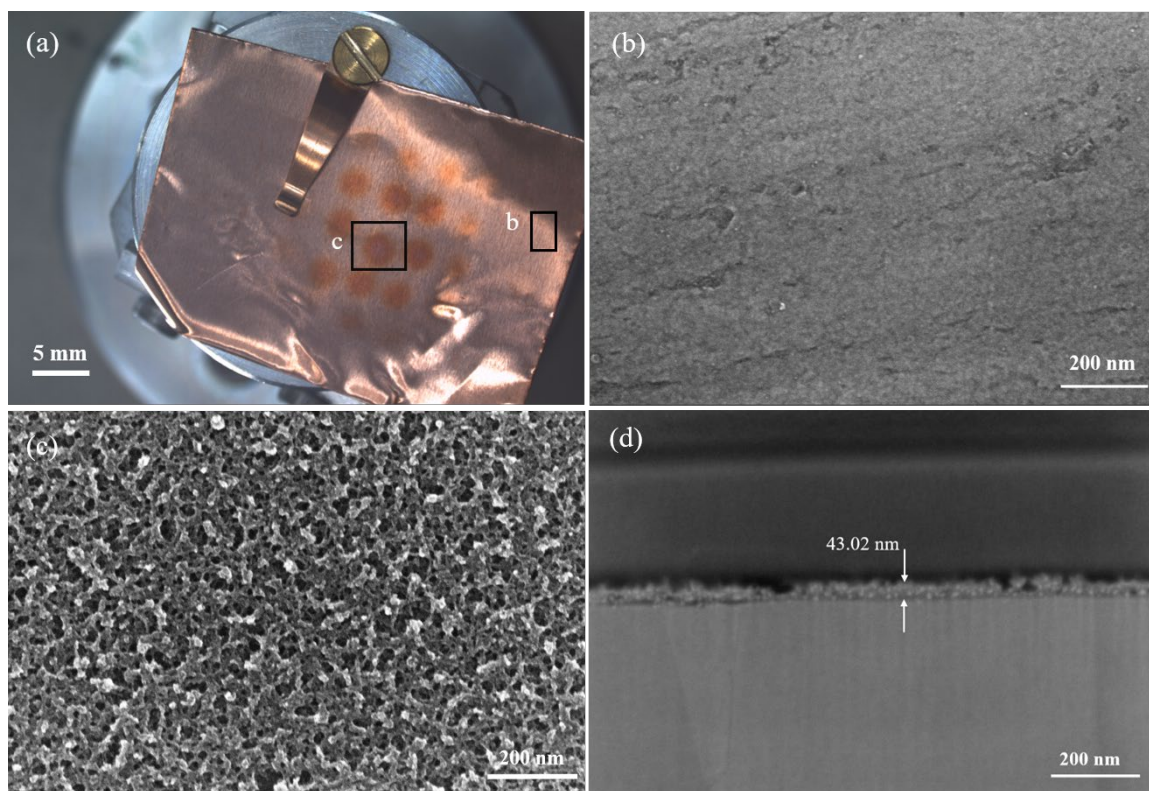
Figure 4.3 (a) Photograph of sample after deposition, (b) plan-view SEM image of substrate at position *b*, (c) plan-view SEM image at position *c*, and (d) cross-section at position *c* showing thickness of deposited nanoparticle layer.

In addition to the network of ~10 nm nanoparticles, larger individual particles were observed on the nanoparticle layer surface, with particle size ranging from 20 nm to 100 nm. Figure 4.4 shows a discrete, larger particle (71 nm in diameter) sitting on top of the continuous porous network.
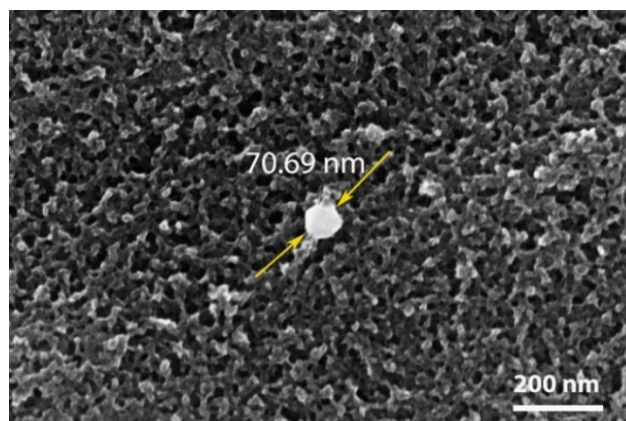
Figure 4.4 Isolated larger tungsten particle sitting on top of nanoparticle layer.

4.3.2   EDS Analysis

EDS analysis shown in Figure 4.5 confirms that both the larger particle and the continuous nanoparticle network are tungsten. This phenomenon suggests that nanoparticle deposition when the substate was stock-still without rotatory may not be completely uniform.
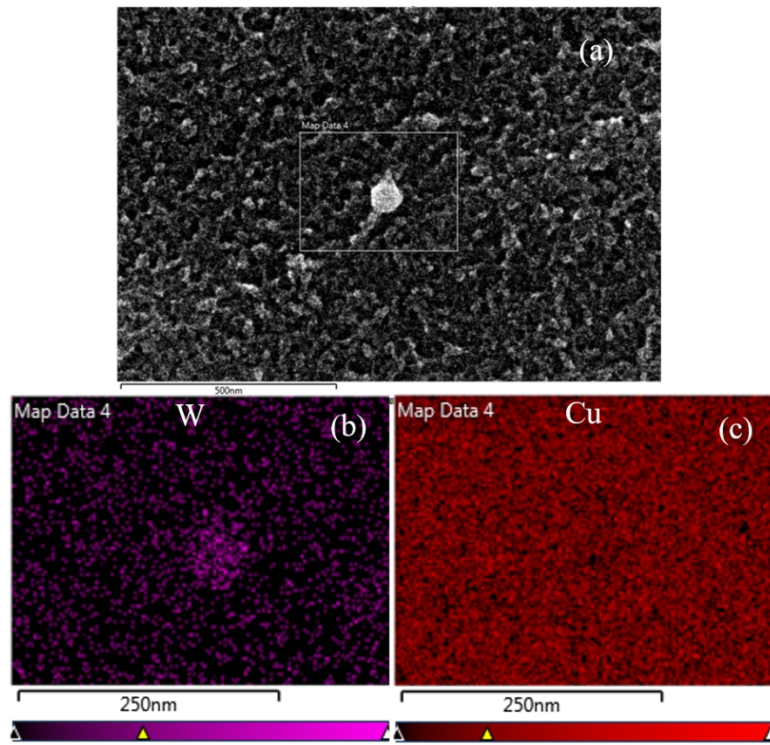
Figure 4.5 Image and EDS elemental maps of discrete, larger tungsten particle on top of nanoparticle network: (a) SEM image, (b) tungsten distribution, (c) copper distribution.

4.3.3   TEM Observations

Figure 4.6 shows TEM observations of the extracted lamella that represents a cross-section. The TEM image in Figure 4.6 (a) indicates that the lamella includes three layers: the copper substrate, the deposited layer of tungsten nanoparticles and a carbon layer

deposited during the extraction process. Figure 4.6 (b) is a high-angle annular dark field (HAADF) image recorded in scanning TEM (STEM) mode, showing atomic number contrast (higher atomic number is brighter). As seen in Figure 4.6 (a) and (b), the deposited layer has a nanoporous structure that results from smaller nanoparticle agglomeration. Figure 4.6 (c) is a STEM-EDS map confirming the deposited layer consists of tungsten nanoparticles.
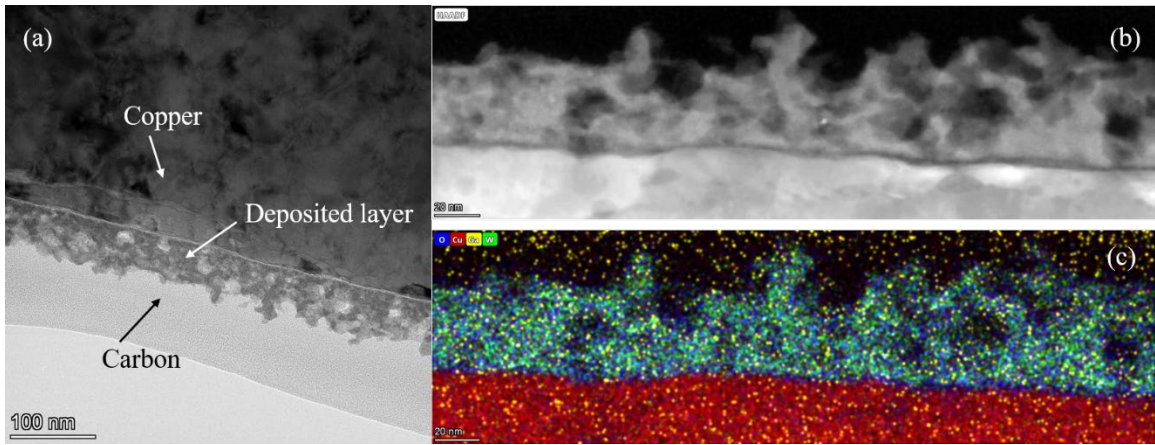
Figure 4.6 TEM results: (a) TEM image, (b) HAADF-STEM image, (c) STEM-EDS map showing distribution of elements throughout the cross-section.

It is noted that the tungsten surfaces are oxidized. The nanoscale dimension of the deposited tungsten particles provides enhanced surface area and small radii of curvature, which should facilitate broader barium coverage in a tungsten-based dispenser cathode. In turn, this should improve the electron emission capability of such cathodes. Finally, for cathodes that experience tungsten surface diffusion during activation, in order to form preferred crystallographic facets, the nanoparticle layer may serve as a source of mobile tungsten.

In summary, a porous layer consisting of tungsten nanoparticles was fabricated using a PVD method. This layer consisted of nanoparticles with diameter ~10 nm, as well

as larger discrete tungsten particles on top of the nanoparticle layer. This nanoscale tungsten may facilitate formation of a preferred surface morphology during activation and lead to enhanced electron emission capability.

4.4   Nanoparticle Deposition on Different Substrates

4.4.1   Thin Film Growth Mode

SEM and TEM results above prove that nano tungsten materials could be successfully fabricated by nano particle generator. And in Figures 4.4 and 4.5 show a bigger size nano particle, on which surface there are some tiny size particles, presents in the deposition. This happens to every sample in this work when the substate is stationary. Figure 4.7, for example, is observation of center dot (displayed in Figure 4.7 (a) with black square) of sample from experiment #3 in Table 4.3, showing that individual bigger size particles are covered by tiny size particles as well.
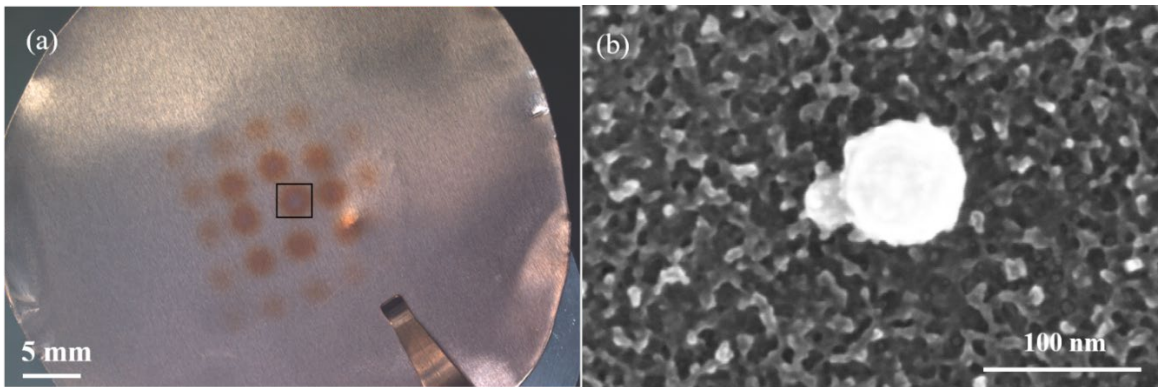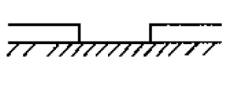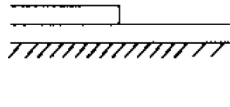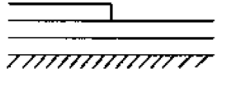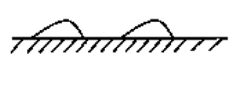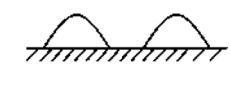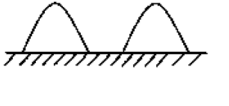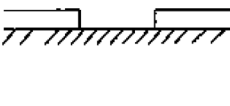
Figure 4.7 (a) sample from experiment #3, (b) bigger size particles sit in porous deposition.

The presence of bigger size particles could be explained by thin film growth modes [60, 61], as shown in Table 4.4. In layer by layer mode (known as Frank-van der Mderwe mode), thin film growth with layer on previous layers. In Island mode (also named Volmer-Weber mode), atoms prefer to interact with deposited atoms. While in Layer plus island

mode (established by Stranski and Kranstanov), a few monolayers form on the surface of substrate, then other film atoms arrive and prefer to stay on top of previous film atoms. Obviously, in the present work, the growth of W in Figures 4.4 and 4.7 is in the third stage of layer plus island mode ($\Theta>2ML$).

Table 4.4 Thin Film Growth Modes at Initial Stage [60].

	$\Theta<1$ ML	$1ML<\Theta<2$ ML	$\Theta>2ML$	
Layer by layer mode				$\varphi = 0$ $\gamma_B > \gamma_A + \gamma^*$
Island mode				$\varphi < 0$ $\gamma_B < \gamma_A + \gamma^*$
Layer plus island mode				γ^* increases during process

*Θ is coverage of substrate in monolayers (ML).

4.4.2 W Nanoparticle Deposition on Silicon Wafer

However, the growth of W is not always in layers plus island mode, it varies with substrate as well as supersaturation because of their different surface energy. When W deposited on Si wafer, separate particles are more likely to form than continuous porous structure on silicon wafer (as shown in Figure 4.8). This is consistent with results reported by Itoh *et al.* [62] in 1991, who revealed that W growth at initial stage on dielectric substrates (like Si, Sapphire) is especially longer and W has an island structure (as displayed in Figure 4.9).
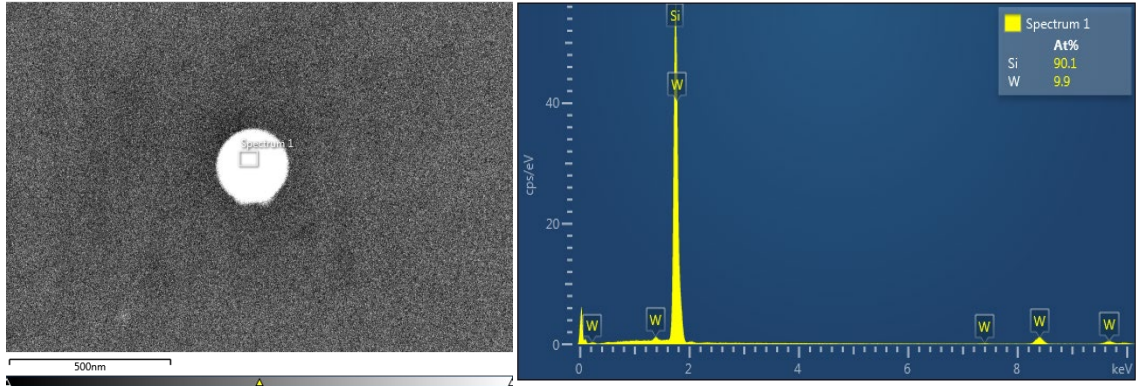
Figure 4.8. Nano W particle deposition on silicon wafer: electron image (left) and EDS spectrum (right)
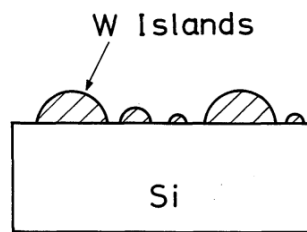
Figure 4.9. Schematic of W growth on Si at initial stage [62]

4.4.3　W Nanoparticle Deposition on Niobium plate

Figure 4.10 represents the results of nano tungsten deposition on Niobium plate, Figure 4.10 (a) is secondary electron image of sample before deposition, Figure 4.10 (b) is topography of sample after deposition showing the surface of substrate is fully covered by several bigger size particles as well as porous structure materials. Nano particle deposition can be demonstrated by the difference between Figure 4.10 (a) and (b). Figure 4.10 (c) is the backscattered electron image proving that bigger size particles and porous structure materials have same grey level, which implies they have same components.
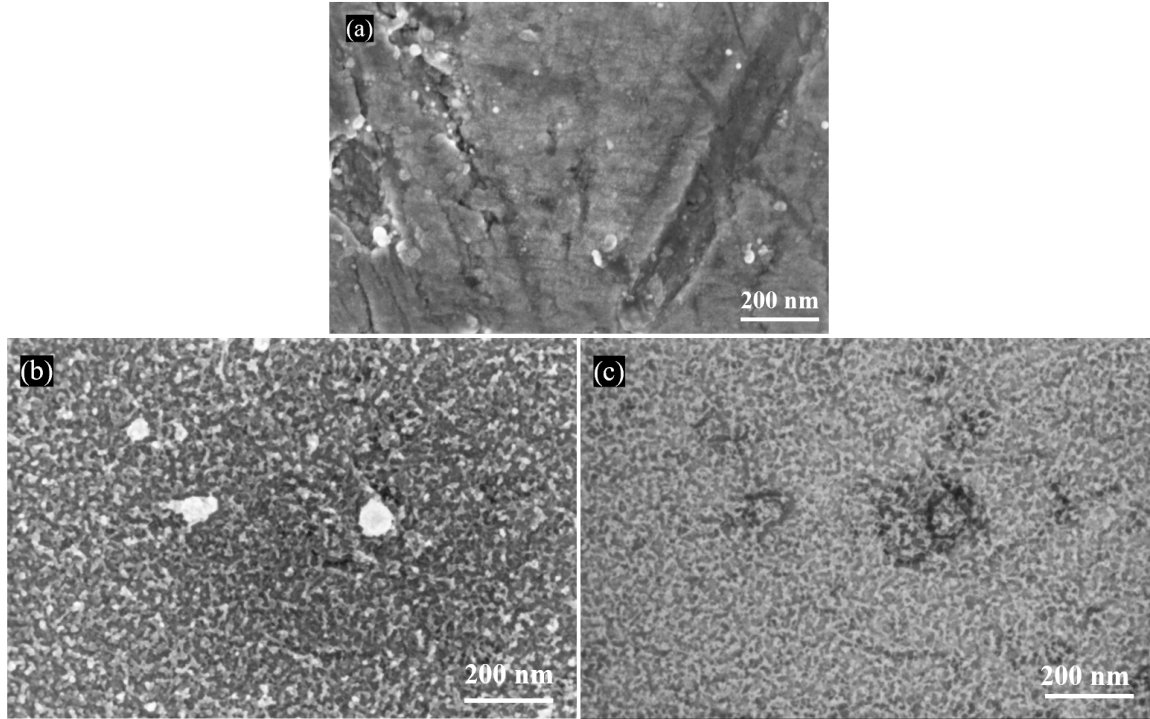
Figure 4.10. Nano W particle deposition on Niobium plate: (a) SE image before deposition, (b) SE image after deposition, (c)Back Scattered Electron (BSE) image after deposition

4.4.4   W Nanoparticle Deposition on Tungsten Pellet

Similar results were obtained when depositing nano tungsten on tungsten pellet which has a porous structure (exhibited in Figure 4.11 (a)), the difference is nano materials forms separate particles when substrate is porous tungsten pellet, at the same time, some 'chain' form deposition (as marked with yellow arrow in Figure 4.11 (b) and (c)) appears which implies the growth mode was changing from island mode to layer mode (or layer plus island) mode as supersaturation increases [60]. Therefore, the initial stage of nano particle deposition on Niobium plate is in layer plus island mode while on porous W pellet is mainly in island mode.
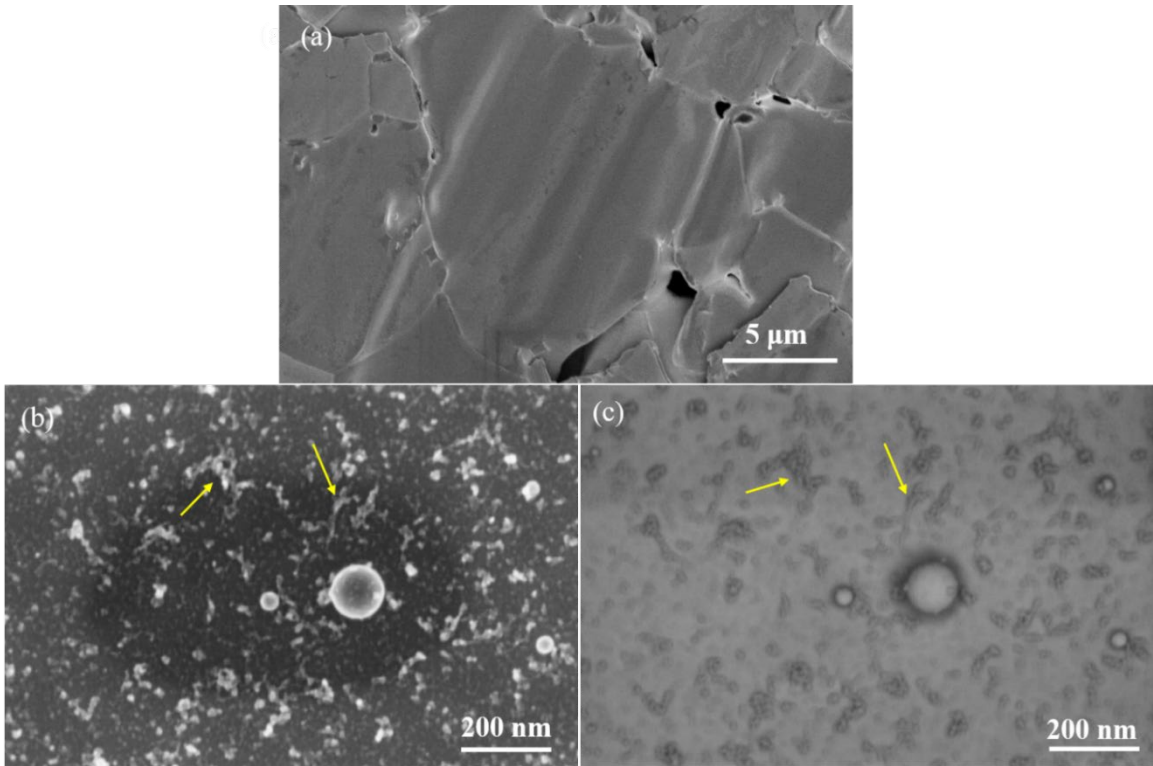
Figure 4.11. Nano W particle deposition on porous tungsten pellet: (a) surface of W pellet before deposition, (b) topography of W pellet after deposition, (c) Back Scattered Electron (BSE) image, arrows in (b) and (c) pointing at 'chain' form structure deposition.

4.4.5   W Nanoparticle Deposition on an Impregnated Cathode

Compared with Silicon, Niobium plate as well as W pellet, the surface of impregnated cathode is more complicated because it has various components, sizes of which are different (Figure 4.12 (a)). Nano particle deposition has been conducted with an impregnated, un-activated scandate cathode (labeled as LL101816S P030717-01#3) from E Beam company. Deposition parameters are listed as experiment #8 in table 3.5. Results are displayed in Figure 4.12. Comparing Figure 4.12 (a) with 4.12 (b), it is clearly seen that on the surface it is fully covered by nano particles. However, like deposition on W pellet, instead of forming a continuous porous structure, nano particles are separate and some of them form 'chain' structure, which can be seen from Figure 4.12 (c).

51
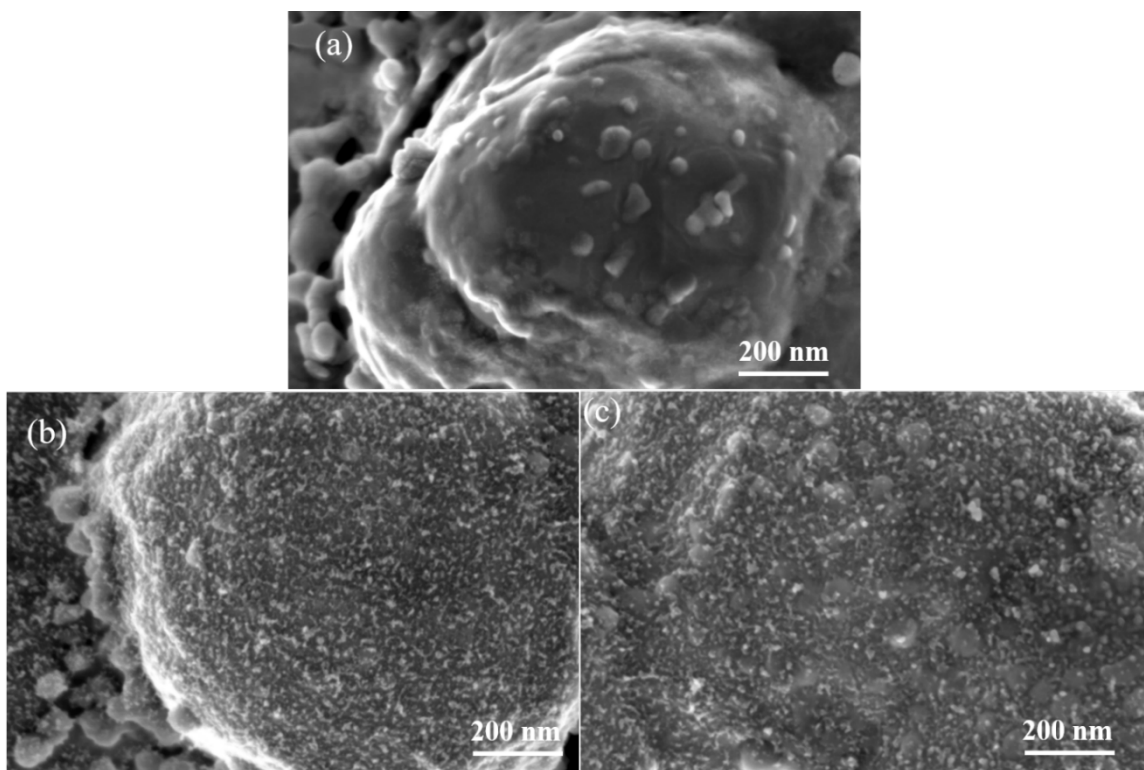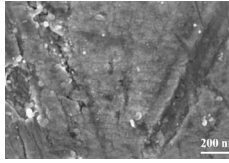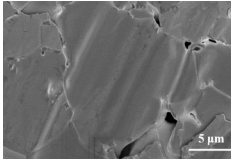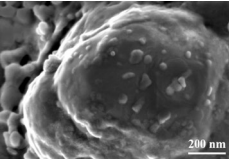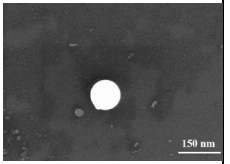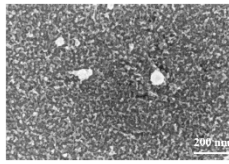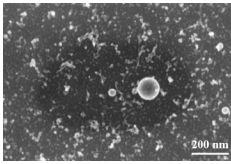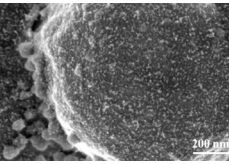
Figure 4.12. W particle deposition on un-activated cathode: (a) topography of cathode before deposition, (b) and (c) topography of cathode after deposition.

Details of deposition parameters on different substrates are shown in Table 4.5. From results above, it can be seen nano W materials can be successfully fabricated, and their structure of early stage, which is controlled mainly by substrate, could be porous structure or separate particles.

Table 4.5 Parameters of Nano W Particle Deposition on Different Substrate

Parameter	Value			
Experiment	#5	#6	#7	#8
Date	06-14-2019	07-05-2019	10-10-2019	03-28-2019
Base pressure	7.0 x10^{-7} Torr	2.97 x10^{-7} Torr	5.68x10^{-7} Torr	7.47x10^{-7} Tor
Pressure A*	9.50 x10^{-1} Torr	8.40 x10^{-1} Torr	9.01 x10^{-1} Torr	9.13 x10^{-1} Torr
Pressure B*	2.70 x10^{-3} Torr	2.10 x10^{-3} Torr	3.00 x10^{-3} Torr	2.60 x10^{-3} Torr
Aggregation length	15 cm	15 cm	9.5 cm	15cm
Power	100 W	125 W	50 W	70W
Substrate	Silicon wafer	Niobium plate	Porous Tungsten pellet	cathode
Distance (substrate to 25 holes)	8.5 mm	8.5 mm	8.5 mm	15mm
Duration	40 min	40 min	45 min	40min
Topography before deposition				
Topography After deposition				

CHAPTER 5. PHYSICAL VAPOR DEPOSITION AND THERMALLY INDUCED FACETING OF
TUNGSTEN NANOPARTICLES

5.1   Introduction

Nanoscale metal particles, such as tungsten (W) [63, 64], copper (Cu) [65], gold
(Au) [66-68], silver (Ag) [68] and bismuth (Bi) [69], have drawn increasing attention from
both industry [63-65, 70] and academia [65, 70]due to their unique properties [64, 66, 71]
and promising characteristics in applications including catalysis [66], biomedical research
[67], memory devices [63, 72, 73], biosensors [69], and semiconductors [63, 72-74].

Among the conventional metal nanoparticles, tungsten nanoparticles have received
a high degree of interest within the scientific research community [2, 63, 64, 75-82].
Historically, bulk tungsten has been used as a refractory material for military and industrial
purposes, as it has high melting point, high hardness, and high creep and corrosion
resistance [64]. Tungsten nanoparticles, which are relatively stable at high temperatures
when compared to other metals [63], possess attractive properties such as high hardness
and wear resistance [75-77]. Therefore, tungsten nanoparticles can be used as a sintering
material [75-81] in powder metallurgy and could potentially be used as a structural material
in next-generation fusion reactors [80, 82]. In addition, nanoscale tungsten particles can be
utilized as an advanced material for improving the emission performance of dispenser
cathodes [2, 83, 84] used in vacuum electron devices, and it has been reported that
application of tungsten nanoparticles can enhance the emission capabilities of thermionic
cathodes [84]. Recently, nanoscale tungsten has also been considered as a candidate for
next-generation semiconductor interconnects [85, 86] because of its high melting point and
the anticipated reduction of the resistivity size effect due to its shorter electron mean free

path compared to the typical material (copper) that is currently used. Given the potential applications noted above, improved processing methods that facilitate greater control of the resulting properties of nanoscale tungsten (such as oxidation, microstructure, morphology) warrant investigation [85].

There are a variety of methods to fabricate tungsten nanoparticles [2, 78-90], including thermal decomposition of $W(CO)_6$ [63] and WCl_6 [87], hydrogen reduction of WO_3 [79, 88, 89], or mechanical milling [90]. In the present work, tungsten nanoparticles were fabricated by a modified physical vapor deposition (PVD) technique [45], which involves a chamber with higher- and lower-pressure chambers separated by apertures that direct aggregated nanoparticles (from the physical vapor in the high-pressure chamber) onto a substrate or other collector in the low-pressure chamber.

Using this method, high purity tungsten nanoparticles were deposited on sapphire substrates and were subsequently characterized using scanning electron microscopy (SEM), X-ray energy dispersive spectroscopy (EDS) and X-ray photoelectron spectroscopy (XPS). Annealing experiments were performed in vacuum to directly observe the evolution of tungsten nanoparticle morphology in response to elevated temperatures. Tungsten nanoparticles grew into islands when heated directly at 1100 °C and with a surrounding pressure of 10^{-7} Torr. In contrast, highly faceted nanoparticles were generated when the starting tungsten material was first pre-heated at 700-850 °C, with a surrounding pressure of 0.5 torr, and then heated at 1100 °C, also with a surrounding pressure of 10^{-7} Torr. The mechanism by which {110} facets formed on tungsten nanoparticles are outlined and discussed in this chapter.

5.2   Materials and Methods

The tungsten nanoparticle fabrication process is the same one used in a previous study that involved the design and construction of a specialized apparatus for different metallic particles [45]. The custom-built nanoparticle generator included two vacuum chambers: a higher-pressure condensation chamber and a lower-pressure deposition chamber. During the nanoparticle deposition process, tungsten atoms are sputtered from a target in the higher-pressure chamber, creating physical vapor. Tungsten atoms collide with the argon process gas as well as with other tungsten atoms, and aggregate to form tungsten clusters [45]. Due to the pressure difference between the two chambers, the clusters and atoms in the higher-pressure chamber travel with the carrier gas flow to the lower pressure chamber. When the tungsten clusters arrive at the substrate, they condense and form nanoparticles on that substrate. The process used in this study is therefore a modified form of PVD.

Prior to deposition, the nanoparticle generator was pumped and baked overnight to reach a base pressure of 10^{-7} Torr. The system was cooled to ambient temperature and then argon gas was introduced to the chamber. The pressures in the condensation chamber and deposition chamber were adjusted by flow of the inert gas (argon) and by differential pumping of each chamber, resulting in a pressure ratio close to 1000:1, with the pressure in the condensation chamber close to 1 Torr. A power of 70 watts was applied to the tungsten target source, which had a diameter of 38.1 mm (1.50 inch), thickness of 3.18 mm (0.125 inch), and a purity of 99.95%, and this generated tungsten nanoparticles in the condensation chamber. In the deposition chamber, the nanoparticles were deposited on sapphire substrates, which were rotated at a speed of 6 revolutions per min (rpm).

Sapphire (α-Al$_2$O$_3$) was used as a substrate in this work due to its stability at high temperatures. After removal from the deposition chamber and before imaging, samples were stored in a vacuum desiccator to minimize surface oxidation. Prior to any heat treatment, the morphology, composition and deposition thickness of nanoparticle samples were characterized by focused ion beam and scanning electron microscopy (FEI Helios G3 dual-beam FIB-SEM), X-ray energy dispersive spectroscopy (Oxford X-Max 80 mm^2 EDS) and X-ray photoelectron spectroscopy (Thermo K-Alpha XPS).

One group of samples was annealed directly at 1100 °C, with a surrounding pressure of 10^{-7} Torr and a range of annealing times. This step occurred in a custom-built ultrahigh vacuum (UHV) chamber system designed for Kelvin probe measurement of work function [91], which also contained a heating stage. A second group of samples underwent pre-heating treatment at intermediate temperatures (700 °C to 850 °C) and surrounding pressure of 0.5 Torr using a heating stage in an environmental SEM (FEI Quanta FEG 250); the background gas contributing to this pressure was remnant ambient air. These samples were subsequently annealed at 1100 °C and surrounding pressure of 10^{-7} Torr (in the custom UHV Kelvin probe chamber); in between these annealing steps, the samples were briefly exposed to laboratory air and were stored in a vacuum desiccator. Details of all heat treatments are listed in Table 5.1. These annealed samples were characterized with SEM, EDS and XPS (Prior to XPS measurements, the spectrometer was carefully calibrated using the adventitious carbon peak to ensure accurate determination of peak energies).

Table 5.1 Thicknesses of tungsten nanoparticle deposition layers and parameters for vacuum heating experiments.

Deposition Thickness	Annealing Condition
40 nm	1100 °C, 10^{-7} Torr for 1h
40 nm	1100 °C, 10^{-7} Torr for 2h
80 nm	1100 °C, 10^{-7} Torr for 2h
80 nm	1100 °C, 10^{-7} Torr for 4h
270 nm	700 °C, 0.5 Torr for 20 min, then 1100 °C, 10^{-7} Torr for 1 h
270 nm	850 °C, 0.5 Torr for 10 min, then 1100 °C, 10^{-7} Torr for 2 h
270 nm	850 °C, 0.5 Torr for 10 min, then 1100 °C, 10^{-7} Torr for 4 h

5.3   Results and Analysis

As shown in Figure 5.1, the color of sample varied with its status, when deposited with tungsten nanoparticles, original white sapphire looked dark grey, whereas it looked blue when it was annealed at 700 °C, 0.5 torr for 20 min and 850 °C, 0.5 torr for 10 min, separately.
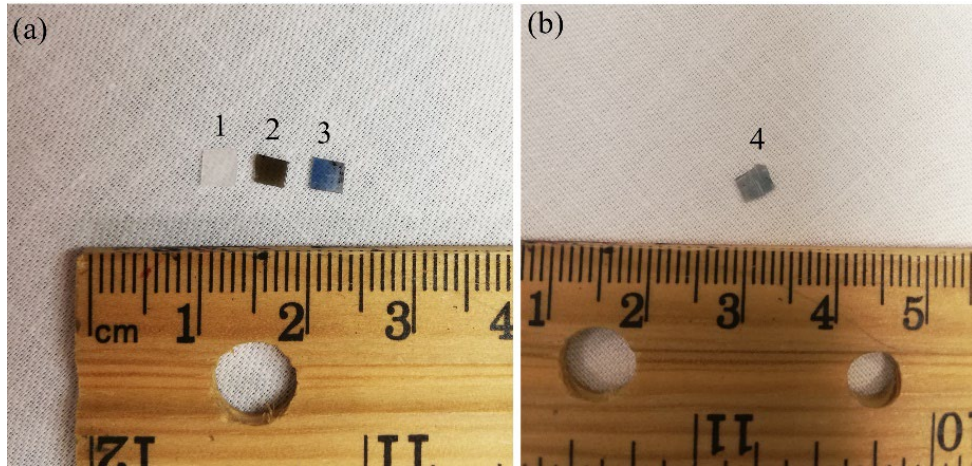
Figure 5.1 Photographs of samples: sapphire without nanoparticles (labeled as 1), nanoparticles without annealing (labeled as 2), nanoparticles annealed at 700 °C, 0.5 torr for 20 min (labeled as 3), and annealed at 850 °C, 0.5 torr for 10 min (labeled as 4)

5.3.1 As-deposited Nanoparticles

Figure 5.2 presents the secondary electron (SE) images and EDS analysis of tungsten nanoparticles deposited on sapphire, with a total deposition thickness of 271 nm. The surface topography (Figure 5.2a) and cross-section (Figure 5.2b) show the structure of deposited tungsten nanoparticles, including a variation of porosity through the thickness. The average diameter of nanoparticles (as observed in Figure 5.2a) was 6 nm, with a standard deviation of 2 nm (as measured directly from SEM micrographs, including ~50 particle measurements for each stated average value). These as-deposited nanoparticles formed a continuous nanoporous structure. EDS elemental maps (Figure 5.2c-f) confirmed the deposition of tungsten on the sapphire substrate.
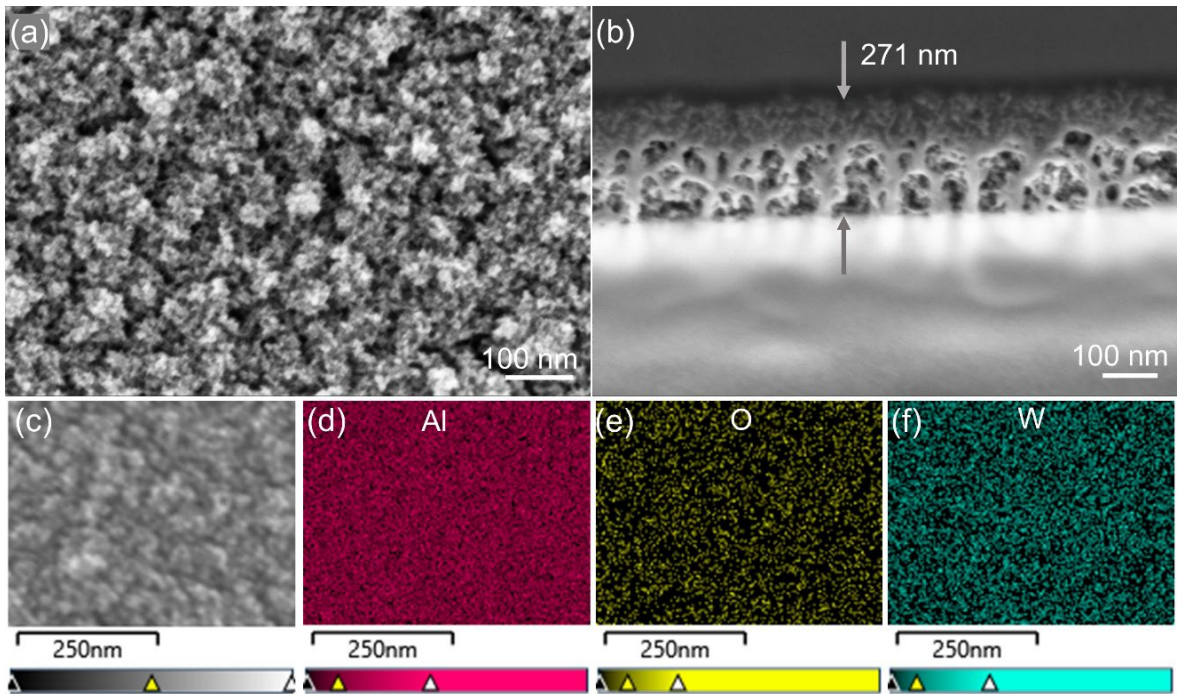
Figure 5.2 Nanoparticles deposited on sapphire: (a) plan view, (b) cross-section view, (c) electron image of region for EDS analysis, and elemental maps for (d) aluminum, (e) oxygen, (f) tungsten.

5.3.2 Nanoparticles after Annealing at 1100 °C, 10^{-7} Torr

Figure 5.3 illustrates the morphologies of tungsten nanoparticles after annealing directly at 1100 °C and with a surrounding pressure of 10^{-7} Torr. These results indicate that the as-deposited continuous nanoporous tungsten layer transformed into larger discrete particles during annealing, and in all cases exhibited surface facets. At the same time, needle-like components were present alongside individual nanoparticles when the annealing duration was 1 hr (Figure 5.3 (a1)), but the needle-like components were not observed when the annealing duration was 2 hrs or 4 hrs (Figure 5.3 (a2), (a4)). Additionally, for the samples imaged in Figure 5.3 (a1) and Figure 5.3 (a2), which had an original deposition thickness of 40 nm, there was no significant change in final nanoparticle size when the annealing duration increased from 1 hr to 2 hrs.
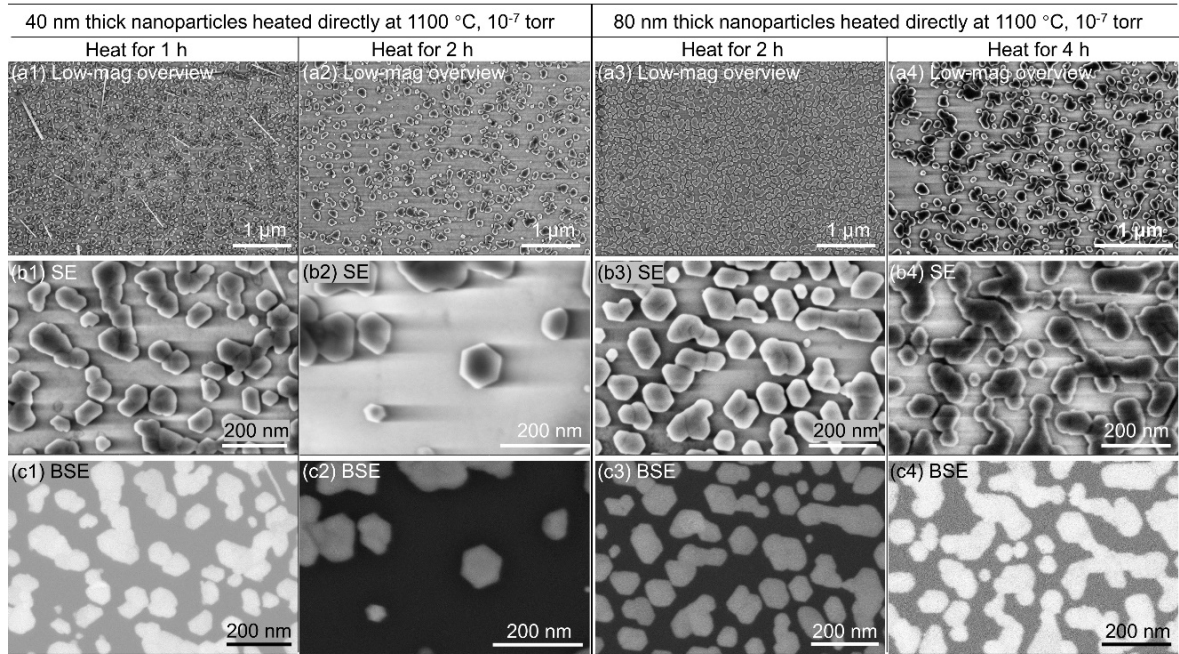
Figure 5.3 SEM micrographs of nanoparticles after annealing at 1100 °C and 10^{-7} Torr. (a1, a2) low-magnification overview of separate 40 nm thick nanoparticle layers heated for 1 hr and 2 hrs, respectively; (a3, a4) low-magnification overview of separate 80 nm thick nanoparticle layers heated for 2 hrs and 4 hrs, respectively; (b1 to b4) SE images of zoomed regions from images a1 to a4; (c1 to c4) backscattered electron (BSE) images corresponding to images b1 to b4.

In comparing Figures 5.3 (a2) and 5.3 (a3), it is seen that a higher number of annealed tungsten nanoparticles were present in the sample with original tungsten deposition thickness of 80 nm (versus 40 nm). This increased areal density of annealed nanoparticles was especially apparent at higher magnification (Figures 5.3 (c2) and 5.3 (c3)). Similarly, Figures 5.3 (a3) and (a4) show that, for samples with an original deposition thickness of 80 nm, the final nanoparticles experienced a higher degree of aggregation when the annealing duration was increased from 2 hrs to 4hrs.

Figure 5.4 presents SEM images and EDS elemental maps of nanoparticles which originally had 40 nm deposition layer thickness and were annealed for 1 hr at 1100 °C, with a surrounding pressure of 10^{-7} Torr. In addition to Al and O signals from the sapphire substrate, W from the nanoparticle layer was also detected (Figure 5.4c). Comparing Figures 5.4b and 5.4d, it appears that the W agglomeration in the mapped region blocks more Al signal than O signal, i.e., the tungsten nanoparticles are partially oxidized. This point will be addressed in more detail later, in the analysis of XPS results.
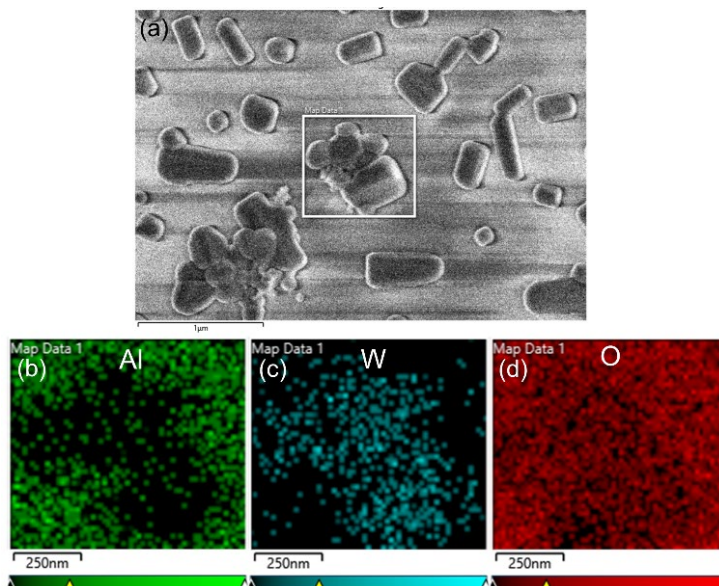
Figure 5.4 SEM images and EDS elemental maps of nanoparticles with an original deposition thickness of 40 nm, after annealing for 1 hr at 1100 °C, 10^{-7} Torr (a) SEM image, and elemental maps for (b) aluminum, (c) tungsten and (d) oxygen.

5.3.3 Nanoparticles annealed at 700 °C, 0.5 Torr +1100 °C, 10^{-7} Torr

Figure 5.5 presents SEM micrographs and EDS spectra of nanoparticles which had a deposition thickness of 270 nm, then were preheated for 20 min at 700 °C with a surrounding pressure of 0.5 Torr, and finally were annealed for 1 hr at 1100 °C with a surrounding pressure of 10^{-7} Torr. As shown in Figure 5.5a, tungsten nanoparticles with a layer deposition thickness of 270 nm appeared to retain the as-deposited nanoporous structure through the preheating stage of 700 °C for 20 min, with a surrounding pressure of 0.5 Torr. Moreover, the average diameter of nanoparticles (as observed in Figure 5.5a) was seen to increase slightly to 8 nm with a standard deviation of 2 nm, and the structure appeared more porous relative to the initial morphology in Figure 5.2a. When the preheated nanoparticles were subsequently annealed for 1 hr at 1100 °C with a surrounding pressure of 10^{-7} Torr, the nanoparticles grew noticeably larger and in some cases formed distinct

nanoparticles, although the majority remained aggregated, as shown in Figures 5.5b, d and g. A small number of nanoparticles exhibited a highly faceted morphology with sharp edges and vertices, as illustrated in SE images (Figures 5.5 c,e) and a corresponding BSE image (Figure 5.5f). The BSE image in Figure 5.5f suggests that the highly faceted nanoparticle has a similar average atomic number to that for the other (aggregated) particles. On the other hand, the EDS spectra suggest there may be a composition difference between them, with the highly faceted nanoparticles being (nearly) pure W (Figures 5.5 g,h) and the aggregated nanoparticles being partially oxidized (Figures 5.5g,i). It is noted that the O signal in Figure 5.5i could also be due to detection of the sapphire substrate at this location, e.g., if the aggregated tungsten particles were not as thick as the faceted tungsten particles.
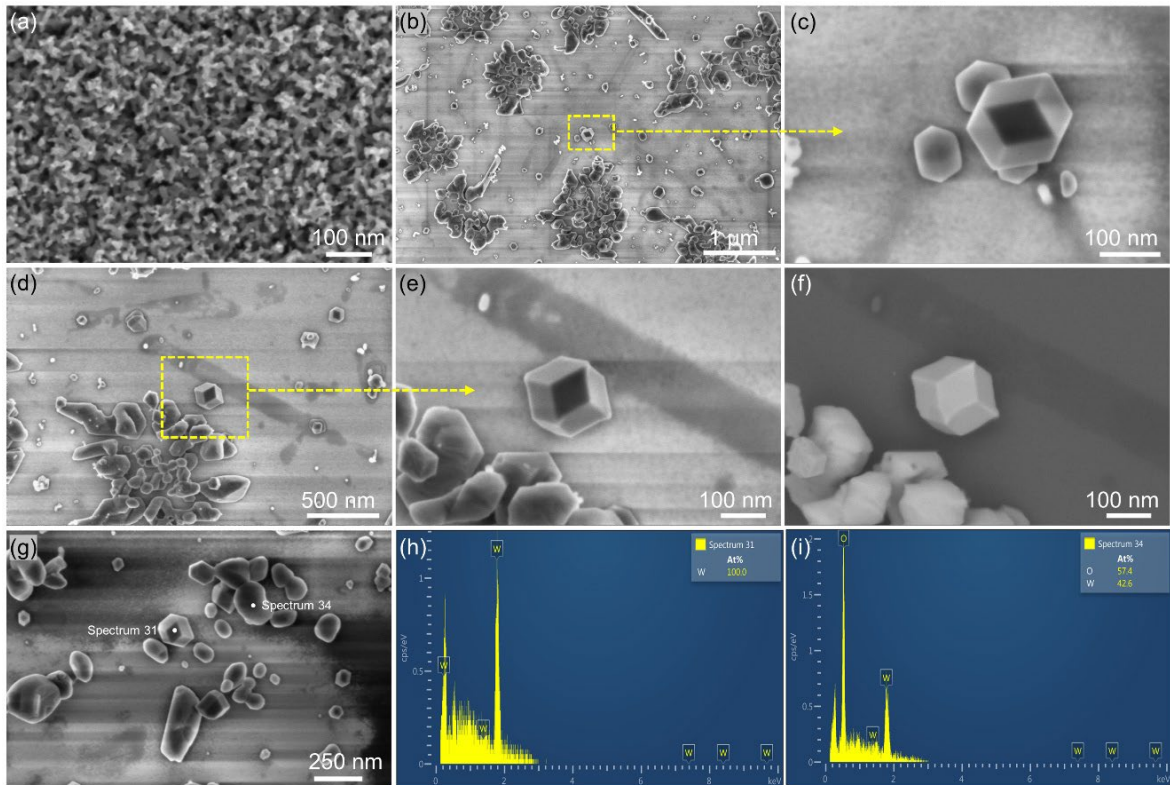
Figure 5.5 SEM micrographs of tungsten nanoparticles: (a) after preheating for 20 min at 700 °C, 0.5 Torr, and (b-g) after annealing for 1 hr at 1100 °C, 10^{-7} Torr. (b) and (d) provide lower-magnification overviews of annealed particles, most of which have aggregated. (c) and (e) show highly faceted individual nanoparticles, which are near but not connected to the aggregated particles. (f) BSE image corresponding to (e). EDS spectra are provided for separate nanoparticles from image (g), namely (h) the highly faceted nanoparticle labeled with spectrum 31, and (i) the nanoparticle labeled with spectrum 34.

SEM images and associated crystal shape of highly facet particles are presented in Figure 5.6, for the tungsten nanoparticle sample that was preheated for 20 min at 700 °C with a surrounding pressure of 0.5 Torr, then annealed for 1 hr at 1100 °C with a surrounding pressure of 10^{-7} Torr. The crystal shape was rotated to match the observed orientation of each nanoparticle and included as an inset in the SEM images (Figures 5.6 a-c), to facilitate comparison between observed and calculated nanoparticle shape. The particle shape simulation tool Wulffmaker [92] was applied to calculate the crystal shape and help identify the facet indices, using the surface energy of different crystallographic facets as input. The analysis indicates that the observed crystal shape was dominated by {110} facets, which implies that {110} W surfaces have the lowest surface energy (γ) among various crystallographic facets, at least under the environmental conditions imposed during annealing experiments in the current study.
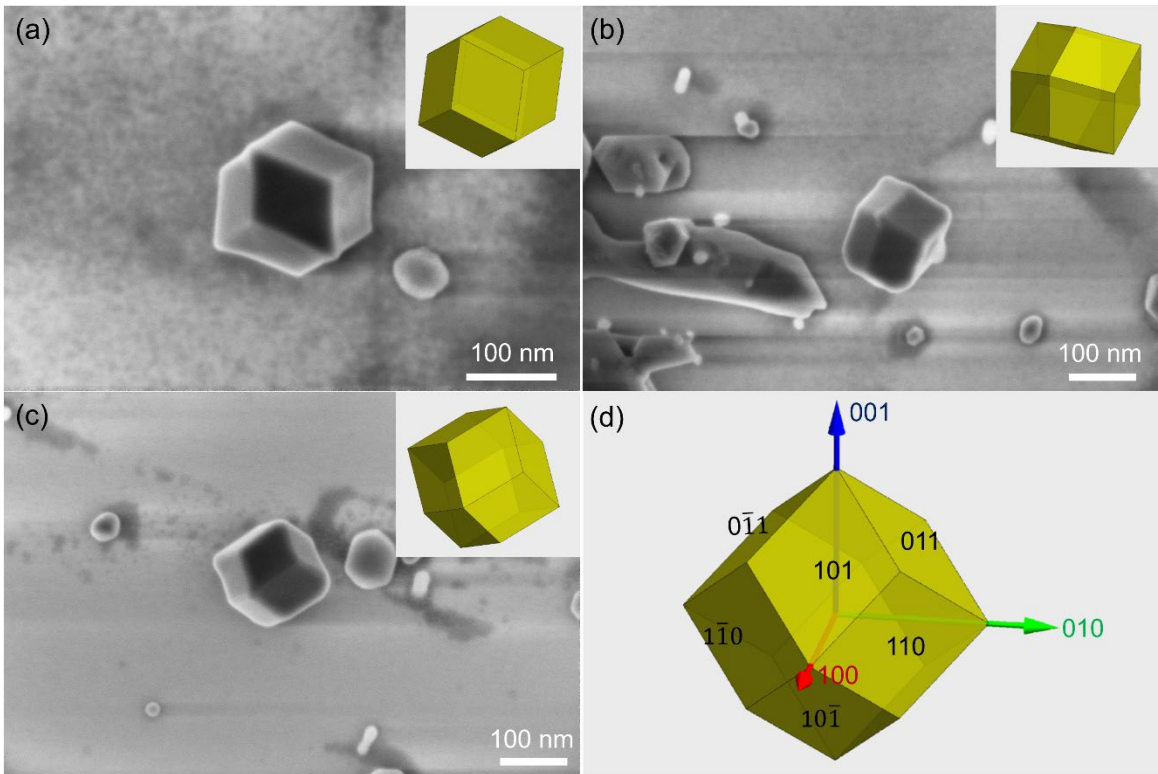
Figure 5.6 SEM images of highly faceted nanoparticles preheated for 20 min at 700 °C, 0.5 Torr and then annealed for 1 hr at 1100 °C, 10^{-7} Torr. (a-c) show different particles in various orientations, along with the corresponding calculated crystal shape (inset). The crystal shape shown in (d) includes specific indices for several facets, all of which belong to the {110} family.

5.3.4 Nanoparticles annealed at 850 °C, 0.5 Torr +1100 °C, 10^{-7} Torr

Figure 5.7 presents observations obtained at several stages of nanoparticle evolution in an individual sample with original deposition thickness of 270 nm. This sample was preheated for 10 min at 850 °C with a surrounding pressure of 0.5 Torr, then annealed for 2 hrs (and again to reach a total of 4 hrs) at 1100°C with a surrounding pressure of 10^{-7} Torr. The nanoparticle network maintained a continuous and open-porous structure during the preheating stage at 850 °C, as shown in Figure 5.7a, and the average diameter of the nanoparticles increased to 10 nm with a standard deviation of 2 nm. During annealing at higher temperature (the first 2 hrs at 1100 °C, 10^{-7} Torr), the deposited tungsten layer

transformed into a bimodal distribution of nanoparticles, with a small number of larger (~100 nm diameter), discrete particles surrounded by numerous smaller (~10 nm diameter) nanoparticles that were partially aggregated, as seen in Figures 5.7b-c. Figure 5.7c reveals that the larger particles were faceted and had higher average atomic number, since they appear brighter than the smaller nanoparticles in this BSE image. This may be due to the presence of a uniformly thick surface oxide on all particles, which would have a greater impact on the average atomic number (and therefore image brightness in BSE mode) for smaller particles. In contrast, Figures 5.7d-e show that when the sample was annealed for an additional 2 hrs (i.e., total of 4 hrs) at 1100 °C with a surrounding pressure of 10^{-7} Torr, significantly fewer tiny particles were observed on the substrate. Instead, the faceted particles grew even larger, relative to the size observed in Figure 5.7c, presumably by consuming neighboring smaller nanoparticles. The larger particles (~200 nm diameter) exhibited clear and sharp facets, edges and vertices, while the remaining smaller nanoparticles tended to agglomerate into nondescript shapes. An EDS spectrum (Figure 5.7f) was obtained from a larger particle in Figure 5.7d and indicated a pure tungsten composition. Similar observations were obtained at other sample locations (e.g., Figures 5.7g-h). Facet indices calculated by Wulffmaker suggest that the large particles exhibit {110} and {100} surface facets (Figure 5.7i), with {110} facets dominating the tungsten. This implies that {110} planes have the lowest surface energy (γ), followed by {100} with the second lowest surface energy. For the annealing conditions applied to this sample, the following relation appears to hold: $\gamma_{(110)} < \gamma_{(100)} < \gamma_{(111)}$.
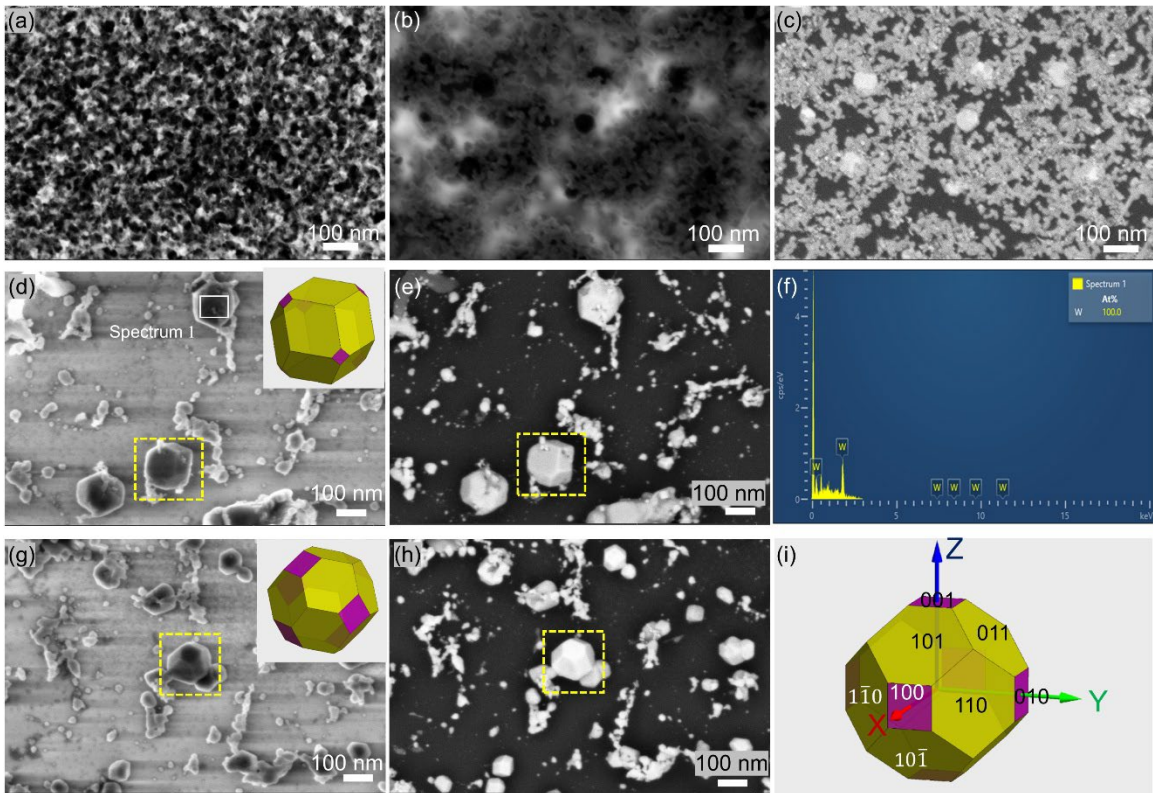
Figure 5.7 SEM micrographs of tungsten nanoparticles: (a) SE image of nanoparticles preheated for 10 min at 850 °C, 0.5 Torr, (b) SE image of preheated nanoparticles after subsequent annealing for 2 hrs at 1100 °C, 10^{-7} Torr, (c) BSE image corresponding to (b); (d) SE image of nanoparticles annealed for a total of 4 hrs at 1100 °C, 10^{-7} Torr, (e) BSE image corresponding to (d); (f) EDS spectrum of nanoparticle labeled as spectrum 1 in (d); (g) SE image of an additional representative faceted particle, (h) BSE image corresponding to (g); (i) schematic of crystal shape calculated using Wulffmaker, including indices of the various facets.

XPS was performed on as-deposited nanoparticles and also on annealed nanoparticles (20 min at 700 °C, with a surrounding pressure of 0.5 Torr), to determine the relative degrees of metallic versus oxidized tungsten in these samples and to provide an indication of surface oxide thickness. These samples correspond to the nanoparticle networks in Figure 5.2a and Figure 5.5a, respectively. Both of these samples involved uniform coverage of the substrate by tungsten; longer annealing times yielded larger faceted particles, along with smaller nanoparticles and large, exposed regions of the substrate, so

XPS results were not conclusive for this sample state and are therefore not presented here. Additionally, the XPS spectra provide information on the oxidation state(s) of tungsten and can be used to calculate the relative fractions of all detected species.

Table 5.2 presents the analyzed data extracted from XPS scans, such as those in Figure 5.8. The detected peaks correspond to metallic tungsten (W), W_xO (x>1), WO_y (2<y<3), and WO_3. In the XPS spectrum for as-deposited nanoparticles (Figure 5.8a), two doublet peaks were observed. The first doublet at 31.35 eV and 33.42 eV corresponds to W 4f7/2 and W 4f5/2 from pure W, respectively [93, 94]. The second observed doublet at 35.93 eV and 38.08 eV corresponds to W 4f7/2 and W 4f5/2 from WO_3, respectively [94, 95]. Additionally, as shown in Figure 5.8 and Table 5.2, spectrum analysis indicates the presence of W_xO and WO_y. In the XPS spectrum for nanoparticles annealed for 20 min at 700 °C (Figure 5.8b), only two peak types were identified: WO_y and WO_3. The second doublet at 35.90 eV and 38.03 eV corresponds to W4f7/2 and W4f5/2 from WO_3, respectively [94, 95], and this identification is similar to that for WO_y in as-deposited tungsten nanoparticles (Figure 5.8a). It is noted that after brief annealing (Figure 5.8b), no metallic tungsten is detected by XPS, implying that the nanoparticles are fully oxidized or at least covered by a thicker oxide layer. The relative fraction of each component included in Table 5.2 indicates that annealing led to an increase in the oxidation state for all W in the near-surface region of the material analyzed by XPS, as that technique probes to a depth of 5-10 nm. Indeed, annealing generated a surface region consisting almost entirely of fully oxidized WO_3. Similar results were obtained during analysis of nanoparticles that had been annealed at 850 °C, 0.5 Torr.
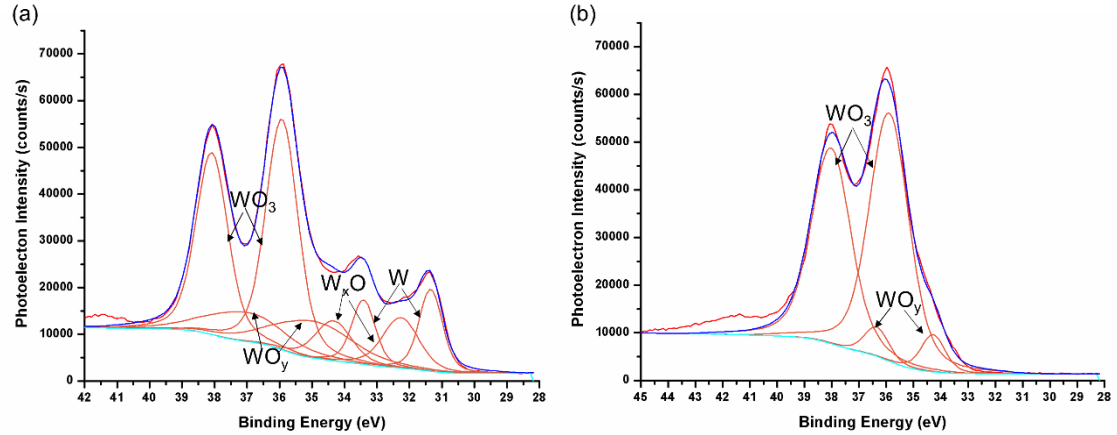
Figure 5.8 XPS spectra of (a) as-deposited nanoparticles, corresponding to Figure 5.2a; and (b) nanoparticles annealed for 20 min at 700 °C, 0.5 Torr, corresponding to Figure 5.5a. Raw data are shown in red; the baseline (cyan) and fitted peaks (blue) are shown for comparison; the orange peaks correspond to peaks for individual chemical species that combine to yield the fitted peaks (blue).

Table 5.2 Detailed information from the analysis of XPS spectra obtained from as-deposited nanoparticles and nanoparticles annealed for 20 min at 700 °C, 0.5 Torr.

Sample	Component	Scan	Peak Binding Energy (eV)	Area (P) CPS.eV	Atomic %
As-deposited W nanoparticles	W	W4f7/2	31.35	17497.99	13.6
		W4f5/2	33.42	13794.04	
	W_xO	W4f7/2	32.27	16736.51	13.0
		W4f5/2	34.34	13195.39	
	WO_y	W4f7/2	34.98	26374.53	20.6
		W4f5/2	37.05	20856.81	
	WO_3	W4f7/2	35.93	67559.61	52.8
		W4f5/2	38.08	53258.67	
Annealed for 20 min at 700 °C, 0.5 Torr	WO_y	W4f7/2	34.28	9572.17	8.4
		W4f5/2	36.35	7545.94	
	WO_3	W4f7/2	35.90	104701.5	91.6
		W4f5/2	38.03	82538.4	

5.4 Discussion

In the current study, tungsten nanoparticles deposited onto substrates formed nanoporous networks and were subsequently annealed to generate larger, faceted particles.

During the sputter deposition process, nanoparticles condensed into clusters within the physical vapor before impinging on the substrate, and then contributed to a growing porous film. Due to the random impingement of tungsten nanoparticles, significant free volume was included in the film and it appeared similar to a nanoporous structure, e.g., such as that described in the work of Kosmidou et al. [96]. Interestingly, the porous film morphology appears to be similar, regardless of whether substrate rotation is applied during deposition (as in the current study) or the substrate remains stationary during deposition (as in a previous study [2]).

Based on characterization of as-deposited and certain annealed specimens, especially using XPS, oxidation of tungsten appears to have occurred when samples were removed from the deposition or annealing chamber and exposed to ambient atmosphere. This is consistent with expectations for tungsten nanoparticles, which form a thin surface oxide layer upon exposure to oxygen. Similar observations were reported by Acsente et al. [80, 97], where a core-shell structure existed in tungsten nanoparticles, specifically metallic tungsten in the core and tungsten oxides ($WO_3 + WO_2$) in the shell.

The formation and decomposition of tungsten oxides play a vital role in heating experiments on tungsten nanoparticles, given their high surface-area-to-volume ratio. When tungsten is heated, the following reactions can occur [40, 98-103] in different temperature regimes:

$$W \text{ (s)} + O_2 \text{ (g)} \leftrightarrow WO_2 \text{ (s)} \qquad\qquad (5)$$

$$WO_2 \text{ (s)} + \tfrac{1}{2} O_2 \text{ (g)} \leftrightarrow WO_3 \text{ (s)} \qquad\qquad (6)$$

$$3WO_3 \text{ (s)} \leftrightarrow (WO_3)_3 \text{ (g)} \qquad\qquad (7)$$
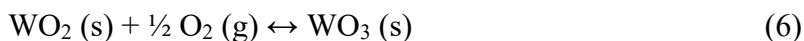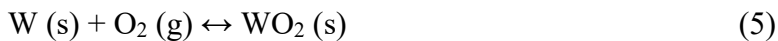
That is, tungsten will react with O_2 to form WO_2, and this WO_2 will react further with O_2 to form solid WO_3, which may eventually sublimate into gas (if a sufficient amount of

oxygen is present [104]) or decompose into metallic tungsten (if the amount of environmental oxygen is extremely low [103]). These oxidation reactions were studied by Gulbransen et al. [98-100], Togaru et al. [104] and Cifuentes et al. [105], and they reported that the mechanism of tungsten oxidation is complex because it is not only controlled by temperature, pressure and time of exposure to atmosphere [98, 99], but it is also affected by sample surface and sample pretreatment [98-100]. Gulbransen et al. [98-100] found that oxidation of tungsten occurs even at ambient temperature. Additionally, for temperatures below 600 °C, the formation of solid WO_2 and solid WO_3 according to Eq. (5) and Eq. (6) can occur simultaneously, with both reactions controlled by oxygen diffusion. While the sublimation of WO_3 according to Eq. (7) can occur starting at 900 °C, it proceeds at an appreciable rate only for temperatures higher than 1000 °C [100]. On the other hand, at intermediate temperatures (600 °C ~ 900 °C), local reactions within edge cracks of sample regions can complicate the overall processes [98, 99]. Importantly, Gulbransen et al. [98] determined that over a broad temperature range (room temperature up to 1300 °C), WO_3 is always the principal oxide, although WO_2 will exist at the metal-trioxide interface.

Overall, studies on the decomposition of tungsten oxides are not as numerous as those on the formation of tungsten oxides. G. Hägg et al. [106] proposed that W_3O can decompose into W and WO_2 according to equation (8):

$$2 \ W_3O \ (s) = 5 \ W \ (s) + WO_2 \ (s) \qquad\qquad (8)$$
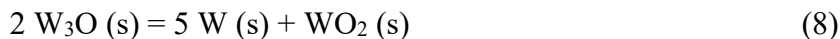
However, this proposed reaction was not paired with experimental observations. Additionally, S. Vaddiraju et al. [103] reported that at high temperatures, the sublimation, condensation and decomposition of nanoscale tungsten oxides can occur simultaneously according to equations (5), (9) and (10), and the system will reach a complex gas-solid equilibrium.

WO_2 (g) → W (s) + O_2 (g)   (9)

WO_3 (g) → W (s) + 3/2 O_2 (g)   (10)

During *in situ* XPS heating experiments, A. Romanyuk et al. [107]observed a peak shift for tungsten oxide nanoparticles, indicating that tungsten oxides can be reduced to metallic tungsten at elevated temperatures in vacuum. Interestingly, their study showed that the thermal stability of tungsten oxide nanoparticles was highly dependent on nanoparticle size: tungsten oxide nanoparticles with smaller size exhibited a greater degree of stability against thermal reduction at elevated temperatures in vacuum [106].

In the current study, the XPS results in Figure 5.8 and Table 5.2 indicate that WO_3 is the principal oxide for both as-deposited and annealed tungsten nanoparticles (20 min at 700 °C, with a surrounding pressure of 0.5 Torr). This is consistent with the interpretations of Gulbransen et al. [98]. Additionally, EDS data in Figures 5.5 and 5.7 show that faceted metallic tungsten nanoparticles can be created from previously heated samples (at intermediate temperatures) when those samples are subjected to high temperature annealing (1100 °C) under high-vacuum conditions (10^{-7} Torr). These observations are consistent with the idea of tungsten oxide decomposition. Moreover, nanoparticle size might also play a role in the decomposition process. As observed in the plan-view images of Figures 5.2, 5.5 and 5.7, average nanoparticle size increased from 6 nm to 8 nm to 10 nm, respectively. For as-deposited tungsten nanoparticles (6 nm average size) that were annealed only at 1100 °C and 10^{-7} Torr, no metallic tungsten particles were detected after the high-temperature anneal. On the other hand, for tungsten nanoparticles that had been subjected to an intermediate anneal of 700 °C (8 nm average size) or 850 °C (10 nm average size), highly faceted metallic tungsten nanoparticles were observed. The results of the current study are consistent with those reported by A. Romanyuk et al. [107], i.e., an

increase in nanoparticle size correlates with a decrease in stability against thermal reduction in a high-temperature vacuum environment. Indeed, a threshold nanoparticle size of ~8 nm appears to be consistent for both studies.

Considering all heating experiments presented here, highly faceted nanoparticles were observed only when the high-temperature, high-vacuum annealing step was preceded by intermediate-temperature annealing (either at 700 °C or 850 °C, with a surrounding pressure of 0.5 Torr). This phenomenon, which has also been described as oxygen-induced faceting, was systematically investigated by A. Szczepkowicz et al. [108-113]. Their study indicated that when oxygen is added to a metallic tungsten surface, it can destabilize that surface by creating a high degree of surface energy anisotropy, followed by a faceting process that is driven by the minimization of the total free surface energy [108]. This appears to be relevant to the tungsten nanoparticle faceting reported in the current study.

The partial pressure of oxygen plays a vital role during the annealing procedures described here. When as-deposited tungsten nanoparticles on sapphire substrates were directly annealed at 1100 °C (with a surrounding pressure of 10^{-7} Torr), sublimation of WO_3 into the gaseous state occurred, while WO_2 and other tungsten oxides (W_xO ($x>1$), WO_y ($2<y<3$)), which are typically stable in the solid phase at high temperature, remained on the substrate. This is postulated to be due to the limited amount of O_2 (~20% of the local 10^{-7} Torr atmosphere) available for reaction, and may explain why unfaceted tungsten oxide particles were observed for all heating experiments in Figure 5.3. Similarly, the influence of oxygen partial pressure on the shape of tungsten particles at different temperatures was recently investigated by Seif et al. [114] . Their calculations indicate that the formation of a particular tungsten nanoparticle Wulff shape requires specific conditions

that may fall within a narrow window, such as extremely low oxygen partial pressure and/or certain chemical conditions to regulate the availability of oxygen to the tungsten surface. The results in Figures 5.5 and 5.7 are consistent with this idea, i.e., that the faceting and morphology of tungsten nanoparticles vary with environmental and processing conditions.

The surface free energy of tungsten is governed by crystallography as well as both temperature [110, 114] and chemical environment [114], and the formation of surface facets on nanoparticles at high temperature is driven by thermodynamics. Overall, a nanoparticle will always tend to reach a shape that can minimize the total surface energy [114]. Additional work by Belyaeva et al. [115] indicates that {110} facets have the lowest surface free energy among {111}, {110}, and {100} facets, with an overall relationship of $\gamma_{(110)} < \gamma_{(100)} < \gamma_{(111)}$. The faceting observed in the current study (see Figures 5.6 and 5.7) is consistent with this relative surface energy relationship, i.e., {110} faces dominated the tungsten nanoparticles so that the nanoparticles can achieve the lowest surface energy. However, there is some debate in the scientific community regarding the relative magnitudes of the {100}, {110}, and {111} surface energies, as described by several theoretical models that deliver contradictory predictions [115]. Investigations by Belyaeva et al. [115] and Wang et al. [116] support the trend $\gamma_{(110)} < \gamma_{(100)} < \gamma_{(111)}$, while others by Yu et al. [117] support the trend $\gamma_{(110)} < \gamma_{(111)} < \gamma_{(100)}$. These details represent an area of disagreement that may warrant further investigation by the scientific community, and additional work could elucidate the nuances of facet evolution during heating. In the current study, metallic tungsten nanoparticles were observed to be dominated by {110}-

oriented facets, albeit with an overall Wulff shape that may depend on annealing temperature.

5.5   Conclusion

Nanoporous layers of deposited tungsten nanoparticles were fabricated using a custom-built apparatus that enabled a modified physical vapor deposition process. As-deposited tungsten nanoparticles existed in a core-shell structure, due to oxidation that occurred upon exposure to air. When directly heated at 1100 °C with a surrounding pressure of 10^{-7} Torr, the nanoparticles grew into larger, discrete particles. For samples that were first preheated by annealing at intermediate temperature (20 min at 700 °C, 0.5 Torr), some tungsten nanoparticles grew and became highly faceted during annealing at higher temperature (1100 °C, 10^{-7} Torr); the Wulff shape of these particles were dominated by {110} facets, consistent with a minimization of surface energy. Preheating of samples at a different intermediate temperature (10 min at 850 °C, 0.5 Torr) followed by annealing at higher temperature (1100 °C, 10^{-7} Torr) also resulted in the formation of highly faceted nanoparticles; in this case, the Wulff shape exhibited a small relative proportion of {100} facets but was still dominated by {110} facets. The results of the current study indicate that the oxidation of tungsten is a key factor in the evolution of surface faceting. Furthermore, there may be a critical size for tungsten nanoparticles that determines their thermal stability, i.e., their resistance to thermal reduction in a high-temperature vacuum environment. Additional studies on the faceting and oxidation of nanoscale tungsten are underway to investigate surface changes in bulk tungsten and will be discussed in the context of the nanoparticle results presented above.

CHAPTER 6. CRYSTALLOGRAPHIC FACETING OF BULK TUNGSTEN SURFACES OBSERVED DURING IN SITU HEATING IN AN ENVIRONMENTAL SCANNING ELECTRON MICROSCOPE

6.1   Introduction

When a conductive body is heated to a sufficiently high temperature, electrically charged particles, which may be electrons or ions, are emitted from it and can be drawn off by a suitable electric field. This phenomenon is called *thermionic emission* [13], and the conductor that can thermionically emit electrons in response to heating is called a '*cathode*' [8, 9]. Since the beginning of the vacuum tube industry in the 20th century, dispenser cathodes have been used extensively as electron sources in a variety of vacuum electron devices (VEDs) for a range of applications, including electron microscopes, traveling wave tubes, high-power microwave devices [3, 4, 18, 21, 22], industrial heating, medical treatment, scientific research [23], civilian communications systems, as well as space-based and military needs [114].

As described above, thermionic emission is theoretically feasible for all conductors heated to suitable temperatures, albeit with some material surfaces being more favorable for emission due to crystallography or surface decoration with other species such as barium [27]. Metals, as the class of materials that are inherently good electrical conductors, were therefore considered as potential cathode materials for thermionic emission. At the same time, because cathodes must be heated to high temperatures to facilitate thermionic emission, refractory metals such as tungsten (W, melting point 3422 °C) were initially studied as cathode materials. Current density during thermionic emission depends strongly on work function of the emitting surface [27]. In turn, work function depends on the particular state of a material surface, including its surrounding environment, e.g., vacuum,

gas, or adsorbed surface monolayer. With increasing performance demands for higher emission current density, significant effort has been invested to modify the surrounding environment and/or surface conditions of dispenser cathodes to lower their effective work function, such as operating the cathode in a high-vacuum chamber, coating the cathode surface with a thin metal film, or filling the porous W cathode with alkali-earth oxides.

Dispenser cathodes, the most widely used electron sources in vacuum electron devices, consist of a porous tungsten matrix impregnated with mixtures of alkaline metal oxides, with BaO-CaO-Al_2O_3 being a typical impregnant mixture [19, 27]. The electron emission performance can be significantly improved by including scandia (Sc_2O_3) in the initial tungsten powder mix, or when introduced in a later processing stage as one of the impregnant materials [2, 19, 27, 118-124], leading to the designation of these emitters as "scandate dispenser cathodes". Due to their exceptional electron emission performance, scandate dispenser cathodes are generally regarded as the most promising next-generation vacuum electron sources [2, 118-125], with the caveat that consistent fabrication and reliable emission performance remain somewhat elusive.

Tungsten is the base material and therefore plays a crucial role in scandate dispenser cathodes. In this application, tungsten powder is sintered into a porous pellet so that it can serve as the matrix for the pore-filling impregnant material and provide suitable surfaces for thermionic emission. Therefore, the structure and chemistry of tungsten grain surfaces influence the emission performance of scandate cathodes. Recent experimental research by Liu *et al.* [3, 21, 29, 126] has revealed that the highly faceted crystallography of tungsten grains contributes significantly to the emission performance of scandate dispenser cathodes. Moreover, it was found that high-performance scandate dispenser cathode

surfaces tend to include equiaxed tungsten grains that exhibit {001}, {110}, and {112} facets [3, 114]. Meanwhile, Seif *et al.* [70, 114] employed density functional theory (DFT) to calculate the equilibrium shape of tungsten grains for emission from scandate dispenser cathodes as a function of temperature and surface energy in an ideal vacuum environment [70], as well as in the case where oxygen, barium and scandium are present [114]. These studies provide important background and context for the current study.

A primary motivation for the current study was to investigate the influence of environment on W surface faceting, including the range of crystallographic facet orientations that can be generated via control of temperature and oxygen partial pressure. Although their DFT calculations provided a wealth of predictions regarding the surface morphology of tungsten grains exposed to different chemical environments, most of the calculations focused on conditions with extremely low oxygen partial pressure ($< 10^{-10}$ Torr, corresponding to an oxygen chemical potential lower than 6.5 eV). Consequently, there was a relative lack of systematic investigation of tungsten cathode surfaces exposed to low-vacuum environments, i.e., higher partial pressures of oxygen such as those relevant to environmental scanning electron microscopy (ESEM) or to sputtering conditions during thin film deposition at elevated temperatures. Therefore, a major goal of this study was to initiate a systematic investigation of tungsten surface faceting.

An additional motivating factor for the current study was to resolve the particular orientation of W surface facets that form in response to the combined effects of temperature and oxygen partial pressure (chemical potential) [70, 114], as W surface oxidation and faceting at elevated temperatures are highly sensitive to grain orientation [104, 117, 127].

Based on those independent studies, it was hypothesized that there should be distinct ranges of environmental conditions where certain crystallographic facets are preferred.

In the present study, *in situ* heating inside an ESEM was performed to investigate faceting of the surfaces of tungsten pellets, which had been fabricated in the standard form of W pellets for use as the matrix material in scandate dispenser cathodes, using micron-scale tungsten powder followed by pressing and sintering. To gain a comprehensive understanding of the formation of facets and the evolution of their morphology on tungsten surfaces, heating experiments were performed on tungsten pellets using two different instruments. The first approach involved an ESEM, which included an *in situ* heating stage; elevated-temperature operation of this stage resulted in a pressure of 0.8 Torr around the sample. The second set of experiments was performed in a custom-built ultrahigh vacuum chamber designed for cathode work function measurements, which lacked scanning electron microscope (SEM) functionality but provided a surrounding pressure of 10^{-8} Torr across the entire temperature range [91, 128]. After cooling to ambient temperature, all samples were characterized using SEM, X-ray energy dispersive spectroscopy (EDS) and X-ray photoelectron spectroscopy (XPS) to identify changes in topography and surface composition. Moreover, the configuration of grains was examined using electron backscatter diffraction (EBSD) and imaging from multiple angles in the SEM. Additionally, a serial sectioning (Slice & View) experiment was performed on a <001>-oriented grain to reconstruct the 3D geometry of the faceted tungsten. Based on the materials characterization observations in this study, the oxidation process for tungsten is discussed extensively, along with an analysis of facet formation using Wulff shape construction software [92].

6.2   Materials and Methods

In this study, porous tungsten pellets (from 3M Technical Ceramics) that had been fabricated from micron-scale (3-6 μm diameter) tungsten powder were characterized. The pellets were initially pressed and sintered before being machined to dimensions of 3.09 mm diameter and 1.30 mm thickness, which is a form of how it serves as a matrix for dispenser cathodes. Prior to conducting heating experiments, each sample was thoroughly characterized using complementary techniques, including focused ion beam and scanning electron microscopy (FIB-SEM, FEI Helios G3 dual-beam system, Hillsboro, OR, USA), X-ray energy-dispersive spectroscopy (EDS, Oxford Instruments, X-Max 80 mm^2, Concord, MA, USA), and X-ray photoelectron spectroscopy (XPS, Thermo Scientific K-Alpha, Madison, WI, USA).

Two instruments with different heating stages were utilized, including an ESEM (FEI Quanta FEG 250, Thermo Scientific, Hillsboro, OR, USA) and a custom-built ultrahigh vacuum (UHV) system that was designed for Kelvin probe measurement of work function [91, 128] using an in-chamber heating stage (e-beam, Inc, Beaverton, OR, USA) [91]. Two different ESEM heating stages (1000 °C heating furnace for the 950 °C annealing experiments, versus 1400 °C heating furnace for the 1000-1250 °C annealing experiments, both manufactured by FEI company, Hillsboro, OR, USA) provided *in situ* thermal control, enabling direct observation of sample evolution as temperature increased. The temperature range investigated in the ESEM experiments spanned from ambient temperature to 1400 °C, and the chamber pressure varied from 0.1 to 1.0 Torr; the background gas contributing to this pressure was remnant ambient air, which contains oxygen at a partial pressure of 0.02 to 0.2 Torr, with the other gaseous species being

primarily N_2 and possibly some amount of H_2O [36]. Meanwhile, the pumping system in the custom-built UHV chamber maintained a consistent pressure of 10^{-8} Torr during heating, and the heater had a maximum temperature of 1200 °C.

The critical distinction between the *in situ* SEM heating experiments and those in the custom-built UHV instrument was the difference in chamber pressure that existed during the two heating procedures. It is noted that the UHV instrument, unlike the ESEM, does not possess the capability for *in situ* imaging of samples, as shown in Table 6.1.

Table 6.1 Comparison between two heating instruments.

Instrument	Pressure range	Heating Capacity	Imaging Function
Environmental SEM *(In Situ SEM heating)*	0.1~ 1.0 torr	25 °C ~ 1400 °C	SEM
Ultra High Vacuum heating Chamber	$10^{-8} \sim 10^{-7}$ torr	25 °C ~ 1100 °C	None

A series of *in situ* SEM experiments was conducted, wherein separate samples were heated to 950, 1100, 1200 or 1250 °C, respectively; the surrounding pressure was 0.8 Torr at all elevated temperatures for this range of ESEM experiments. Sample temperature was initially increased, in increments of 50 or 100 °C, to a moderate intermediate value (400, 500, 500 or 800 °C, respectively; see **Figure 6.1**) to warm up the stage assembly, before it was= incrementally raised to the final target temperature. To track the evolution of morphology, each sample was held at every incremental heating step for a period of 10 to 15 minutes and secondary electron SEM images were recorded after temperature had stabilized. Finally, upon reaching the target temperature, the sample was held there for 10 to 15 minutes, after which the heater power was switched off to ensure the sample

experienced the most rapid cooling rate possible; these rates are indicated below for the respective *in situ* experiments (as shown in Figure 6.1).
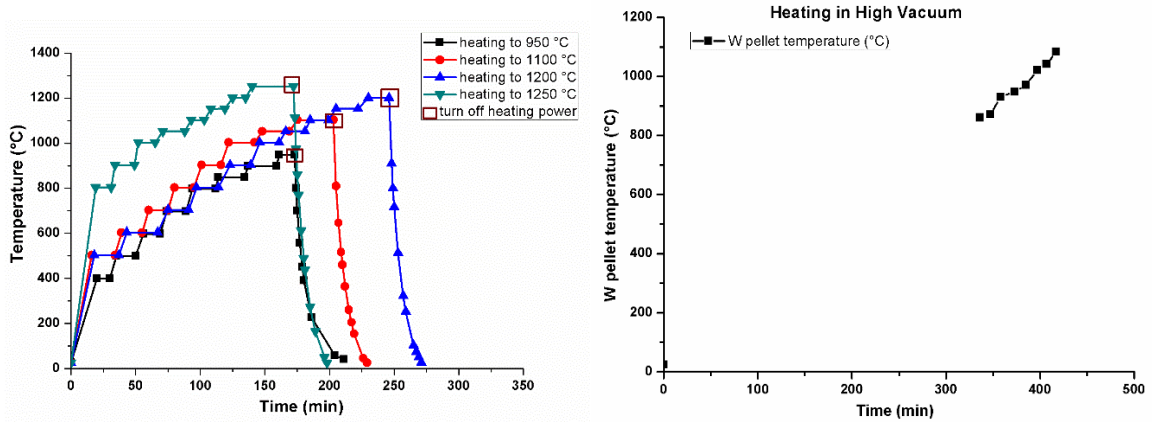
Figure 6.1 Specimen heating schedules for the *in situ* SEM experiments performed in this study (left). For each experiment, temperature was increased incrementally to the target level, and specimens cooled naturally after the heater power was turned off. And Temperature of specimen during Ultra High Vacuum heating (right).

For comparison, an additional tungsten pellet was subjected to heating in the custom-built UHV chamber at a pressure of 10^{-8} Torr. A disappearing filament optical pyrometer was used to measure sample temperature, but it could only read temperature when the sample was glowing, which limited the measurable temperature range to 800 °C and above. This sample was held at 1100 °C for 10 to 15 minutes. Upon turning off the heater power, the sample stopped glowing within several seconds, which prevented determination of the exact cooling rate for the UHV heating experiments.

Following each heating experiment, the cooled samples were imaged using high-resolution SEM (in the FEI Helios G3 FIB-SEM), which offered imaging capabilities superior to those of the ESEM (FEI Quanta FEG 250) where *in situ* experiments were performed. EBSD (Oxford Instruments Nordlys Max[2] detector, Concord, MA, USA) was performed on annealed samples after heating experiments to validate the structure and orientation of tungsten surface facets. After this, a series of the Slice & View (serial

sectioning) FIB-SEM experiments were carried out on a {001} grain (with nominal <001> orientation normal to the grain surface plane normal) of an annealed tungsten sample. This was performed using serial sectioning software (Thermo Scientific, Hillsboro, OR, USA) to control the serial sectioning process in the FIB-SEM. Visualization also included 3D reconstruction using Avizo software (Thermo Scientific, Hillsboro, OR, USA). Prior to the serial sectioning process, the sample surface was prepared by depositing a protective carbon layer on the selected area, followed by extraction of the region of interest from the tungsten pellet. During serial sectioning, the sample was tilted at 52°, allowing the ion beam to sequentially mill the sample in 15 nm thick increments while the electron beam obtained backscattered electron (BSE) images after each slice. A total of 482 BSE images were generated, which were then subjected to noise reduction and alignment using Avizo software. Subsequently, 3D reconstruction was performed. Furthermore, in order to interpret observations of the tungsten surface after annealing and also to determine the surface free energies of low index facets, the equilibrium crystal shape was modeled using Wulffmaker [92], a commonly used software tool for calculating and simulating faceted particle shapes.

6.3   Results and Analysis

6.3.1   Original Samples

As previously stated, the pristine tungsten sample was characterized prior to the heating experiments. **Fig. 6.2**a depicts a representative, low-magnification SEM image of a tungsten pellet. Higher-magnification secondary electron images showing the tungsten surface are presented in **Fig. 6.2**b and the inset **Fig. 6.**2 (b1). These indicate that the sample exhibited a smooth surface before heating, albeit displaying swirl marks resulting from the

manufacturing process (lathe turning), as is typical for a scandate cathode pellet. Features

were detected at the edges of tungsten grains, as denoted by the arrow in **Fig. 6.2**b. EDS

elemental analysis (accelerating voltage of 18 kV) was performed on those features and on

the flat tungsten surface, as shown in **Fig. 6.2**c and d. Meanwhile, EDS mapping was

performed over the area indicated by the white box in **Fig. 6.2**e (accelerating voltage of 3

kV, to enhance surface sensitivity and reveal more detail of surface features), with results

presented in **Fig. 6.2**f and g. In addition to the W signal, oxygen (O) was detected during

EDS point scans and mapping (**Fig. 6.2**c, d and g), indicating the W surface included some

amount of O, likely due to room-temperature oxidation of W. Comparing EDS results in

Fig. 6.2c and d, it is seen that the features detected at the edges of tungsten grains (spectrum

1) contain significantly more O than does the flat W surface (spectrum 2). EDS mapping

results in **Fig. 6.2**f and g confirmed these features as tungsten oxides. Note that a carbon

signal was detected by EDS but was not included in Fig**. 6.2**c and d, as it was attributed to

the typical surface contamination measured by EDS.
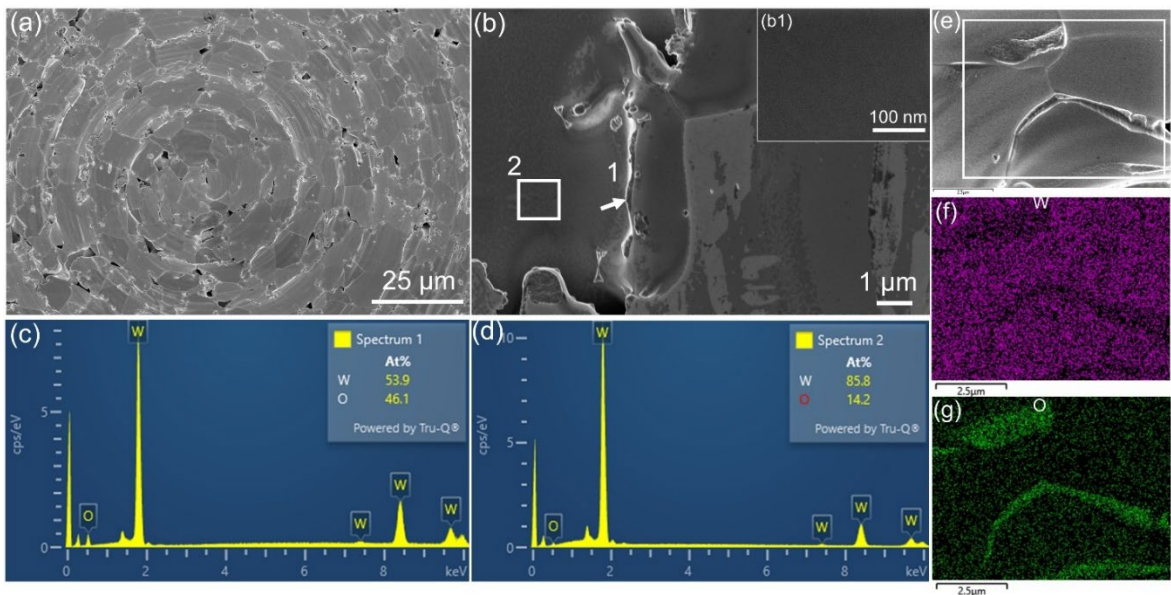
Figure 6.2 Characterization of the tungsten pellet prior to heating. (a) SEM image showing machining marks on the original tungsten surface; (b) higher-magnification image of the surface with an inset (b1) indicating a lack of surface topography; (c) and (d) show EDS elemental analyses at locations 1 (spot analysis) and 2 (area analysis, as indicated in (b)), respectively, with both EDS analyses performed with 18 kV beam voltage. (e) high-magnification image of the surface area for EDS mapping analysis; (f) and (g) are EDS maps of W and O content, performed with 3 kV beam voltage to make EDS analysis more sensitive to the near-surface region of the specimen.

6.3.2   Environmental SEM Annealing Experiments

6.3.2.1 In situ SEM imaging

During the *in situ* heating experiments conducted in the ESEM, no noticeable changes were immediately observed when the sample was heated to the target temperature of 950 °C under a pressure of 0.8 Torr. However, when tungsten pellets were heated to target temperatures of 1100 °C, 1200 °C, and 1250 °C with a surrounding pressure of 0.8 Torr, the surfaces of grains were observed to change rapidly, in several ways. It is noted that the SEM images taken during *in situ* heating experiments exhibited low contrast, which is typical for such experiments. Consequently, the SEM images were post-processed using software (ImageJ) to adjust the histogram of pixel intensities. Select SEM images that were recorded during *in situ* heating experiments are shown in **Figure 6.3** and **Figure 6.4**.

Figure 6.3 displays a series of secondary electron (SE) images acquired during an *in situ* ESEM heating experiment where the sample was heated to 1100 °C under a pressure of 0.8 Torr. As depicted in **Figures 6.3**(a-c), no significant changes were observed on the sample surface for temperatures lower than ~1000 °C. However, when the temperature reached 1053 °C, certain features on the sample surface began to deteriorate visibly. These features are consistent with the tungsten oxide noted in **Figure 6.2**b above, and it is expected that tungsten oxide would sublimate at this temperature [99, 101], *e.g.*, leading to

the disappearance of the feature noted by yellow arrows in **Figures 6.3** (d-f). The sublimation is primarily attributed to the formation of gaseous tungsten trioxide (WO_3) resulting from the following chemical reactions that occur during the annealing process, noting that the total pressure of 0.8 Torr in the ESEM includes remnant oxygen and other gases [36, 99, 101, 115]:

$$W\ (s) + O_2\ (g) \leftrightarrow WO_2\ (s) \tag{11}$$

$$WO_2\ (s) + \tfrac{1}{2}\ O_2\ (g) \leftrightarrow WO_3\ (s) \tag{12}$$

$$3WO_3\ (s) \leftrightarrow (WO_3)_3\ (g) \tag{13}$$
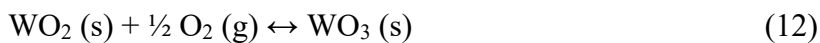
After being held at 1053 °C for 10-15 minutes, the W surface was noticeably rougher, as seen in **Figure 6.3**e, and indicated with the blue arrow. When sample temperature was held at ~1100 °C, sublimation of tungsten oxide advanced significantly and the W surface became even rougher, with distinct topography as shown in **Figure 6.3**f. Additionally, it was observed that a gap opened along a grain boundary, as denoted by the red dashed ellipse in **Fig. 3**e and f. The opening of this gap is attributed to tungsten oxide sublimation. These three types of changes at the tungsten surface (disappearance of tungsten oxide features, surface roughening, and opening of grain boundaries) may be governed by the same driving force, which would most likely be the breakdown of WO_3 via sublimation, which would thereby remove W atoms from the sample surface. This is addressed in more detail in the Discussion section below.
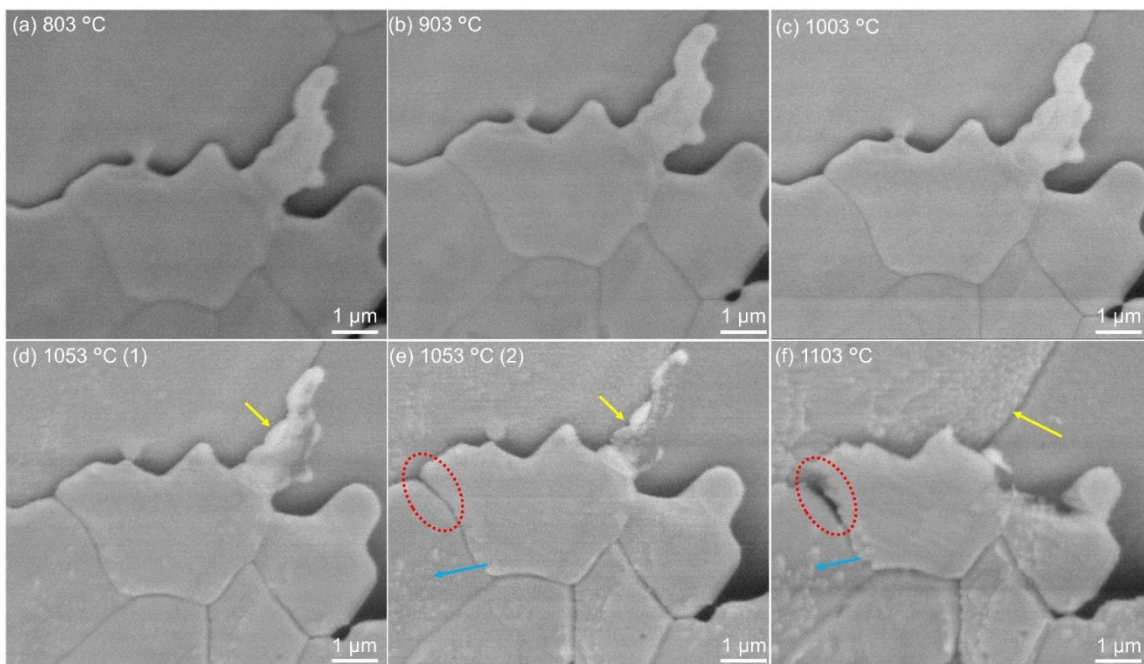
Figure 6.3 SEM micrographs of the sample heated to a maximum temperature of ~1100 °C, under a pressure of 0.8 Torr. Images recorded at (a) 803 °C, (b) 903 °C, (c) 1003 °C, (d) 1053 °C immediately after temperature stablized, (e) after holding at 1053 °C for 10-15 min, (f) 1103 °C.

Figure 6.4 depicts the morphology of a different tungsten sample during a heating experiment with maximum temperature of 1200 °C and surrounding pressure of 0.8 Torr. The irregular shape in the center of **Figure 6.4**a was consistent with tungsten oxide features described above, and it did not change noticeably when held at temperatures below ~1000 °C (**Figures.** 6.4 (a-d)), which is consistent with the observations in **Figure 6.3**. However, as temperature increased, certain surface features progressively disappeared, *e.g.*, as indicated by the yellow arrow in the SE image recorded at 1003 °C (**Figure 6.4**e). When sample temperature was held at 1053 °C for 15 minutes, the irregular shape indicated in the center of **Figures 6.**4(f-g) gradually disintegrated. At a sample temperature of 1103 °C, sublimation of tungsten oxide was observed to continue, and the tungsten surface continued to roughen while being held there for 15 minutes, *e.g.*, as indicated by the blue arrow in

Figure 6.4i. The irregular shape (presumably tungsten oxide) disappeared rapidly when temperature was raised to 1153 °C, and the tungsten surface became significantly rougher (**Figures 6.**4(j-k)). At 1201 °C, the irregular shape disappeared completely, and the surfaces of most tungsten grains exhibited significant degrees of faceting (**Figure 6.4**l). It is noted that, during the subsequent cooling process, sample surface morphology did not change.
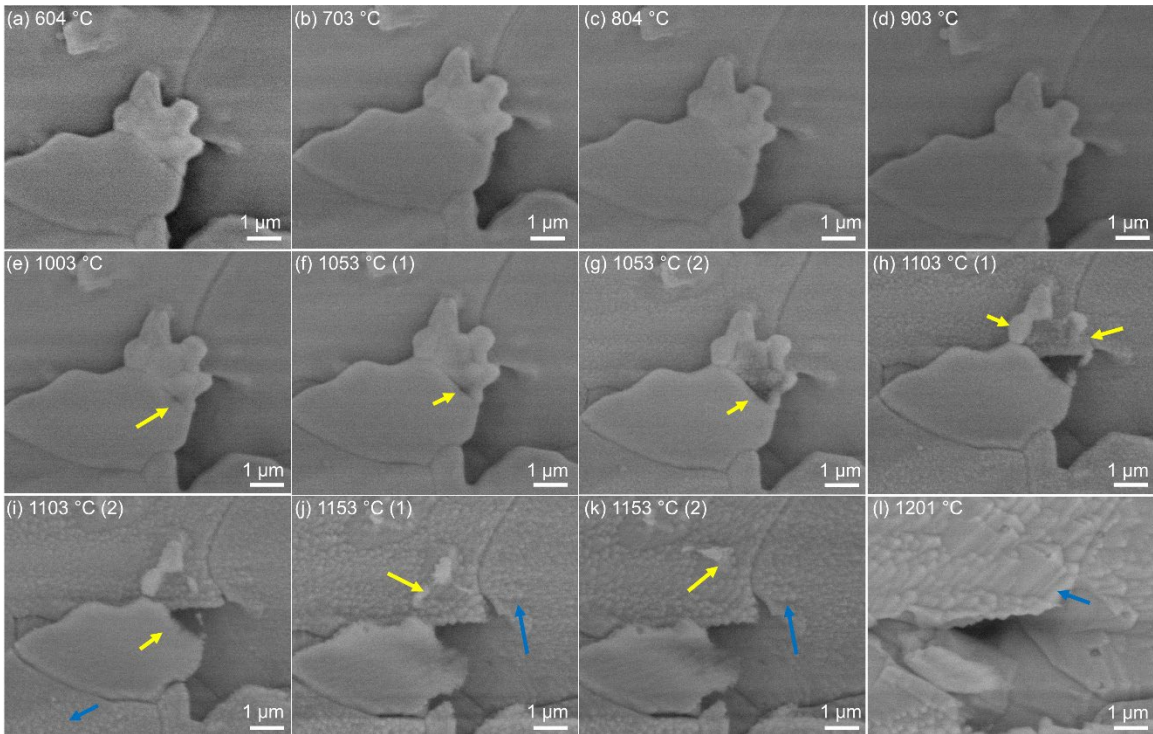
Figure 6.4. SEM micrographs of a new tungsten sample during *in situ* heating to a maximum temperature of ~1200 °C. Images recorded at 604 °C, 703 °C, 804 °C, 903 °C, 1003 °C, 1053 °C, 1103 °C, 1153 °C and 1201 °C; pressure was 0.8 Torr throughout the experiment. Multiple images are shown for select temperatures (1053 °C, 1103 °C and 1153 °C), to show the evolution of surface morphology during temperature holds of 15 minutes each. Extensive surface faceting was observed at 1200 °C, which corresponds to a homologous temperature of 0.40 for tungsten.

While **Figure 6.3** and **Figure 6.4** show that tungsten surfaces roughened when the temperature surpassed 1050 °C, this does not appear to be the critical temperature that

triggers surface faceting for tungsten. The roughening process can initiate at a lower temperature [98, 99], although this may not be immediately evident during *in situ* SEM heating experiments due to resolution limits in the ESEM.

6.3.2.2 Characterization of W Samples Annealed in the ESEM (Pressure ~0.8 Torr)

6.3.2.2.1 SEM

After cooling from the maximum annealing temperature to room temperature, each sample was transferred to the Helios FIB-SEM for more detailed characterization. **Figure 6.5** presents the morphologies of the range of samples annealed in the ESEM. Higher-resolution imaging of tungsten samples did reveal nanoscale surface roughening after *in situ* SEM heating experiments, as shown in **Figure 6.5** (a2, a3), where surface roughness was observed even for a maximum heating temperature of 950 °C. The inset image in **Figure 6.5** (a4) shows this incipient faceting. It was anticipated that tungsten surfaces would exhibit greater degrees of roughness as the maximum heating temperature increased, and this was consistent with the observations in **Figure 6.5** (a2, b2, c2, and d2).

Furthermore, as the maximum heating temperature increased, the tungsten surface facets grew in size, as depicted in **Figure 6.5** (a3, b3, c3, d3), and details of the shape of surface facets changed as well. After annealing at 950 °C, the tungsten surface exhibited a relatively limited degree of faceting (**Figure 6.5** (a3, a4)), which was only clearly observed at high magnifications. However, when the annealing temperature was raised to 1100 °C, a distinct pyramid structure with sharp edges and pointed vertices formed, as indicated by the green and white arrows in **Figure 6.5** (b3). Nanoscale features (bright white spots, denoted by white arrows) were observed at the vertices of some pyramids. However,

comparing **Fig. 5** (a3) (b3) with (c3), it is observed that these nanoscale features decreased in size and number as temperature increased from 950 °C to 1200 °C. When the annealing temperature reached 1250 °C, these nanoscale features disappeared almost entirely, as seen in **Fig. 5** (d3). In addition to the nanoscale features, a series of terraces was observed on certain facet sidewalls, as denoted by the yellow arrow in **Figure 6.5** (b3). Subsequently, when the sample was annealed at 1200 °C, the facet surfaces appeared to be smoother, as shown in **Figure 6.5** (c3). Nevertheless, compared to the facets observed after annealing at 1100 °C, the faceted observed after annealing at 1200 °C were larger and they exhibited fewer sharp edges, fewer terraces appearing on facet sidewalls, and smaller nanoscale features at the vertices; these are indicated with green, yellow, and white arrows, respectively. A subset of small grains exhibited smoother edges and rounded vertices, *e.g.*, as indicated by the orange box in **Figure 6.5** (c3), and these may be further evolved than most grains on this surface, with a morphology approaching that of tungsten exposed to higher temperature. After annealing at 1250 °C, exceptionally large, faceted grains were observed, exhibiting edges and vertices that were more noticeably rounded, with fewer terraces visible on the facet sidewalls. Furthermore, no nanoscale features (bright white spots) were observed at the vertices of larger facets, as shown in **Figure 6.5** (d3), although some were visible at the vertices of smaller facets.
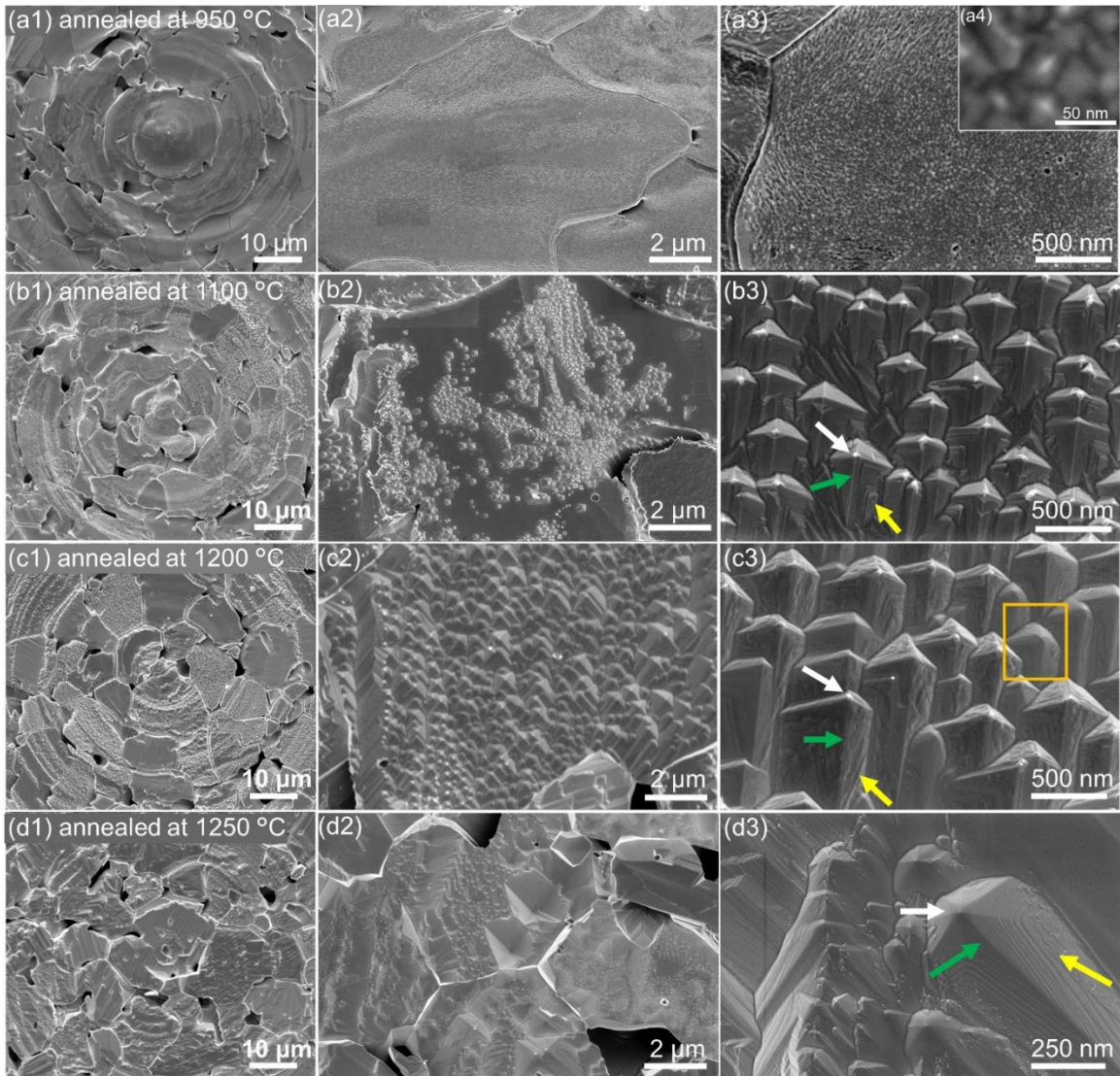
Figure 6.5. The morphology of samples annealed at various maximum temperatures. (a1, b1, c1, and d1). Low-magnification images showing the tungsten surfaces after *in situ* SEM heating at 950 °C, 1100 °C, 1200 °C, 1250 °C, respectively; chamber pressure was 0.8 Torr in all cases. (a2, b2, c2, d2) Higher-magnification images of regions shown in (a1, b1, c1, d1), respectively, where surface facets are more readily identified. (a3, b3, c3, d3) Higher-magnification images of regions shown in (a2, b2, c2, d2), respectively, where the detailed morphology of surface facets can be seen. (a4) High-magnification inset image of region shown in (a3), with nanoscale incipient surface facets.

6.3.2.2.2   EDS

Additional SEM observations and EDS analysis were performed to identify the nanoscale features (bright white spots) present at the vertices of certain pyramidal facets

91

and on the flat regions of the W surface, as shown in **Fig. 6** for a faceted tungsten surface after annealing at 1100 °C and surrounding pressure of 0.8 Torr. Comparison of the high-magnification SE and BSE images in **Fig. 6**a-b indicates that the nanoscale features have a similar grey level (and therefore average atomic number) compared with the tungsten base, but these nanoscale features are surrounded by a thin layer of a phase with lower average atomic number. Therefore, the nanoscale features are interpreted to consist primarily of tungsten, surrounded by an oxide shell. Because the strongest W peak (the Mα peak at 1.774 keV) is used for EDS analysis, and in order to reduce the penetration depth (interaction volume) of the incident electron beam with respect to the W base material, a lower beam voltage of 3 kV was used for EDS analysis of a representative bright feature at the vertex of a pyramid, as shown in **Fig. 6**c, spectrum 7 (this is also discussed in more detail in the Supplementary Materials). For comparison, EDS analysis was also performed on the relatively flat region of the W surface with 3 kV beam voltage (see **Fig. 6**c, spectrum 13). **Fig. 6**d and **Fig. 6**e show that W and O were detected at both locations. However, a significantly higher O content (31.8 at.%) was detected at the vertex of the pyramid than on the flat W pellet surface (11.5 at.%). It is noted that a carbon (C) signal was also detected in the EDS scans of both regions (although not included in spectra 7 and 13), but this is attributed to the typical contamination of sample surfaces exposed to ambient air.

There are multiple hypotheses regarding the composition of this nanoscale feature. Szczepkowicz *et al.* [109-113] observed a similar faceting phenomenon and vertex morphology in their work on vacuum annealing of tungsten, and suggested that these nanoscale vertex features could be pure tungsten resulting from exposure to oxygen and annealing at specific temperatures. However, Oleksy [129] proposed that during the

faceting process, an adsorbed monolayer containing oxygen remains on the tungsten surface. On the other hand, Yu *et al.* [117] reported that W_2C and another unidentified carbide were detected on a pure tungsten sample surface after high-vacuum annealing, and this was attributed to carbon contamination as a result of sample exposure to air. In the current study, this annealed sample was exposed to air during transfer from the ESEM to the Helios FIB-SEM. Therefore, although it is difficult to determine the exact chemical composition of the nanoscale feature on the top of the pyramid, it is reasonable to assume that the tungsten surfaces, including the nanoscale vertex feature, are oxidized to some degree. On the other hand, considering that those nanoscale features gradually disappeared as temperature increases during heating (see **Fig. 6.5** a3, b3, c3 and d3), thus those nanoscale features could be tungsten oxides.
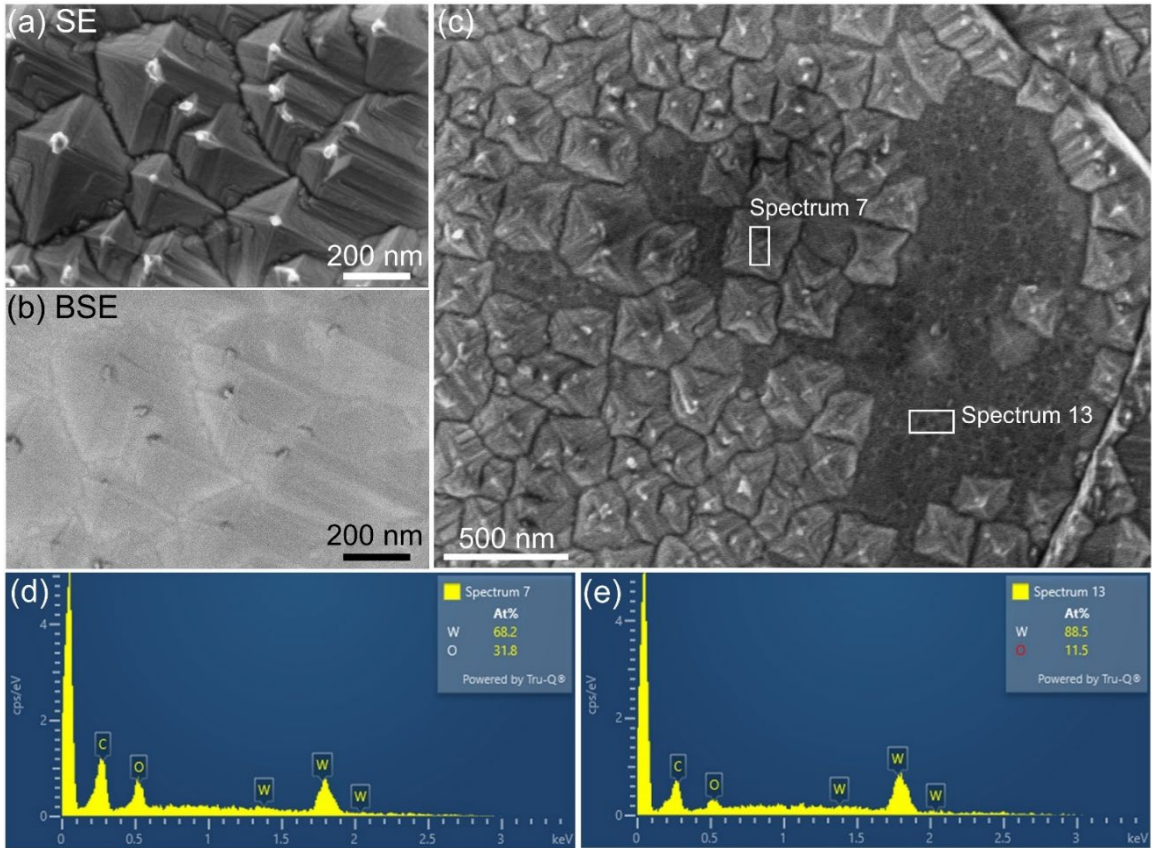
Figure 6.6. (a) high magnification SE image of faceted surface of tungsten pellet after annealing at 1100 °C, 0.8 Torr and (b) the corresponding BSE image of (a); (c) electron image for EDS analysis, (d) EDS spectrum from a bright nanoscale feature at the vertex of faceted W, and (e) EDS spectrum of the relatively flat surface; both (c) and (d) were performed at low voltage (3 kV) to enhance surface sensitivity.

6.3.2.2.3   *EBSD*

Figures 6.7 and **6.8** depict EBSD scanning and SEM tilted-sample imaging results for the tungsten sample annealed at 1100 °C, pressure 0.8 Torr. The surface facets of this sample exhibit only sharp edges (no rounding) and sharp vertices (some with nanoscale features). Three grains labeled as *1*, *2*, *3* in **Figure 6.7**a correspond to green, blue, and red in the EBSD inverse pole figure (IPF) color map (**Figure 6.7**b). The color map indicates the nominal surface planes of these grains correspond to {101}, {111} and {001} planes, respectively. Their respective surface morphologies in **Figure 6.7** (c-1, c-2 and c-3) differ and are influenced by the underlying grain orientation. The surface facets on grain 3 protrude directly out of the image plane and exhibit a rather symmetric structure, consistent with the grain orientation being a low-index axis of symmetry.
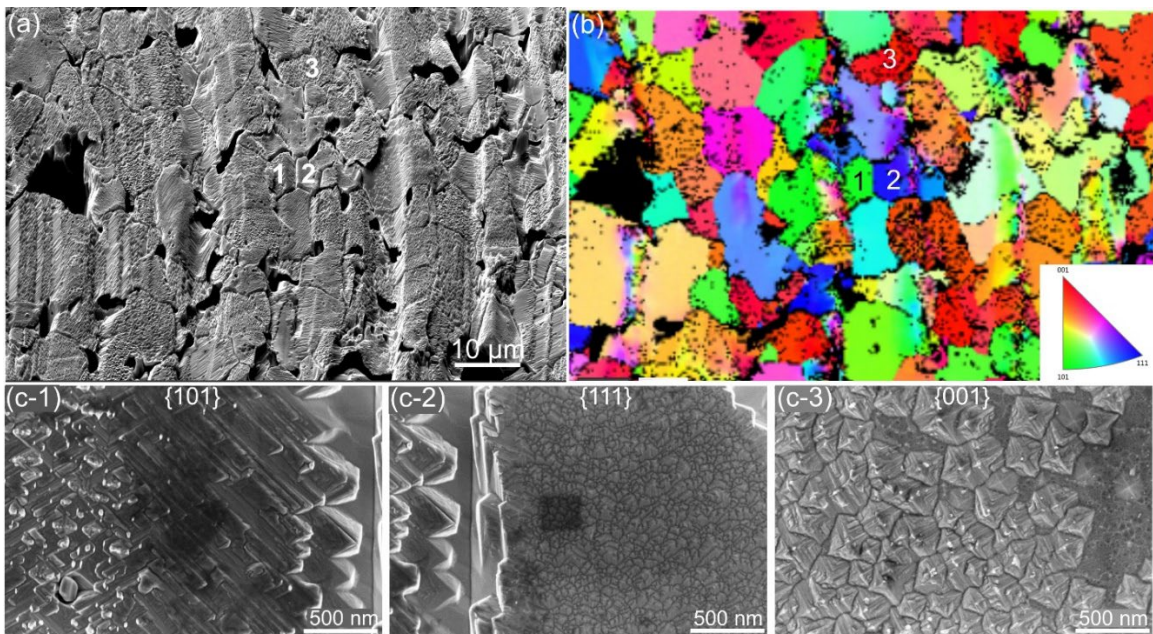
Figure 6.7. Evaluation of the dependence of faceted surface morphology on grain orientation. (a) SEM image of sample after annealing at 1100 °C, 0.8 Torr. (b) EBSD analysis of the polycrystalline tungsten sample, with inverse pole figure color map indicating out-of-plane crystal orientation. (c-1, c-2, c-3) Higher-magnification SEM images of surface morphology at locations 1, 2 and 3 from (a).

6.3.2.2.4   SEM TILTED SAMPLE IMAGING

To investigate this further, SEM imaging of grain 3 was performed continuously as the sample was tilted about the vertical axis of the image, over an angular range of -10.0° to 60.0° with an increment of 2.0° per tilt step. **Figure 6.8**a presents an enlarged image of grain 3, with the vertex of the central grain denoted as *A*, and the right edge of the base of the faceted pyramid (where it meets the nominal grain surface plane) indicated as the line *BC*. This grain was selected for this experiment because *BC* is parallel to the tilt axis. As the stage was tilted, the distance between point *A* and line *BC* steadily decreased. Notably, at a tilt angle of 45.0°, point *A* lay along line *BC* (in projection), as shown in **Figure 6.8**b. This means that the plane normal of facet *ABC* is tilted 45° from the normal to the {001} grain, and the *ABC* facet normal should therefore be a <101> direction. In order to provide an alternative, possibly clearer representation of the position of vertex *A* versus line *BC*, plan view and perspective schematic drawings of the faceted pyramid structure are presented in **Figure 6.8**c-d, respectively. With the angle between the facets and base being 45°, the faceted structure appears to correspond to the top half of an octahedron, as shown in **Figure 6.8**d (note that a more nuanced interpretation is provided later). Since the base of the faceted pyramid is a {001} plane, the facets should be {101} planes.
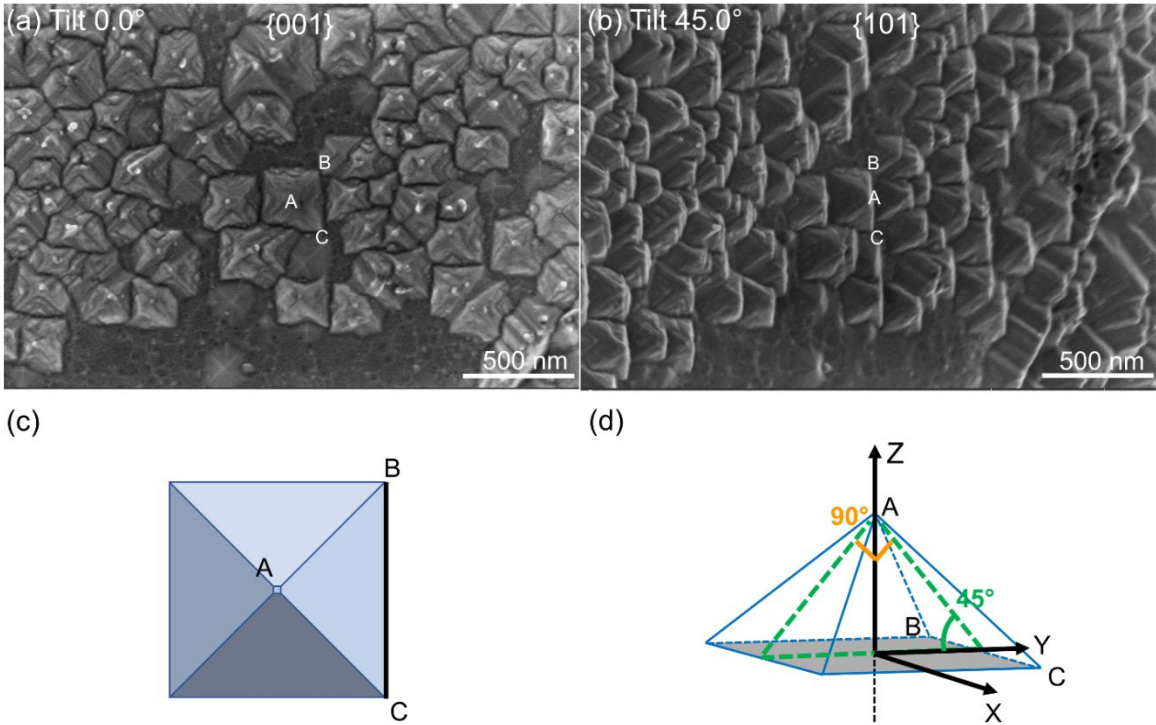
Figure 6.8. SEM tilted-sample imaging and analysis: (a) SEM image of the {001} grain with stage tilt angle 0.0°. (b) SEM image of the grain with a nominal surface plane of {001}, but at a stage tilt angle of 45.0°, resulting in a view along a <101> crystallographic direction. (c) Plan view and (d) schematic drawings of the faceted pyramid.

6.3.2.2.5   *3D RECONSTRUCTION*

In order to gain further insight into the faceting of tungsten pellet samples, the Slice & View (serial sectioning) FIB-SEM technique was applied to grains from the sample after annealing at 1100 °C and surrounding pressure of 0.8 Torr. And extensive measurements of the angle between two opposing faces of the faceted pyramids were made using Avizo, as illustrated in **Figure 6.9**. Specifically, the grain enclosed by the red dashed line in **Figure 6.9**a corresponds to the same grain depicted in **Figure 6.7**, with a nominal surface plane of {001}. **Figure 6.9**b presents a higher magnification SE image of this grain, corresponding to the area encompassed by the orange dashed line in **Figure 6.9**a. Additionally, **Figure**

6.9c shows a plan view of the reconstructed surface region by using software Avizo, delimited by the white box in **Figure 6.9**a.

The BSE image in **Figure 6.9**d depicts a cross-section along the yellow dashed line *l* (where *l* passes through the vertex of pyramid M and is parallel to the X-axis). It is seen that the vertex of pyramid N was not aligned with *l*, despite the apparent apex angle of the opposing facets for pyramid M being nearly 90° as measured in **Figure 6.9**d. Therefore, the angle between each pair of opposing facets was measured from the 3D reconstruction using a virtual cross-section aligned parallel to the base of each faceted pyramid. For example, as demonstrated in **Figure 6.9**e, the reconstructed volume was sliced along the white dashed line *l'* (shown in **Figs. 9**b and c). This cross-section slice passed through the vertices of pyramids M and N, and the apex angles of pyramids M and N were measured to be 90.7° and 89.6°, respectively. Furthermore, the apex angle of pyramid M was also measured along the direction of the white dashed line *l''* in **Figure 6.9**c, which is perpendicular to white dashed line *l'*. The same procedure was followed for other faceted pyramids, indicated by the purple marks in **Figure 6.9**f. Based on 31 measurements, the average value of the apex angle was 90.8°, as shown in **Figure 6.9**g. This outcome corroborates the determination from the SEM tilted-sample imaging and analysis shown in **Figure 6.8**.
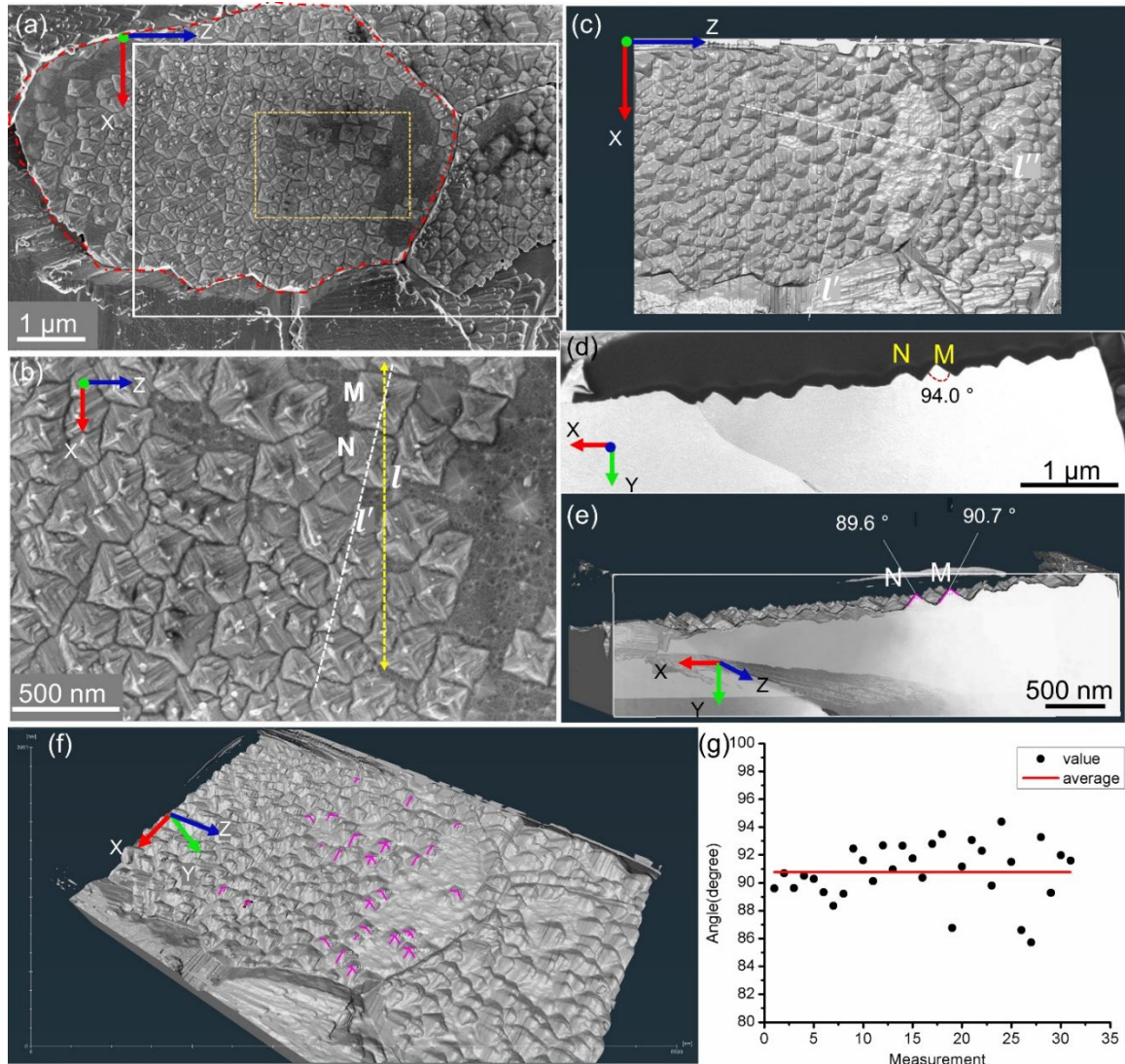
Figure 6.9. 3D reconstruction of the surface of grain *3* (same grain that was shown in **Figures. 6.7** and **6.8**): (a) SE image of the grain with a nominal surface plane of {001}. (b) SE image of the area in the orange dashed box in (a). (c) 3D reconstructed surface structure corresponding to the white box in image (a). (d) BSE image of a slice passing through pyramids M and N, following the yellow dashed line *l*. (e) Cross-section generated from the 3D reconstruction along the white dashed line *l'*, passing through the middle of pyramids M and N. (f) The faceted pyramids in the 3D reconstruction whose apex angles were measured, are indicated with purple marks. (g) Plot of all measured angles between opposing facets (as marked in (f)) and their average value indicated by the red line. The X-Y-Z axes indicated in each image were generated by Avizo.

6.3.2.3 Simulation of the Faceted Particle Shape Corresponding to W Surfaces

To further understand the Wulff shapes (and therefore the crystallographic facets) that would be expected on W surfaces, the software package Wulffmaker was used in this study. The use of Wulffmaker was not solely intended to model the equilibrium crystal shape, but also to evaluate the relative surface energies for {100}, {110} and {111} facets, and thereby confirm the dominant {110} facet orientation that was observed experimentally. The {110} surface energy is the lowest of the three facet variants, according to the literature [36, 115-117]. Various combinations of relative surface energies (keeping {110} as the lowest value) were used as input to Wulffmaker, and the calculated Wulff shapes were compared to experimental observations. It became apparent that a rhombic dodecahedron was the best match, consistent with the dominant {110} faceting, and it also explained the pyramidal surface faceting exhibited by {100}-oriented grains.

The final result of the calculated and simulated particle shape from Wulff maker is shown in **Fig. 6.10**a, which shows a rhombic dodecahedron. This shape differs from the experimental observations noted above because it is only a portion of the Wulff shape appears on annealed and faceted tungsten surfaces which is regular for the Wulff shape when the pure metal reacts with environments [130-132]. The vertical axis (blue) in **Fig. 6.10**a is an axis of four-fold rotational symmetry and corresponds to a {001} nominal grain surface plane normal, i.e., it is parallel to the Z-axis in **Fig. 6.8**d. The axes indicated in **Fig. 6.10** were generated by Wulffmaker and they represent lattice vectors of the crystal lattice; in fact, they also correspond to the orthogonal X-Y-Z axes in **Fig. 6.8**d. The portion of the Wulff shape that directly relates to the faceted pyramids in SEM images (**Figs. 6.8-6.9**) is demarcated by the gray plane in **Fig. 6.10**b. The region above the gray plane is a pyramid with four surface facets and a square base (indicated by the blue square). This region is

also shown in **Fig. 6.10**c, viewed from "above" along a <001> direction, and it mirrors the view of the faceted pyramid structure shown in **Fig. 6.8**c. The rhombic dodecahedron crystal shape from Wulffmaker therefore exhibits only {110} surface facets. It is noted that the relative surface energies used in Wulffmaker calculations were $\gamma_{(110)} = 0.758$, $\gamma_{(111)} = 1.00$, and $\gamma_{(001)} = 1.08$. In this case, $\gamma_{(111)}$ was 31.9% higher than $\gamma_{(110)}$, and $\gamma_{(001)}$ was 42.5% higher than $\gamma_{(110)}$.
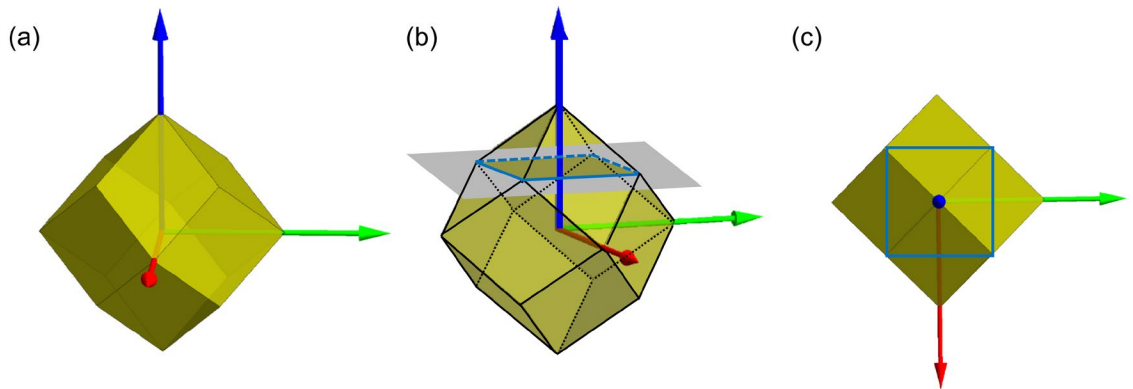
Figure 6.10 (a) Wulff shape of faceted particle showing the ideal grain shape that matches experimental SEM observations. (b) Top region of Wulff shape, above the gray plane, is a pyramid that exhibits a portion of the overall faceted particle shape and is consistent with plan-view SEM observations presented earlier. (c) A top view of the Wulff shape includes a section (outlined by the blue square) that corresponds to the view of pyramids on a faceted tungsten grain that has overall {001} orientation.

6.3.2.4 Dimensions of Facets on W Surfaces

The facet dimensions were measured for tungsten samples after various *in situ* annealing experiments, and these results are summarized in **Fig. 6.11**, which shows the size distributions as a function of temperature and grain orientation. In some cases, the exposed facet dimensions vary significantly with grain orientation, *e.g.* the {101} grains in **Fig. 6.7**(c-1) exhibit long faceted sidewalls due to a combination of facet crystallography and relative grain orientation. To make a more consistent comparison, facet size was taken to be the width of a faceted pyramid, as measured across the dimension that represents the

intersection of faceted growth with the nominal grain surface plane. This approach removed any artificially long facet sidewall dimensions, such as those in **Fig. 6.7**(c-1). As was seen in **Fig. 6.5**, facet size increased with higher annealing temperature, and this is reflected in **Fig. 6.11**a. The dependence of facet size on grain orientation is shown in **Fig. 6.11**b, for the specimen annealed *in situ* at 1100 °C in the ESEM. Overall, {001} grains exhibited the most prominent facets, i.e., the largest average facet size (width of faceted pyramids). Excluding their long sidewalls, the surface facets on {011} grains exhibited the middle size distribution for the three grain orientations counted here. Finally, {111} grains exhibited the smallest facet size and appeared to be relatively stable against thermal growth of surface facets.
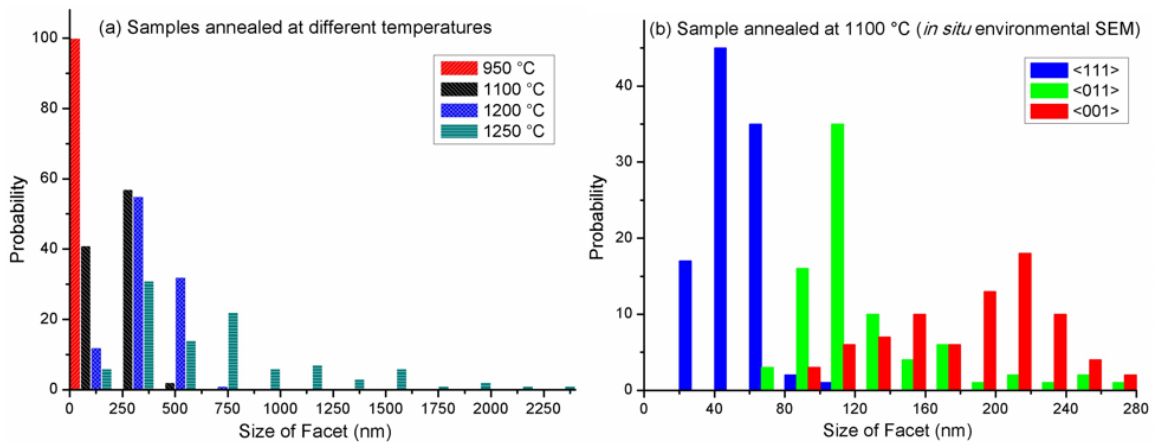
Figure 6.11 Histograms of facet size, measured for different annealing temperatures and different grain orientations. (a) Facet size after *in situ* annealing in the ESEM at 950 °C, 1100 °C, 1200 °C and 1250 °C, with a surrounding pressure of 0.8 Torr in all cases. (b) Facet size after annealing at 1100 °C, with separate histograms for each nominal grain orientation. Histogram bin size is defined by the bounding tick marks on the horizontal axis.

6.3.3   Characterization of W Samples Annealed in UHV (Pressure ~10^{-8} Torr)

A different tungsten specimen was annealed at 1100 °C under 10^{-8} Torr in an ultrahigh vacuum chamber, after which the surface exhibited a generally flat and smooth appearance, as shown in **Fig. 6.12**a-b. While the surface exhibited limited regions of

nanoscale surface roughness, *e.g.*, in the grain boundary region highlighted by the arrow in **Fig. 6.12**c, no surface facets were observed after UHV annealing.
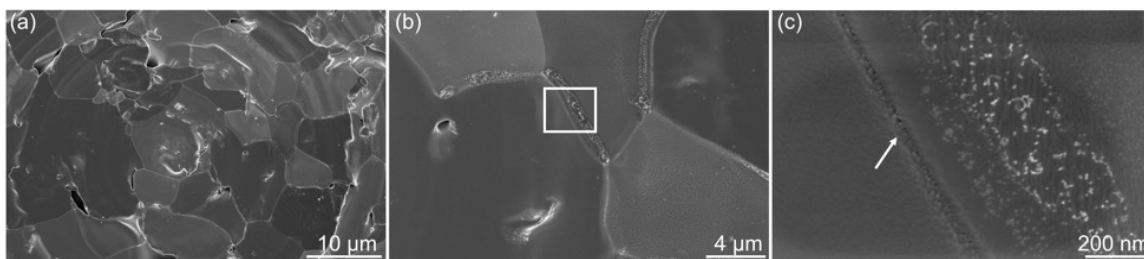
Figure 6.12 SEM images of tungsten sample after annealing at 1100 °C, 10^{-8} Torr. (a) Polycrystalline grain structure and (b) zoomed image of several grains, showing that most grain surfaces are smooth and featureless. (c) Higher-magnification view of the region marked by white box in (b), revealing nanoscale features near grain boundaries but no facets.

6.3.4   XPS analysis

6.3.4.1 XPS Analysis of the Initial (unannealed) Tungsten Samples.

X-ray photoelectron spectroscopy (XPS) was used to characterize the composition and bonding state of tungsten surfaces, and these results are presented in **Fig. 6.13** and **Table 6.2** for the initial (unannealed) tungsten samples. Tungsten can form various complex oxides such as W_3O, WO_2, $WO_{2.3}$, and WO_3 **[133, 134]**. In this study, W_xO and WO_y (where x>1, 2<y<3) were utilized to represent the intermediate oxide species between metallic tungsten and WO_3. The fitted W4f spectrum (blue line) in **Fig. 6.13** indicates the presence of metallic tungsten (W4f7/2 at 31.40 eV and W4f5/2 at 33.56 eV), as well as various tungsten oxides including W_xO (where x > 1), WO_y (where 2 < y < 3), and WO_3 (W4f7/2 at 36.09 eV and W4f5/2 at 38.17 eV). These XPS findings are consistent with the EDS results depicted in **Fig. 6.2**, in terms of indicating the presence of fully metallic versus oxidized (and partially oxidized) tungsten surface regions.

The EDS data presented in **Fig. 6.2** indicate that the primary constituent of the original specimen (to a depth of 230 nm, as seen from the Supplemental Materials) was

102

pure tungsten with some degrees of oxides on the surface, whereas the XPS data in **Fig. 6.13** and **Table 6.2** suggest that the surface components were primarily tungsten oxide. This disparity can be attributed to the difference in surface sensitivity between the two techniques. XPS can detect only a thin surface layer, typically ~10 nm (or less) in thickness, whereas the depth of detection for EDS depends on applied voltage but is generally on the order of hundreds of nm, even with a low accelerating voltage of 3 kV (as seen in **Fig. 6.2** f-g), the electrons can penetrate 25 nm deep into tungsten, much deeper than it of XPS. It is plausible that a nanometer-scale oxide film covered the entire specimen surface, since tungsten can readily oxidize even at ambient temperature [36, 94].
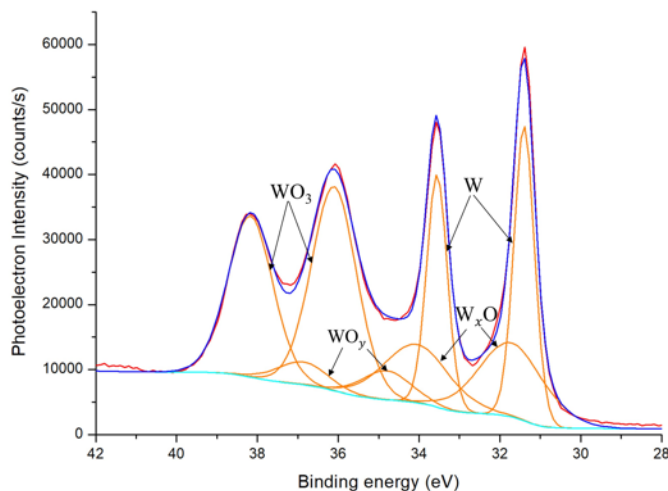
Figure 6.13. Fitted XPS scan of the original tungsten pellet, prior to heating. Experimentally measured data are shown in red; the baseline (cyan) and fitted peaks (blue) are shown for comparison; the orange peaks correspond to peaks for individual chemical species that combine to yield the fitted peaks (blue).

Table 6.2. Results from the analysis of XPS data (for W4f peaks) obtained from the original tungsten sample.

Component	Scan	Peak Binding Energy (eV)	Peak Area (CPS.eV)	Atomic Fraction (%)
W	W4f7/2	31.40	29,398.55	28.1
	W4f5/2	33.56	23,175.50	
W_xO (x>1)	W4f7/2	31.72	23,519.45	22.5
	W4f5/2	34.07	18,540.88	
WO_y (2<y<3)	W4f7/2	34.81	6,968.30	6.7
	W4f5/2	36.88	5,493.26	
WO_3	W4f7/2	36.09	44,600.40	42.7
	W4f5/2	38.17	35,159.44	

6.3.4.2 XPS Analysis of the ESEM Annealed Samples.

X-ray photoelectron spectroscopy was also performed on specimens that had been subjected to annealing at 0.8 Torr during *in situ* SEM heating experiments, and these results are presented in **Fig. 6.14** and **Table 6.3**. The XPS spectra of annealed specimens revealed a significant reduction in the intensity of all tungsten oxide (W_xO, WO_y and WO_3) peaks, with WO_3 peaks exhibiting an especially significant decrease (here, a representative XPS scan of a specimen annealed in the ESEM at 1250 °C (0.8 Torr) was included in **Fig. 6.14**). However, the intensity of metallic tungsten (W) peaks increased significantly, almost doubling in most cases, as plotted in **Fig. 6.15**. The atomic fraction of WO_3 decreased to 5.8%, 8.3%, 7.5%, and 5.4% for specimens annealed at 950 °C, 1100 °C, 1200 °C, and 1250 °C, respectively, as listed in **Table 6.2**. These values were considerably lower than those of the original specimen (42.7%). Conversely, the atomic fraction of metallic tungsten (W) increased from 28.1% in the original specimen to 53.3%, 47.6%, 46.8%, and 58.9% for specimens annealed at 950 °C, 1100 °C, 1200 °C, and 1250 °C, respectively. The plot of metallic and oxidized tungsten components in **Fig. 6.15** shows that annealing

at progressively higher temperatures results in a significant increase in the amount of metallic W, as well as a significant decrease in the total amount of intermediate oxides (red dot data markers).
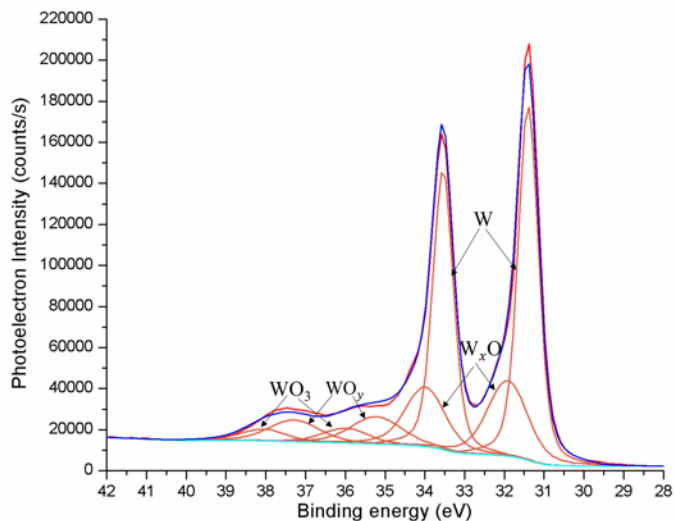
Figure 6.14. Fitted XPS scan of the specimen after annealing in the ESEM at 1250 °C (0.8 Torr). Experimentally measured data are shown in red; the baseline (cyan) and fitted peaks (blue) are shown for comparison; the orange peaks correspond to peaks for individual chemical species that combine to yield the fitted peaks (blue).

Table 6.3. The atomic percentage of each metallic/oxide tungsten component in the near-surface region of a sample after annealing in the ESEM, as determined from XPS spectra of annealed specimens.

Component Peak	Atomic Fraction (%)			
	Annealed at 950 °C, 0.8 Torr	Annealed at 1100 °C, 0.8 Torr	Annealed at 1200 °C, 0.8 Torr	Annealed at 1250 °C, 0.8 Torr
W	53.3	47.6	46.8	58.9
W_xO (x>1)	29.8	35.7	37.8	24.5
WO_y (2<y<3)	11.1	8.4	7.9	11.2
WO_3	5.8	8.3	7.5	5.4
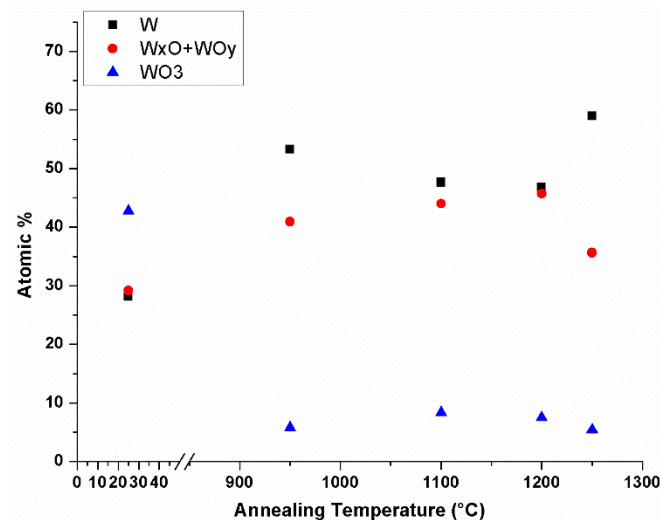
Figure 6.15. Relative amounts of metallic/oxide tungsten surface components after annealing in the ESEM, based on the XPS analysis results presented in **Table 1** and **Table 2**.

6.3.4.3 XPS Analysis of the UHV Annealed Sample

Tungsten specimens were also annealed in a UHV environment, at 1100 °C with a surrounding pressure of 10^{-8} Torr. Results from XPS analysis of such a sample are presented in **Fig. 6.16** and **Table 6.4**. These results indicate that the atomic fraction of metallic tungsten (W) was significantly higher than that for the original tungsten sample surface, whereas the WO_3 fraction was significantly lower. These findings are consistent with those observed for specimens annealed during *in situ* heating experiments in the ESEM (**Fig. 6.14**). In fact, UHV annealing (10^{-8} Torr) appears to have been more effective than ESEM annealing (0.8 Torr) in terms of producing metallic W (albeit without surface faceting), since the W content after 1100 °C UHV heating matches that obtained after 1250 °C ESEM heating.

106
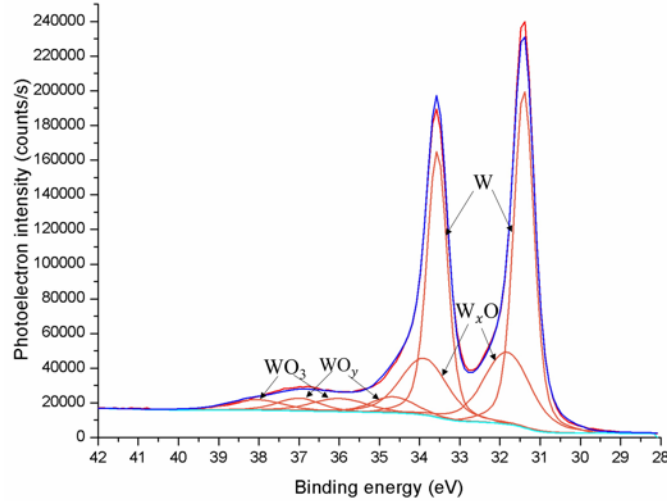
Figure 6.16. Fitted XPS scan of the specimen after annealing in the UHV chamber at 1100 °C, 10^{-8} Torr. Experimentally measured data are shown in red; the baseline (cyan) and fitted peaks (blue) are shown for comparison; the orange peaks correspond to peaks for individual chemical species that combine to yield the fitted peaks (blue).

Table 6.4. Atomic percentage of each metallic/oxide tungsten component in the near-surface region of a tungsten specimen after UHV annealing (10^{-8} Torr).

Annealing Condition	Component	Atomic Fraction %
1100 °C, 10^{-8} torr	W	58.9
	W_xO (x>1)	28.8
	WO_y (2<y<3)	6.0
	WO_3	6.3

6.4   Discussion

6.4.1   Tungsten oxidation process

A central goal of this study was to explore the morphological evolution of tungsten surfaces exposed to different environmental conditions (temperature and vacuum) during annealing in low- and high-vacuum systems. A set of *in situ* heating experiments was performed in an environmental scanning electron microscope, where tungsten pellets were

107

subjected to elevated temperatures at a pressure of 0.8 Torr. The observations from these experiments (disappearance of tungsten oxide features on the sample surface) suggested that sublimation of the oxide occurred, *e.g.*, as illustrated in **Fig. 6.3** and **Equations (5) - (7).**

To elaborate, tungsten sample surfaces undergo a series of reactions with O_2, when exposed to elevated temperatures. Metallic tungsten initially forms WO_2, which further oxidizes to solid WO_3. In the presence of a sufficiently high oxygen concentration, solid WO_3 subsequently transforms into gaseous WO_3. This process is referred to as sublimation or volatilization, and the role of oxygen has been described in several studies by other researchers [36, 98, 99, 101, 103, 104, 107, 135-139]. Intermediate tungsten oxides on the sample surface would also follow the same path to further oxidation and sublimation. Conversely, if the amount of environmental oxygen is limited, solid WO_3 transforms into metallic tungsten and liberates oxygen in a process known as decomposition [36, 99]. In the present study, *in situ* heating in the ESEM was conducted at a pressure of 0.8 Torr, which includes remnant oxygen from the sample loading process. Therefore, sufficient O_2 was present to facilitate the formation of WO_2 and WO_3 from tungsten (as well as intermediate oxides), according to **Equations** (5) and (6). This resulted in the observed disappearance of WO_3 via sublimation, as depicted in **Figs. 6.3** and 6.4.

The oxidation mechanism of tungsten is complicated [138, 139] and has been systematically investigated by Gulbransen *et al.* [98, 99, 136]. At intermediate temperatures, tungsten reacts with oxygen to form two oxide layers, with the outer layer consisting of WO_3 and the inner layer comprising other tungsten oxides (*i.e.*, W_xO ($x>1$) and WO_y ($2<y<3$)). The sublimation temperature T_s for WO_3 is typically lower than 800

°C [98] for thick tungsten oxide film samples exposed to ambient air; it is assumed that T_s would not change significantly in the ESEM environment (pressure of 0.8 Torr). In our previous study, we described the oxidation of tungsten nanoparticles [36] and posited that a thin surface oxide layer formed on the tungsten nanoparticle surfaces, resulting in the formation of a core-shell structure.

When the temperature is below T_s, a tungsten oxide film forms on the surface, which hinders further diffusion of oxygen into tungsten. And the total amount of oxides (W_xO ($x>1$), WO_y ($2<y<3$), and WO_3) on the sample surface increases, and the area of bare metallic W (if present in this initial stage) decreases. When the temperature exceeds T_s by a moderate amount, $e.g.$ up to 950 °C. solid WO_3 begins to sublimate, exposing areas of metallic W or intermediate oxides ($W_xO + WO_y$) that can be further oxidized. This oxidation processes are controlled by the environmental availability of oxygen and the diffusion of oxygen through cracks in the surface oxide layers [98], which in turn are governed by temperature.

The oxidation process appears to be more activated soon after the sample temperature exceeds 1200 °C, as shown by the significant changes in metallic and oxide phase fractions in **Fig. 6.15**. Gulbransen et al. [91, 98, 136] found that the rate of WO_3 sublimation increases significantly above 1200 °C, and in fact exceeds the rate of tungsten oxidation. This is consistent with the increase in metallic tungsten signal detected by XPS for specimens annealed at 1250 °C in the ESEM (**Table 6.3**).

6.4.2   Oxidation and Sublimation as Driving Forces for Surface Faceting

As oxygen near the surface of tungsten samples was consumed through oxidation and sublimation, faceting of the tungsten surface occurred, but only during annealing in the

ESEM (0.8 Torr pressure). Experimental observations such as those depicted in **Fig. 6.5** revealed that tungsten faceting occurred on the surfaces of specimens that were annealed at 950 °C, 1100 °C, 1200 °C, and 1250 °C in the higher-pressure vacuum environment (ESEM). However, faceting did not occur on the surfaces of tungsten annealed at 1100 °C in a UHV environment (10^{-8} Torr pressure), as seen in **Fig. 6.12**.

The disparity in faceting between samples annealed at different pressures (and presumably different oxygen partial pressures) can be attributed to oxidation-sublimation driven surface restructuring. Yu *et al.* [117] reported a similar phenomenon in 2019 and found that a large-scale surface terraces were observed on their rolled tungsten sheet when experienced oxidation at elevated temperature under high vacuum. Considering the large-scale surface terrace height of their tungsten sample (hundreds of nanometers), Yu *et al.* [117] thought that the faceting process was unlikely driven by surface atoms diffusion, they proposed and verified that the preferential oxidation was the main mechanism of surface faceting instead. The faceting size in the current work is also up to hundreds of nanometers, meaning the driven force for our tungsten sample surface faceting should be preferential oxidation of tungsten grains and sublimation of tungsten oxides rather than surface diffusion. Thus, the surface faceting of our tungsten samples is controlled by the availability of oxygen to tungsten surface during the annealing procedure. This could explain why samples annealed at a higher pressure in the ESEM (0.8 Torr) tended to form a faceted surface morphology, while samples annealed under UHV conditions (10^{-8} Torr) remained flat and planar, regardless of annealing temperature.

6.4.3 Facet Size

The findings presented in **Figs. 6.5**, 6.**7** and 6.**11** suggest that facet size is dependent on both the annealing temperature and the grain orientation. Facet size tends to increase with higher annealing temperature as the oxidation rate of tungsten increases with temperature.

The size of surface facets is also influenced by grain orientation, since oxidation of tungsten is a crystal orientation dependent property. Bartlett et al.[127] found that the order of oxidation rates was {001} > {111} > {110} for the single crystalline tungsten when it was annealed at 2050 °C under a pressure of 10^{-6} atom (~10^{-4} Torr). On the other hand, Schlueter et al. [138, 139] reported that the oxidation rate of different orientation of tungsten grain follows the order: {001} > {110} > {111} within a temperature range 720-870 K (447-597 °C) under 1 atmosphere (760 Torr), with the oxidation rate of grains with orientations close to {001} two times higher than it of {111} [138, 139] and they explained that atomic surface density of low indexed surface was the critical reason for the oxidation rate difference between those gains with different orientation. A higher oxidation rate on tungsten grains with orientation close to {001} therefore will result in a larger facet size. In the present study, for the tungsten pellet annealed at 1100 °C for 15 minutes in the ESEM (surrounding pressure of 0.8 Torr), grains with orientations close to {001} exhibited larger, more prominent facets than those with orientations close to {110} (see **Fig. 6.11**). In contrast, grains with orientation close to {111} exhibited much smaller surface facets, as depicted in **Fig. 6.7**. This finding is in line with the work of Yu *et al.* [117], who also reported that surface faceting is influenced by grain orientation for rolled tungsten sheet subjected to grinding-polishing-electropolishing. However, in their study, grains with

orientation close to {111} exhibited a tendency to form prominent and coarse facets, while grains with orientation close to {001} tended to remain smooth. Yu *et al.* [117] attributed this observation to the oxidation of tungsten during annealing and stated that with a very limited supply of oxygen, grains with orientation close to {111} would form {001} planes, which could be due to that their samples were different from ours and the accessible oxygen level in that work was significantly lower than in the current study. Given the significant difference in annealing temperature and pressure (1500 °C for 24 h under a pressure of 10^{-5} mbar), it could explain why the facet formed on the tungsten surface in the work of Yu *et al* [117] differs from the facet in the current study

The fact that the tungsten pellets in this study formed faceted pyramids with {110} planes after ESEM annealing is interesting. As discussed above, the surface faceting observed here results from preferential oxidation of specific W planes, followed by sublimation of the oxide and formation of {110} facets. Additionally, these {110} facets correspond to the crystallographic planes that have the lowest surface energy. For tungsten, the relative magnitudes of the low-index surface energies $\gamma_{(001)}$, $\gamma_{(110)}$ and $\gamma_{(111)}$ are still a matter of some debate [135], although it is generally accepted that {110} faces have the lowest surface energy among {001}, {110}, and {111}. This would apply in either of the situations that have been investigated by other groups, *i.e.* whether the order is $\gamma_{(110)} < \gamma_{(111)} < \gamma_{(001)}$ [117] or $\gamma_{(110)} < \gamma_{(001)} < \gamma_{(111)}$ [36, 135]. Therefore, the observation in the current study that {110} facets dominate the surface morphology of annealed and faceted tungsten is consistent with $\gamma_{(110)}$ being the lowest surface energy, at least with respect to the other low-index facets {001} and {111}.

Notably, tungsten surfaces exhibiting rounded edges and sharp vertices were observed following annealing at 1200 °C for 15 minutes under a surrounding pressure of 0.8 Torr, as indicated by the orange box in **Fig. 6.5** (c3). Additionally, surfaces exhibiting rounded edges and rounded vertices were observed following annealing at 1250 °C for 15 minutes (0.8 Torr), as indicated by white and green arrows in **Fig. 6.5** (d3). Observations related to the vertex-rounding transition were consistent with calculations by Seif *et al.* [70], who explained that tungsten particle shape is a function of temperature, availability of oxygen, and chemical environment. Seif *et al.* [70] also predicted that {110} facets should dominate tungsten particles for all temperatures between 0 and 2000 K (when annealed in a pure vacuum). Moreover, their calculations suggest that the round edges of tungsten grain are due to the formation of {112} facets, and that the round vertices are due to the appearance of {100} facets.

Besides temperature and grain orientation, facet size is also a function of time and oxygen level. Szczepkowicz *et al*. [109-113] tested their [111]-oriented W tip in environments with various oxygen levels and found that the formed the size of {112} facets generally increase with the amount of available oxygen [108], although their results also suggest that excessive oxygen levels can hamper the formation of surface facets. On the other hand, facet size was observed to increase with annealing time, e.g., the facet size in studies by Szczepkowicz *et al*. [109-113] was only several nanometers for samples annealed for 80 seconds [111], whereas Yu *et al* [117] observed facet planes that were hundreds of nanometers (and even micron-scale) in size after annealing of W sheet for 24 hours.

6.5   Conclusions

This chapter presents the findings of an extensive investigation into the morphological evolution of bulk tungsten surfaces annealed at high temperatures and exposed to varying levels of vacuum. To achieve this, two sets of heating experiments were conducted on porous tungsten pellets using *in situ* environmental SEM heating and ultrahigh vacuum heating in a custom-built chamber, with surrounding pressures of 0.8 Torr and 10^{-8} Torr, respectively. The following conclusions are drawn:

- Oxygen plays a critical role in the process of bulk tungsten surface faceting, and tailoring the oxygen level allows a degree of control over final morphology. The ESEM annealing experiments conducted at 0.8 Torr resulted in tungsten oxide sublimation and tungsten surface faceting in the presence of oxygen. It was demonstrated that the *in situ* ESEM could be effectively utilized for investigating bulk tungsten faceting, despite the level of available oxygen being significantly higher during *in situ* heating than in the UHV chamber. In contrast, the surfaces of samples annealed under UHV remained flat and smooth except in the vicinity of grain boundaries; these surfaces remained flat due to a lack of oxygen-induced faceting.

- Temperature and grain orientation influence the size of bulk tungsten surface faceting. Observations from *in situ* ESEM heating experiments indicate that significant tungsten surface faceting occurs at temperatures of ~1000 °C under a pressure of 0.8 Torr, and facets grow as temperature increases beyond this, dominated by {110} facets. Grains with orientation close to {001} exhibited a higher tendency to develop pronounced {110}

facets. The morphology of such facets was observed to evolve with temperature, with annealing at 1200 °C and 1250 °C leading to the emergence of rounded edges and vertices.

- SEM tilted-sample imaging and serial sectioning tomography yielded consistent determinations of surface facet orientation, demonstrating the effectiveness of both techniques for indexing facets. However, it is imperative to account for the way(s) that a faceted polyhedron (Wulff shape) intersects with a nominal surface plane of a grain with particular crystallographic orientation. In our investigation, the software tool Wulffmaker was employed to determine Wulff shape and assist in the indexing of experimentally observed surface facets.

- The findings in this chapter are consistent with our previous work on tungsten nanoparticles that were heat treated under a similar range of processing conditions. This holds significant implications for the design of tungsten-based materials with targeted surface facets and may benefit other aspects of tailored crystal engineering.

CHAPTER 7. GROWTH AND FACETING OF TUNGSTEN AND OXIDES IN SCANDATE CATHODE PARTICLES DURING IN SITU HEATING IN THE SCANNING ELECTRON MICROSCOPE

7.1 Introduction

Dispenser cathodes, which are thermionic electron emitters, are conventionally fabricated with porous tungsten as the base material and alkaline metal oxide mixtures (typically BaO-CaO-Al$_2$O$_3$ in a ratio of 6:1:2 or 4:1:1) added as impregnant materials [1, 27, 120, 140-145]. These cathodes are used as electron sources in vacuum electron devices (VEDs) for a variety of applications that require high-brightness electron beams [3, 4, 18, 21-23, 27, 114, 118, 119, 125, 142, 146-150], including cathode ray tubes [18], electron microscopes [23], traveling wave tubes [3, 4, 18, 21-23, 27, 123, 142, 146-148], and high-power microwave devices [18, 22, 151]. Additionally, dispenser cathodes are utilized extensively for industrial heating, medical treatment, and scientific research purposes [23, 123, 146-148].

To meet the increasing performance demands for dispenser cathodes, novel cathodes doped with scandia (Sc$_2$O$_3$) were developed and were shown to be capable of high emission current densities well above 10 A/cm^2 [27], as well as lower operating temperatures below 1000 °C$_b$ (brightness temperature, measured with respect to a tungsten filament) [3, 4, 21, 22]. These "scandate" cathodes are typically prepared using a complicated process that includes an activation step, i.e., heating at 1150 to 1200 °C$_b$ in a vacuum chamber for an extended time that can range from 10 to 100 hours [3, 4, 21, 22, 27, 146]. It is noted that scandate cathodes exhibit a knee temperature, which represents a transition from temperature-limited to space-charge-limited electron emission, at a temperature of ~850 °C$_b$ [3, 27]. This temperature is therefore relevant to a scandate cathode's surface state, in

116

addition to the activation temperature noted above. Previous studies have documented that certain high-performance scandate cathodes develop a faceted and terraced tungsten surface morphology when properly activated, and this differs significantly from the initial scandate cathode surface morphology prior to activation. The activated, highly faceted surface also exhibits a low work function that facilitates electron emission [3, 4, 21, 22, 27]. These observations indicate that critical changes in cathode materials occur during the activation process and that scandate cathodes develop a particular surface state favorable for thermionic emission performance. However, it is not understood exactly how such a surface is generated during the activation process.

A common method for monitoring the activation process of a dispenser cathode is to measure its electron emission under appropriate biasing conditions in a vacuum test apparatus [3, 26, 91, 123, 128, 146-148, 152-154]. When combined with characterization of cathode surface morphology by electron microscopy of pre- and post-activated scandate cathodes, these emission measurements are effective in identifying surface material characteristics that correlate with good cathode performance, *i.e.,* this approach is effective for knowing the desirable end state that should be achieved during cathode processing and activation. However, the exact changes in surface state and the times/temperatures at which these changes occur, are not well understood. Clarifying the changes in cathode surface materials during activation would enhance the understanding of a cathode's high-temperature surface state during operation and would facilitate optimization of processing approaches to yield activated cathodes that consistently perform well. For this reason, *in situ* observations of cathode surface evolution are critical to a complete understanding of cathode behavior.

Designing experiments for *in situ* observation of scandate dispenser cathode evolution is challenging, because the cathodes are typically used in a high vacuum environment (~10^{-6} mbar) [2] at operation temperatures approaching 1000 °C$_b$ [118]. Moreover, scandate cathodes are made from materials with sizes ranging from the micron scale (grains of tungsten in the porous body) [2] to the nanoscale (scandium oxide added to the tungsten in powder metallurgical processing or as a component of the impregnant compounds) [1], which makes it difficult to implement real-time observation of all relevant features of a scandate cathode surface. An additional challenge is that conventional *in situ* heating experiments in the scanning electron microscope (SEM) are performed with a furnace-type stage, which generates a chamber pressure of ~1 Torr [155-157] at elevated temperatures. This pressure is significantly higher than that experienced by a cathode during activation and operation in its relevant environment (10^{-6} mbar).

For appropriate observation of scandate cathode materials under relevant environmental conditions, a better alternative to conventional furnace-type SEM heating stages is a micro-electro-mechanical system (MEMS)-based chip heater, which can rapidly heat small specimens to 1200 °C while maintaining a chamber pressure in the range of 10^{-6} to 10^{-7} mbar [118, 158, 159]. These MEMS-based chip heaters require specimen dimensions limited to several tens of microns, and therefore sample preparation can represent an additional challenge. In the current study, an impregnated but un-activated scandate cathode with appropriate tungsten grain size was partially crushed, to generate fragments that could be studied in this manner. Several fragments were transferred to heater chips, and a series of *in situ* heating experiments was subsequently performed at temperatures and chamber pressures approximating the processing and operating

conditions of a scandate cathode. *In situ* SEM images and videos were recorded during the heating experiments, to observe the behavior of scandate cathodes and to reveal the dynamic morphology changes in an environment representative of dispenser cathode operating conditions.

7.2   Materials and Methods

The materials studied in this chapter were obtained from specimens that had been prepared using standard cathode processing techniques. Preliminary complementary results were presented in [118]. The initial specimen was a tungsten-based scandate pellet (fabricated by 3M Technical Ceramics) that was made from a blend of 2.0 μm tungsten (W) powder and nanoscale (<50 nm diameter) Sc_2O_3 powder that had been mixed thoroughly. The mixture was processed using powder metallurgical methods to obtain a sintered porous pellet with a final density of 70%. This pellet was then impregnated with a 6BaO-1CaO-$2Al_2O_3$ ceramic mixture but was not activated following this impregnation step.

Subsequent heating experiments up to the standard activation temperature of 1200 °C were instead performed in the SEM, for *in situ* observation of changes in material phase and morphology. To prepare specimens for *in situ* heating experiments, the as-impregnated cathode pellet was manually crushed and ground into tiny fragments. A portion of these particles was then dispersed on a silicon (Si) wafer and loaded into a focused ion beam and scanning electron microscope dual-beam instrument (FIB-SEM; FEI Helios G3). Utilizing a tungsten needle (nanomanipulator) in the FIB-SEM, an individual fragment from the crushed pellet was transferred from the Si wafer and attached to a MEMS heater chip (Fusion Thermal E-chip from Protochips Inc.). The MEMS heater chip had a continuous silicon nitride (SiN) coating, a heating membrane area measuring 350 x 1000 $μm^2$, and a

periodic array of circular holes (8 μm diameter) that can be used for transmission electron microscopy observations (these were not performed in the current study). Electron beam welding and ion beam milling were utilized to affix and detach each cathode fragment from the tungsten needle, facilitating successful transfer and attachment of the cathode particles to the heater chip. After each fragment was loaded onto its own E-chip, electron beam deposition of tungsten was applied once more to attach the sample to the heater chip, thereby improving thermal conduction and minimizing sample vibration during the heating experiments. The process of loading an individual fragment to a heater chip is shown schematically in **Figure 7.1**.

Before heating, each fragment was characterized using SEM imaging and X-ray energy dispersive spectroscopy (EDS) in the FIB-SEM chamber. *In situ* heating experiments were performed under a vacuum of $10^{-6} \sim 10^{-7}$ mbar, with sample temperature controlled by "Protochips Fusion" software (Protochips Inc.). The heating rate ranged from 0.1 °C/s to 0.3 °C/s. Once the sample reached the target temperature, it was held there for 10 to 15 minutes, after which it was cooled at a controlled rate of 0.1 °C/s to 0.3 °C/s. During each *in situ* heating experiment, SEM images and videos were recorded to document changes in morphology of the cathode fragment.
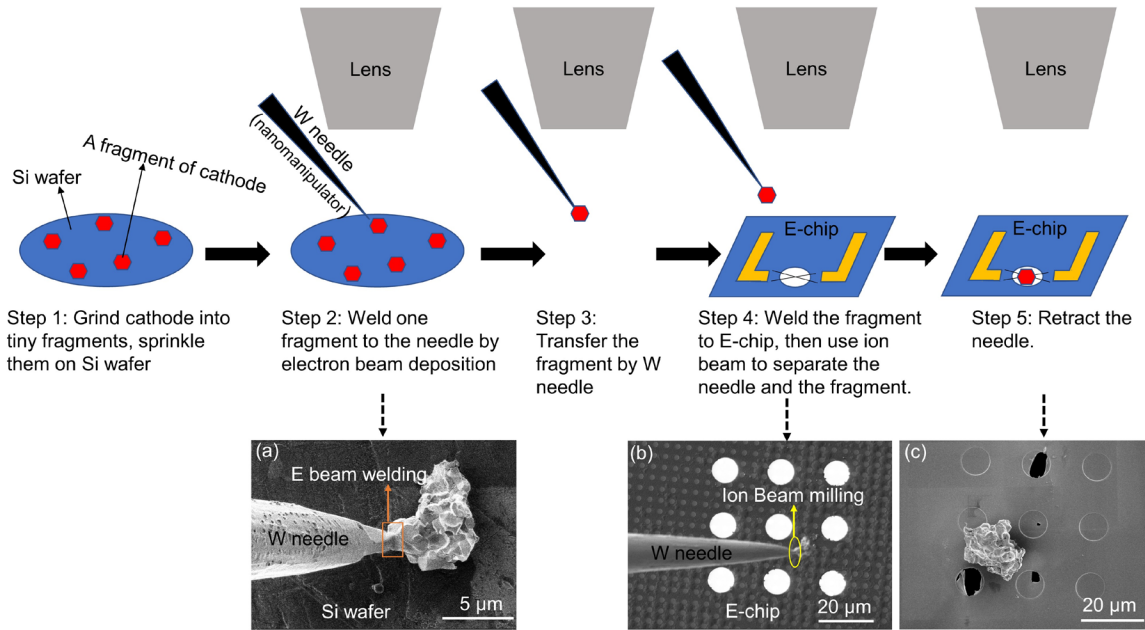
Figure 7.1. Schematic of the procedure for loading a cathode fragment sample onto a MEMS-based chip for *in situ* heating in the SEM. Steps 1 to 5 involve the selection and transfer process from a Si wafer to the heater chip. (a-c) SEM images corresponding to steps 2, 4 and 5, illustrating key transfer steps including attachment and detachment of the cathode fragment and W needle.

7.3   Results and Analysis

Figure 7.2 presents an analysis of the microstructure, morphology and distribution of elements and phases in the initial fragment from the tungsten-based scandate cathode, after attachment to the SiN-coated E-chip but before the heating experiment. The secondary electron (SE) images in **Figure 7.2** (a1-a5) reveal that the fragment contains a mixture of sub-micron and micron-scale particles, some of which exhibit relatively smooth surfaces. The corresponding backscattered electron (BSE) images in **Figure 7.2** (b1-b5) indicate that most of the larger particles are tungsten, based on their relative brightness due to higher atomic number. The EDS elemental maps in **Figure 7.2** (c-i) suggest that the irregular-shaped regions are impregnant materials, consisting of elements including Ba, Ca, Al, O, and Sc. The lower-magnification BSE images (**Figure 7.2** (b1-b3)) suggest that the

impregnant materials may exist as multiple phases, based on their difference in brightness. However, it is difficult to state this with confidence based on **Figure 7.2** alone, so a more detailed set of observations will be presented below. It is noted that Si and N were also detected by EDS, due to the SiN coating on the E-chip, but these were not included in the maps in **Figure 7.2**.
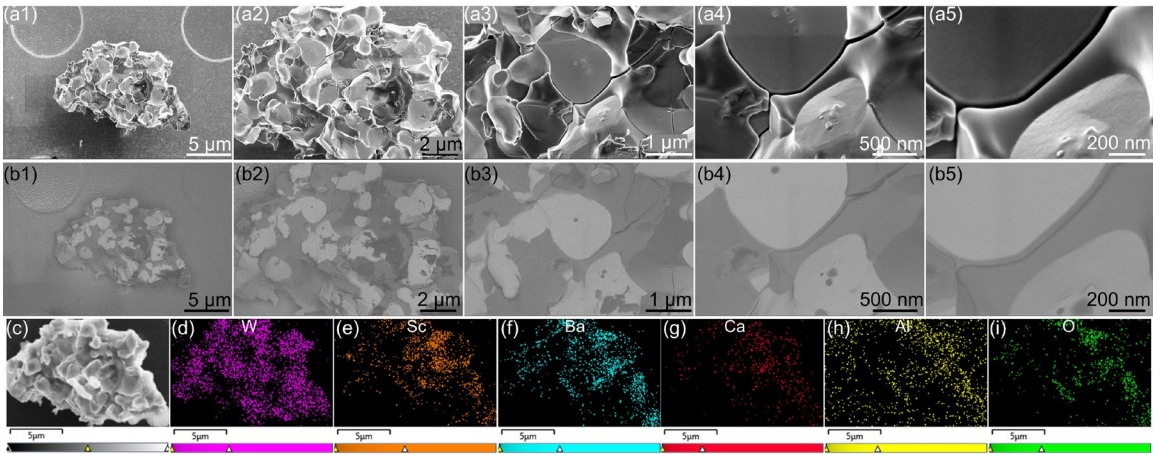
Figure 7.2. A fragment from an impregnated tungsten-based scandate cathode, after it was attached to the SiN-coated E-chip but before the sample was heated. (a1)-(a5) Secondary electron images of the fragment. (b1)-(b5) BSE images corresponding to (a1)-(a5), respectively. (c) Electron image of the region selected for EDS analysis and elemental mapping, with individual maps for (d) W, (e) Sc, (f) Ba, (g) Ca, (h) Al, and (i) O.

     Figure 7.3 presents the EDS analysis of this initial fragment from a different perspective, with EDS signal overlaid on the SE image in order to determine the distribution of elements more precisely. A BSE image of the particle is shown in **Figure 7.3a**, where the histogram and gamma of the image were adjusted using ImageJ to differentiate the gray levels more clearly. Individual elemental maps (Al, Ca, Ba, Sc, W and O) are shown in **Figure 7.3** (b-h), with the electron image in the background. Comparison of the elemental maps with the BSE image (**Figure 7.3**a), it is seen that the bright grains in the BSE image

can be clearly identified as tungsten (W), as it has the highest atomic number (Z=74) of all elements in this sample. Ca is difficult to identify in correlation with discrete regions of the fragment, due to its low EDS signal count (**Figure 7.3**c). Additionally, its atomic number (Z=20) is similar to that of Sc (Z=21), making it difficult to distinguish their oxides in a BSE image. The majority of the medium-gray (i.e., non-tungsten) regions of the fragment appears to consist of a mixed oxide containing Ba, Al and Sc, as indicated by the white arrows in **Figure 7.3**a.

A complicating factor in this analysis is that the contrast effect for BSE imaging does not emanate solely from compositional contrast based on average atomic number, but it can also be influenced by sample topography [46]. To mitigate this effect for the rough fragment, an in-column detector (ICD) for BSE imaging was used, reliably generating signal at all locations of the sample and providing a plan-view BSE image (**Figure 7.3**a). However, the collection of X-rays for elemental mapping was still affected by sample surface roughness, due to the off-axis angle of the detector, meaning that EDS collection was significantly hindered in locally deep regions of the fragment. Therefore, it is difficult to correlate gray level with composition for every sample region visible in the BSE image. For example, the darkest regions in the BSE image (**Figure 7.3**a) should be oxide particles containing low atomic number elements (on average), but their composition cannot be determined directly from **Figure 7.3**. A further complicating factor regarding identification of individual phases visible in the BSE image is that the impregnant oxides most likely exist as mixed phases, as a result of the impregnation phase that involves infiltration of molten material (BaO-CaO-Al_2O_3) into the porous W. It is anticipated that the molten oxide dissolves some or all of the pre-existing scandia particles in the W-Sc_2O_3 sintered body,

which could result in one or more mixed oxide phases residing in the tungsten pores after solidification. It is noted, however, that a small number of individual Sc_2O_3 particles appear to remain after impregnation, based on comparison of EDS elemental maps, *e.g.*, as indicated by the orange arrow in **Figure 7.3a** that points to a particle showing Sc but effectively no Ba or Al.
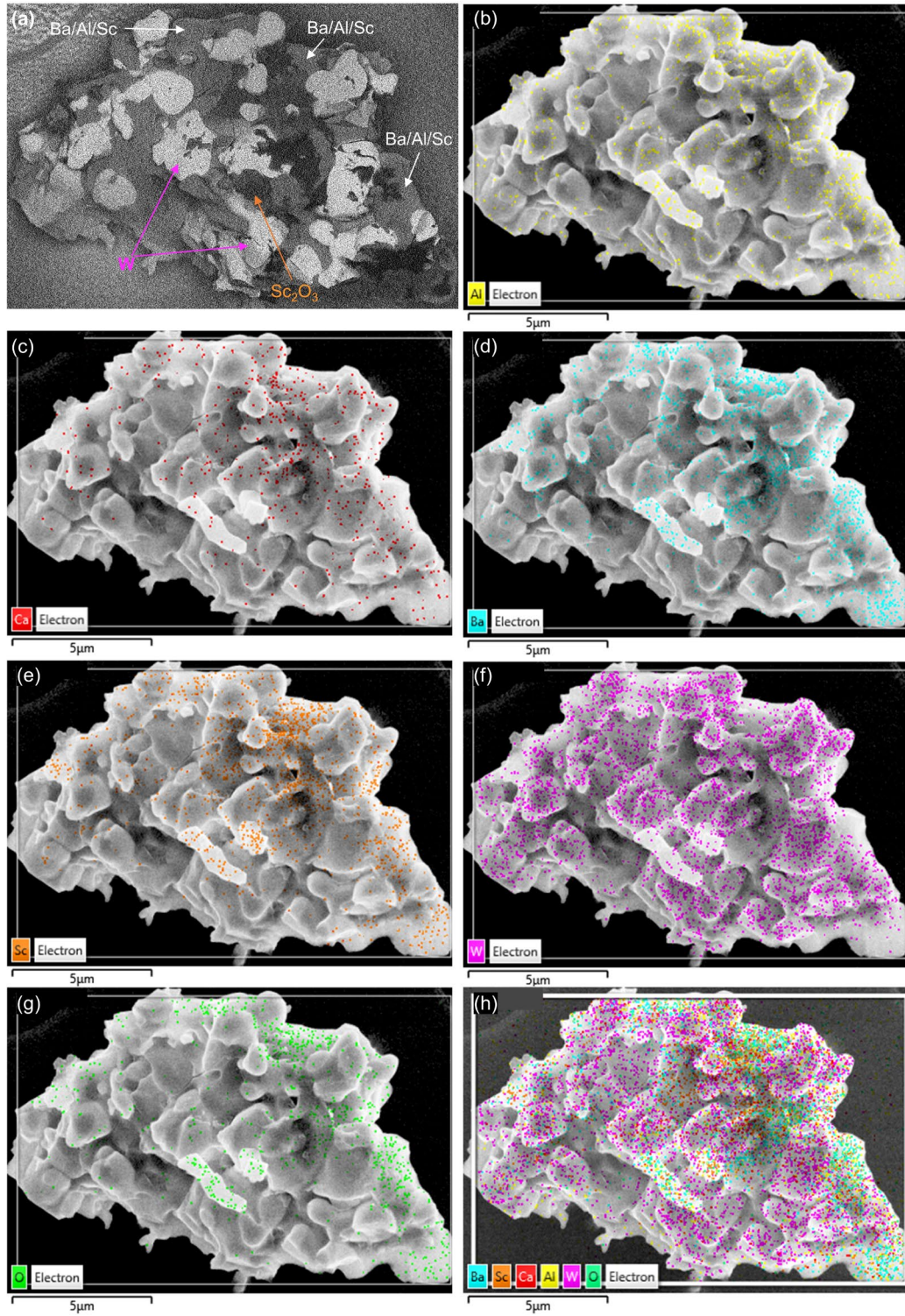
Figure 7.3. (a) BSE image of scandate dispenser cathode fragment prior to heating, along with EDS elemental maps overlaid on SE image for (b) Al, (c) Ca, (d) Ba, (e) Sc, (f) W, (g) O. (h) Composite elemental map (on SE image) showing all elements and indicating mixed oxide phases (Ba/Al/Sc).

Figure 7.4 presents images acquired during an *in situ* SEM heating experiment conducted in the FIB-SEM, with a chamber pressure of $10^{-6} \sim 10^{-7}$ mbar. The fragment was heated on the E-chip to 850 °C and held there for 15 min. The initial image in **Figure 7.4**(a) portrays the morphology of tungsten particles and impregnated materials in a scandate cathode fragment at room temperature. As temperature was raised to approximately 600 °C, some of the impregnant materials experienced growth and formed small features with a rod-like morphology, as indicated by the yellow arrows in **Figures 7.4**(b) and (c). At 712 °C (**Figure 7.4**(d)), these and other impregnant regions underwent continued growth, changing from a rod-like shape to a set of more equiaxed, highly faceted grains, as shown in **Figure 7.4**(g). As the temperature increased to 800 °C (**Figure 7.4**(e)), these faceted crystallites grew larger, with some appearing to grow along (and in contact with) the surface of the tungsten grain, as denoted by the yellow arrows in **Figure 7.4**(h). As the temperature approached 850 °C, the impregnant materials continued to increase in size, as demonstrated in **Figures 7.4**(f) and (i). Additionally, these grains consolidated as they grew, resulting in fewer and larger particles, which is readily apparent when comparing **Figures 7.4**(g) and (i). Finally, no significant changes in tungsten grain morphology were observed during *in situ* heating experiments up to 850 °C, *i.e.*, the grains remained unaltered compared to their initial state at room temperature.
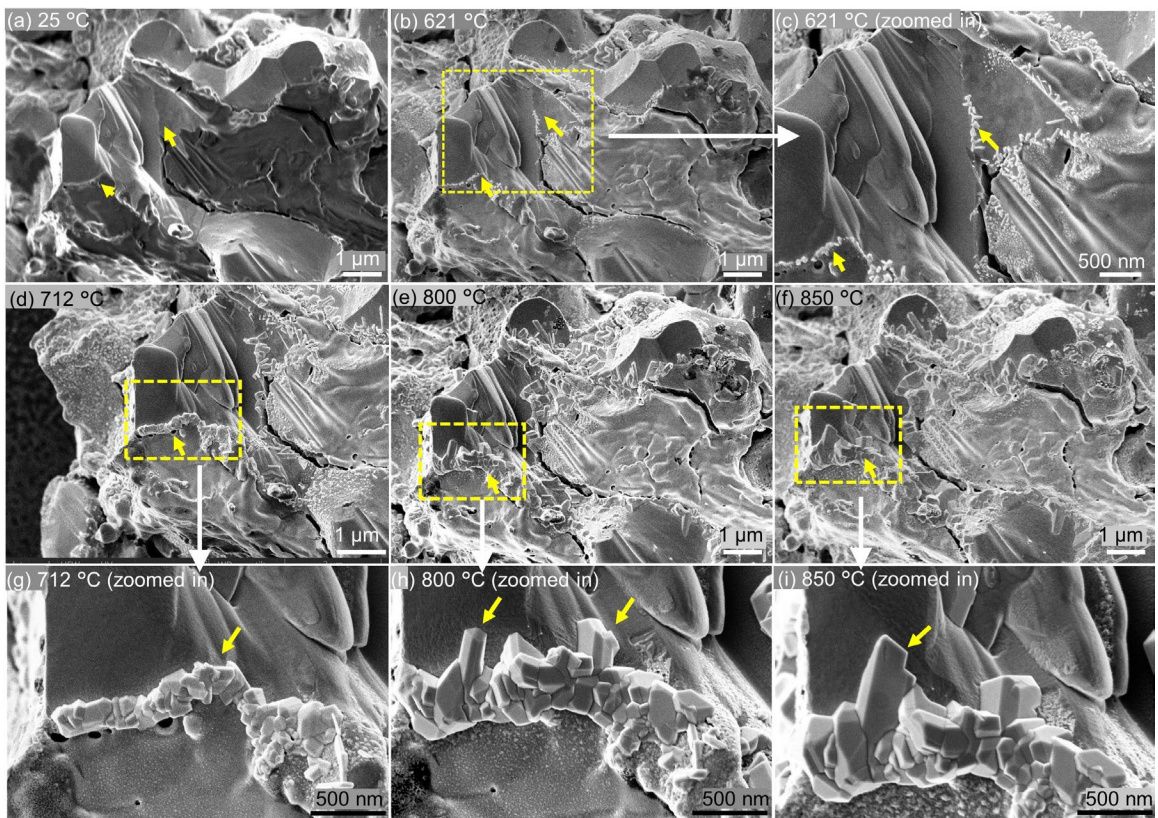
Figure 7.4 Secondary electron SEM images of the sample during *in situ* annealing to 850 °C: (a) 25 °C; (b) 621 °C and (c) higher magnification view of the area in yellow box in (b), showing the emergence of nanoscale rod-like features; (d) 721 °C; (e) 800 °C; (f) 850 °C; (g), (h), (i) are higher magnification views of the areas in yellow boxes in (d), (e), and (f), respectively. These show the continued growth and consolidation of impregnant oxide crystallites.

During *in situ* heating, EDS analysis of the sample was attempted, but the EDS detector was unable to obtain a measurable signal for sample temperatures above 400 °C. As a result, EDS scans and a corresponding image were recorded after the sample cooled from 850 °C to 25 °C, for the same region that was imaged in **Figure 7.4** (i). As shown in the SE image of **Figure 7.5** (a), the faceted crystal shapes in the impregnant material region remained unchanged from their state in **Figure 7.4** (i) after cooling, while the tungsten grain morphology remained consistent with **Figure 7.4** (i). It is noted that the sample view changed slightly during cooling, due to sample rotation on the E-chip as temperature

decreased. However, careful inspection of **Figure 7.4** (i) and **Figure 7.5** (a) confirms that the crystallite configuration did not change. The BSE image in **Figure 7.5** (b) shows impregnant materials that exhibit multiple gray levels, suggesting that distinct phases may exist as a result of phase separation. Moreover, the layered EDS map in **Figure 7.5** (c) provides details of the elemental distribution in this sample region, revealing that strong Ba and O signals were detected throughout the majority of this region, except in the areas where metallic tungsten was detected (bright regions in **Figure 7.5** (c)). Focusing on the EDS point scan of the faceted region (Spectrum 1) in **Figure 7.5** (d), it is observed that the faceted impregnant particle contains 5.1 at.% Ba and 12.0 at.% Al, as well as other elements expected in the annealed cathode fragment. The tungsten signal is attributed to the metallic W region behind the faceted impregnant feature, which is sufficiently thin to allow the EDS interaction volume to extend beyond the faceted feature; this is consistent with previously reported findings [118]. Liu *et al.* **[21]** observed a similar result in their study of an activated scandate cathode and proposed that the impregnant phase corresponded to the compound $BaAl_2O_4$, albeit with excess O detected. The ratio of Ba to Al in the faceted feature (Spectrum 1 of **Figure 7.5** (d)) is approximately 1:2, which is consistent with the chemical formula $BaAl_2O_4$ and which also agrees with the measurements reported by Liu *et al.* **[21]**.
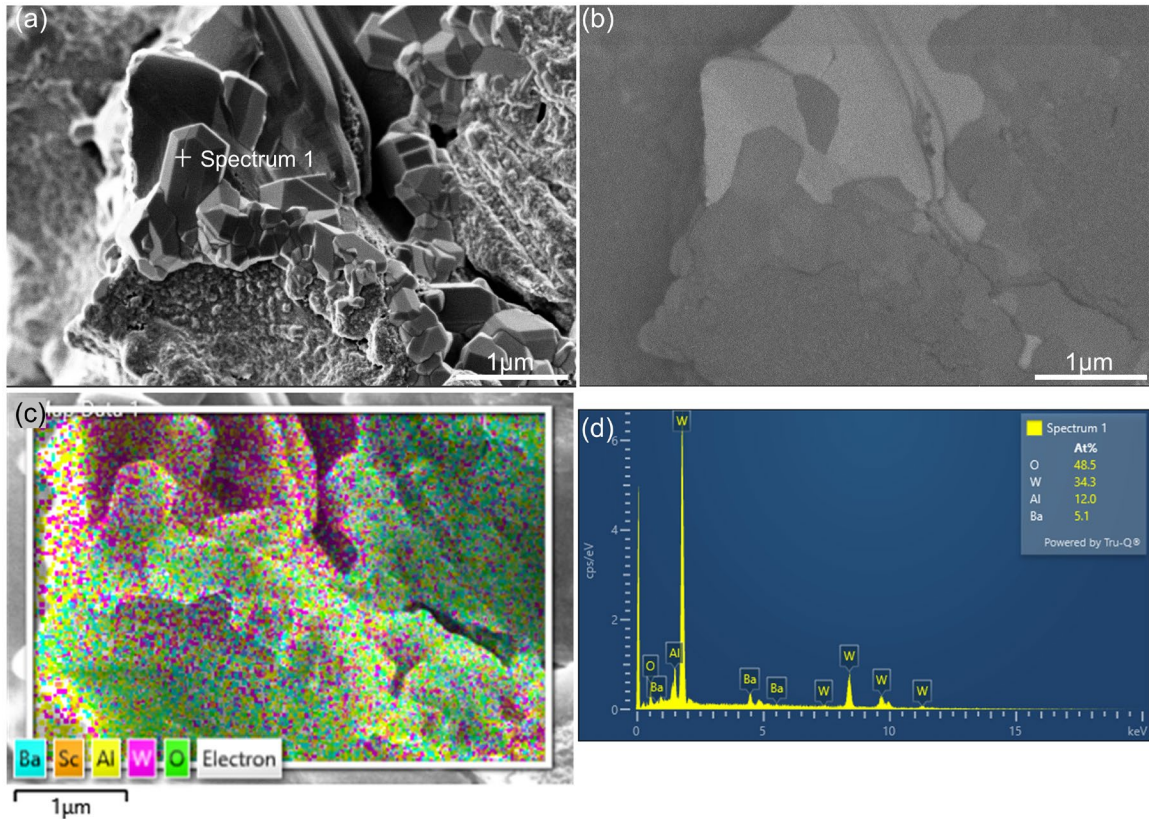
Figure 7.5 Micrographs and the corresponding EDS analysis of the scandate cathode fragment after it had cooled from 850 °C to 25 °C. (a) Secondary electron (SE) image of the scandate cathode fragment, and (b) backscattered electron (BSE) image of the same region. A layered EDS map of this region is presented in (c), and an EDS point analysis of faceted impregnant material is shown in (d) for the location labeled as Spectrum 1 in image (a).

An *in situ* heating experiment from 25 °C to 1000 °C with a surrounding pressure of 10^{-6} to 10^{-7} mbar was performed in the Helios SEM to observe another fragment (from the same scandate cathode pellet as above), with selected secondary electron images presented in **Figure 7.6**. After reaching the target annealing temperature of 1000 °C, this sample was held for 10 min, at which point the sample started shaking, vibrating and rotating, and eventually flipped over. Comparing the morphology at 850 °C in **Figure 7.4** (i) with the morphologies at temperatures above 900 °C in **Figure 7.6**, it can be seen that phase separation of impregnate materials became conspicuous and impregnant faceting continued.

Additionally, certain impregnant particles began to migrate and eventually formed an array of small discrete islands. At the same time, impregnant particles gradually evaporated as the temperature increases from 900 °C to 1000 °C, as denoted by the yellow arrows and dashed ovals in **Figure 7.6**. Finally, it was observed that nanoscale facets began to form on the tungsten grain surfaces.
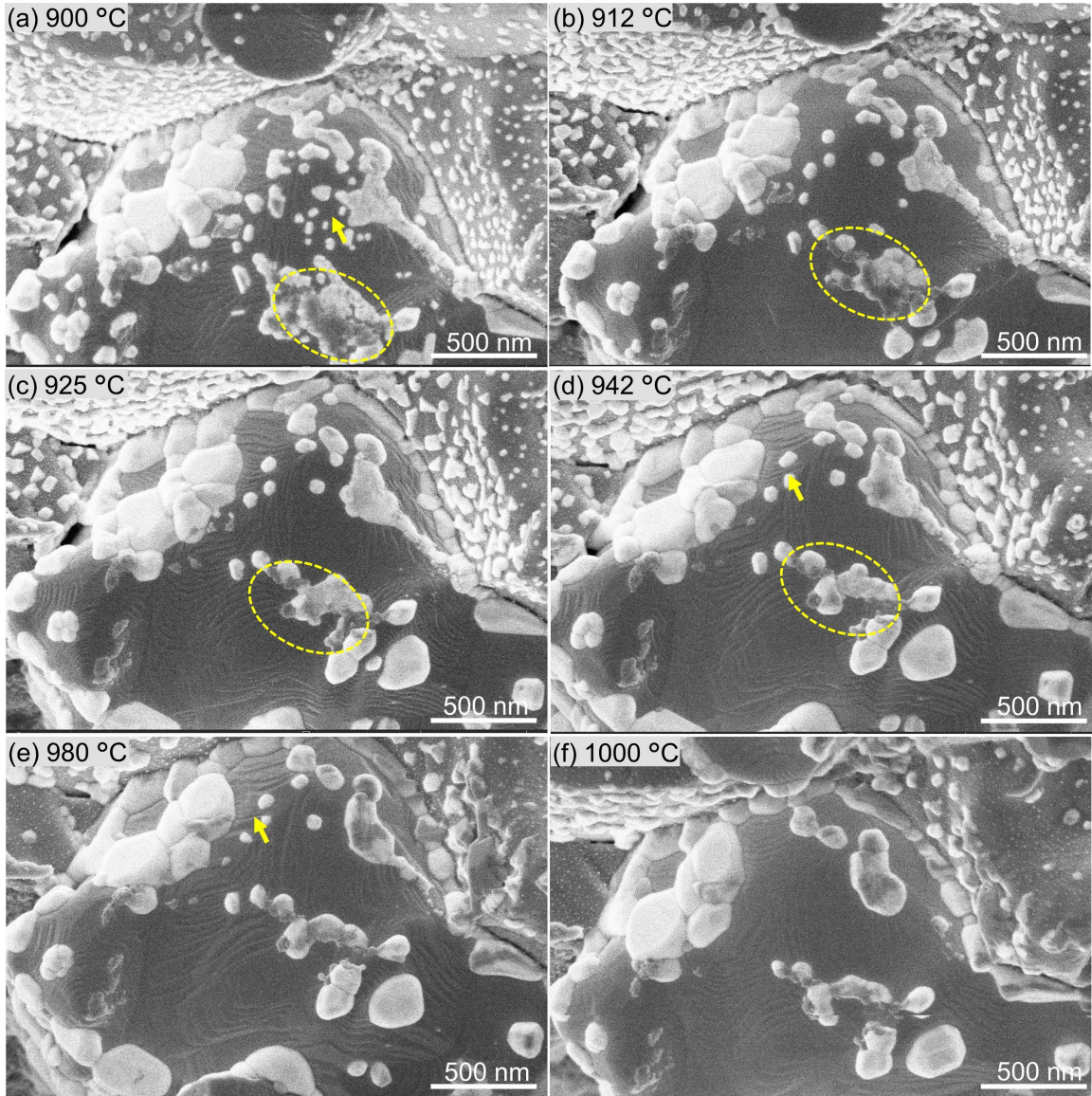
Figure 7.6 Morphology of the sample when annealed to 1000 °C with a surrounding pressure of 10^{-6} ~10^{-7} mbar: (a) 900 °C, (b) 912 °C, (c) 925 °C, (d) 942 °C, (e) 980 °C, (f) 1000 °C. In these images, the tungsten grains are dark gray, while the surface oxide particles are relatively bright.

Figure 7.7 presents SEM images of a fragment obtained from the same original scandate cathode pellet, at a temperature of 1200 °C and surrounding pressure of 10^{-6} to 10^{-7} mbar. Remarkably, the impregnant material particles underwent a rapid 'boil-off' phenomenon when the sample was held at 1200 °C for ~20 minutes. The completion of this boil-off process, i.e., the disappearance of the impregnant particles, occurred within 1-2 minutes for some particles, but took ~20 minutes for most particles (see **Figure 7**). Once all the impregnant had boiled off, no further discernible change was observed on the tungsten surfaces, even after maintaining sample temperature at 1200 °C for another 40 minutes.

Significant vibration and rotation of the sample were observed during heating experiments at high temperatures, e.g., 1200 °C, which resulted in some degradation of SEM image contrast as seen in **Figure 7**. Additionally, it appeared that the SiN membrane of the E-chip was damaged by the tungsten fragment during the high temperature hold at 1200 °C, resulting in a hole in the E-chip. This is most likely due to a chemical reaction between W and SiN. It is noted that the reactions between fragment and E-chip, as well as formation of a hole in the E-chip, occurred after the observations that are reported in this chapter.

Additionally, *in situ* observations were recorded during cooling after the heating experiments that involved maximum temperatures of 850 °C, 1000 °C, and 1200 °C. However, no meaningful changes were observed in the cathode fragments during cooling.

Moreover, all E-chips developed cracks near the end of each *in situ* experiment, as sample temperature decreased below ~400 °C, which in most cases prevented the sample from being preserved for further analysis after each experiment. A notable exception was the sample cooled from 850 °C and imaged as shown in **Figure 7.5**.
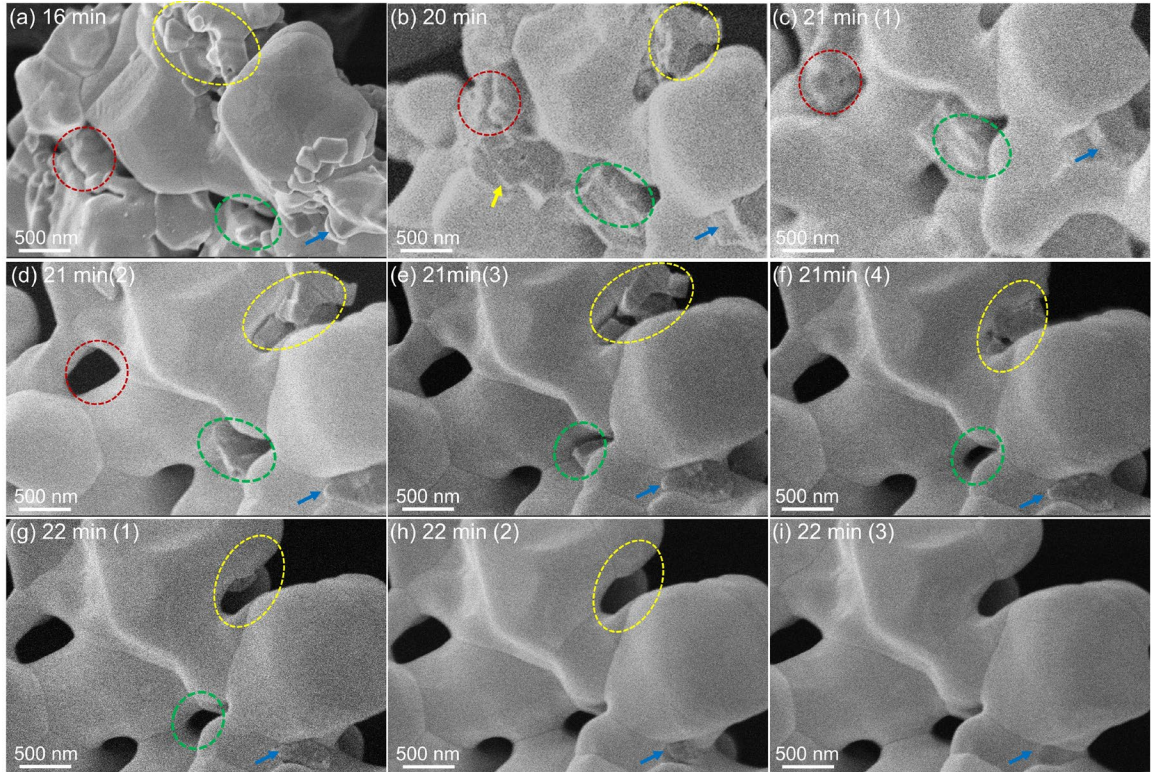
Figure 7.7 SE images recorded at different times while a cathode fragment was held at 1200 °C under a surrounding pressure of 10-6 ~10-7 mbar: (a) 16 min, (b) 20 min, (c-f) 21 min, (g-i) 22 min. Three impregnant material particles are indicated by dashed ovals in (a), and all these particles gradually disappeared during the high-temperature hold. The impregnant particle indicated by the blue arrow in (a) shrank significantly but did not disappear entirely within the first 22 minutes of this heating experiment.

7.4 Discussion

7.4.1 Behavior of Impregnant Materials During Heating Experiments

The current study focused on the materials contained in a scandate dispenser cathode, which includes the ceramic mixture 6BaO-1CaO-2Al$_2$O$_3$ as an impregnant material infiltrated into porous tungsten, and nanoscale scandium oxide (Sc$_2$O$_3$) powder that had been mixed with tungsten powder before sintering and was therefore located on the surfaces of tungsten ligaments before infiltration of the impregnant. Through *in situ* heating experiments conducted on a fragment of the scandate dispenser cathode, intricate details regarding the behavior of impregnant material at elevated temperatures and under high vacuum conditions (10^{-7} to 10^{-6} mbar) were revealed. **Figures** 7.**4** and 7.**5** demonstrate that faceted features grow out of impregnant particles at ~620 °C and these faceted features continue to develop as temperature rises.

Concurrently, there appears to be phase separation of the impregnant, with formation of barium-aluminum oxide as the faceted feature (**Figure 7.5** (d)). Given the EDS analysis in **Figure 7.5** (d), this faceted oxide appears to be BaAl$_2$O$_4$, consistent with previous studies [3, 4, 21] by Liu et. al. Furthermore, with increasing temperature, the impregnant material continues to migrate on tungsten surfaces and phase separation is apparent at 1000 °C (**Figure 7.6**). It is noted that the images in **Figure 7.6** were obtained in SE mode, because the BSE detector was not able to record images at high temperatures. However, images obtained at room temperature after the heating experiment, e.g., **Figure 7.5** (b), are consistent with the description of phase separation.

7.4.2 Incipient Faceting and Formation of Terraces on W Grains

The emergence of terraces on tungsten grains was observed when the temperature exceeded 900 °C, as depicted in **Figure 7.6**. However, even after a temperature hold at 1200 °C for 1 hour, the tungsten ligaments did not exhibit a highly faceted morphology. Full faceting would be expected during complete activation of a scandate cathode, as described by Liu et al. [6, 11-14] and Vancil et al. [38, 39]. The observation of only incipient faceting activity, i.e. formation of terraces on W surfaces as opposed to full faceting, is attributed to an artificially high amount of free surface area for the cathode fragment, in comparison to the available free surface area in a dispenser cathode pellet. The additional surface area enhances the loss or 'boil-off' of impregnant material, e.g. via sublimation in the high vacuum SEM environment. This would significantly alter the relative amounts of impregnant versus tungsten surface area, and likely change the kinetics of W surface transport an evolution of surface morphology as tungsten surface faceting is contingent on environmental factors and on temperature, as discussed in our prior work [32, 40]. The absence of a highly faceted structure for the tungsten grains in the current study suggests incomplete activation of the scandate cathode fragment.

7.4.3 Scandate Dispenser Cathode Activation

To complete the activation process for a dispenser cathode, it must be heated to a specific temperature range (1150-1200 °C) for several hours [4, 26, 27]. Typically, heating at 1200 °C for more than 4 hours is required to activate cathodes according to industry practice [26]. The activation procedure can sometimes be complex. Mantica [26] emphasized the importance of employing the correct activation schedule as it directly impacts the performance and lifespan of dispenser cathodes. In this study, heating

experiments were conducted with a temperature ramp ranging from 0.1 °C/s to 0.3 °C/s. The sample was maintained at 1200 °C for 1 hour. However, it was not feasible to extend the duration at 1200 °C due to damage to the silicon carbide (SiN) membrane of the E-chip caused by the high temperature and the reaction between SiN and tungsten at high temperature. This damage resulted in the formation of holes, rendering it impossible to continue holding the sample, thereby preventing full activation of the dispenser cathode fragment within the heating duration of the experiment.

Another possible reason that the cathode fragment was not able to be activated in this study is the high amount of free tungsten surface area that was not covered by impregnant phases. This reflects an insufficient amount of impregnant material and may indicate an inadequate ratio of impregnant to W surface area for the heated scandate cathode fragments, thereby preventing the W from forming surface facets. To activate a scandate cathode, it is necessary to have a sufficient amount of impregnant material; however, due to the use of small fragments in the current study, it was challenging to control the amount of impregnant (and ratio to W surface area). Scandate cathode activation is more complicated than simply heating the sample to a certain temperature and holding it there. Instead, it involves careful control of material environments, *e.g.*, infiltrating a molten impregnant into the porous tungsten-scandia body, which involves molten ceramic (impregnant) sweeping through the pores and over the W ligament surfaces, where they can react with nanoscale scandia and facilitate W mass transport to produce faceted tungsten [4, 114].

A third potential reason for the incomplete activation of the scandate cathode fragment could be a temperature disparity between the conventional cathode activation

apparatus and the *in situ* heating stage employed in the present study. Extensive investigations on scandate dispenser cathodes have been conducted by numerous researchers, including Liu et al. [3, 4, 21, 22, 142] and Vancil et al. [28, 160], etc. However, in all of these studies, temperature was measured and reported in terms of tungsten "brightness temperature", typically obtained using a disappearing filament optical pyrometer that continuously compares the hot specimen to a heated tungsten filament. For example, Vancil et al. [27, 160] and Liu et al. [3, 4] reported a knee temperature (representing the transition from temperature-limited electron emission to space-charge-limited emission) of ~800 °C$_b$, *i.e.*, using tungsten brightness temperature [27] to describe their cathodes. To achieve full activation of their dispenser cathodes, they heated in a high vacuum environment at ~1150 °C$_b$ (tungsten brightness temperature) [3, 27, 161]. Similarly, Wang et al. [162] and Busbaher et al. [163] reported the activation of their scandate cathodes at 1150 °C$_b$ (tungsten brightness temperature) for a duration of 2 hours. Additionally, most cathode activation studies report temperature in terms of tungsten brightness, including for other cathode types [164-168]. However, the difference between tungsten brightness temperature and true temperature is seldom addressed, with rare exceptions such as the study from Kordesch et al. [169] (although the equation in that particular publication may not be applicable to our current work).

The relationship between true temperature and the brightness temperature of tungsten has been studied since 1917 [170] and can generally be calculated using the equation proposed by Rutgers et al. [171]:

$$\frac{1}{S} - \frac{1}{T} = 1.0410 \times 10^{-4} \log\big(0.92 \times \varepsilon(\lambda, T)\big) \tag{1}$$

In equation (1), *S* represents the brightness temperature, *T* denotes the true temperature, ε signifies the emission of tungsten, and λ represents the wavelength of radiation [171]. Rutgers et al. [171] range of brightness temperature (*S*) values from 1000 to 3200 K, along with their corresponding true temperature (*T*) values. This approach yields an estimated true temperature of ~850 °C corresponding to a tungsten brightness temperature of 800 °C$_b$. Similarly, an estimated true temperature of ~1230 °C is equivalent to a tungsten brightness temperature of 1150 °C$_b$. Therefore, 850 °C and 1230 °C may be more accurate and relevant temperatures with respect to scandate cathode activation. The annealing temperatures used in the current study did not quite reach the corrected temperature of 1230 °C, *i.e.*, it is possible that the maximum temperature and/or annealing time were insufficient to induce the anticipated amount of W surface faceting. Overall, the (true) temperatures reported in the current study should be reduced by 50 to 80 °C to obtain brightness temperatures for comparison to the parameters used in industry.

Here, *in situ* heating experiments were conducted up to 1200 °C, as this represents the highest temperature attainable when using the E-chip. Achieving a longer duration, *e.g.*, 1 hour at 1200 °C, poses challenges for the Helios FIB-SEM. Long hold times resulted in the SE images becoming completely washed out, with no contrast or recognizable features. Only shorter duration holds were possible, *e.g.*, 22 minutes at 1200 °C (see **Figure 7**). Moreover, the E-chip is not designed to withstand prolonged heating periods. Thus, there remain challenges to be addressed in future research on *in situ* heating studies of scandate cathodes.

7.5   Conclusions

This chapter presents a targeted series of *in situ* heating experiments performed using MEMS-based heater chips in a scanning electron microscope (SEM) under high vacuum conditions (10^{-6} to 10^{-7} mbar). The experiments specifically focused on the behavior of impregnated but un-activated scandate cathode fragments, leading to insightful observations regarding the growth, faceting, and migration and phase separation characteristics of these impregnated materials at intermediate temperatures relevant to cathode processing.

- EDS analysis of faceted impregnant particles indicated they were predominantly composed of barium-containing oxides, with $BaAl_2O_4$ occurring frequently.

- As temperature was increased, impregnants exhibited phase separation and began to sublimate.

- Concurrently, nanoscale terraces emerged on tungsten surfaces, although the tungsten did not achieve a highly faceted morphology.

- As samples approached a temperature of 1200 °C, impregnant materials underwent rapid dissipation, most likely via sublimation.

The challenges encountered during these *in situ* heating experiments on MEMS heater chips were acknowledged and discussed, also pointing to opportunities for further investigation into the *in situ* heating behavior of scandate cathodes.

8.1   Introduction

Dispenser cathodes are extensively utilized as electron sources in vacuum electron devices (VEDs) across various fields, including medical, industrial, scientific research, and even military applications [2, 18, 19, 23, 118, 119, 123, 126, 146, 157]. These dispenser cathodes typically employ refractory metals, with tungsten being the common choice, to form a porous matrix, to which alkaline metal oxide(s) (usually $BaO-CaO-Al_2O_3$) are added as impregnant materials [2, 123, 146, 157]. Recently, in an effort to develop a cathode capable of producing higher current density at lower operational temperatures, scandate (Sc_2O_3) has been introduced as one of the impregnated materials in dispenser cathodes [1, 3, 4, 21, 22, 121, 142]. This modification, now referred to as the "scandate cathode," has exhibited significantly enhanced emission performance, with the current density surpassing 10 A/cm^2 even at temperatures below 1000 °C [27, 123, 146, 172-175]. The fabrication process of such a scandate cathode typically begins with scandia-doped tungsten powder, which is then pressed and sintered into a porous tungsten pellet. Subsequently, this pellet is impregnated with a mixture of $BaO-CaO-Al_2O_3$ and undergoes activation and emission property testing [3, 4].

Despite the remarkable current emission performance of the scandate-add dispenser cathode, it is burdened by several issues, including poor emission uniformity, inadequate reproducibility, and limited lifetimes [27, 123, 126], which have impeded its widespread industrial application. Extensive efforts and studies have been conducted to address these

139

issues and obtain a more comprehensive understanding of the scandate cathode [27, 29, 120, 146, 164, 174, 176].

Extensive investigations into scandate cathodes have thus far encompassed a wide range of aspects. Notably, Bugaris *et al.* [1] and Zhang *et al.* [121, 177] have undertaken thorough analyses of the original powder composition of scandate cathodes. In a similar vein, Vancil *et al.* [28] have examined the effects of powder doping processing on the performance characteristics of scandate cathodes. Moreover, Liu *et al.* [3, 4, 21, 126, 142, 178] have conducted surface characterization and near-surface cross-sectioning at various stages of scandate cathode development. More specifically, when comparing the near surface region of scandate cathode at different stages of processing, Liu *et al.* [178] found that the pore structure in the tungsten matrix were first filled with Sc_2O_3 powder during pressing and sintering process, and then were infiltrated by impregnate materials at the impregnating process. Besides, Liu *et al* [3] also reported that highly faceted W grains, covered with nanoparticles were consistently observed on activated scandate cathode surfaces, which provided insightful information of scandate cathode emission surface.

Additionally, Huang *et al.* [164] have investigated the influence of structural properties on emission characteristics [4, 120], while Seif *et al.* [70, 114, 147, 148] and Miller-Murthy *et al.* [179] have performed calculations to determine the surface energy of particles in relation to the emission properties of scandate cathodes. All of these investigations have shed light on the properties of the scandate cathode and have contributed to an improved understanding thereof. Powder chemical analysis reveals the components and their distribution in the powder before pressing and sintering, while surface characterization provides information on morphological changes before and after

activation. Near-surface cross-sectioning uncovers the activities of the emission layer's materials after activation. None of these techniques or studies can offer a comprehensive overview of the scandate cathode, encompassing the surface, near-surface, deep range, and bottom of the cathode with a single study of the same cathode.

This chapter presents a pioneering application of Broad Ion Beam (BIB) technique for achieving complete cross-sectioning, enabling a comprehensive examination of the entire structure of a scandate cathode, encompassing both the emitting surface and the bottom region. Within this study, full-length cross-sectioning was performed on scandate cathodes at various stages of production and activation, including: (1) the $W-Sc_2O_3$ pellet that was pressed and sintered with scandia-doped tungsten powder, (2) the impregnated yet inactive scandate cathode, (3) the activated and emission-tested cathode exhibiting satisfactory performance, and (4) the activated cathode with inadequate emission capabilities. Before the cross-sectioning, scanning electron microscope (SEM) and X-ray photoelectron spectroscopy (XPS) were performed on all the samples to investigate the cathodes surface micrograph and chemical elements. After cross-sectioning, scanning electron microscope (SEM) and X-ray Energy-Dispersive Spectroscopy (EDS) analyses were carried out to characterize the morphology of tungsten grains and the distribution of impregnated elements throughout the entire cross-section of a scandate cathode. Consequently, this systematic approach enables a series of investigations to evaluate the impregnant infill in scandate cathodes during their development. Furthermore, the comparison of cross-sectioning characterization between the 'good' and 'bad' cathodes facilitates a straightforward assessment of the underlying mechanisms at play within these cathode structures.

8.2   *Materials and Methods*

This study examines four samples provided by E Beam, Inc. (Beaverton, OR, USA). These include: 1) a tungsten pellet (2 mm in diameter and 1 mm in thickness) pressed and sintered with scandia-doped tungsten powder, 2) an impregnated but inactive scandate cathode, 3) an activated cathode with good emission performance, and 4) an activated cathode with poor emission performance (see **Table 8.1**). All four samples underwent processing using the same batch of scandia-doped tungsten powder (LL061821-SE4), enabling comparison of their material morphology. Additionally, samples #2, #3, and #4 underwent impregnation with a barium calcium aluminate mixture (6BaO-1CaO-2Al2O3), which melted and entered the pellet from the top (emitting surface side). Samples #3 and #4 were activated, though they were not subjected to long-term emission testing in a close-spaced diode (CSD) assembly. The activity curves of samples #3 and #4 are presented in **Figure 8.1**. Analysis of the emission curves in **Figure 8.1** reveals that sample #3 exhibits excellent emission performance with a knee temperature of 869 °C_b (brightness temperature, relative to tungsten), whereas sample #4 lacks a discernible knee temperature, indicating poor performance as a scandate cathode.

Table 8.1 List of scandate dispenser cathodes states

Sample No.	Status before full-length cross sectioning
#1	W+Sc pellet
#2	impregnated but inactivated scandate cathode
#3	activated and emission-tested 'good' cathode
#4	activated but emission-tested 'bad' cathode
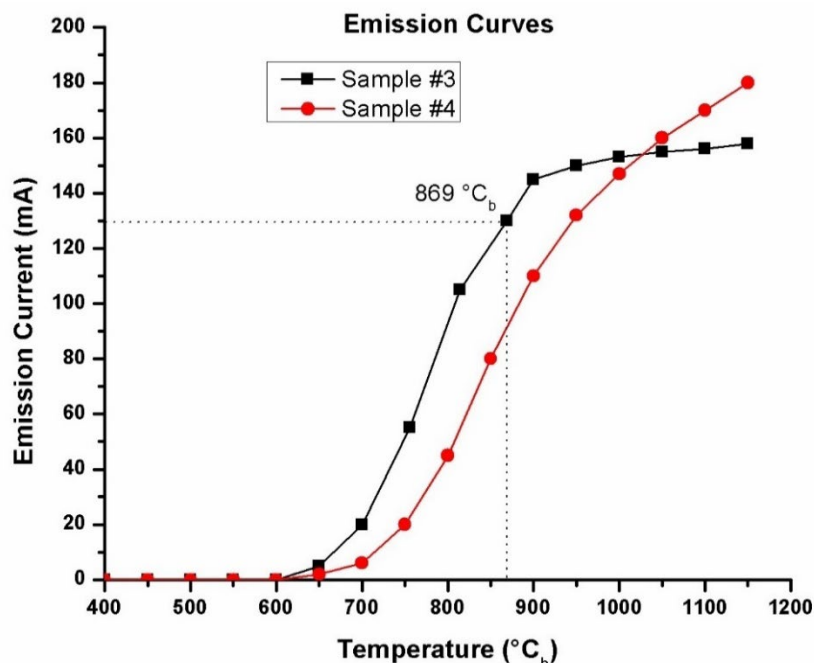
Figure 8.1. Activity curves for samples #3 and #4. Black square represents data points recorded from sample #3, red dots represent data points recorded from sample #4.

These samples were characterized using focused ion beam and scanning electron microscopy (FIB-SEM, FEI Helios G3 dual-beam system, Hillsboro, OR, USA), and X-ray photoelectron spectroscopy (XPS, Thermo Scientific K-Alpha, Madison, WI, USA) to examine their original top/emission surfaces.

After surface characterization the samples were placed into a nitrogen filled glove box and manually fractured (roughly in half) to produce a cross-section. The cross-sections with then mounted onto a silicon wafer using copper tape inside the glove box and placed inside an isolation stage before transfer to the Cooling Cross-Section Polisher (JEOL IB-19520 CCP cryo cross-section polisher), as depicted in **Figure 8.2**. During cross-sectioning, 8 kV argon ions were used to mill the cathode cross-section while it was cooled with liquid nitrogen in a vacuum environment. To minimize curtaining and achieve a smooth cross-section finish, a shielding plate and sample stage swing were employed. It is

noted that Millimeter-scale cross-sections do not involve mechanical grinding or chemical polishing. Upon completion of the cross-sectioning, SEM imaging (FIB-SEM, FEI Helios G3 dual-beam system, Hillsboro, OR, USA) and EDS mapping and line scanning (Oxford Instruments X-Max 80 mm^2 detector, Concord, MA, USA) were performed across the entire pellet thickness.
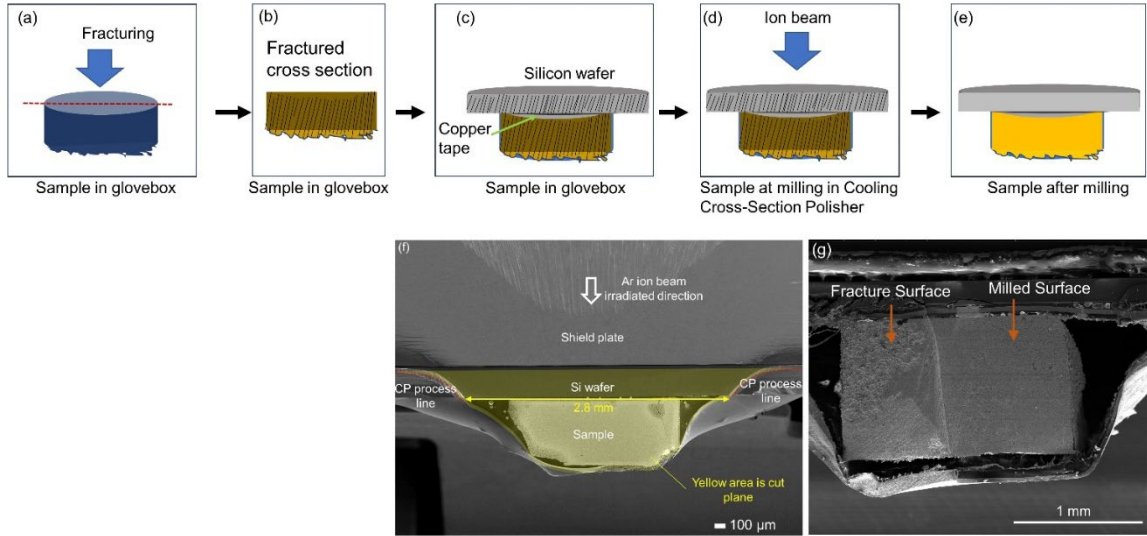
Figure 8.2 Schematic procedure of full-length cross sectioning: (a) fracturing sample in glovebox manually, (b) fractured cross section has a rough surface, (c) attached the fractured cross section to a silicon wafer with a copper tape, (d) ion beam cutting and (e) sample after cutting; SEM image of (f) sample in cross section polisher with and (g) sample after cutting with a comparison between facture surface and Milled surface.

8.3   Results and Analysis

Secondary electron (SE) images of the surface of all the samples listed in **Table 8.1** are displayed in **Figure 8.3**. Images in **Figure 8.3**(a1-d1) provide an overview of the surface of these samples at low magnification where differences are hardly discernible. However, upon closer inspection, it becomes evident that sample #1 (sintered W-Sc pellet) consists of micro-scale grains (tungsten particles) and nano-size particles (supposed to be scandate), as shown in **Figure 8.3** (a2-a3). In contrast, **Figure 8.3** (b2-b3) illustrates the

micrograph of sample #2, the impregnated but inactivated cathode. Compared with **Figure 8.3** (a2-a3), it is clear that tungsten grains in **Figure 8.3** (b2-b3) are covered in areas by a darker material, assumed to be impregnant materials, which also fills the pores between the tungsten grains. Furthermore, **Figure 8.3** (c2-c3) presents the surface images of sample #3, an activated cathode with good emission performance, which exhibits a limited number of coarse ($\geq$100 nm diameter) mixed oxide surface particles and fine nanoscale (10-20 nm diameter) particles decorating the highly faceted tungsten facets, consistent with the findings of Liu et al [3, 4, 21, 126, 142]. Lastly, **Figure 8.3** (d2-d3) displays the surface images of sample #4, another activated cathode but with poor emission performance. While the tungsten particles are also highly faceted, it appears to have significantly more of the coarse oxide particles and a lack of fine nanoscale particles on the tungsten facets.
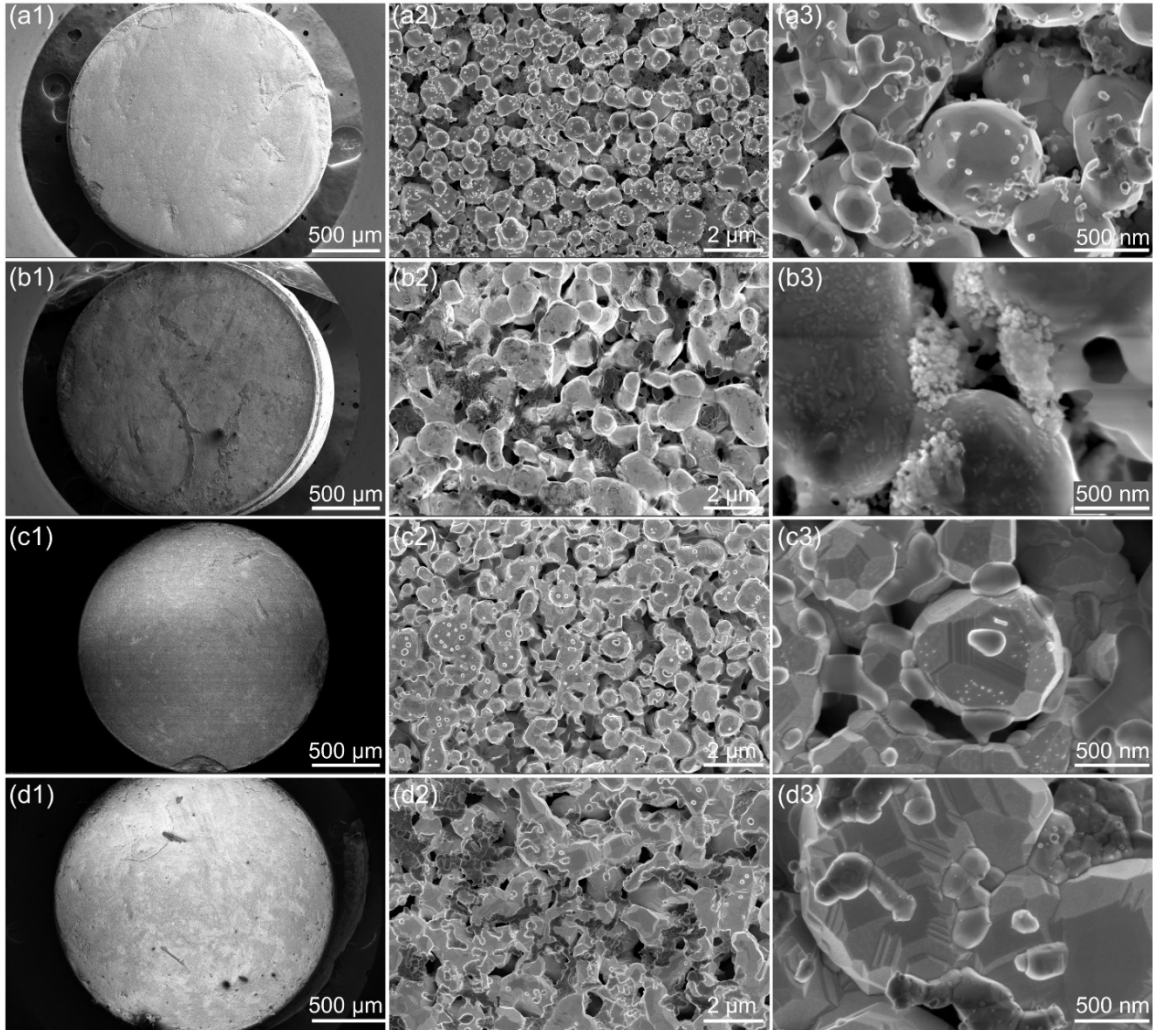
Figure 8.3 SEM micrograph of the samples' surface before cross-sectioning: (a1), (b1), (c1) and (d1) are overview of sample #1, sample #2, sample #3 and sample #4, respectively; (a2-a3), (b2-b3), (c2-c3), (d2-d3) are zoomed in images of sample #1, sample #2, sample #3 and sample #4, correspondingly.

A summary of the XPS measurements conducted on samples #1-#4 is shown in **Table 8.2**. For sample #1, which is simply a pellet sintered from scandia-doped tungsten powder, only signals for W, Sc, and O were detected. In sample #2, XPS results revealed the presence of Al, Ba, and Ca, as expected due to the impregnates (BaO-CaO-Al$_2$O$_3$). Comparing sample #2 with sample #1, there is a noticeable decrease in Sc detected on the surface, dropping from 7.8 at. % in the sintered pellet to a level smaller than 0.1 at. % in

the impregnated pellet. This value then roughly averages out to 2.0 at. % for the activated

cathodes (samples #3 and #4). Similarly, the amount of W detected by XPS followed the

same trend for all four samples. It was 34.5 at. % for the sintered pellet, reduced to 1.1 at.

% for the impregnated pellet, and then increased to 13.1 at. % and 18.2 at. % for sample

#3 and sample #4, respectively, after activation.

One possible explanation is that there may still be Sc on the surface of the

impregnated cathode, but it could be "covered up" by impregnate material. This impregnate

material could then be reduced by the activation process, once again exposing the Sc on

the surface. Regarding the two activated cathodes, XPS detected a significant amount of

Al and Ba, but the amount of Ca was so limited that it was challenging to detect it by XPS.

Furthermore, despite differences in their emission performance, it's difficult to discern

much variation through XPS. However, it is observed that the amount of Ca is relatively

moderate, making it challenging to detect even by XPS.

Table 8.2 Summary of XPS measurements on the samples' surface before cross-sectioning.

Element (at. %)	Sample #1	Sample #2	Sample #3	Sample #4
Al	<0.1	14.2	24.3	22.7
Ba	<0.1	9.6	10.0	9.3
Ca	<0.1	7.5	<0.1	<0.1
O	53.5	67.6	49.3	47.1
Sc	12.1	<0.1	3.3	2.7
W	34.5	1.1	13.1	18.2
Sum	100.0	100.0	100.0	100.0

Secondary electron SEM images of the full-length cross-sections of all samples are

presented in **Figure 8.4**. It was observed that both sample #1 (the sintered pellet) and

sample #2 (the impregnated inactivated cathode) exhibit uniform cross-sections, as

illustrated by the representative SEM images in **Figure 8.4** (a2, b2). In contrast, the full-

length cross-section images of sample #3 and #4 reveal that activated cathodes feature a denuded zone with open porosity in the ~10 μm layer immediately beneath the emitting surface., as seen in **Figure 8.4** (c2, d2). Notably, the emission layer of sample #3 (an activated cathode with good emission performance) appears uniform, as depicted in **Figure 8.4** (c2), whereas the emitting surface of sample #4 (an activated cathode with poor emission performance) displays a non-uniform structure, with some regions showing less pore structure and others showing more pore structure, as indicated by A and B in **Figure 8.4** (d2). However, no significant differences were observed between sample #3 and #4 regarding the morphology of tungsten grains and impregnates, as shown in **Figure 8.4** (c3-d3). Additionally, no irregularities were noted in the central or bottom regions of sample #4.
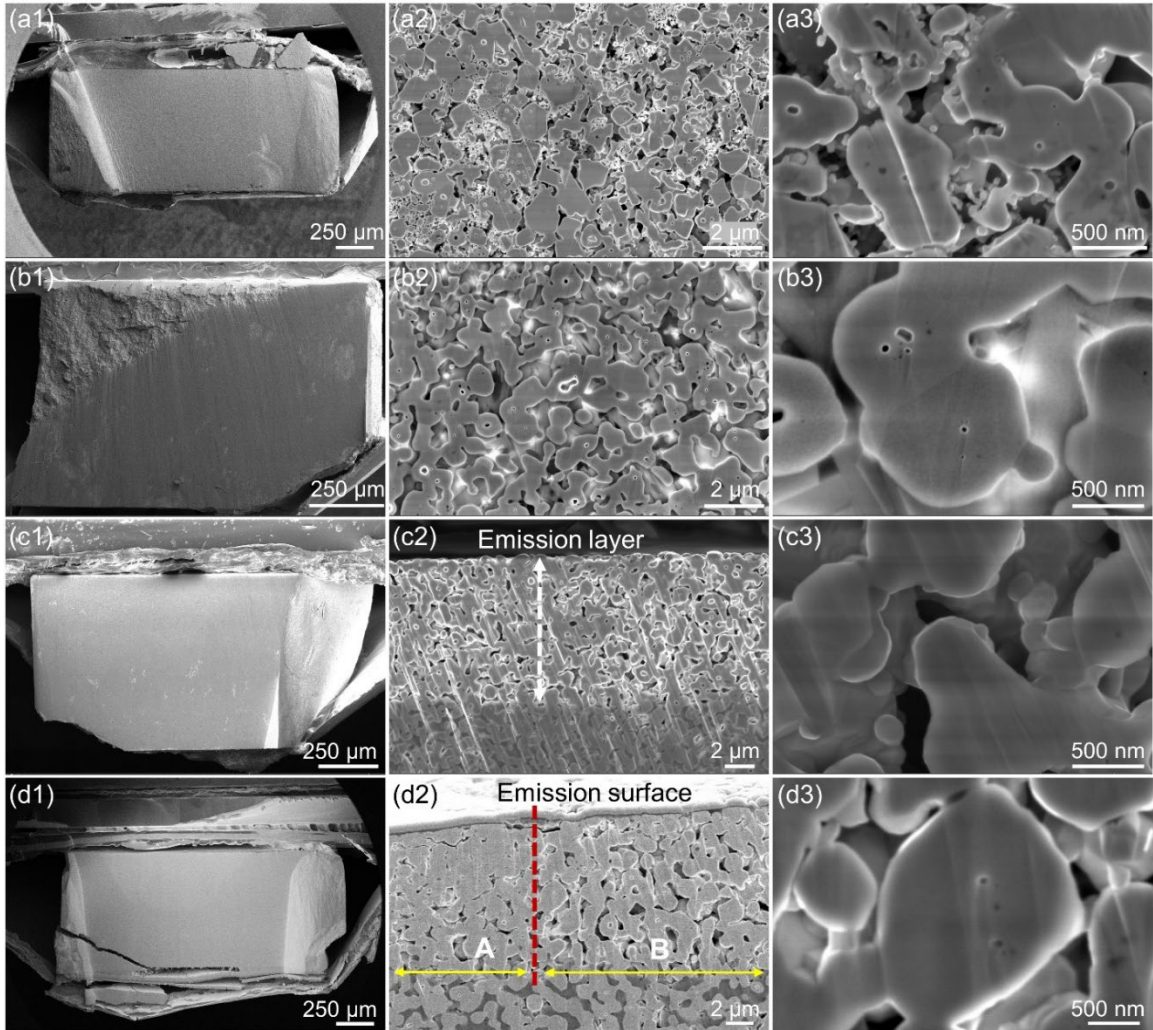
Figure 8.4. SEM images of the cross-section of each sample: (a1-d1) are low magnification images showing the cross-section of sample #1, #2, #3, and #4, respectively; (a2-b2) are zoomed in images of the regions shown in (a1-b1), respectively, showing the representative images of the cross-section of sample #1 and #2; (c2-d2) are the near surface area images of the cross-section of sample #3 and #4; (a3-b3) are higher-magnification images of regions in (a2-b2); (c3-d3) are higher magnification images of the near surface area (emission layer) of sample #3 and #4.

The full length cross-section of sample #1, the sintered W-Sc pellet, is shown in **Figure 8.5**. The region marked by the box in **Figure 8.5**a was designated for both EDS mapping and line scan. EDS mapping results in **Figures 8.5** b-e reveal that the cross-section of sample #1 features an even structure with no detectable large aggregates of

scandia at this level. Meanwhile, the findings of the EDS line scan in **Figure 8.5**f suggest that elements W, Sc, and O exhibit a homogeneous distribution throughout the pellet thickness, except at the pellet top and bottom where oxygen is seen to increase significantly, likely due to sample mounting and processing with adhesives. It is important to note that carbon was excluded from the EDS mapping and line scan to emphasize the more pertinent elements.
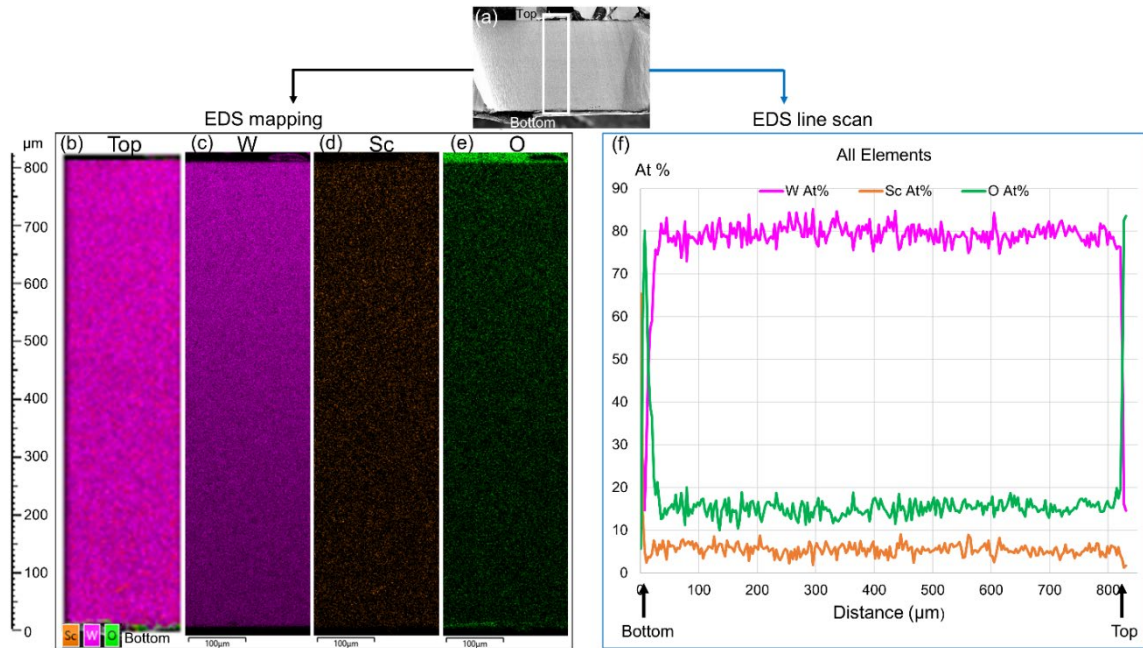
Figure 8.5 EDS analysis of the cross-section of sample #1: (a) general view of the cross-section of sample 1 with the region for EDS mapping and line scan, (b) composite EDS elemental map, (c) tungsten (W), (d) scandium (Sc), (e) oxygen (O), (f) elementals line scan.

EDS analysis of sample #2, impregnated cathode studied prior to activation, is shown in **Figure 8.6**. In **Figure 8.6**a, an electron image highlights the EDS analyzed region, marked by a white box, while **Figure 8.6**b overlays compositional distribution onto the electron image of the selected region. Additionally, **Figures 8.6**c-h display the distribution of W, Sc, Ba, Ca, Al, and O along the cross-section, with higher magnifications

150

of EDS mapping at the top region shown in **Figures 8.6**c1-h1, respectively. The distribution of elements W, Ba, Ca, and Al appears generally homogeneous from the top to the bottom of the cathode, as depicted in **Figures 8.6**c, e, g, and i. However, the distribution of Sc and O shows relative unevenness when comparing the top and bottom portions. There appears to be a "hole" in the impregnant phase distribution at lower left of EDS maps (e1) Ba, (g1) Al, and (h1) O; however, there is no "hole" in the W or Sc maps (c1, d1). It is noted that there does not appear to be a denuded (open - porosity) layer near either surface of the cathode at this stage of processing.

Notably, **Figure 8.6**d indicates a higher Sc signal detected at the bottom (~100 μm from the bottom end) compared to the top of the cathode. Similarly, more O signal is detected at the top half (~350 μm from the top end) of the cathode, as observed in **Figures 8.6**h and i. (It is worth noting that O was excluded from the line scan in **Figure 8.6**i to emphasize the relevant elements.) The uneven distribution of Sc and O is likely attributable to the manufacturing process of the cathode. In this process, scandate cathodes were fabricated by die-pressing and sintering scandia-doped tungsten powder into a porous pellet, followed by infusing molten materials ($BaO-CaO-Al_2O_3$) into the porous body [4, 28, 172, 180, 181] and subsequent washing with deionized water to remove excess impregnated materials [4]. One possible explanation for this result is that the process of impregnation results in scandate, which is on a nano scale, being melted into the $BaO-CaO-Al_2O_3$ mixture and flowing downwards to the bottom of the pellet as the impregnant mixture penetrates the pore structure of the cathode, resulting in an uneven distribution of scandia through the cathode thickness as illustrated in **Figure 8.6**d and h. It is seen that

there is an apparent tradeoff between Ba and Sc content through the thickness of the impregnated pellet, as indicated by **Figure 8.6**i.
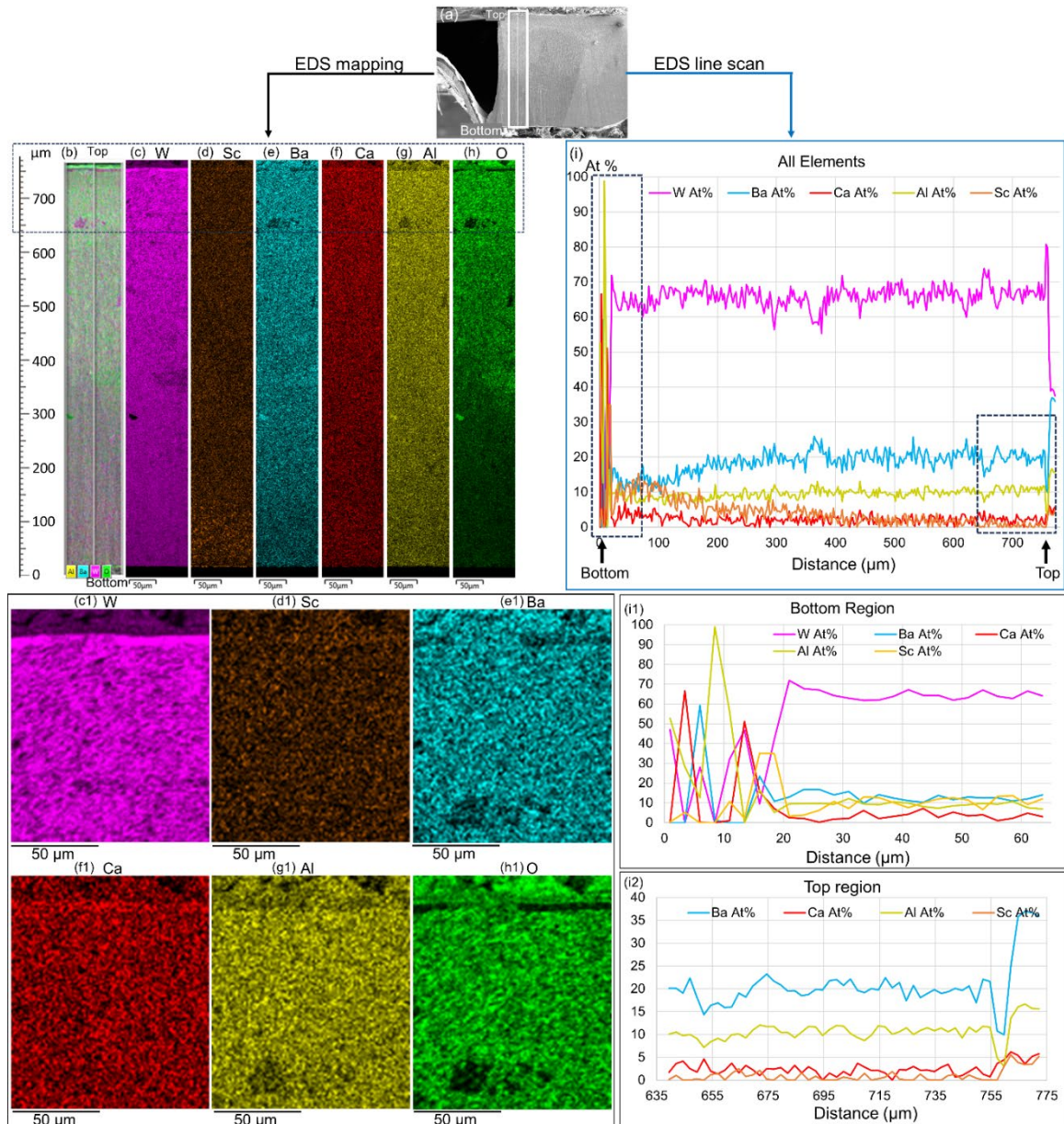
Figure 8.6 EDS analysis of the cross-section of sample #2: (a) general view of the cross-section of sample #2 with the region for EDS mapping and line scan, elemental maps for (b) EDS elemental distribution overlapped with electron image; (c) tungsten, (d) scandium, (e) barium, (f) calcium, (g) aluminum, (h)oxygen, and their top regions were zoomed in and displayed in (c1), (d1), (e1), (f1), (g1), and (h1) respectively; (i) elementals line scan with its zoomed-in bottom region and top region showing in (i1) and (i2), separately.

After pressing, sintering and impregnation of the porous matrix with impregnant material, the final step in cathode fabrication is activation. **Figure 8.7** displays EDS elemental mapping and line scans of the full-length cross-section of sample #3, representing an activated scandate cathode with good emission performance. In **Figure 8.7a**, an overview of the cross-section is provided, with a white box marking the selected area for EDS analysis. **Figure 8.7b** presents elemental distribution mapping overlaid on an electron image. The distribution of the W signal, as detected in **Figure 8.7**c, suggests consistent W content throughout the thickness of the cathode. Conversely, the distribution of the Sc signal in **Figure 8.7**d indicates relatively higher Sc concentration at the cathode's bottom, while other elements such as Ba, Ca, Al, and O exhibit varying levels throughout the thickness (**Figure 8.77**e-h). Higher magnification EDS mapping of the top region is depicted in **Figure 8.7**c1-h1, revealing that region near emitting surface has uniform W levels but a thin (~10 µm) layer with decreased levels of impregnates and Sc. Additionally, the EDS line scan in **Figure 8.7**i provides a clear overview of element distribution along the cathode's thickness. **Figure 8.7**j, presenting W-normalized composition against a constant W level, offers a clearer understanding of element richness or scarcity in the impregnant-depleted zone and at the cathode's bottom. It's evident that impregnant materials in the near-surface region have largely disappeared, with relatively low Sc content, consistent with the findings in **Figure 8.7**c1-h1. Meanwhile, the cathode's bottom region exhibits relatively higher Sc and Ca content and lower Ba content. Overall, the results in **Figure 8.7** depict the distribution of impregnations in a scandate cathode post-activation.
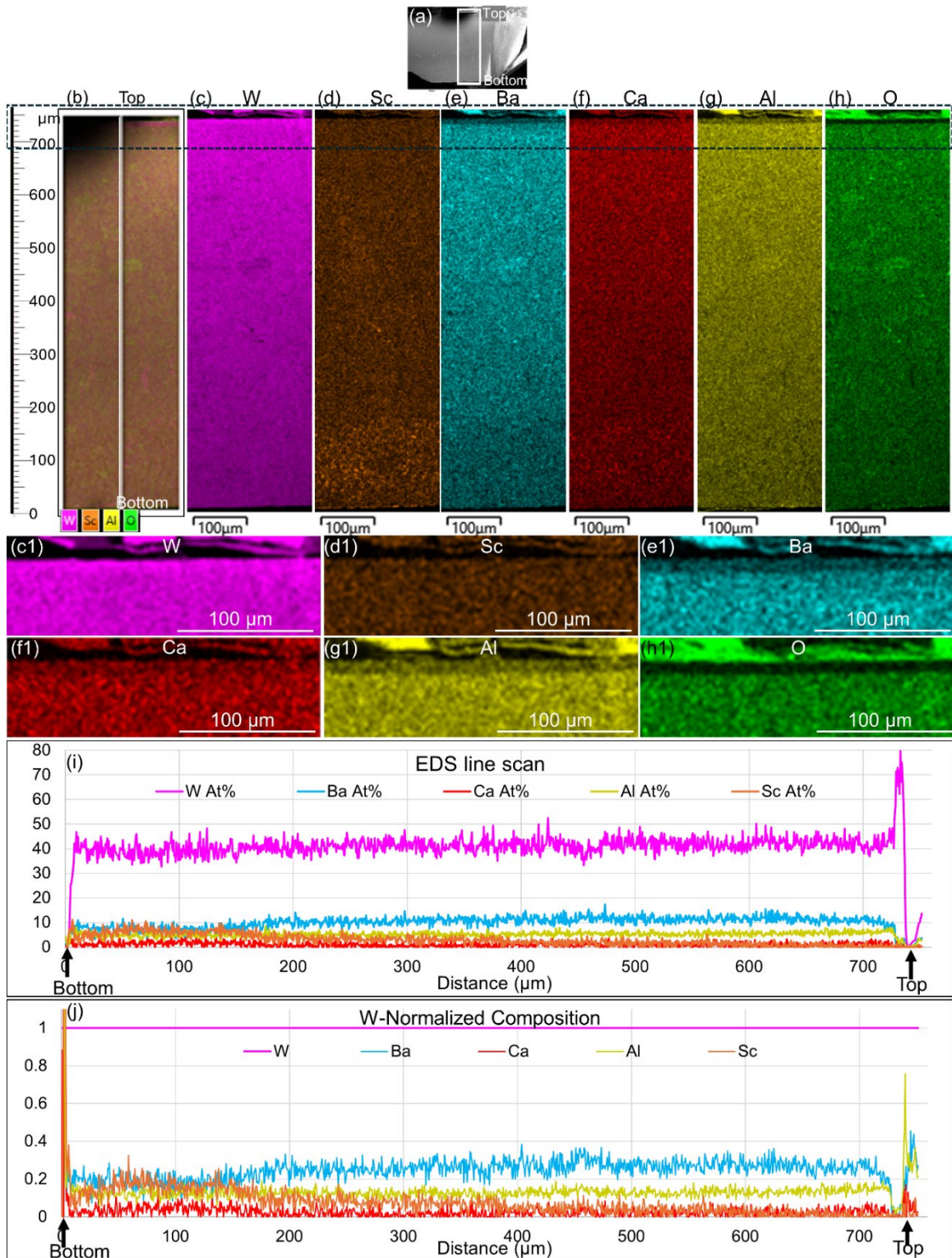
Figure 8.7 EDS analysis on the cross-section of sample #3: (a) general view of the cross-section of sample #3 with the region for EDS mapping and line scan, elemental maps for (b) EDS elemental distribution overlapped with electron image; (c) tungsten, (d) scandium, (e) barium, (f) calcium, (g) aluminum, (h)oxygen, (i) elementals line scan and (j) Normalizing composition (versus a constant W level).

Large-area SEM imaging and EDS mapping of cross-section of sample #3 (activated and tested "good" scandate cathode) is presented in **Figure 8.8**. In **Figure 8.8**a, a high-resolution secondary electron (SE) image reveals the emission layer atop the region, displaying higher porosity compared to the layer below. **Figure 8.8**b presents a backscattered electron image (BSE) of **Figure 8.8**a, with a darker grey level indicating a depletion of impregnates in the top emission layer and a higher concentration below. **Figure 8.8**c overlays a composite elemental map onto the SE image, illustrating that the top region (emission layer) consists primarily of tungsten, while impregnates (Sc/Ba/Ca/Al) remain in the matrix below. Furthermore, an EDS line scan depicted in **Figure 8.8**d reveals that the top region is rich in tungsten (over 70 at%), with low relative content of impregnated materials (< 5 at% for each element), which significantly increases in the region below. Examining the distribution of matrix tungsten and impregnated materials (Sc, Ba, Ca, Al, and O) in **Figures 8.8**e-j confirms the absence of impregnates on the emission surface (top region), while the region below is abundant in impregnates. Notably, **Figures 8.8**f and 8h provide a clear indication of the distribution tendency of Ca and Sc compared to the EDS line scan in **Figure 8.8**d. Overall, the porous tungsten matrix and impregnant fill are distributed rather uniformly throughout the pellet of this "good" scandate cathode.
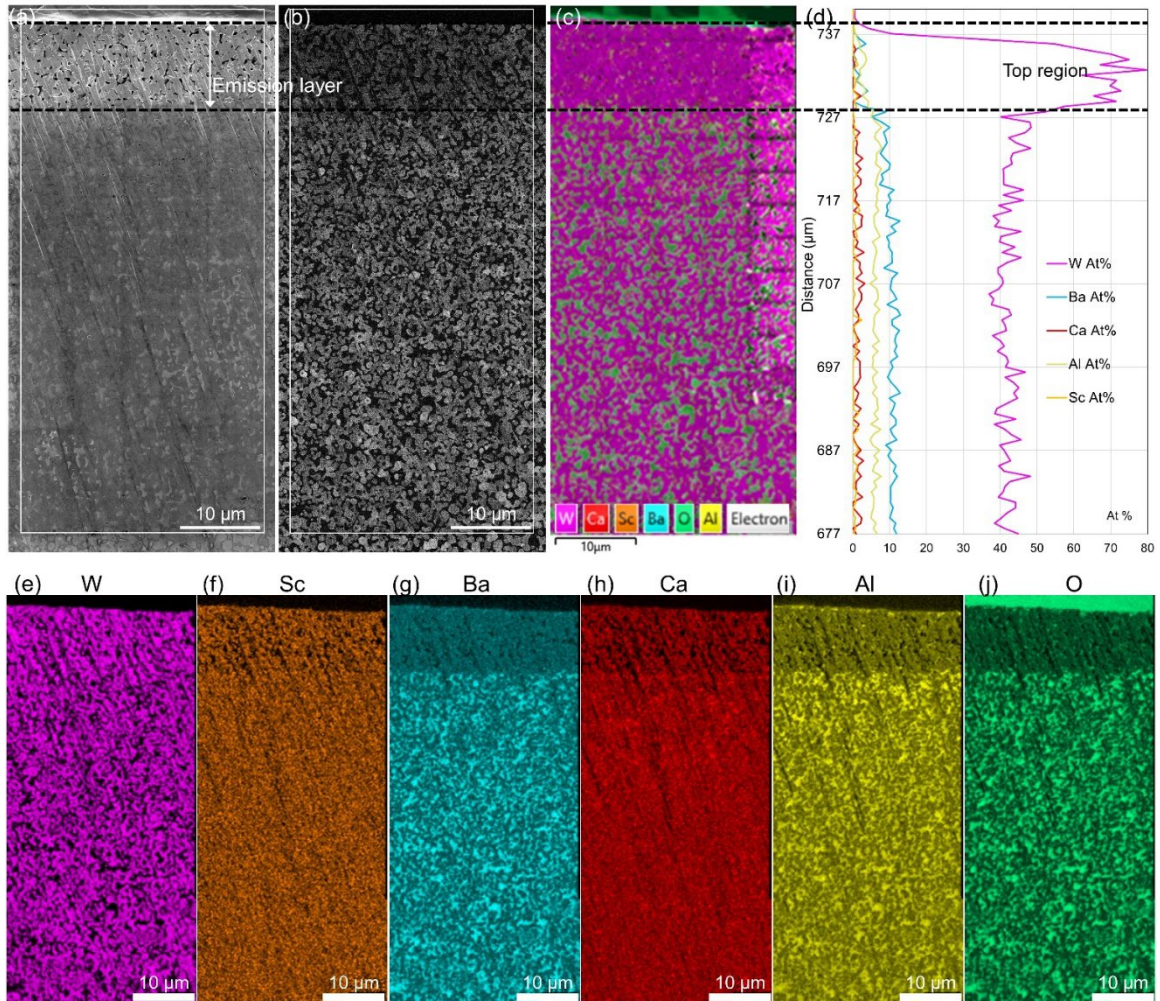
Figure 8.8 High resolution large area SEM images and EDS analysis of the cross section of sample #3: the top region (the emission surface). (a) a high-resolution large area SE image, (b) BSE image of (a), (c) composite elemental map (on SE image) showing all elements; (d) EDS line scan showing content of each element, and (e-j) are individual elemental distribution maps of tungsten, scandium, barium, calcium, aluminum, and oxygen, respectively.

Large-area SEM imaging and EDS mapping of cross-section of sample #4 (activated and tested "bad" scandate cathode) are shown in **Figure 8.9**. In **Figure 8.9**a, the SE image reveals that the top region, serving as the emission surface, has a higher degree of openness and porosity compared to the underlying area. Overlaying the composite elemental map onto the SE image in **Figure 8.9**b highlights the tungsten-richness of the

top region, while the area beneath the emission surface contains a higher concentration of impregnated materials (Sc/Ba/Ca/Al). Examining the distribution of tungsten in **Figure 8.9**c indicates that the top layer of tungsten is denser and less porous than the region below. Similarly, the distribution maps of Sc, Ba, Ca, Al, and O in **Figures 8.9**d-h suggest that these impregnated materials are predominantly present in the region beneath the emission layer. Additionally, it's evident that the emission layer is not uniform; certain regions exhibit higher density and less porosity while others show the opposite characteristics. The regions with a more porous structure within the emission layer are denoted by white boxes in **Figures 8.9**a-h, with corresponding images/maps presented in **Figures 8.9**a1-h1. A comparison with the activated 'good' cathode in **Figure 8.9** reveals that a 'good' activated cathode typically features a uniform emission layer with tungsten exhibiting a more porous structure, as also observed in **Figure 8.4** (c2, d2).
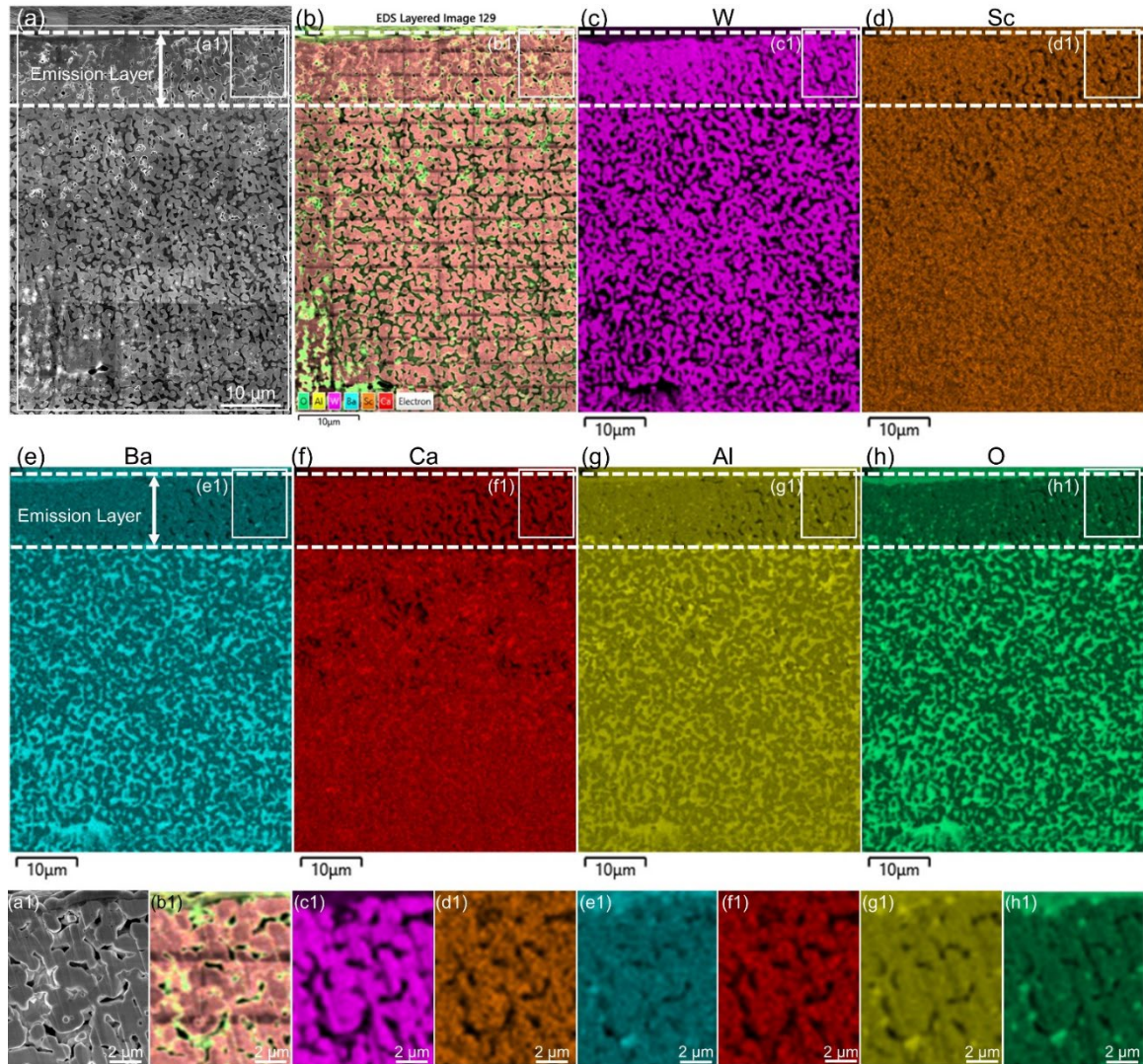
Figure 8.9 High resolution large area SEM image and EDS mapping of cross-section of sample #4: the top region (the emission surface). (a) a large area high resolution SE image, (b) composite elemental map (on SE image) showing all elements; (c-h) individual elemental distribution maps of tungsten, scandium, barium, calcium, aluminum, and oxygen, separately; (a1-h1) are zoomed in images of selected area marked with white box in (a-h) showing the opened porous structure.

8.4   Discussion

8.4.1   Process of Fabricating an Impregnated Scandate Cathode

Full-length cross-sectioning was conducted on various stages of the scandate dispenser cathodes, including sintering, impregnation, and activation, which are the typical steps in fabricating an impregnated scandate cathode. Traditionally, fabricating an

impregnated scandate cathode involves two essential steps [4, 176]. Firstly, scandia-doped tungsten precursor powder is die-pressed and then sintered into a porous tungsten pellet under a certain atmosphere at high temperatures [182, 183]. Two common techniques for making the scandia-doped tungsten precursor powder are the liquid-solid (L-S) and liquid-liquid (L-L) doping methods [4, 126, 162, 184]. In this study, all samples were made using the L-L doping technique, as it ensures a more uniform distribution of scandia within the powder [4, 28, 151]. Sample #1 represents a sintered scandia porous tungsten pellet, marking the completion of the first step. The Energy Dispersive X-ray Spectroscopy (EDS) results of sample #1 in **Figure 8.5** confirm the uniform distribution of scandia powder in the pellet after this initial step.

The second step involves melting an alkali mixture of $BaO-Al_2O_3-CaO$ powder on top of the tungsten-scandia doped pellet, allowing the molten mixture to penetrate and diffuse into the porous pellet body, followed by washing away excess impregnates on the top with deionized water [4]. Previously, the only way to evaluate this step was to observe its topography and assess its uniformity. However, full-length cross-sectioning now provides an effective means to evaluate the properties of this step more comprehensively. Sample #2 represents an impregnated but inactive scandate cathode, indicating completion of the second step. Nevertheless, EDS analysis of sample #2 in **Figure 8.6** reveals that a significant amount of scandia was pushed by the molten $BaO-Al_2O_3-CaO$ powder to the bottom of the cathode, resulting in an accumulation of Sc/Sc_2O_3. Similarly, accumulations of Sc/Sc_2O_3 were also observed in at the pellet bottom of samples #3 and #4. However, sample #3 resulted in an activated cathode with good emission performance, whereas sample #4 exhibited poor emission performance during activation. Despite of that, there is

no sufficient evidence whether the accumulations of Sc/Sc$_2$O$_3$ at the pellet bottom affects the emission performance and life of a scandate dispenser cathode.

8.4.2   Activating an Impregnated Scandate Cathode

Prior to conducting emission testing in close-spaced diode (CSD) devices, impregnated scandate cathodes must undergo activation in a high vacuum environment at temperatures around 1150 °C$_b$ (tungsten brightness temperature) for several thousand hours [3, 4, 21, 27]. In this study, both Sample #3 and Sample #4 underwent this activation process before materials characterization. During activation, materials at the cathode's top region are evaporated, resulting in an emission layer with an open porous structure and fewer impregnated materials in the pores [30]. Recent research by Liu et al. [142] and Balk et al. [125] has shown that a thin layer of Sc-Ba-O forms on the tungsten grain's outermost layer, consistent with findings by Yamamoto et al. [185-187]. Successfully activated tungsten grains exhibit high faceting, as depicted in Figure 2 (c2-c3). Additionally, previous work by the authors demonstrated that impregnated materials also undergo faceting at intermediate temperatures during activation [172]. Liu et al [4] noted that impregnates and scandium migrate to the emission surface during the dispenser cathode's operation at high temperatures as materials at the top region are evaporated.

There are significant differences between well-performing activated scandate cathodes (Sample #3) and poorly performing ones (Sample #4). These differences include the topography of the emission surface, composite distribution along the cross-section, and tungsten gain densification at the emission layer. A well-performing activated scandate cathode typically exhibits highly faceted micron-scale tungsten grains decorated with impregnates ranging from hundreds to a few nanometers. Moreover, nanoscale Sc$_2$O$_3$ dots

cover the tungsten grain faces, as depicted in **Figure 8.3** (c3). Additionally, the emission surface of such a cathode usually has a porous structure with impregnates (BaO-CaO-Al_2O_3) uniformly distributed along the entire length of the dispenser cathode, as illustrated in **Figures 8.7** and 8.**8**. In contrast, a poorly performing activated scandate cathode, like Sample #4, lacks these characteristics. Instead, irregularly shaped tungsten grains and aggregated impregnates form sub-micro or even micro-scale clusters, as observed in **Figure 8.3** (d2 and d3). Furthermore, there is a deficiency of nanoscale Sc_2O_3 dots on the tungsten grain faces, and the emission surface of the poorly performing cathode is non-uniform, with the tungsten powder at the emission layer exhibiting higher density and lower porosity, as evident from region 'A' in **Figure 8.4** (d2).

8.4.3   Reasons for Poor Emission Performance

Identifying the inherent reasons for Sample #4's poor emission performance is challenging. As mentioned earlier, when comparing samples #3 and #4, it appears that the accumulation of Sc/ Sc_2O_3 at the bottom of the pellet does not necessarily impact activation results or emission performance. One potential explanation is that original powder prior to die-pressing and sintering is not uniform as Liu [4] mentioned that it is difficult to control and predict tungsten particle size when applying liquid-liquid (L-L) doping methods to make W-Sc_2O_3 powder. On the other hand, another alternative explanation is that the densification of tungsten powder in the emission layer of the cathode pellet could be a factor contributing to the failure of sample #4. Selcuk et al. [182, 183, 188-190] conducted research on porous tungsten pellets for dispenser cathodes and concluded that porosity and its distribution are crucial properties. Pores in a dispenser cathode pellet act as channels [183, 188] for impregnated materials to migrate or feed into surface pores during high-

temperature operation. Therefore, all pores must be open and form a pore-particle interlinked structure [189, 190], and more importantly, they should be uniformly distributed. It is evident that the pores on the emission surface of sample #4 are not uniform, and some are closed. Furthermore, Selcuk et al. [182, 183, 188-190] found that the die-pressing and sintering step is pivotal in determining the porosity and its distribution along the tungsten pellet as this step was proceeded at a very high temperature. Therefore, it is possible that the die-pressing and sintering process did not proceed flawlessly for sample #4, leading to affected pores and ultimately resulting in poor emission performance.

8.5   Conclusion

In this study, cathode materials at various processing stages—from the powder stage through die-pressing and sintering, impregnation, and activation—were examined using characterization techniques including XPS, SEM, and EDS with full pellet cross-sectioning. It has been demonstrated that broad ion beam (BIB) milling represents a valuable new specimen preparation technique enabling the characterization of the entire cathode pellet without introducing artifacts that could complicate result interpretation. Previous traditional specimen preparation techniques facilitate the characterization of surface and near-surface regions but cannot access deeper sample regions.

The application of broad ion beam (BIB) milling to scandate cathodes suggests a systematic series of evaluations to assess impregnant infill of scandate cathodes. It was observed that Sc_2O_3 is abundant at the bottom of all impregnated dispenser cathodes in this work. And a well performance scandate dispenser cathode has a uniform open pore emission surface, but a poor performance cathode has non-uniform pores with closed pores at the emission surface instead. This discovery offers cathode manufacturers a more

comprehensive understanding of cathodes, revealing both global and local distributions of materials and phases. This achievement will inform manufacturing processes for high-performance cathodes, enhancing understanding of materials and microstructure of high-brightness electron emitters, and supporting demonstrator efforts. Moreover, it will enable the design and fabrication of new materials for high current density thermionic emission.

9.1 *Summary and Conclusions*

This section concludes the presentation of the majority of the work that has been done during this PhD project. This dissertation began with an introduction of the phenomenon and concept of *thermionic emission*, its mechanism and its critical component '*cathode*', and then moved to the historical development of various dispenser cathodes, with emphasis on impregnated dispenser cathodes. Moreover, thin film deposition and physical vapor deposition were introduced in the opening chapter. Then it was followed by a comprehensive overview of a custom-made equipment – "nanoparticle generator", which was lent from Ohio University. Lots of development work was done on the nanoparticle generator to improve and optimize the system, which resulted in new capabilities of fabricating nano particles with uniform particle size and distribution.

The base material of scandate dispenser cathodes, which is tungsten, was the key subject of this research. Both nano scale tungsten and bulk tungsten were studied regarding their surface faceting under high temperature.

9.1.1 Nano scale W particles faceting

In this work, tungsten nanoparticles were fabricated utilizing physical vapor deposition and deposited on sapphire (α-Al$_2$O$_3$) substrates with nanoparticle generator. The particles generated using this procedure were found to form a network with a continuous nanoporous structure. To study the influence of temperature and pressure on the stability and morphology of tungsten nanoparticles, a multitude of varying pre-heating steps were applied to these nanoscale tungsten particles in a vacuum chamber. The morphology and structure of the annealed tungsten particles were investigated by a series of materials

characterization techniques including scanning electron microscopy, X-ray energy dispersive spectroscopy and X-ray photoelectron spectroscopy. It is found that:

- The tungsten nanoparticles grew into nonuniform islands when annealed directly at 1100 °C, under a pressure of 10^{-7} Torr.

- Conversely, the deposited tungsten network transformed into individual, highly faceted nanoparticles when first pre-heated at an intermediate temperature, followed by annealing at 1100 °C, under a pressure of 10^{-7} Torr.

- Wulff analysis indicated that these well-developed tungsten particles exhibit {110} crystallographic facets.

9.1.2 Bulk W surface faceting

Furthermore, surface faceting of tungsten pellets was studied during *in situ* heating inside an environmental scanning electron microscope (ESEM), which allowed for direct, high-fidelity observation of morphological changes in response to high-temperature annealing under a moderate vacuum (0.8 Torr). Additionally, a second set of tungsten samples was annealed in an ultra-high vacuum chamber (10^{-8} Torr), albeit without direct observation via ESEM.

This study revealed that oxygen plays a crucial role in tungsten surface faceting and in a morphological transition to vertex rounding. Furthermore, this chapter discusses relevant techniques for identifying the crystallographic indices of surface facets. It is demonstrated that a combination of electron backscatter diffraction, tilted-sample imaging from multiple angles, and serial sectioning in a focused ion beam system can be effectively deployed to determine the geometry of faceting, which in turn can be verified with the aid

of software for generating Wulff shapes. The influence of processing environment on tungsten surface faceting enables the possibility of designing and controlling the morphology and crystallographic facets of tungsten surfaces.

- ESEM annealing on W at 0.8 Torr resulted in oxide sublimation and surface faceting.

- The surfaces of samples annealed under UHV remained flat and smooth.

- Temperature and grain orientation influence the size of bulk W surface faceting.

- SEM tilted-sample imaging and serial sectioning tomography were applied for facet index.

- Wulffmaker was used for the relative surface energies of low-index facets.

9.1.3 *In situ* observations of scandate dispenser cathode

On the other hand, a series of *in situ* heating experiments was conducted on un-activated impregnated scandate fragments by using a micro-electro-mechanical system-based heater chip in a scanning electron microscope under a pressure of 10^{-6} mbar. The results demonstrated the growth and migration of impregnates in cathodes at elevated temperatures, which are favorable for understanding the behavior of scandate cathode materials. It was the first time to report the real time observations of scandate cathode with a high-resolution technique in a high vacuum chamber close to its actual operate condition, which provide an insight on the morphology evolvement of scandate cathode materials.

9.1.4 Through thickness cross-section of key stages of scandate dispenser cathodes

Then the dissertation presents a thorough cross-sectional analysis of the entire cathode thickness using the Broad Ion Beam Milling technique. This method offers a

comprehensive view of the complete cathode cross-section, encompassing both the emitting surface and the base of the scandate cathode. Leveraging this full-length cross-section data, the distribution of impregnated materials and tungsten particle faceting along the cross section were observed and analyzed using scanning electron microscopy and Energy-Dispersive X-ray Spectroscopy. It was found that Sc_2O_3 is abundant at the bottom of all impregnated dispenser cathodes in this work. And a well performance scandate dispenser cathode has a uniform open pore emission surface, but a poor performance cathode has non-uniform pores with closed pores at the emission surface instead. The findings in this work provide extensive insights into the impact of impregnated materials on tungsten faceting.

9.2 *Original scientific contribution of this dissertation*

The work presented in this dissertation holds original scientific contributions of major significance to the field of materials science and engineering.

- First of all, physical vapor deposition was applied to deposit tungsten nanoparticles. A combination of experimental techniques (such as SEM, XPS, and EDS) and software simulations were used to study the structural properties of the developed nanoporous structures. The results elucidate the mechanisms governing the formation of faceted structures of W nanoparticles during annealing. The findings provide valuable insights into the synthesis and control of faceted nanoparticles, which are crucial for various applications, including catalysis, sensing, and energy storage. And nanoscale W materials are very important to the semiconductor industry, which proves the applicability of this work.

167

- Second, chapter 6 investigates the crystallographic faceting of bulk tungsten surfaces using *in situ* heating in an environmental scanning electron microscope (ESEM). The study observes the formation of faceted structures on the tungsten surface at high temperatures and characterizes their crystallographic orientations. The findings contribute to a better understanding of the surface behavior of tungsten at elevated temperatures and provide valuable insights into its thermal stability and potential applications in high-temperature environments. It also helps to address longstanding questions related to the degradation of tungsten alloy related nuclear reactor materials.

- Moreover, chapter 7 investigates how impregnated scandate cathode samples undergo material transformations when subjected to *in situ* heating in a scanning electron microscope (SEM). This study provides valuable insights into the behavior of scandate cathode materials under varying temperature conditions, which is crucial for optimizing their performance in electron emission applications. The observations made during the experiments shed light on the thermal stability and phase transitions occurring in the cathode samples, contributing to a deeper understanding of their properties and potential applications in electron emission devices.

- Chapter 8 makes a significant scientific contribution by providing a thorough characterization of scandate cathodes, examining the entire cathode thickness. This chapter introduces a new approach using the Broad Ion Beam Milling technique to obtain a complete cross-sectional view of

various stages of cathodes. By using this method, the distribution of impregnated materials and tungsten particle faceting across the cathode cross-section was observed and analyzed. These findings provide valuable insights into the impact of impregnated materials on tungsten faceting, which is crucial for optimizing scandate cathode performance in vacuum electron devices. This achievement will improve manufacturing processes for high-performance cathodes, enhance our understanding of the materials and microstructure of high-brightness electron emitters, and support demonstrator efforts. Additionally, it will aid in the design and fabrication of new materials for high current density thermionic emission.

9.3 Future Work

Based on the results and discoveries in this dissertation, continuous research can be done in the future as the extensive of scandate dispenser cathode study.

9.3.1 Characterization and analysis of scandate dispenser cathodes

Firstly, there are some remaining unanalyzed data regarding cathode characterization obtained in December 2021. These include:

a) EDS, SEM, XPS analysis on powder 0618

b) EDS, SEM, XPS analysis on four B-type cathodes

c) XPS analysis on anodes (D0361 and D0360)

d) High-resolution large area surface SEM mapping for D0361 K2 and D0360 K4

It is worth noting that all these samples were sourced from e-beam Inc. Additionally, D0361 and D0360 are activated cathode test vehicles, with D0361 exhibiting poor emission performance while D0360 demonstrates good emission performance. The

analyses mentioned in c) and d) have the potential to form the basis of 2 or 3 article papers: one focusing on comparing the performance of good and poor performance cathodes using SEM high-resolution large area surface imaging, and another on the characterization of impregnated cathodes, from powder to activated states.

Furthermore, a significant amount of characterization has been carried out on 3M cathodes, encompassing XPS, SEM, EDS, full-length cross-section, and even EBSD analyses. However, none of this data has been organized into any publications to date. Should these findings be permitted for publication in the future, they could potentially lead to multiple papers, with a particular focus on evaluating 3D printed dispenser cathodes in comparison to those made using standard processes.

9.3.2 Observation of tungsten nanoparticle faceting by in situ TEM annealing

Secondly, delving into the evolution of faceting in tungsten nanoparticles remains a compelling avenue of research. This dissertation reveals that tungsten nanoparticles transition into highly faceted particles dominated by {110} faces after preheating between 700-850° C at 0.5 Torr, followed by annealing in Ultra High Vacuum at 1100 °C with a surrounding pressure of 10^{-7} Torr. An intriguing prospect arises if Ultra High Vacuum (ultra-low-pressure) annealing could be conducted through *In Situ* annealing in TEM, enabling direct observation of the real-time shaping changes in tungsten nanoparticles. This approach promises to unveil more insightful details regarding the evolution of tungsten nanoparticle shapes.

The experimental design for this topic should mirror the methodology outlined in Chapter 5. Specifically, tungsten nanoparticles could be deposited onto sapphire (Al_2O_3) using a nanoparticle generator. Subsequently, these nanoparticles should undergo

annealing at 700-850 °C, 0.5 Torr for 15-20 minutes, followed by extraction of a TEM lamella from the annealed sample. The pivotal and final step entails conducting *in situ* heating within TEM at a temperature of 1100-1200 °C and a surrounding pressure of 10^{-7} Torr.

9.3.3 *In situ* observation of dispenser cathode activation process

To fully activate a dispenser cathode, it needs to hold the cathode at 1150-1200 °C$_b$ for long time (in order of hours). In this study, it is found that it is challenging to activate a dispenser cathode fragment by *in situ* heating with E-chip in Helios SEM. Because the maximum temperature of E-chip, by the time of this dissertation, can reach is only 1200 °C. And more importantly, it usually takes hours or even days to fully activate a dispenser cathode, the available E-chip could not survive heating at such high temperature for more than 1 hour. If in the future, a better E-chip (i.e., higher temperature and longer heating duration) is available, it will allow direct observation the activation process of dispenser cathode in Helios SEM. Micro-scale tungsten grain faceting process will then be revealed.

9.3.4 Investigation of the relationship between SEM image greyscale and Work function

A series of secondary electron images were captured when studying pure tungsten pellets in Chapter 6, and it has been found that tungsten grains with different grain orientation present various grey levels in the SE images. Thus, it is possible that there is a certain relationship between work function/grain orientation and SE images grey level for pure tungsten grains. More experiments need to be done to verify this assumption.

9.3.5 Surface faceting of Cobalt nanoparticles

Based on the faceting of tungsten nanoparticles, more study on nanoparticles faceting of metals could be performed on the nanoparticle generator. Here Cobalt

nanoparticles draw our attention because its phase transformation temperature from FCC to HCP is 450 °C [191, 192] , and during special cases BCC structure will coexist with FCC structure [193].

APPENDICES

APPENDIX.I Monte Carlo Simulation on Distribution of Electron Trajectories into

Tungsten for the EDS Experiments

Supplementary Materials for Chapter 6

It is important to understand the penetration depth when interpreting X-ray energy dispersive spectroscopy (EDS) analysis of composition for a sample surface. In the current study, Monte Carlo simulation [194-196] was performed to estimate the distribution of electron trajectories into tungsten for the EDS experiments. Results of the calculations performed with Monte Carlo simulation software Casino v2.51 [195] are presented in Figs. S1-S4 below. For all calculations, the number of simulated electrons was 20,000, the number of displayed trajectories was 2000, incident electron beam radius was 10 nm, and the minimum electron energy was 0.05 keV. These calculations illustrate the expected penentration and spreading of the electron beam as it propagtes into the speciman. For an incident beam voltage of 3 kV (see Figs. S1 and S2, corresponding to the low beam engergy EDS experiment in this study to enhance surface sensitivity), simulations indicate that 90% of incident electron trajectories will penetrate no deeper than 25 nm into the W sample (50% will be limited to 14 nm or less). In contrast, for an incident beam voltage of 18 kV (as seen in Figs. S3 and S4, corresponding to the higher-energy EDS experiments in the current study), simulations indicate that 90% of incident electron trajectories will penetrate no deeper than 230 nm into the W sample (50% will be limited to 72 nm or less).
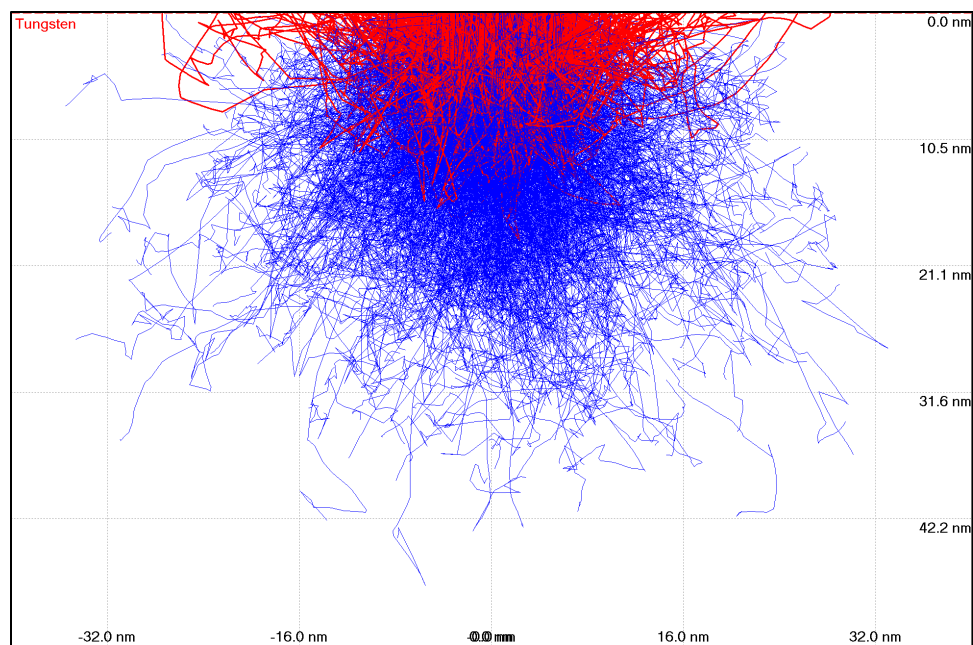
Figure S1. Distribution of electron trajectories that penetrate into tungsten, for an incident beam voltage 3 kV in the scanning electron microscope. Red lines indicate paths along which backscattered electrons would be generated, whereas blue lines indicate locations where X-rays would be emitted.
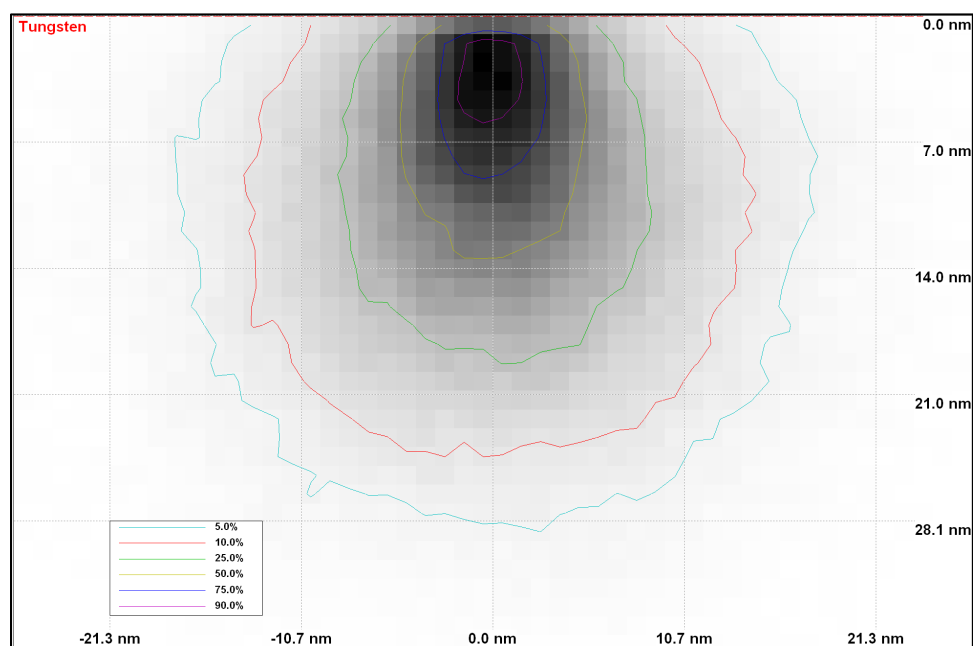
Figure S2. Calculated contour lines indicating the extent of electron penetration into tungsten, for electron trajectories resulting from 3 kV incident beam voltage. The outermost contour (blue line labeled "5.0%") represents the depth to which only 5.0% of incident electrons will penetrate, i.e. 95% of incident electrons will penetrate no more than 28 nm.
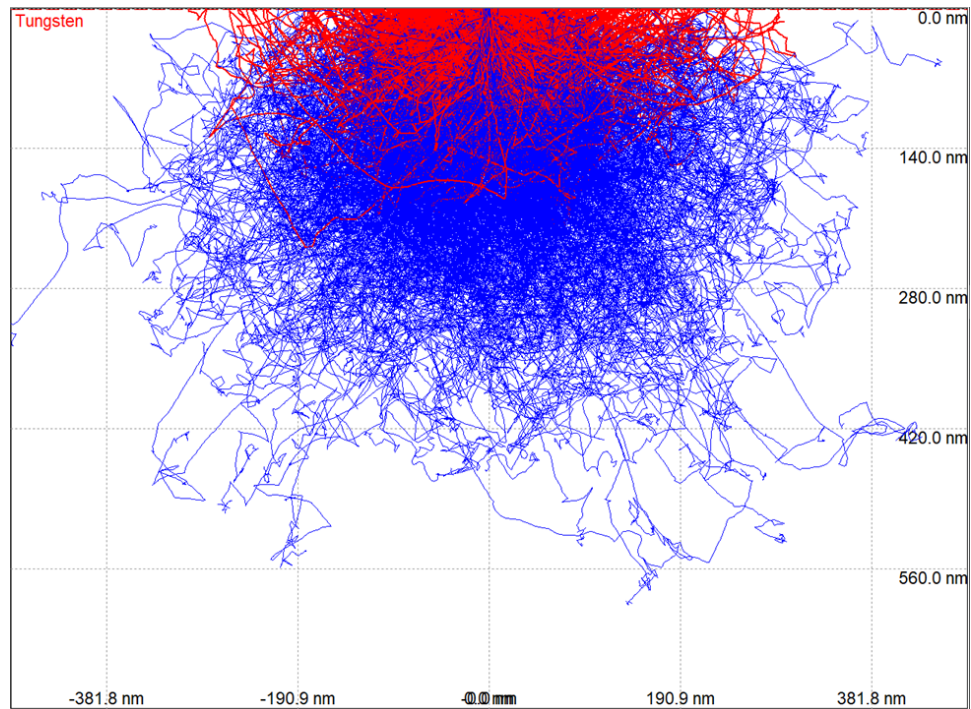
Figure S3. Distribution of electron trajectories that penetrate into tungsten, for an incident beam voltage 18 kV in the scanning electron microscope. Red lines indicate paths along which backscattered electrons would be generated, whereas blue lines indicate locations where X-rays would be emitted.
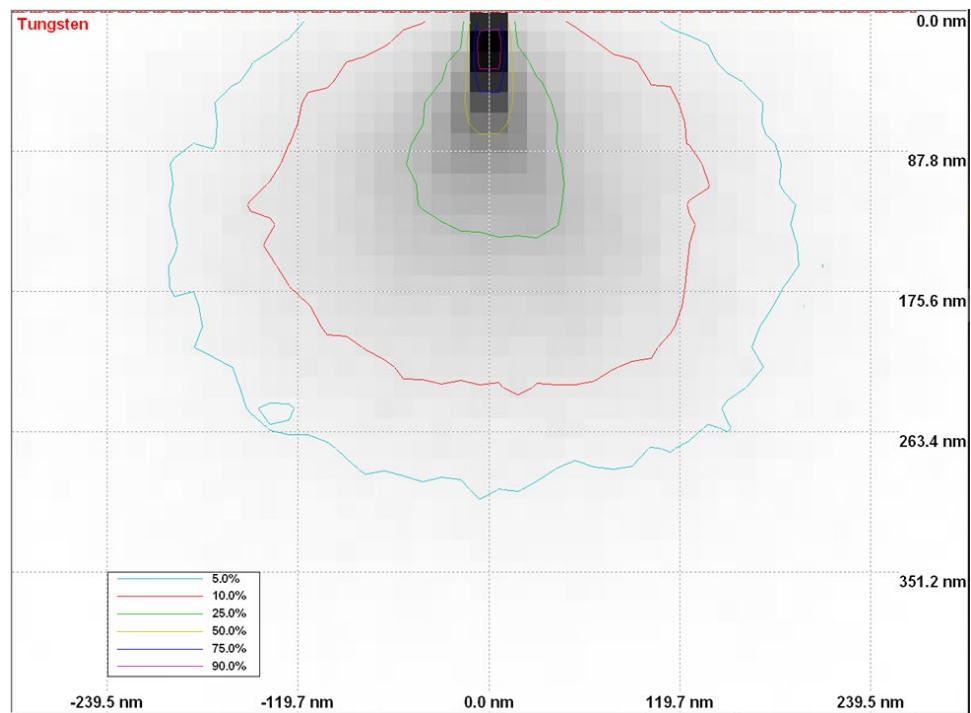
Figure S4. Calculated contour lines indicating the extent of electron penetration into tungsten, for electron trajectories resulting from 18 kV incident beam voltage. The

outermost contour (blue line labeled "5.0%") represents the depth to which only 5.0% of incident electrons will penetrate, i.e. 95% of incident electrons will penetrate no more than 300 nm.

1.   He, J., *A Study of the Electron Beam Scattering Under Various Gaseous Environment.* 2003.

2.   Group, M.E.M.R. *Monte Carlo programs.* 2023   [cited 2023 12-16]; Available from: https://www.memrg.com/programs-download.

3.   Haglöf, F., et al., *Experimental study of carbides in the Ti–Cr–C system.* Journal of Materials Science, 2019. **54**: p. 12358-12370.

II.1, Introduction of Nanoparticle Generation

The Nano-particle generator equipment is a custom-made system in Prof. Dr. Thomas John Balk's lab at the University of Kentucky, which was loaned from Prof. Dr. Kordesch at Ohio University. Pandya S.G, who was Prof. Dr. Kordesch's previous student, worked on this system and finished her PhD study. Anyone who has interest in the history of this equipment could read her dissertation "*Modification of Inert Gas Condensation Technique to Achieve Wide Area Distribution of Nanoparticles and Synthesis and Characterization of Nanoparticles for Semiconductor Application*".

Significant modifications and updates have been made to this system since it arrived at Prof. Dr. Thomas John Balk's lab in 2018. It is currently located in lab 118, Sam Whalen building, University of Kentucky. Any individual who has interest in or/and needs to access it, should contact and get permission from Prof. Dr. John Balk (John.balk@uky.edu) first.

Please read this manual carefully before any operation on the equipment. It is also recommended to read Chapter 3.2.1 and Chapter 4 of this dissertation to have a better understanding of the nanoparticle generator. Also please note that this operation manual is the first version of the optimized system based on its setting as of now (2024), it might need to be updated if the equipment experiences more modifications in the future.

First of all, most of the components are named as the tags in the Figures AII-1 and AII-2. Before any nanoparticle deposition, it is good to read and record the base pressure from the pressure gauge. Please note that the system should always be in a high vacuum condition (10^{-7} torr) when the system is idle.
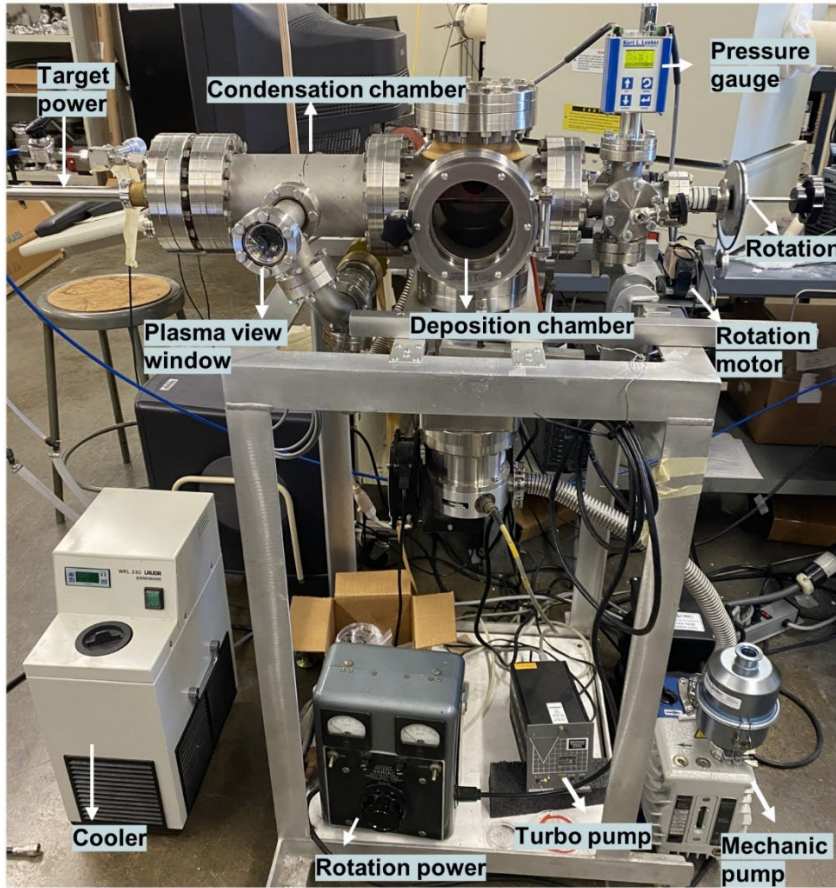
Figure AII-1. Front view of nanoparticle generator and names of its components.
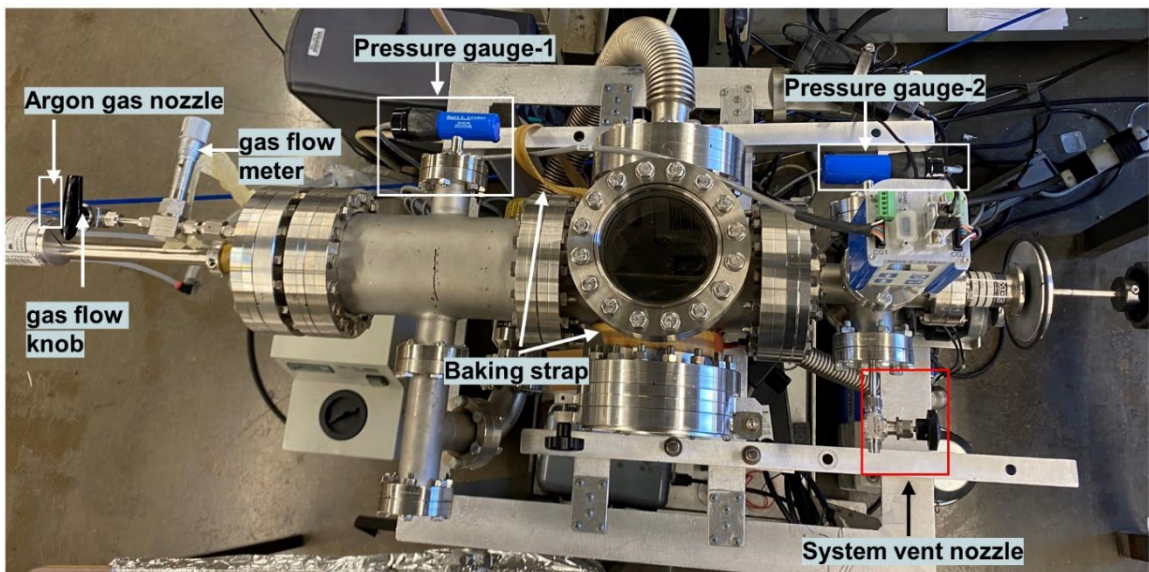
Figure AII-2 Top view of nanoparticle generator and names of some components.

II.2. Operation steps:

II.2.1 Before nanoparticle deposition: Check the system pressure

(1) Please ensure you wear gloves and sleeves, which are readily available in the lab, while operating the equipment.

(2) Verify the system pressure, which can be read from the pressure gauge. It should ideally be at 10^{-7} torr, as indicated in **Figure AII-3** (IG: 2.44E-7 torr). If the pressure reading is not displayed on the gauge, press the 'Menu' button on the panel and select the 'IG ON' option by pressing 'ENTER'.

The measurement range of the IG (ionization gauge) spans from 1×10^{-9} to 1×10^{-2} torr, while the CG (Convection gauge) ranges from 1×10^{-4} to 1000 torr. When the system pressure reaches approximately 10^{-7} torr, it exceeds the measurement range of CG1 and CG2, causing them to display 0000 or 10^{-4} torr, as shown in the left picture of **Figure AII-3**. For more detailed information about this pressure gauge, please consult the manual available on the Kurt J. Lesker company website regarding the *Ionization Gauge / Dual Convection with Integrated Controller & Display, 392 Series Ionization Vacuum Gauge*.

Figure AII-3 Pressure of nanoparticle generator system: 10^{-7} torr (left) and how to turn on the IG (right). IG: ionization gauge; CG: Convection gauge. Noted that CG1 is connected with condensation chamber, CG2 is connected with deposition chamber.

<u>II.2.2. Venting the system</u>

(3) Both the tube pump and mechanical pump are active in maintaining the system pressure at 10^{-7} torr. To load the sample, it's necessary to halt the pumping process and vent the nanoparticle generator. Please follow steps (a) to (d) below to stop the pumping and vent the system.

(a) Disable the 'IG' by pressing the 'Menu' button on the panel. Next, select the 'IG OFF' option using the 'DOWN' button, and confirm by pressing 'ENTER', as demonstrated in **Figure AII-3**.

Figure AII-4. How to turn off the IG

(b) To deactivate the tube pump, move the 'stop' button to halt its operation and switch the power button from 1 to 0, as depicted in **Figure AII-5** (a).

(c) Press the designated button to power down the mechanical pump, as shown in **Figure AII-5 (b).**

(d) Rotate the black knob to initiate venting of the nanoparticle generator, as illustrated in **Figure AII-6**. Please perform step (d) immediately after completing step (c). This is crucial because if both pumps are turned off and the pressure in the nanoparticle generator remains close to 10^{-7} torr, there's a risk of oil from the mechanical pump being drawn into the deposition chamber due to pressure differentials between the chamber and the pump.
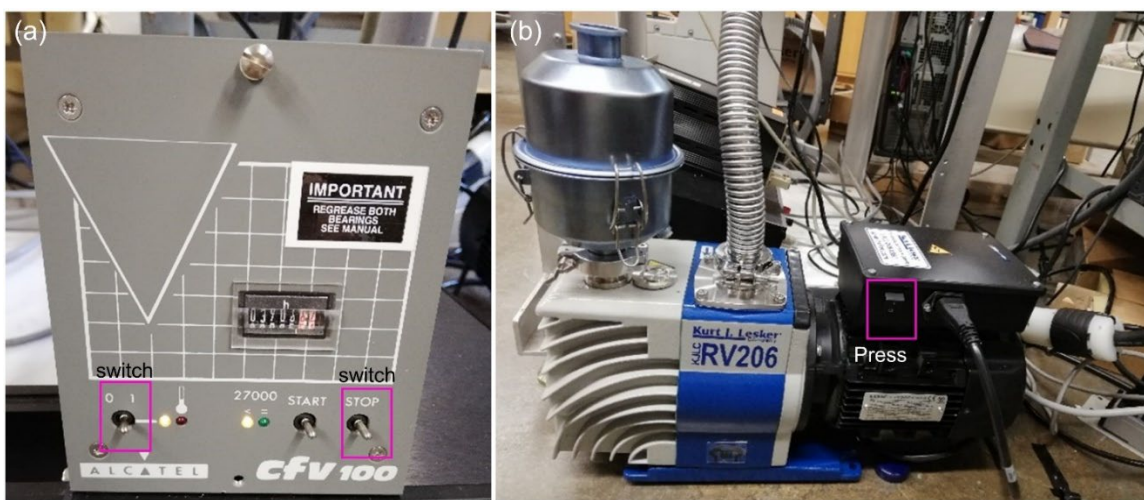
Figure AII-5. Turn off pumping components of nanoparticles generator: (a) tube pump, (b) mechanical pump.
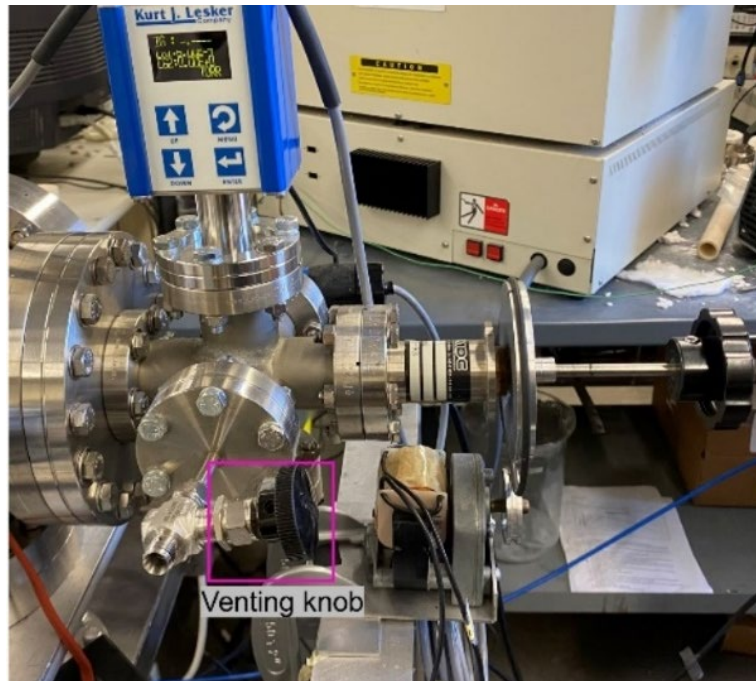
Figure AII-6. Turn the black knob to vent the nanoparticle generator.

II.2.3. Loading the sample substrate to the chamber

(4) Once the nanoparticle generator is vented to atmospheric pressure, it's time to open the front window and load the sample substrates. These substrates serve as the surface for nanoparticle deposition. As nanoparticles emanate from the source, they traverse from the condensation chamber to the deposition chamber and eventually settle onto the substrate. Substrates can vary and include materials such as silicon (Si) wafers, sapphire (Al_2O_3), pure metal sheets, clean glass, or specialized items like tungsten-scandate pellets or dispenser cathodes. They should align with the experimental objectives.

a) Rotate the black knob to open the front window, as demonstrated in **Figure AII-7** (a).

b) Secure the sample substrate, like a silicon wafer or sapphire (Al2O3), onto a metal sheet using carbon tape. Then affix the metal sheet onto an aluminum disc to create a disc combo, as illustrated in **Figure AII-7** (b).
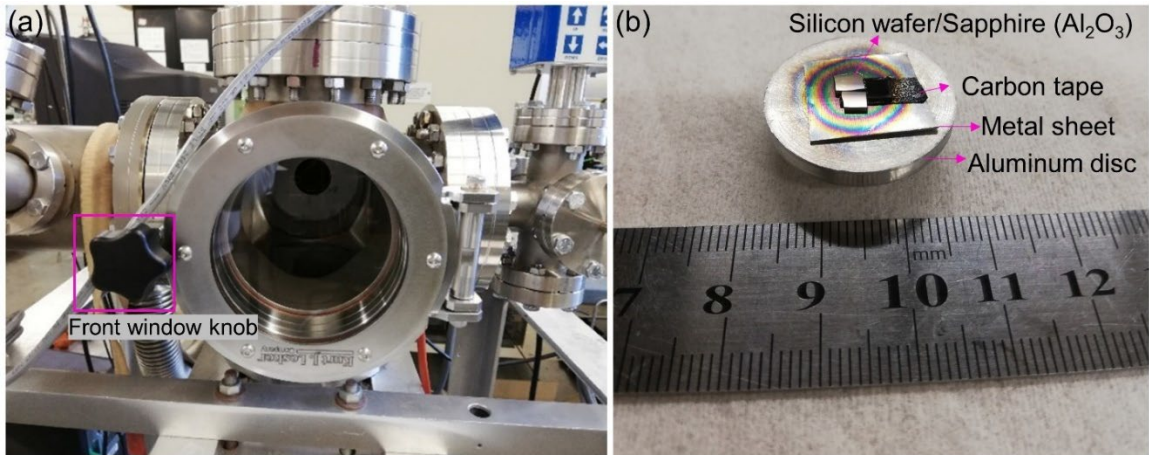
Figure AII-7. The front window (a) and sample substrate arrangement with an aluminum disc (b).

c) Fasten the disc combo onto the large disc within the chamber, which should already be screwed onto the stick, as depicted in **Figure AII-8** (a).

d) Once completed, confirm the stable attachment of the disc combo to the large disc by rotating the stick using the rotatory knob. Refer to **Figure AII-8** (b).

e) Close the front window securely by turning the black knob as shown in **Figure AII-7** (a), ensuring the window is properly sealed.
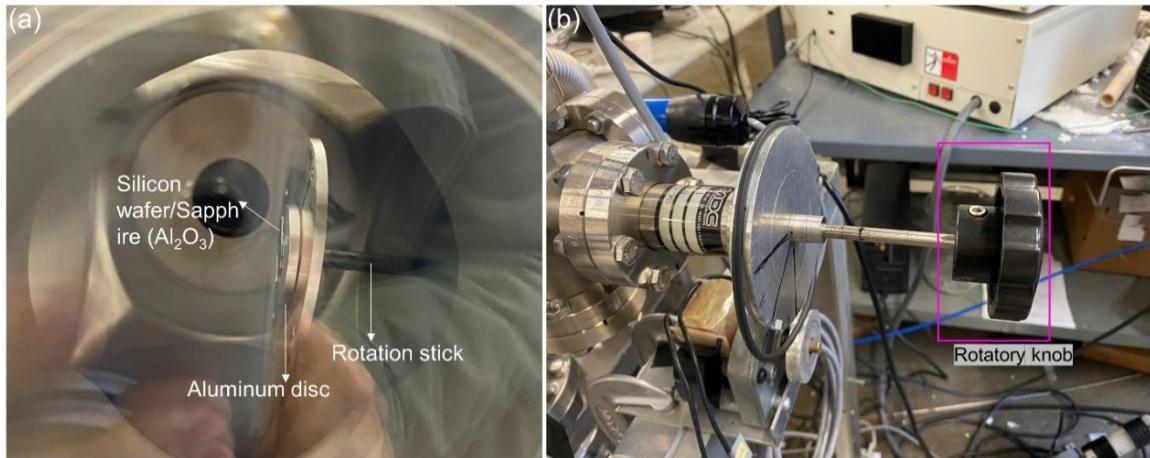
Figure AII-8. Sample substrate loaded in the chamber (a), and rotatory knob (b).

II.2.4. Pumping the system

(5) The preparation for loading sample substrates is now complete, and the system is ready for pumping.

i. Close the vent by rotating the black knob as indicated in **Figure AII-6**.

ii. Activate the mechanical pump (depicted in **Figure AII-5** (b)), noting the time and initial pressure displayed on the convection (pressure) gauge screen.

iii. Once the pressure reading on CG1 reaches approximately 5×10^{-3} Torr, switch on the tube pump. Follow these steps to activate the tube pump:

(01) Adjust the power button from 0 to 1;

(02) Engage the start button, as demonstrated in **Figure AII-9**.
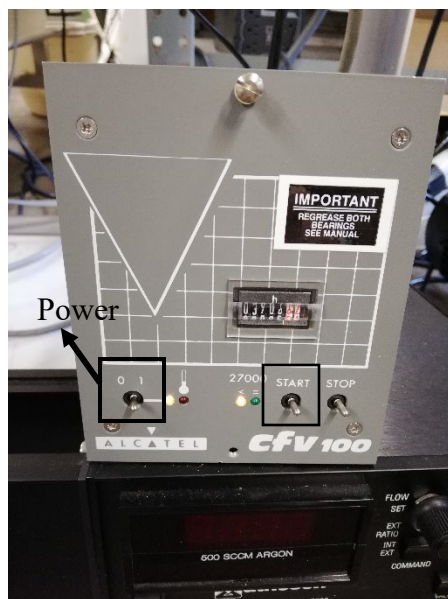
Figure AII-9. How to turn on the tube pump.

iv. When CG2 reads 0000, switch on the Iron Gauge (IG) and record the pressure.

Here's how to activate the IG:

Push the 'MEAU' button, which will prompt the screen to display 'IG ON';

Then press the 'ENTER' button, and the screen will display the IG value. Refer to

Figure AII-10.

Figure AII-10 Turn on the IG when CG2 is 0000.

II.2.5. Baking the system

Baking the chamber aids in removing any water or moisture present in the nanoparticle generator. It's important to understand that baking the system isn't necessary for every nanoparticle deposition experiment. However, if achieving the ideal pressure ($<5 \times 10^{-7}$ torr) is difficult or takes an extended period, it may be due to water or moisture clinging to the inner walls of the chamber. In such cases, the system requires baking.

Figure AII-11 Heat strap of the nanoparticle generator.

To initiate the baking process, utilize the heat strap attached to the system.

a) Position the strap outside the chamber, ensuring it avoids contact with any heat-sensitive materials.

b) Adjust the heat strap to 45%, following the instructions in Figure **AII-11**.

c) Bake the nanoparticle generator overnight. Note that the system's pressure will rise during baking due to air expansion in the heated chamber. Utilize a hot warning tag, as depicted in Figure AII-12. If necessary, inform lab personnel that the baking process is active and the nanoparticle generator equipment will be hot.

d) After 12-24 hours, deactivate the heat strap by reducing the heating power to 0.

a) Allow the system to cool to ambient temperature. Then, record the pressures indicated by IG, CG1, and CG2 on the pressure gauge. Ensure the IG value is below 5×10^{-7} torr. This IG value represents the base pressure for nanoparticle generation.

Figure AII-12. Hot warning tag for the nanoparticle generator: 'Caution! Equipment Baking May Be Hot".

II.2.6. Water chiller

(6) Turn on the water chiller. Before beginning nanoparticle deposition, it's essential to activate the water chiller. Water chillers play a critical role in the nanoparticle generation process by cooling down the sputtering gun, which operates at high voltage and becomes very hot during sputtering.

Before activating the water chiller, ensure the water level is adequate by opening the black lid (refer to **Figure AII-13** (a)). It should always contain a full supply of distilled water. If it's insufficient, replenish it with distilled water.

Next, press the green button indicated in **Figure AII-13** (b). The temperature of the water will be displayed on the screen adjacent to the green button, as illustrated in **Figure AII-13** (c). It should not exceed 25°C.
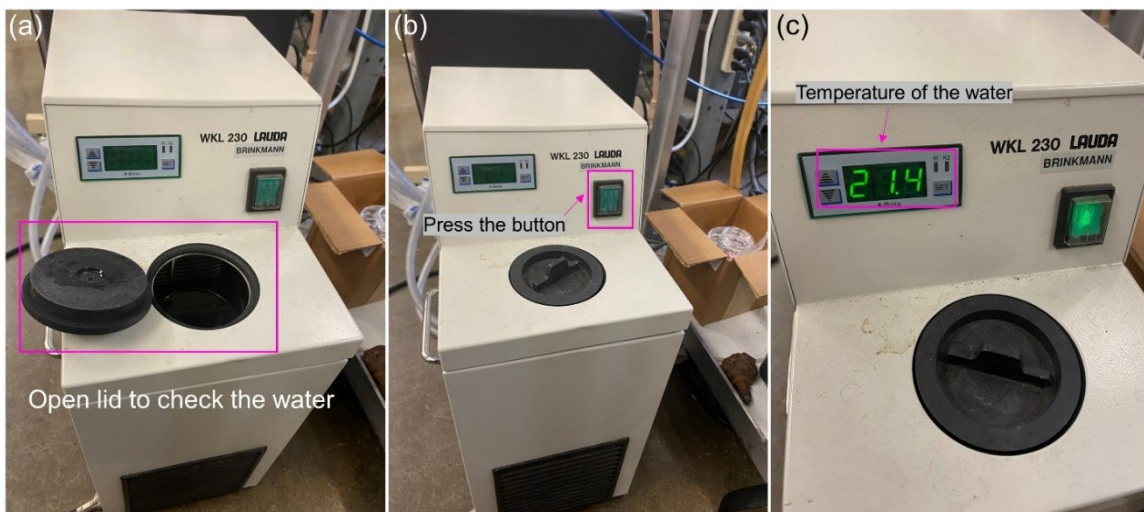
Figure AII-13. Water chiller of the nanoparticle generator (a) how to check the water level, (b) turn on the water chiller, (c) temperature of the water in the chiller.

When the water chiller is running, wait for approximately 30 seconds and check for any water leaks around the chiller or at the connection points. There should be no leaks while the sputtering process is ongoing. If you notice a leak, turn off the water chiller. If the leak is coming from the water tube joint, tighten the connection securely. If the leak is from the water chiller itself, troubleshoot the issue with the water chiller.

II.2.7. Sputtering Power source

(7) Sputtering gun power

One end of the power cable for the sputtering gun is linked to the sputtering gun itself (refer to **Figure AII-14** (a)), while the other end must be connected to position gun 2 (as illustrated in **Figure AII-14** (b)). This position is situated behind the thin film/sputtering system near the office window. To ascertain this precise location, reach out

to the individual in charge of the thin film/sputtering system. At the time of this manual's publication, that person is Mike (mjdeti2@uky.edu).
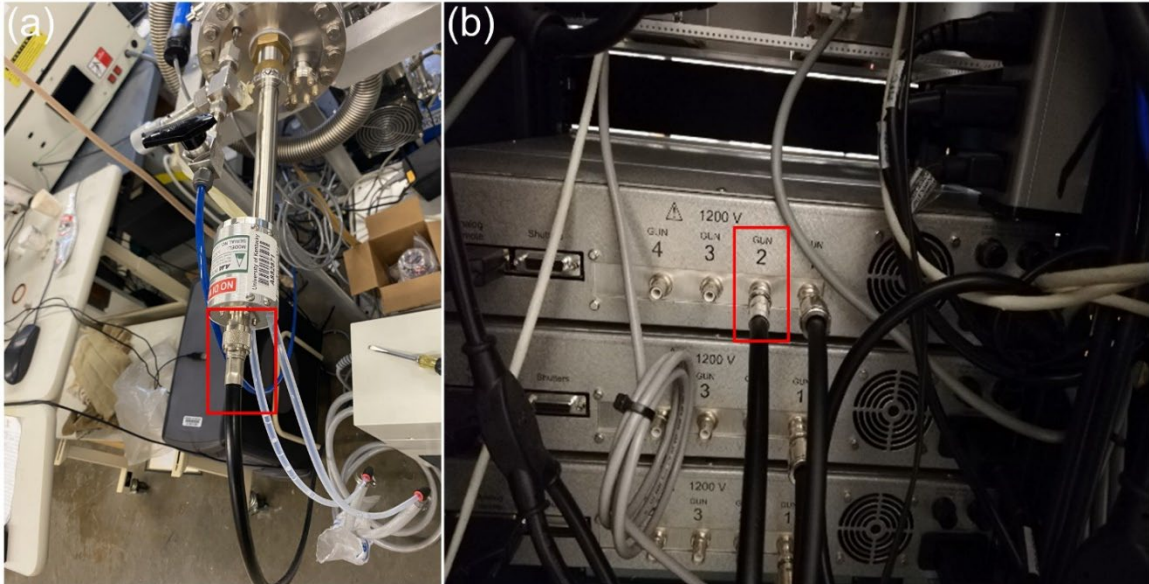
Figure AII-14. Sputtering power cable: one end is connected to the gun (a), and the other end should be connected with the power source with position 2.

II.2.8. Argon gas flow

(8) flow argon gas to prepare deposition

By this moment, the system base pressure should be 10^{-7} torr. Now it is ready to flow Argon gas in the chamber. Here are the steps to flow Argon in:

(a) Close the golden valve (as seen in **Figure AII-15**) (which is under the condensation chamber) by turning the knob all the way and a little bit back.
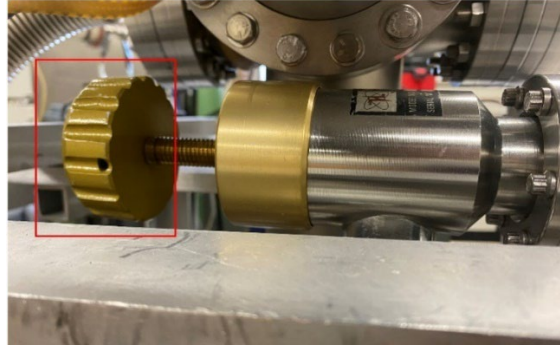
Figure AII-15. Golden valve under the condensation chamber

(b) Record the pressure, <u>turn off the IG</u>. The way to turn off the Iron Gauge is seen in **Figure AII-10**.

(c) Switch the black handle to open the gas flow valve (labeled as '1' in Figure AII-16), then carefully and slowly turn on the gas flow control meter (labeled as '2' in **Figure AII-16**). Observe CG1 and CG2, adjust gas flow control meter and wait until pressure is stable. For tungsten (W) nanoparticle deposition, it is recommended to keep the ration of CG1 vs CG2 close to 1000:1 (with CG1 close to 0.9-1 torr), as seen in Figure AII-16 (right). <u>Please record the pressure of CG1 and CG2 here</u>.
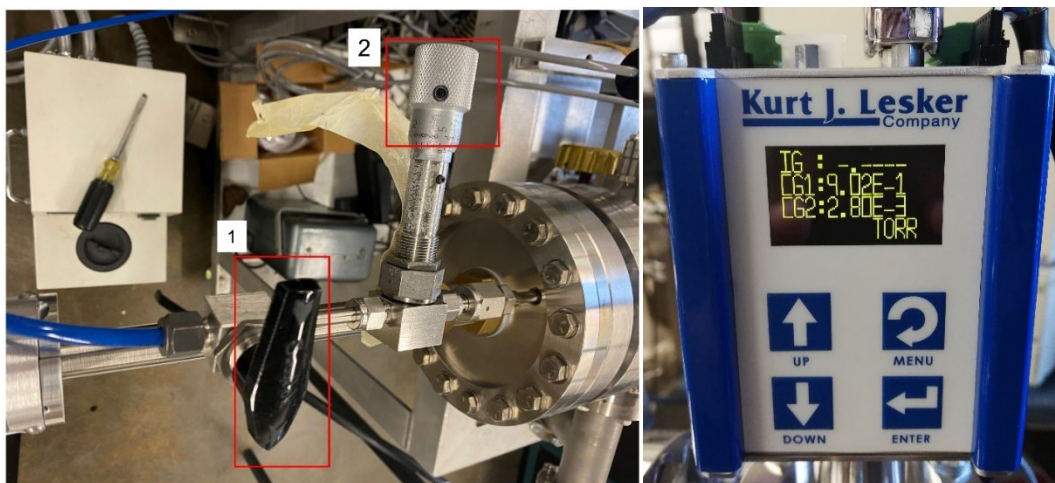
Figure AII-16. Argon Flow in (left) and pressure (right).

II.2.9. Turn on substrate rotatory

(9) substrate rotation control. When the pressure is stable, it is ready to turn on the substrate rotatory. Please note that it is also able to deposit nanoparticles without substrate rotation, as seen in Chapter 4 in this dissertation. However, the deposition without substrate rotation could result in a non-uniform deposition, instead a rotatory substrate will result in a more uniform nanoparticle deposition. Whether using a rotatory substrate or not depends on your experimental propose.

Here are steps to use a rotatory substrate:

(01)   Use the black rubber band to connect the rotatory bearing (as shown in Figure AII-17 (a)).

(02)   Check the motor wire connection and make sure they are stably contacted.

(03)   Turn on motor power by switching the button to 'ON' and turn the black knob (as shown in **Figure AII-17** (b)) to increase voltage. It is recommended to increase voltage to 70 Volts, which will make the substrate rotate at a speed of 6 revolutions per minute. Please note that when the substrate is rotated, the pressure of the chamber might be increased a little bit, which is challenging to avoid it due to the joint between the rotatory stick and the chamber.
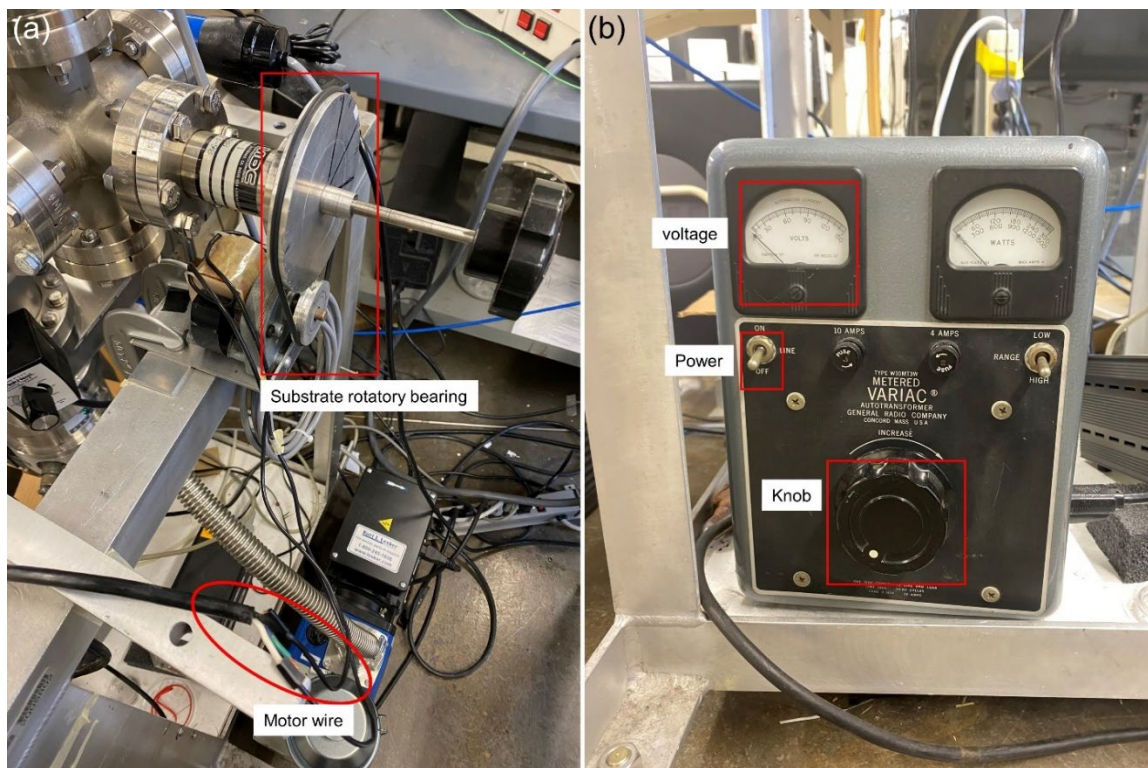
Figure AII-17 Substrate rotatory (a) and its power control (b).

II.2.10. Nanoparticle deposition

(10) Depositing nanoparticles.

(a) Turn on the power supply by switching the handle from 0 to 1 (**Figure AII-18 (a)**);

(b) Turn the round button to select the gun 2 (**Figure AII-18** (b)) and press the round button to confirm.

(c) Switch the round button to set the value of power (setting value), press the round button to confirm (**Figure AII-18** (c)).

(d) Finally press the black button near the DC ON to start the plasma.

(e) Record the duration of the deposition (normally the deposition process runs 30min-1h); and record the value of SET (setting value) as well as ACT (actually value) (**Figure AII-18** (c)).

(f) Record the color of the sputtering gun when the plasma is on.

(g) Record the pressure of chambers (CG1 and CG2) during deposition.
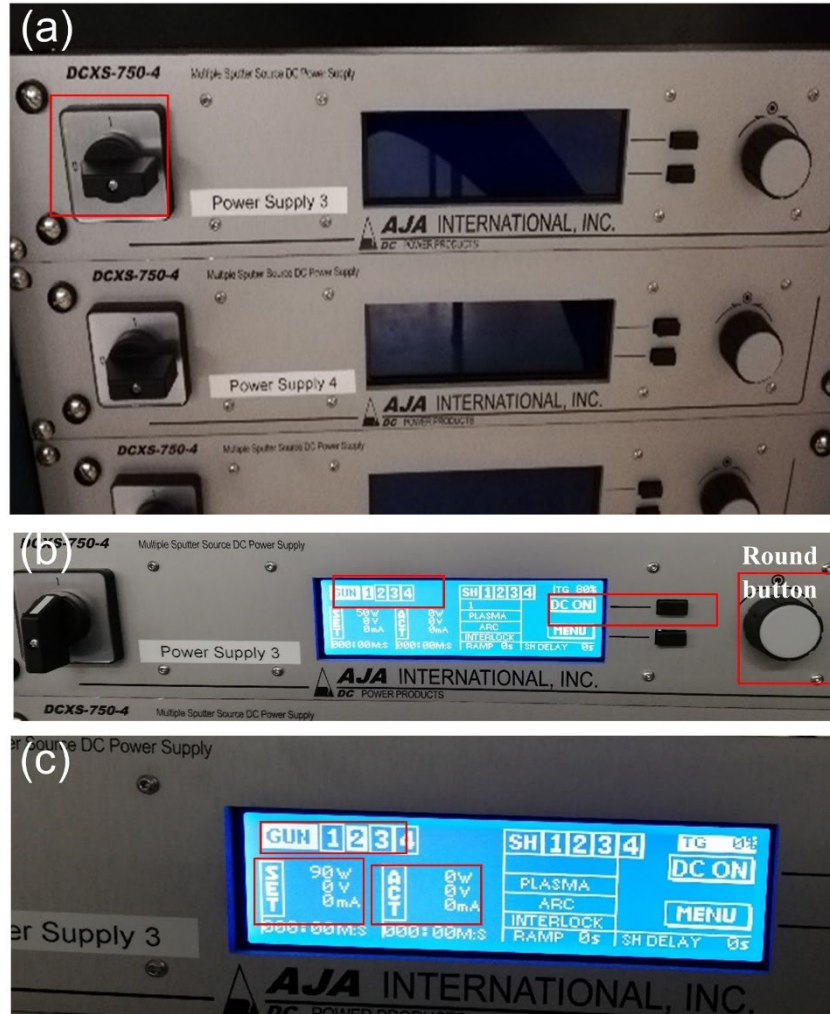
Figure AII-18 (a) turn on the power; (b) switch the round button to select gun 2; (c) set the value of power.

(h) When the time reaches the designed time, Press the button STOP which is in the position MEAU (**Figure AII-18(**b)) again to stop the plasma, and switch the power supply from 1 to 0 (**Figure AII-18** (a)).

(i) Close the gas flow valve (**Figure AII-16** (a))

(j) Stop the substrate rotation by turning the rotation power knob in **Figure AII-17 (b)** so that the voltage is 0, and switch the rotation power button to 'off'.

(j) Open the golden valve all the way (**Figure AII-15**)

II.2.11. Taking out the deposited sample

To remove the sample from the chamber, the system needs to be vented. Please follow the steps outlined in section **II.2.2 Venting the system** to vent the system properly. Once the nanoparticle generator is vented to atmospheric pressure, it's then appropriate to open the front window and extract the sample substrates.

After removing the sample, ensure to close the front window and proceed with the steps in section **II.2.4 Pumping the system** to pump the system accordingly.

Finally, remember to turn off the water chiller.

II.3. Characterization of the Deposited Nanoparticles

It's recommended to utilize the FIB-SEM Helios 660 at the Electron Microscopy Center of UK for characterizing the morphology, deposition thickness of the nanoparticles can be figured out by using the cross-sectioning function of FIB. Additionally, employing EDS can help examine the composition.

REFERENCES

1. Bugaris, D.E., et al. *High-Performance Scandate Cathode*. in *2019 International Vacuum Electronics Conference (IVEC)*. 2019. IEEE.

2. Bai, H., M.J. Beck, and T.J. Balk. *Deposition of Tungsten Nanoparticles for Potential Use in Dispenser Cathodes*. in *2020 IEEE 21st International Conference on Vacuum Electronics (IVEC)*. 2020. IEEE.

3. Liu, X., et al., *Scandate cathode surface characterization: Emission testing, elemental analysis and morphological evaluation.* Materials Characterization, 2019. **148**: p. 188-200.

4. Liu, X., *Characterization of Nanostructure, Materials, and Electron Emission Performance of Next-generation Thermionic Scandate Cathodes*, in *Chemical and Materials Engineering*. 2019, University of Kentucky.

5. Whittingham, M.S., *Lithium batteries and cathode materials.* Chemical reviews, 2004. **104**(10): p. 4271-4302.

6. Redhead, P., *The birth of electronics: Thermionic emission and vacuum.* Journal of Vacuum Science & Technology A: Vacuum, Surfaces, and Films, 1998. **16**(3): p. 1394-1401.

7. Guthrie, F., *On a New Relation between Heat and Electricity.* Proceedings of the Royal Society of London, 1872. **21**: p. 168-169.

8. Thomson, J.J., *XL. Cathode rays.* The London, Edinburgh, and Dublin Philosophical Magazine and Journal of Science, 1897. **44**(269): p. 293-316.

9. Thomson, J.J., *LVIII. On the masses of the ions in gases at low pressures.* The London, Edinburgh, and Dublin philosophical magazine and journal of science, 1899. **48**(295): p. 547-567.

10. Falconer, I., *Corpuscles, electrons and cathode rays: JJ Thomson and the 'discovery of the electron'.* The British journal for the history of science, 1987. **20**(3): p. 241-276.

11. *J.J. Thomson – Nobel Lecture*. [cited 2023 Aug 22]; Available from: https://www.nobelprize.org/prizes/physics/1906/thomson/lecture/.

12. Richardson, O., *LXXVII. Thermionics.* The London, Edinburgh, and Dublin Philosophical Magazine and Journal of Science, 1909. **17**(102): p. 813-833.

13. Reimann, A.L., *Thermionic emission*. 1934, London: Chapman & Hall.

14. Nottingham, W.B., et al., *Thermionic emission*. 1956: Springer.

15. Kittel, C., *Introduction to solid state physics*. 2005: John Wiley & sons, inc.

16. Richardson, O.W., *Thermionic phenomena and the laws which govern them.* Nobel lecture, 1929. **12**.

17. Dushman, S., *Electron emission from metals as a function of temperature.* Physical Review, 1923. **21**(6): p. 623.

18. Swartzentruber, P.D., *Microstructure and work function of dispenser cathode coatings: effects on thermionic emission*. 2014, University of Kentucky.

19. Yamamoto, S., *Fundamental physics of vacuum electron sources.* Reports on Progress in Physics, 2005. **69**(1): p. 181.

20. Hashim, A.A., *Electrical Studies on New Generations of Oxide Cathodes for CRT Applications*. 2005: Sheffield Hallam University (United Kingdom).

21. Liu, X., et al., *Near-Surface Material Phases and Microstructure of Scandate Cathodes.* Materials (Basel), 2019. **12**(4).

22. Zhou, Q., et al., *BaxScyOz on W (0 0 1),(1 1 0), and (1 1 2) in scandate cathodes: Connecting to experiment via µO and equilibrium crystal shape.* Applied Surface Science, 2018. **458**: p. 827-838.

23. Ives, R.L., et al., *Controlled-Porosity Cathodes for High-Current-Density Applications.* IEEE Transactions on Plasma Science, 2010. **38**(6): p. 1345-1353.

24. Liu, Y.-W., et al., *Study on the emission properties of the impregnated cathode with nanoparticle films.* IEEE transactions on electron devices, 2012. **59**(12): p. 3618-3624.

25. Gamzina, D., *Machining Methods for Nano-Composite Scandate Tungsten Cathodes*. 2012: University of California, Davis.

26. Mantica, A., *SURFACE PROPERTIES, WORK FUNCTION, AND THERMIONIC ELECTRON EMISSION CHARACTERIZATION OF MATERIALS FOR NEXT-GENERATION DISPENSER CATHODES*, in *Chemical and Materials Engineering*. 2023, University of Kentucky.

27. Kirkwood, D.M., et al., *Frontiers in Thermionic Cathode Research.* IEEE Transactions on Electron Devices, 2018. **65**(6): p. 2061-2071.

28. Vancil, B., et al., *Scandate dispenser cathodes with sharp transition and their application in microwave tubes*. IEEE Transactions on Electron Devices, 2014. **61**(6): p. 1754-1759.

29. Balk, T.J., et al. *Materials characterization of surface phases in scandate cathodes*. in *2018 IEEE International Vacuum Electronics Conference (IVEC)*. 2018. IEEE.

30. Forman, R., *A proposed physical model for the impregnated tungsten cathode based on Auger surface studies of the Ba-OW system*. Applications of Surface Science, 1979. **2**(2): p. 258-274.

31. Umrath, W., *Fundamentals of vacuum technology*. 1998.

32. Venables, J., *Introduction to surface and thin film processes*. 2000: Cambridge university press.

33. *Residual gas analyzer*. [cited 2023 09/05]; Available from: https://en.wikipedia.org/wiki/Residual_gas_analyzer.

34. Ohring, M., *Materials Science of Thin Films: Depositon and Structure*. 2001: Elsevier.

35. Guziewicz, E., et al., *ALD grown zinc oxide with controllable electrical properties*. Semiconductor Science and Technology, 2012. **27**(7): p. 074011.

36. Bai, H., et al., *Physical vapor deposition and thermally induced faceting of tungsten nanoparticles*. Materials Characterization, 2023: p. 112724.

37. Escorcia-Díaz, D., et al., *Advancements in nanoparticle deposition techniques for diverse substrates: a review*. Nanomaterials, 2023. **13**(18): p. 2586.

38. Wang, H., *Adsorbate-induced nanoscale faceting of rhenium surfaces*. 2008: Rutgers The State University of New Jersey, School of Graduate Studies.

39. Gotoh, Y., et al., *Work function of low index crystal facet of tungsten evaluated by the Seppen-Katamuki analysis*. Journal of Vacuum Science & Technology B: Microelectronics and Nanometer Structures Processing, Measurement, and Phenomena, 2007. **25**(2): p. 508-512.

40. Zhou, J., et al., *Three-Dimensional Tungsten Oxide Nanowire Networks*. Advanced Materials, 2005. **17**(17): p. 2107-2110.

41.   Xie, Y.P., et al., *Crystal facet-dependent photocatalytic oxidation and reduction reactivity of monoclinic WO3 for solar energy conversion.* Journal of Materials Chemistry, 2012. **22**(14): p. 6746-6751.

42.   Yamazaki, H., et al., *Structure analysis of oxygen-adsorbed tungsten (0 0 1) surface.* Surface science, 2001. **477**(2-3): p. 174-178.

43.   Woodward, P., A. Sleight, and T. Vogt, *Structure refinement of triclinic tungsten trioxide.* Journal of Physics and Chemistry of Solids, 1995. **56**(10): p. 1305-1315.

44.   Gonzalez, M., et al. *Quality and Performance of Commercial Nanocomposite Scandate Tungsten Material*. in *2019 International Vacuum Electronics Conference (IVEC)*. 2019. IEEE.

45.   Pandya, S.G., *Modification of Inert Gas Condensation Technique to Achieve Wide Area Distribution of Nanoparticles and Synthesis and Characterization of Nanoparticles for Semiconductor Applications*. 2016.

46.   Leng, Y., *Materials characterization: introduction to microscopic and spectroscopic methods*. 2013: John Wiley & Sons.

47.   Newbury, D.E. and N.W. Ritchie, *Performing elemental microanalysis with high accuracy and high precision by scanning electron microscopy/silicon drift detector energy-dispersive X-ray spectrometry (SEM/SDD-EDS)*. Journal of materials science, 2015. **50**: p. 493-518.

48.   Shindo, D. and T. Oikawa, *Energy Dispersive X-ray Spectroscopy*, in *Analytical Electron Microscopy for Materials Science*. 2002, Springer Japan: Tokyo. p. 81-102.

49.   instrument, O. *What is EDS/EDX?*   [cited 2023 10 30]; Available from: https://nano.oxinst.com/campaigns/what-is-eds/edx.

50.   Tunes, M.A., et al., *A contamination-free electron-transparent metallic sample preparation method for MEMS experiments with in situ S/TEM.* arXiv preprint arXiv:2012.02941, 2020.

51.   Dumitraschkewitz, P., et al., *MEMS-Based in situ electron-microscopy investigation of rapid solidification and heat treatment on eutectic Al-Cu.* Acta Materialia, 2022. **239**: p. 118225.

52. *Heating E-chips - Fusion Select.* [cited 2023 10 31]; Available from: https://protochips.shop/products/fusion-thermal-echips.

53. *Transmission Electron Microscopy vs Scanning Electron Microscopy.* [cited 2023 10 03]; Available from: https://www.thermofisher.com/us/en/home/materials-science/learning-center/applications/sem-tem-difference.html#:~:text=The%20main%20difference%20between%20SEM,sample)%20to%20create%20an%20image.

54. [cited 2023 10-03]; Available from: http://emc.engr.uky.edu/equipment/equipment-list/x-ray-photoelectron-spectroscopy.

55. Schütze, A. and D.T. Quinto, *Pulsed plasma-assisted PVD sputter-deposited alumina thin films.* Surface and Coatings Technology, 2003. **162**(2-3): p. 174-182.

56. Venkataraj, S., et al., *Characterization of niobium oxide films prepared by reactive DC magnetron sputtering.* physica status solidi (a), 2001. **188**(3): p. 1047-1058.

57. Mattox, D., *The low pressure plasma processing environment*, in *Handbook of Physical Vapor Deposition (PVD) Processing*. 2010, Elsevier Inc. p. 157-193.

58. Hattori, Y., et al., *Synthesis of tungsten oxide, silver, and gold nanoparticles by radio frequency plasma in water.* Journal of alloys and compounds, 2013. **578**: p. 148-152.

59. Tracy, C. and D. Benson, *Preparation of amorphous electrochromic tungsten oxide and molybdenum oxide by plasma enhanced chemical vapor deposition.* Journal of Vacuum Science & Technology A: Vacuum, Surfaces, and Films, 1986. **4**(5): p. 2377-2383.

60. Kaiser, N., *Review of the fundamentals of thin-film growth.* Applied optics, 2002. **41**(16): p. 3053-3060.

61. Venables, J., *Nucleation and growth of thin films: recent progress.* Vacuum, 1983. **33**(10-12): p. 701-705.

62. Itoh, H., et al., *Mechanism for initial stage of selective tungsten growth employing a WF6 and SiH4 mixture.* Japanese journal of applied physics, 1991. **30**(7R): p. 1525.

63. Magnusson, M.H., K. Deppert, and J.-O. Malm, *Single-crystalline Tungsten Nanoparticles Produced by Thermal Decomposition of Tungsten Hexacarbonyl.* Journal of Materials Research, 2011. **15**(7): p. 1564-1569.

64. Sun, G.-D., et al., *A low-cost, efficient, and industrially feasible pathway for large scale preparation of tungsten nanopowders.* International Journal of Refractory Metals and Hard Materials, 2019. **78**: p. 100-106.

65. Magdassi, S., M. Grouchko, and A. Kamyshny, *Copper Nanoparticles for Printed Electronics: Routes Towards Achieving Oxidation Stability.* Materials (Basel), 2010. **3**(9): p. 4626-4638.

66. Antunez-Garcia, J., et al., *Coalescence and Collisions of Gold Nanoparticles.* Materials (Basel), 2011. **4**(2): p. 368-379.

67. Wang, S., et al., *Challenge in Understanding Size and Shape Dependent Toxicity of Gold Nanomaterials in Human Skin Keratinocytes.* Chem Phys Lett, 2008. **463**(1-3): p. 145-149.

68. Brust, M. and C.J. Kiely, *Some recent advances in nanostructure preparation from gold and silver particles: a short topical review.* Colloids and Surfaces A: Physicochemical and Engineering Aspects, 2002. **202**(2-3): p. 175-186.

69. Mayorga-Martinez, C.C., et al., *Bismuth nanoparticles for phenolic compounds biosensing application.* Biosens Bioelectron, 2013. **40**(1): p. 57-62.

70. Seif, M.N. and M.J. Beck, *Surface excess free energies and equilibrium Wulff shapes in variable chemical environments at finite temperatures.* Applied Surface Science, 2021. **540**: p. 148383.

71. Lue, J.-T., *A review of characterization and physical property studies of metallic nanoparticles.* Journal of physics and chemistry of solids, 2001. **62**(9-10): p. 1599-1612.

72. Guan, W., et al., *Fabrication and charging characteristics of MOS capacitor structure with metal nanocrystals embedded in gate oxide.* Journal of Physics D: Applied Physics, 2007. **40**(9): p. 2754-2758.

73. Paul, S., et al., *Langmuir− Blodgett film deposition of metallic nanoparticles and their application to electronic memory structures.* Nano Letters, 2003. **3**(4): p. 533-536.

74. Boley, J.W., E.L. White, and R.K. Kramer, *Mechanically sintered gallium-indium nanoparticles.* Adv Mater, 2015. **27**(14): p. 2355-60.

75. Ryu, T., et al., *Chemical vapor synthesis (CVS) of tungsten nanopowder in a thermal plasma reactor.* International Journal of Refractory Metals and Hard Materials, 2009. **27**(1): p. 149-154.

76. Ryu, T., et al., *The sintering behavior of nanosized tungsten powder prepared by a plasma process.* International Journal of Refractory Metals and Hard Materials, 2009. **27**(4): p. 701-704.

77. Wang, H., et al., *Sinter-ability of nanocrystalline tungsten powder.* International Journal of Refractory Metals and Hard Materials, 2010. **28**(2): p. 312-316.

78. Qin, M., et al., *Fabrication of tungsten nanopowder by combustion-based method.* International Journal of Refractory Metals and Hard Materials, 2017. **68**: p. 145-150.

79. Ahangarkani, M., *In-situ formation of tungsten nano-particles by oxidation-reduction mechanism-New approach in sintering activating by means of oxide nanostructures.* Materials Letters, 2020. **261**: p. 127128.

80. Acsente, T., et al., *Synthesis of flower-like tungsten nanoparticles by magnetron sputtering combined with gas aggregation.* The European Physical Journal D, 2015. **69**(6).

81. Arnas, C., et al., *Thermal balance of tungsten monocrystalline nanoparticles in high pressure magnetron discharges.* Physics of Plasmas, 2019. **26**(5): p. 053706.

82. Stokker-Cheregi, F., et al., *Pulsed laser removal of tungsten nanoparticle aggregates: Surface analysis and visualization of particle ejection dynamics.* Optics & Laser Technology, 2021. **135**: p. 106664.

83. Barik, R.K., et al., *A novel approach to synthesis of scandia-doped tungsten nano-particles for high-current-density cathode applications.* International Journal of Refractory Metals and Hard Materials, 2013. **38**: p. 60-66.

84. Barik, R.K., et al., *Development of Nanoparticle-Based High Current Density Cathode for THz Devices Application.* IEEE Transactions on Electron Devices, 2016. **63**(4): p. 1715-1721.

85. Choi, D. and K. Barmak, *On the potential of tungsten as next-generation semiconductor interconnects.* Electronic Materials Letters, 2017. **13**(5): p. 449-456.

86. Lita, A.E., et al., *Tuning of tungsten thin film superconducting transition temperature for fabrication of photon number resolving detectors.* IEEE transactions on applied superconductivity, 2005. **15**(2): p. 3528-3531.

87. Schottle, C., et al., *Tungsten nanoparticles from liquid-ammonia-based synthesis.* Chem Commun (Camb), 2014. **50**(35): p. 4547-50.

88. Won, C.-W., et al., *Size control of tungsten powder synthesized by self-propagating high temperature synthesis process.* Materials research bulletin, 1999. **34**(14-15): p. 2239-2245.

89. Wu, X.-w., et al., *Crystal growth of tungsten during hydrogen reduction of tungsten oxide at high temperature.* Transactions of Nonferrous Metals Society of China, 2009. **19**: p. s785-s789.

90. Oda, E., K. Ameyama, and S. Yamaguchi, *Fabrication of Nano Grain Tungsten Compact by Mechanical Milling Process and Its High Temperature Properties.* Materials Science Forum, 2006. **503-504**: p. 573-578.

91. Mantica, A.M., M.J. Detisch, and T.J. Balk, *Thermionic Emission Characterization of M-Type Cathodes Using Kelvin Probe in an Ultra-High Vacuum Environment.* IEEE Transactions on Electron Devices, 2023.

92. Zucker, R.V., et al., *New software tools for the calculation and display of isolated and attached interfacial-energy minimizing particle shapes.* Journal of Materials Science, 2012. **47**(24): p. 8290-8302.

93. Aouadi, M.S., et al., *Characterization of sputter deposited tungsten films for x‑ray multilayers.* Journal of Vacuum Science & Technology A: Vacuum, Surfaces, and Films, 1992. **10**(2): p. 273-280.

94. *XPS NIST.* 10 23; 2023:[Available from: https://srdata.nist.gov/xps/EngElmSrchQuery.aspx?EType=PE&CSOpt=Retri_ex_dat&Elm=W.

95. Peignon, M., C. Cardinaud, and G. Turban, *A kinetic study of reactive ion etching of tungsten in SF 6/O 2 RF plasmas.* Journal of the Electrochemical Society, 1993. **140**(2): p. 505.

96. Kosmidou, M., et al., *Vacuum thermal dealloying of magnesium-based alloys for fabrication of nanoporous refractory metals.* MRS Communications, 2019. **9**(1): p. 144-149.

97. Acsente, T., et al., *Tungsten nanoparticles with controlled shape and crystallinity obtained by magnetron sputtering and gas aggregation.* Materials Letters, 2017. **200**: p. 121-124.

98. Gulbransen, E. and K. Andrew, *Kinetics of the oxidation of pure tungsten from 500 to 1300 C.* Journal of the Electrochemical Society, 1960. **107**(7): p. 619.

99. Gulbransen, E., *Oxidation of Tungsten and Tungsten Based Alloys.* Vol. 1. 1960: Wright Air Development Division, Air Research and Development Command, US ….

100. Gulbransen, E. and W. Wysong, *Thin oxide films on tungsten.* TRANSACTIONS OF THE AMERICAN INSTITUTE OF MINING AND METALLURGICAL ENGINEERS, 1948. **175**: p. 611-627.

101. Berkowitz, J., W.A. Chupka, and M.G. Inghram, *Polymeric gaseous species in the sublimation of tungsten trioxide.* The Journal of Chemical Physics, 1957. **27**(1): p. 85-86.

102. Ivanov, V.E.e., *High temperature oxidation protection of tungsten.* Vol. 583. 1969: National Aeronautics and Space Administration.

103. Vaddiraju, S., H. Chandrasekaran, and M.K. Sunkara, *Vapor phase synthesis of tungsten nanowires.* Journal of the American Chemical Society, 2003. **125**(36): p. 10792-10793.

104. Togaru, M., et al., *Direct observation of tungsten oxidation studied by in situ environmental TEM.* Materials Characterization, 2021. **174**: p. 111016.

105. Cifuentes, S.C., M.A. Monge, and P. Pérez, *On the oxidation mechanism of pure tungsten in the temperature range 600–800°C.* Corrosion Science, 2012. **57**: p. 114-121.

106. Hägg, G. and N. Schönberg, *ß-Tungsten'as a tungsten oxide.* Acta Crystallographica, 1954. **7**(4): p. 351-352.

107. Romanyuk, A., et al., *Thermal stability of tungsten oxide clusters.* The Journal of Physical Chemistry C, 2008. **112**(30): p. 11090-11092.

108. Bryl, R. and A. Szczepkowicz, *The influence of the oxygen exposure on the thermal faceting of W[111] tip.* Applied Surface Science, 2006. **252**(24): p. 8526-8532.

109. Szczepkowicz, A., et al., *A comparison of adsorbate-induced faceting on flat and curved crystal surfaces.* Surface Science, 2005. **599**(1-3): p. 55-68.

110. Szczepkowicz, A. and R. Bryl, *From hill-and-valley faceting to global faceting of a crystal: oxygen-covered tungsten.* Surface Science, 2004. **559**(2-3): p. L169-L172.

111. Szczepkowicz, A. and R. Bryl, *Observation of vertex-rounding transition for a crystal in equilibrium: Oxygen-covered tungsten.* Physical Review B, 2005. **71**(11).

112. Szczepkowicz, A., *Oxygen-covered tungsten crystal shape: Time effects, equilibrium, surface energy and the edge-rounding temperature.* Surface science, 2011. **605**(17-18): p. 1719-1725.

113. Szczepkowicz, A., *The kinetics of hill-and-valley faceting of oxygen-covered tungsten.* Surface Science, 2012. **606**(3-4): p. 202-208.

114. Seif, M.N., T.J. Balk, and M.J. Beck, *Deducing surface chemistry and annealing conditions from observed nanoparticle shapes: A study of scandate cathodes.* Applied Surface Science, 2022: p. 154541.

115. Belyaeva, A., et al., *Surface energy anisotropy for the low-index crystal surfaces of the textured polycrystalline bcc tungsten: experimental and theoretical analysis.* Вопросы атомной науки и техники, 2017.

116. Wang, S., E. Tian, and C. Lung, *Surface energy of arbitrary crystal plane of bcc and fcc metals.* Journal of Physics and Chemistry of Solids, 2000. **61**(8): p. 1295-1300.

117. Yu, H., et al., *Surface terraces in pure tungsten formed by high temperature oxidation.* Scripta Materialia, 2019. **173**: p. 110-114.

118. Bai, H. and T.J. Balk. *Observations of Temperature-Induced Material Transformations in Impregnated Scandate Cathode Samples During in situ Heating in the SEM.* in *2022 23rd International Vacuum Electronics Conference (IVEC).* 2022. IEEE.

119. Balk, T.J., et al. *Characterization of the materials, phases and morphology typical of high-performance scandate cathodes*. in *2022 23rd International Vacuum Electronics Conference (IVEC)*. 2022. IEEE.

120. Gao, J.Y., et al., *A review on recent progress of thermionic cathode.* Tungsten, 2020. **2**(3): p. 289-300.

121. Zhang, X., et al. *Effects of Scandia distribution on surface structure of scandate cathodes*. in *2018 IEEE International Vacuum Electronics Conference (IVEC)*. 2018. IEEE.

122. Lu, Z., et al., *Study on Low-Temperature Emission Performance of Scandate Cathode with Micro-Blade-Type Arrays.* Materials, 2019. **13**(1): p. 100.

123. Seif, M.N., T.J. Balk, and M.J. Beck, *Desorption from Hot Scandate Cathodes: Effects on Vacuum Device Interior Surfaces after Long-Term Operation.* Materials (Basel), 2020. **13**(22).

124. Wang, J.-S., et al., *Reduction behavior of tungsten oxide with and without scandia doping.* Rare Metals, 2021. **40**: p. 687-692.

125. Balk, T.J., Bai, H., Detisch, M.J., & Vancil, B., K., *The Nature and Distribution of Materials at the Emitting Surface and Throughout the Thickness of High-Performance Scandate Cathodes*, in *International IEEE Vacuum Electronics Conference (IVEC)*. 2024, IEEE: Monterey, California.

126. Liu, X., et al. *Analysis of faceted tungsten grains on the surfaces of scandate cathodes fabricated from LS and LL powders*. in *2018 IEEE International Vacuum Electronics Conference (IVEC)*. 2018. IEEE.

127. Bartlett, R. and J. McCamont, *The influence of crystal orientation on the oxidation of tungsten.* Journal of The Electrochemical Society, 1965. **112**(2): p. 148.

128. Mántica, A.M., M.J. Detisch, and T.J. Balk, *High-temperature contact potential difference measurement of surface work function using in vacuo Kelvin probe.* Vacuum, 2023: p. 112169.

129. Oleksy, C., *Solid-on-solid model of overlayer-induced faceting.* Surface science, 2004. **549**(3): p. 246-254.

130. Meltzman, H., et al., *The equilibrium crystal shape of nickel.* Acta Materialia, 2011. **59**(9): p. 3473-3483.

131. Chatain, D., V. Ghetta, and P. Wynblatt, *Equilibrium shape of copper crystals grown on sapphire.* Interface Science, 2004. **12**: p. 7-18.

132. Chatain, D., P. Wynblatt, and G.S. Rohrer, *Equilibrium crystal shape of Bi-saturated Cu crystals at 1223 K.* Acta materialia, 2005. **53**(15): p. 4057-4064.

133. Madey, T.E., et al., *Nanoscale surface chemistry over faceted substrates: structure, reactivity and nanotemplates.* Chemical Society Reviews, 2008. **37**(10): p. 2310-2327.

134. Khyzhun, O.Y., *XPS, XES and XAS studies of the electronic structure of tungsten oxides.* Journal of Alloys and Compounds, 2000. **305**(1-2): p. 1-6.

135. Wilkinson, P., *The properties of evaporated gold and tungsten oxides.* Journal of Applied Physics, 1951. **22**(2): p. 226-232.

136. Gulbransen, E., K. Andrew, and F. Brassart, *Kinetics of oxidation of pure tungsten, 1150°–l615° C.* Journal of the Electrochemical Society, 1964. **111**(1): p. 103.

137. Blackburn, P.E., M. Hoch, and H.L. Johnston, *The vaporization of molybdenum and tungsten oxides.* The Journal of Physical Chemistry, 1958. **62**(7): p. 769-773.

138. Schlueter, K. and M. Balden, *Dependence of oxidation on the surface orientation of tungsten grains.* International Journal of Refractory Metals and Hard Materials, 2019. **79**: p. 102-107.

139. Schlueter, K., M. Balden, and T.F. da Silva, *Evaluating crystal-orientation-dependent properties on polycrystalline tungsten: Example oxidation.* International Journal of Refractory Metals and Hard Materials, 2020. **88**: p. 105189.

140. Swartzentruber, P.D., T. John Balk, and M.P. Effgen, *Correlation between microstructure and thermionic electron emission from Os-Ru thin films on dispenser cathodes.* Journal of Vacuum Science & Technology A, 2014. **32**(4).

141. Swartzentruber, P.D., M.J. Detisch, and T.J. Balk, *Composition and work function relationship in Os–Ru–W ternary alloys.* Journal of Vacuum Science & Technology A, 2015. **33**(2).

142. Liu, X., et al., *Observation of Ultrathin Sc-Containing Surface Layer on Life-Tested Scandate Cathodes.* IEEE Transactions on Electron Devices, 2023.

143. Gong, T., et al. *Environmental Stability of 612-aluminate with Different Phase Structures*. in *2023 24th International Vacuum Electronics Conference (IVEC)*. 2023. IEEE.

144. Sun, J., et al. *Investigation on Scadium Thin Films on Dispenser Cathodes*. in *2023 24th International Vacuum Electronics Conference (IVEC)*. 2023. IEEE.

145. Cai, Y., et al., *Synthesis of impregnants for dispenser cathodes via homogeneous-lyophilization: Phase structure, optical response and emission property of four aluminates.* Ceramics International, 2024. **50**(7): p. 11341-11350.

146. Seif, M.N., et al., *A Review of Sc-containing" Scandate" Thermionic Cathodes.* arXiv preprint arXiv:2202.04745, 2022.

147. Seif, M.N., et al., *Sc-Containing (Scandate) Thermionic Cathodes: Fabrication, Microstructure, and Emission Performance.* Ieee Transactions on Electron Devices, 2022. **69**(7): p. 3513-3522.

148. Seif, M.N., et al., *Sc-containing (scandate) thermionic cathodes: Mechanisms for Sc enhancement of emission.* IEEE Transactions on Electron Devices, 2022. **69**(7): p. 3523-3534.

149. Kapustin, V., et al., *Physical operating principles of scandate cathodes for microwave devices.* Technical Physics, 2017. **62**: p. 116-126.

150. Shukla, S., A. Singh, and R. Barik, *Synthesis of Rhenium–Scandia doped tungsten nanoparticles for shrinkage investigation.* Journal of Sol-Gel Science and Technology, 2020. **95**(2): p. 384-392.

151. Wang, J., et al., *Sc2O3–W matrix impregnated cathode with spherical grains.* Journal of Physics and Chemistry of Solids, 2008. **69**(8): p. 2103-2108.

152. Gao, J., et al., *The effect of Ir and Sc on the emission capacity of W-Ir matrix scandate cathodes prepared via a novel in situ method.* Acta Materialia, 2023: p. 119400.

153. Zhou, Y., et al., *Thermionic Emission Capability of the Ba–Sc–Al–O Compound Synthesized by High-Temperature Solid-State Process.* IEEE Transactions on Electron Devices, 2023. **70**(3): p. 1294-1298.

154. Wang, M., et al., *Effect of tungsten powder particle shape on the emission properties of the barium tungsten cathode.* Advanced Powder Technology, 2023. **34**(9): p. 104133.

155. Podor, R., et al., *Direct Observation of the Surface Topography at High Temperature with SEM.* Microsc Microanal, 2020. **26**(3): p. 397-402.

156. Gregori, G., et al., *In situ SEM imaging at temperatures as high as 1450 C.* Microscopy, 2002. **51**(6): p. 347-352.

157. Bai, H., Briot, N. J., Beck, M., & Balk, T. J. , *Crystallographic Faceting of Bulk Tungsten Surfaces Observed During In Situ Heating in an Environmental Scanning Electron Microscope.* Materials Characterization, 2024. **212**: p. 113925.

158. Howe, J., et al., *Early Experiments with a New In Situ SEM Heating Technology.* Microscopy and Microanalysis, 2017. **17**(S2): p. 432-433.

159. Mujin, M., M. Nakamura, and M. Matsumoto, *In-situ FE-SEM observation of the growth behaviors of Fe particles at magmatic temperatures.* Journal of Crystal Growth, 2021. **560-561**: p. 126043.

160. Vancil, B., et al. *Recent Progress on Scandate Cathodes*. in *2020 IEEE 21st International Conference on Vacuum Electronics (IVEC)*. 2020. IEEE.

161. Kresse, R., et al., *Barium and barium compounds.* Ullmann's encyclopedia of industrial chemistry, 2000.

162. Wang, Y., et al., *Emission mechanism of high current density scandia-doped dispenser cathodes.* Journal of Vacuum Science & Technology B, Nanotechnology and Microelectronics: Materials, Processing, Measurement, and Phenomena, 2011. **29**(4): p. 04E106.

163. Busbaher, D., et al. *Performance comparison between sintered tungsten dispenser cathodes and nano-composite scandate dispenser cathodes*. in *2013 IEEE 14th International Vacuum Electronics Conference (IVEC)*. 2013. IEEE.

164. Huang, Z., et al., *Structure and emission properties of barium calcium aluminates synthesized by room-temperature solid-state reaction approach.* Materials Chemistry and Physics, 2021. **263**: p. 124418.

165. Swartzentruber, P., et al. *Direct work function measurement of activated M-type dispenser cathodes*. in *IEEE International Vacuum Electronics Conference*. 2014. IEEE.

166. Kordesch, M., et al. *Model scandate cathodes investigated by thermionic emission microscopy*. in *2010 8th International Vacuum Electron Sources Conference and Nanocarbon*. 2010. IEEE.

167. Kordesch, M.E. and C. Wan. *Barium de-wetting and thermionic emission from Ba on W*. in *2013 26th International Vacuum Nanoelectronics Conference (IVNC)*. 2013. IEEE.

168. Zheng, Q., et al., *Effect of Sc2O3 addition on the phase composition and electron emission performance of Co-precipitated aluminates for impregnated cathodes.* Ceramics International, 2021. **47**(13): p. 18831-18837.

169. Vaughn, J.M., et al., *Thermionic electron emission microscopy of metal-oxide multilayers on tungsten.* IBM Journal of Research and Development, 2011. **55**(4): p. 14: 1-14: 6.

170. Worthing, A., *The true temperature scale of tungsten and its emissive powers at incandescent temperatures.* Physical Review, 1917. **10**(4): p. 377.

171. Rutgers, G.A.W. and J.C. De Vos, *Relation between brightness, temperature, true temperature and colour temperature of tungsten. Luminance of tungsten.* Physica, 1954. **20**(7-12): p. 715-720.

172. Bai, H.B., T. J., *Observation of Growth and Faceting of Scandate Cathode Particles by In Situ Heating in SEM*

173. Wang, J., et al., *Advances in high emission Sc 2 O 3-W matrix cathode materials.* Applied Microscopy, 2016. **46**(1): p. 20-26.

174. Wang, J., et al., *A review on scandia doped tungsten matrix scandate cathode.* Tungsten, 2019. **1**: p. 91-100.

175. Seif, M.N., T.J. Balk, and M.J. Beck. *Temperature effects on desorption behavior and characteristic wulff shapes of scandate cathodes*. in *2020 IEEE 21st International Conference on Vacuum Electronics (IVEC)*. 2020. IEEE.

176. Van Oostrom, A. and L. Augustus, *Activation and early life of a pressed barium scandate cathode.* Applications of Surface Science, 1979. **2**(2): p. 173-186.

177. Zhang, X., *The Study of Scandate Cathode and Its Characterization Under Various Stages of Processing*. 2019.

178. Liu, X., et al. *Characterization of scandate cathode at different stages of processing*. in *2018 IEEE International Vacuum Electronics Conference (IVEC)*. 2018. IEEE.

179. Miller-Murthy, S., M. Seif, and M.J. Beck, *Scandium wetting of tungsten surfaces in "scandate" thermionic cathodes*. Surfaces and Interfaces, 2022. **35**: p. 102476.

180. Wang, Y., et al., *Development of high current-density cathodes with scandia-doped tungsten powders*. IEEE Transactions on Electron Devices, 2007. **54**(5): p. 1061-1070.

181. Liu, X., et al. *Characterization of Material Phases on the Surface and in the Near-Surface Region of Scandate Cathodes*. in *2020 IEEE 21st International Conference on Vacuum Electronics (IVEC)*. 2020. IEEE.

182. Selcuk, C., et al., *Effect of basic powder particle properties on densification of porous tungsten*. Powder metallurgy, 2003. **46**(2): p. 117-120.

183. Selcuk, C., N. Morley, and J. Wood, *Porous tungsten with controlled porosity by low temperature sintering*. Powder metallurgy, 2005. **48**(1): p. 17-22.

184. Yuan, H., et al., *Characteristics of scandate-impregnated cathodes with sub-micron scandia-doped matrices*. Applied surface science, 2005. **251**(1-4): p. 106-113.

185. Yamamoto, S., et al., *Formation mechanism of a monoatomic order surface layer on a Sc-type impregnated cathode*. Japanese Journal of Applied Physics, 1989. **28**(3R): p. 490.

186. Yamamoto, S., et al., *Work function and microstructure of a monoatomic order surface layer grown on a (W　Sc2W3O12)-coated impregnated cathode*. Vacuum, 1990. **41**(7-9): p. 1759-1762.

187. Yamamoto, S., et al., *Electron emission enhancement of a (W-Sc2O3)-coated impregnated cathode by oxidation of the coated thin film*. Japanese journal of applied physics, 1988. **27**(8R): p. 1411.

188. Selcuk, C. and J. Wood, *Reactive sintering of porous tungsten: A cost effective sustainable technique for the manufacturing of high current density cathodes to be*

used in flashlamps. Journal of materials processing technology, 2005. **170**(1-2): p. 471-476.

189. Selcuk, C., et al., *Reactive sintering of porous tungsten for higher homogeneity.* Powder metallurgy, 2004. **47**(1): p. 81-84.

190. Selcuk, C., N. Morley, and J. Wood, *Effect of post-sintering heat treatment on porous tungsten in relation to sintering swelling.* Powder metallurgy, 2004. **47**(3): p. 267-272.

191. Yıldız, Y.G., *Exchange bias effect revealed by irreversible structural transformation between the HCP and FCC structures of Cobalt nanoparticles.* Phase Transitions, 2020. **93**(4): p. 429-437.

192. *Cobalt.* [cited 2024 03/14]; Available from: https://web.archive.org/web/20081002060936/http://www.americanelements.com/co.html.

193. Ram, S., *Allotropic phase transformations in HCP, FCC and BCC metastable structures in Co-nanoparticles.* Materials Science and Engineering: A, 2001. **304**: p. 923-927.

194. He, J., *A Study of the Electron Beam Scattering Under Various Gaseous Environment.* 2003.

195. Group, M.E.M.R. *Monte Carlo programs.* 2023 [cited 2023 12-16]; Available from: https://www.memrg.com/programs-download.

196. Haglöf, F., et al., *Experimental study of carbides in the Ti–Cr–C system.* Journal of Materials Science, 2019. **54**: p. 12358-12370.

<center>VITA</center>

Huanhuan Bai was born in Xiang Yang, Hubei province, China. She worked as a materials engineer in industry from 2016 to 2018. Later she joined Prof. Dr. T. John Balk's research group at the University of Kentucky in September 2018 for the pursuit of a Ph.D. degree in Materials Science and Engineering.

Education:

2009 – 2013 B.S., Material Science and Engineering, University of Science and Technology　Beijing, China

2013 – 2016 M.S., Material Science and Engineering, University of Science and Technology　Beijing, China

Honors and Awards:

2023 Outstanding MSE Graduate Student Award

Publications:

Peer reviewed journal papers:

1. **Huanhuan Bai**, Nicolas J. Briot, Matthew J. Beck, and T. John Balk. "Crystallographic faceting of bulk tungsten surfaces observed during *in situ* heating in an environmental scanning electron microscope." *Materials Characterization* (**2024**): 113925. https://doi.org/10.1016/j.matchar.2024.113925

2. **Huanhuan Bai**, Tyler L. Maxwell, Martin E. Kordesch, T. John Balk. "Physical Vapor Deposition and Thermally Induced Faceting of Tungsten nanoparticles." *Materials Characterization,* **198**, p. 112724 (**2023**). https://doi.org/10.1016/j.matchar.2023.112724

3. Wuqiang Yang, Min Xu, **Huanhuan Bai,** Ye Meng, Litao Wang, Lifa Shi, Yinghao Pei, Jian Zhang, Lei Zheng. "Concentration depth distribution of grain boundary segregation measured by wavelength dispersive X-ray spectroscopy." Ultramicroscopy, 159, pp. 432-437, **2015**. https://doi.org/10.1016/j.ultramic.2015.03.004

4. **Huanhuan Bai**, Ping Yang, Understanding the Weiss Zone Law. Metal World, **2013**.

Conference papers

1. **Huanhuan Bai** and Thomas John Balk. "Observations of Temperature-Induced Material Transformations in Impregnated Scandate Cathode Samples During in situ Heating in the SEM." 2022 23rd International Vacuum Electronics Conference (IVEC). IEEE, **2022**.

2. T. John Balk, Michael J. Detisch, **Huanhuan Bai**, Xiaotao Liu, Mujan N. Seif, Matthew J. Beck and Bernard K. Vancil. "Characterization of the Materials, Phases and Morphology Typical of High-Performance Scandate Cathodes." IEEE 21st International Conference on Vacuum Electronics (IVEC), **2022**.

3. **Huanhuan Bai**, Matthew J. Beck, and Thomas John Balk. "Deposition of Tungsten Nanoparticles for Potential Use in Dispenser Cathodes." IEEE 21st International Conference on Vacuum Electronics (IVEC), pp. 389-390, **2020**.

Presentations:

Gave a poster presentation at conference *21st International Conference on Vacuum Electronics (IVEC), 2022* in California (April 2022).